Engineered Damping :

From mitigating impacts through hierarchical structured materials to enhancing actuation forces via non-Hermitian metamaterials.

By

Abhishek Gupta

A dissertation submitted in partial fulfillment
of the requirements for the degree of

Doctor of Philosophy
(Mechanical Engineering)

at the
UNIVERSITY of WISCONSIN-MADISON
2024

Date of Final Oral Exam: 05/07/2024

The dissertation is approved by the following members of the Final Oral Committee:

Ramathasan Thevamaran, Assistant Professor, Mechanical Engineering
Christian Franck, Professor, Mechanical Engineering
Melih Eriten, Associate Professor, Mechanical Engineering
Pavana Prabhakar, Associate Professor, Civil and Environmental Engineering
Jacob Notbohm, Associate Professor, Mechanical Engineering

Abstract

This thesis focuses on two interdependent research thrusts: (i) investigating the fundamental structure-property-function relationship in hierarchically architected vertically aligned carbon nanotube (VACNT) foams for mitigating impacts in sports and military that could cause traumatic brain injury, and (ii) investigating the formation of exceptional points (EP) in passive non-Hermitian metamaterials with viscoelastic damping, and experimentally demonstrating the enhancement of an applied actuation force in the vicinity of an EP. Both research thrusts are centered around utilizing engineered damping to create novel materials and structures suitable for extreme engineering applications.

VACNT foams are renowned for their exceptional energy absorption capabilities, which rival those of stochastic metallic foams, while they are lightweight with mass densities comparable to polymeric foams. However, transitioning these foams from the laboratory to engineering applications requires addressing fundamental knowledge gaps in the structure-property-function relationship. We performed a comprehensive structural and mechanical characterization of VACNT foams using synchrotron X-ray scattering, quasistatic compression, stress-relaxation, and broadband dynamic mechanical analysis (DMA).

When subjected to quasistatic compression, VACNT foams exhibit a preconditioning effect—a softening in the constitutive stress-strain response with increasing compression cycles. Contrary to the prevailing belief that the preconditioning effect arises from mesoscale reorganization of fibers, the synchrotron X-ray scattering experiments we performed as function of the compression cycles revealed that the preconditioning occurs due to a nanoscale permanent strain induced in the walls of multi-walled CNTs, in addition to mesoscale rearrangement of fibers.

The range of experiments—from stress-relaxation and quasistatic compression to dynamic mechanical analysis we performed across broad frequency, amplitude, and pre-strain levels—reveal that the VACNT foams exhibit strain-rate-independent behavior. As the viscoelastic models typically used for damping are unsuitable for modeling VACNT foams, we have developed a rate-independent model based on frictional damping, incorporating springs and frictional elements to represent the stiffness of nanotube bundles and van der Waals frictional interactions between nanotubes. This model effectively captures both the quasistatic and dynamic mechanical behavior of VACNT foams,

providing a physics-based accurate representation compared to existing models.

To enhance the specific energy absorption in VACNT foams, we further introduce mesoscale architectures of thin close packed cylinders, concentric cylinders, and nested fractal cylinders, which exploit the structural characteristics of the additional hierarchy as well as the interactive fiber morphology. We discovered a synthesis-induced size effect that promotes more vertical alignment and denser packing of CNTs in confined regions that lead to significantly enhanced specific energy absorption. Along with this size-effect, tailoring the architecture's geometric parameters in the concentric cylinders allowed us to achieve a desirable linear density-dependent scaling of mechanical properties in VACNT foams. This linear scaling enables achieving much low density foams without significantly reducing their mechanical properties.

As designing protective materials require not only the consideration of mechanical properties of the materials, but also the protective pad's geometry, we have developed a scale-free dimensional analysis-guided framework that facilitates the design of thin and lightweight energy-absorbing materials that can effectively absorb kinetic energy while limiting acceleration and compressive strain within specified desirable limits. Our findings and the analytical design framework not only enhance the fundamental understanding of VACNT foams and similar fibrous structured materials but also open up new avenues for the design of architected materials for various protective applications.

On contrary to the above utility of energy absorbing materials for impact mitigation, the recent emergence of non-Hermitian physics and the notion of EPs in elastodynamics has promoted damping as a novel design element for creating dynamical symmetries to achieve novel functionalities. While sharp orthogonal bifurcation of eigenmodes at the EP has been utilized to create hyper-sensitive sensors, their realization require gain, typically achieved through active feedback control mechanisms. In our study, we show that viscoelastic materials respecting the Kelvin-Voigt fractional derivative model exhibit a desirable, nearly frequency-independent loss tangent. Such materials used as a non-Hermitian element in an entirely passive dynamical systems can still lead to a desirable sharp bifurcation at an EP. Additionally, we experimentally demonstrate the formation of an EP in a passive elastodynamic system and its ramification in achieving an unusual enhancement of an applied actuation force. Our EP-based actuation enhancement boosts the conventional Purcell amplification by a universal factor of 2 while maintaining the quality (Q-factor) of the signal at a constant value. These findings open up new possibilities for utilizing viscoelastic materials to

realize EPs in passive elastic systems and exploit them not only for hypersensitive sensing, but also to enhance actuation in a new class of mechanical indenters and robotic actuators.

Dedication

To all the custodians of science.

Declaration

I hereby declare that this thesis is my own work, and all sources of information have been acknowledged and referenced appropriately.

Acknowledgements

First and foremost, I would like to express my deepest gratitude to my PhD advisor, Prof. Ramathasan Thevamaran. His guidance has been instrumental in shaping my PhD journey and fostering my professional as well as personal growth. His zeal for pursuing challenging projects and ability to motivate us to bring out-of-the-box quality in our work has been the highlight of our mentor-mentee relationship. In addition to mentoring me in research, Prof. Thevamaran has also played the role of a career coach. From the moment I expressed my desire to pursue academia and become a tenure-track faculty member at an R1 university, he has consistently supported my ambition and tailored his mentoring approach to guide me towards my goal. His quote "In our lives, we don't often encounter many opportunities to shine, so we must seize those chances when they arise." is the wisest and deepest advice I have ever received. I will forever be grateful for my time spent in Thevamaran Lab and thankful to Prof. Thevamaran for being the chief architect in shaping my career.

I would like to express my gratitude to all of my collaborators, especially Prof. Tsampikos Kottos from Wesleyan University and Dr. Eric Meshot from Lawrence Livermore National Lab. Their expertise in their respective fields has been a great source of knowledge and inspiration. I am also grateful to all of my coauthors with whom I have published exciting and acclaimed research articles: Dr. Steven Weigand, Dr. Denis T. Keane, Dr. Komal Chawla, Dr. Arkady Kurnosov, Dr. Jizhe Cai, Dr. Claire Griesbach, Dr. Yanghao Fang, William Tuxbury, and Dr. Abhijeet Bhardwaj. I extend my gratitude to my committee members, Prof. Christian Franck, Prof. Pavana Prabhakar, Prof. Melih Eriten, and Prof. Jacob Notbohm. Their guidance and mentorship during my qualifying exam and preliminary exam have greatly improved the quality of my dissertation. I am also thankful to all the faculty I took courses with and the department

staff, especially Sara Hladilek, Caitlin Scott, Kassi Akers, Dina Christenson, and Kathy Wegner, for their help with various aspects of my degree progression, lab purchases, and affairs related to student organization GEMS.

I am incredibly grateful to my labmates for giving me a conducive environment for collaboration and learning together. A huge shout-out to Yanghao Fang, Bhanugoban Maheswaran, Mathushan Manivannan, Paranjoy Basak, and Daniyar Syrlybayev. I have also had the privilege of mentoring undergraduate researchers in Thevamaran Lab: Dhanvi Bharadwaj, Jiayan Zhang, and Nicholas Jaegersberg. It is really satisfying to see them transition into graduate school.

My life in Madison wouldn't have been as eventful if it weren't for the friends I made here, especially Ahlan, Akash, Vipul, Bhumesh, Nidhi, Kanika, and Abhijeet. I am also grateful to my friends in India, with whom I stayed connected remotely and shared the ups and downs of my PhD journey. Above all, I thank my parents, my grandmother, and my sister for trusting me to travel halfway around the world in pursuit of my ambition. I am grateful to the University of Wisconsin-Madison for allowing me to become a part of the Wisconsin Idea and positively impact society with my research. As a proud Badger, I will continue to pursue my curiosity for science, educating and influencing people's lives through scientific research and innovations.

Research and innovation thrive on the support of dedicated funding agencies and government programs, without which many scientific pursuits would not be possible. I would like to acknowledge the financial support (Award Number W911NF2010160) provided by the Solid Mechanics Program of the U.S. Army Research Office through Dr. Denise Ford. This funding was instrumental in advancing my fundamental research on VACNT foams and non-Hermitian metamaterials, allowing me the freedom to build custom experimental setups by purchasing cutting-edge scientific instruments, thereby enriching my experimental work. Additionally, I am thankful for the support from the U.S. Office of Naval Research under the PANTHER program (Award Number N000142112044) through Dr. Timothy Bentley. This funding supported my work on developing architected VACNT foams for shock-absorbing applications. The resources and opportunities provided by both funding agencies significantly enriched my PhD journey, enabling me to explore innovative ideas and make meaningful contributions to my field.

Contents

List of Figures

List of Tables

Chapter 1

Introduction

1.1 Goals and contributions

The goals of this dissertation are twofold: (i) To investigate the fundamental structure-property-function relationship in hierarchical vertically aligned carbon nanotube foams for applications in impact mitigation. (ii) To theoretically study the formation of exceptional points (EP) in passive elastodynamic systems with viscoelasticity and experimentally demonstrating an actuation force enhancement in the vicinity of EP. Following are the key contributions of this thesis

- **Key contribution made in research thrust-I**

    1. We present direct measurements and evidence for the nanoscale origin of mechanical preconditioning in hierarchical vertically aligned carbon nanotube foams by performing synchrotron X-ray scattering and mass attenuation measurements.
    2. We have developed the most accurate constitutive model known to date for VACNT foams, employing rate-independent multi-scale frictional damping. Our model explains the origin of the Payne effect in VACNT foams and similar fibrous materials.
    3. In VACNT foams with mesoscale architectures, we demonstrate a synergistic enhancement in energy absorption, compressive strength, and modulus at low densities. This enhancement is attributed to a synthesis-induced size effect resulting from confined CNT growth. Additionally, we show a desirable linear density-dependent scaling of mechanical properties, enabling lightweight materials with constant specific (density-normalized)

properties.

4. We have developed a scale-free dimensional analysis-guided framework for the design of shock absorbers. This framework enables creating effective shock-absorbers to dissipate kinetic energy from impacts while maintaining acceleration and maximum compression strain within desired limits.

- **Key contributions made in research thrust-II**

1. We investigate the requirements for the dynamic mechanical properties of viscoelastic materials to achieve exceptional points in passive elastic systems. We discover that viscoelastic materials following the Kelvin-Voigt fractional derivative model exhibit a nearly frequency-independent loss tangent. This property allows for the achievement of exceptional points with sharp orthogonal bifurcation.

2. We experimentally demonstrate exceptional points in an elastodynamic metamaterial system of coupled oscillators with non-Hermitian differential loss, achieved using viscoelastic polydimethylsiloxane (PDMS), a KVFD material. Additionally, we showcase an unusual enhancement of the applied actuation force when the system operates in the vicinity of an exceptional point. This is a first-of-its-kind experimental demonstration of emissivity enhancement due to an exceptional point in any physical system.

1.2 Background and motivation

Materials that dissipate energy upon the application of an external load are useful in various protective and shock absorbing applications [1–3]. These dissipative materials permeate all aspects of our daily lives, from the protective foam liners in helmets to the soles of our shoes. Our bodies themselves are naturally equipped with skin and soft tissues to protect our internal organs from blunt impacts and life-threatening injuries. Materials such as cork, luffa, clay, nacre, and seashells are some examples of naturally occurring dissipative and protective materials [4, 5]. On the other hand, polymeric and metallic foams, rubbers, soft composites, and architected lattice materials are some examples of man-made dissipating materials [6–8]. The performance of a dissipative material hinges on its ability to absorb a significant amount of energy while exerting minimal force on the

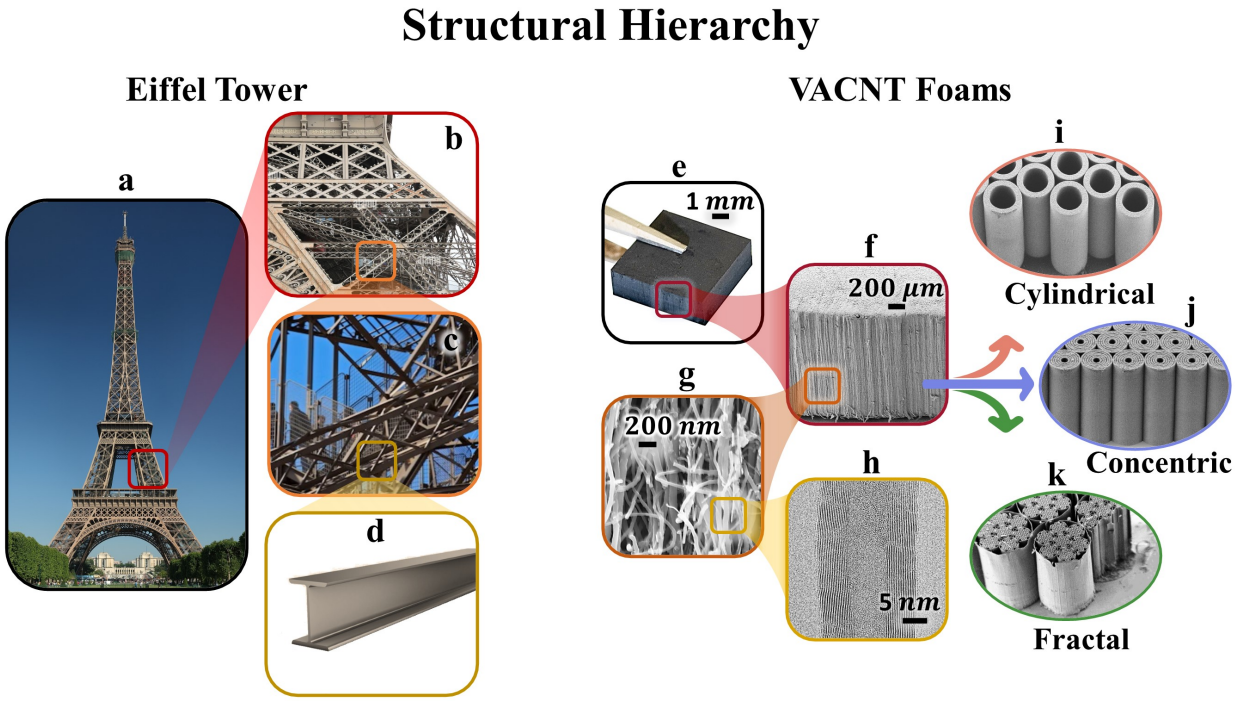

Figure 1.1: (a) The Eiffel Tower and its multiscale structural hierarchy, spanning from tens of meters (b) to the centimeter (c, d) scale (source: eiffeltickets.com). Scanning electron microscopy (SEM) images of hierarchical vertically aligned carbon nanotube (VACNT) foam with multiscale structural hierarchy from the macroscale (e) to the nanoscale (h). Architected VACNT foams with different mesoscale architectures (i, j, k).

protected object. Additionally, these materials must possess strength, lightweight, fracture resistance, and thermal stability across a broad temperature range, from the freezing cold of the Arctic to the scorching heat of the Sahara. However, these properties are typically mutually exclusive; improving one quality often comes at the expense of another [9–11]. For example, mechanical properties such as strength and stiffness are directly proportional to density, making it challenging to achieve superior mechanical properties in lightweight materials using conventional methods. Many natural materials have evolved to become simultaneously strong, tough, and lightweight due to their efficient multilevel hierarchical structure [10, 12]. Adopting hierarchical architectures in synthetic materials has resulted in lightweight mechanically-effective structures with synergistic improvement in otherwise antagonistic properties [11]. One such material is hierarchical vertically aligned carbon nanotubes (VACNT) foams that we predominantly investigate in this thesis [13].

1.3 Hierarchical VACNT foams

Vertically aligned carbon nanotube (VACNT) foams are touted for their superior energy absorption, high stiffness, fracture strength, and thermal stability, all while remaining lightweight [11, 13, 14]. These properties arise from a multi-length scale hierarchical structure that spans from the macro-scale to the nanoscale. In Figure 1.1, we present a side-by-side analogy of the structural hierarchy of the Eiffel Tower, a large-scale structure, and our VACNT foam. The multi-length scale structural hierarchy of the Eiffel Tower contributes to its strength and incredibly lightweight design. Calculations show that if we were to pack the Eiffel Tower in a rectangular box, the amount of air in the box would weigh even more than the tower itself. This is due to its construction using self-similar truss structures at larger and intermediate length scales (Figure 1.1(b,c)), eventually leading up to I-cross-section beams as the smallest components (Figure 1.1(d)). Similarly, VACNT foams exhibit a rich structural hierarchy starting from individual multi-walled CNTs at the nanoscale (Figure 1.1(h)), a random forest of entangled CNTs at the microscale (Figure 1.1(g)), and a structure of nominally vertically aligned CNTs at the mesoscale (Figure 1.1(f)) all culminate in a monolithic, seemingly solid foam at the macroscale (Figure 1.1(e)). This structural hierarchy makes VACNT foams very lightweight, with densities (approximately 200 kg/m^3) comparable to commonly used polymeric foams [13].

1.3.1 FCCVD synthesis and mechanical properties

We synthesize VACNT foams using a floating catalyst chemical vapor deposition (FCCVD) process [11, 15]. This process involves injecting a solution of Toluene (carbon source) and Ferrocene (iron catalyst) into a furnace heated to 1100 Kelvin (Figure 1.2(a)). At this temperature, the Toluene vaporizes and breaks down into individual carbon atoms. A mixture of Argon and Hydrogen gases carries the Toluene inside the furnace, where the carbon atoms bond together to form carbon nanotube samples on silicon wafer substrates placed inside the furnace. On a plain silicon wafer, the CNTs grow over the entire surface, resulting in a non-architected VACNT foam (Figure 1.1(f)). Due to the bottom-up growth nature of CNTs (Figure 1.2(b)), as the sample grows, more CNTs nucleate, and the density of CNTs keeps increasing with height, resulting in an overall linear density gradient [14, 15], with the bottom region (substrate side) being less dense compared to

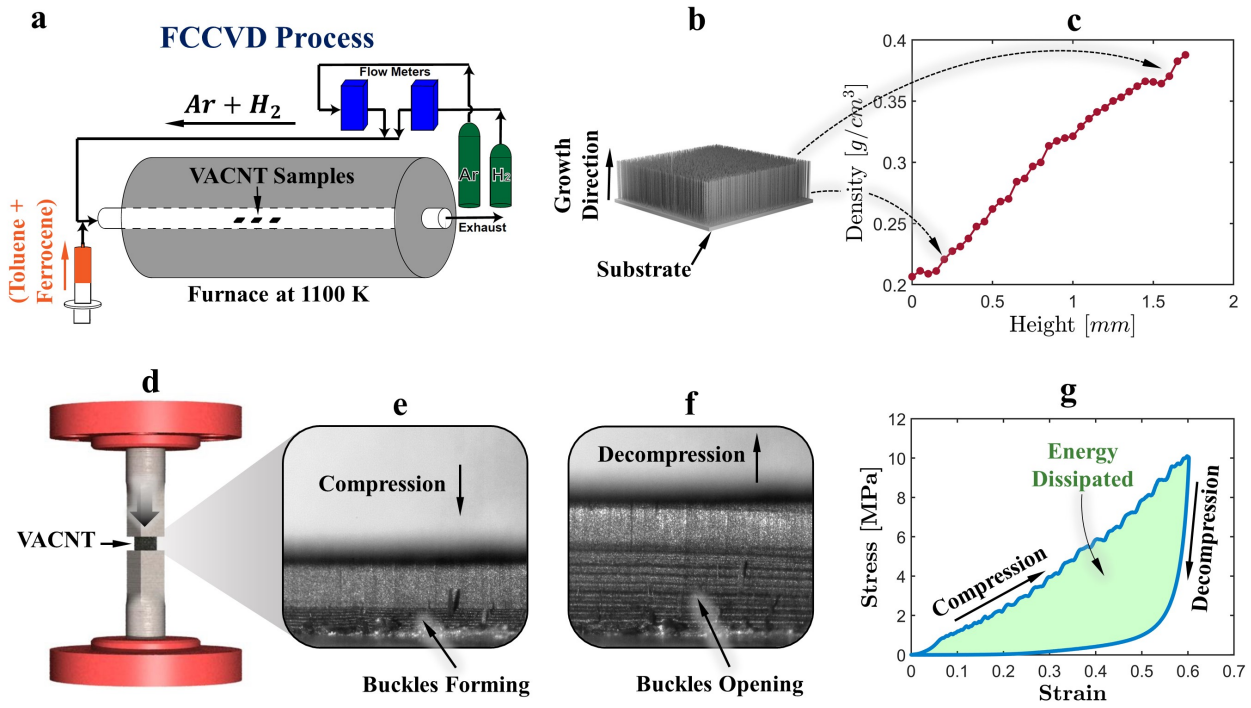

Figure 1.2: (a) An illustration of the floating catalyst chemical vapor deposition (FCCVD) process for synthesizing VACNT foams. (b) An illustration of a VACNT sample grown on a silicon wafer substrate. (c) Variation of mass density as a function of height. (d) An illustration showing quasistatic compression of a VACNT foam sample. (e,f) High-speed camera images of a VACNT foam sample undergoing compression and decompression. (g) Quasistatic measured stress-strain response of a VACNT foam sample showing energy dissipated within the stress-strain cycle.

the top region (Figure 1.2(c)). This synthesis-induced density gradient influences how the VACNT foam behaves under an exerted compressive load (Figure 1.2(d)).

When a VACNT foam sample is compressed, the lower density bottom region, which is proportionally softer, collapses first by forming buckles—a wavy folding pattern on the surface (Figure 1.2(e)). As the sample is compressed further, the buckles propagate upwards from the bottom to the top, while the denser and stiffer topmost region remains almost intact [14, 15]. Upon releasing the compressive load, the buckles open like springs, resulting in almost complete recovery ($\sim$ 90%) of the sample (Figure 1.2(f)). During this compression and decompression cycle, the VACNT foam dissipates an enormous amount of energy due to the frictional interactions between the individual nanotubes (Figure 1.2(g)). This energy dissipation (W_{dis}) is generally an order of magnitude higher than that of commonly used polymeric foams with similar densities [13]. Furthermore, the mechanical properties of VACNT foams are thermally stable over a wide range of temperatures, from very cold (-196°C) to very high temperatures (1000°C), unlike polymeric foams [16].

1.3.2 Architected VACNT foams

While non-architected VACNT foams exhibit exceptional mechanical properties, their properties can only be tuned by varying synthesis parameters such as ferrocene concentration, hydrogen percentage, and furnace temperature, which have a limited range of tunability [17]. To achieve better tunability in mechanical properties suitable for various applications, we introduce an additional level of structural hierarchy by incorporating mesoscale architectures [11, 18]. Figure 1.2(i,j,k) shows SEM images of three different architected VACNT foams with mesoscale architectures of closely packed hollow cylinders, concentric cylinders, and fractal architecture. To synthesize architected VACNT foams, we use a photolithography-assisted pre-patterned silicon wafer substrate with a chromium layer to prevent CNT growth in specific areas. CNTs only grow in regions where chromium is not present, resulting in VACNT foams with predefined mesoscale architecture (Figure 1.3(a,b,c)). We synthesized multiple VACNT samples by varying the architectural parameters, such as internal diameter, cylinder wall thickness, and gap between cylinders in cylindrically architected foams (Figure 1.3(a)); internal diameter, cylinder wall thickness, inner gap, and number of concentric rings in concentrically architected foams (Figure 1.3(b)); and the order of self-similarity in fractal architecture (Figure 1.3(c)).

In Figure 1.3(d), we compare the hysteretic energy dissipation (W_{dis}) of non-architected and architected VACNT foams with polymeric [6, 7], metallic [19–22], and other 3d-printed architected foams [23, 24] found in the literature. Both architected and non-architected VACNT foams exhibit higher energy dissipation (W_{dis}) and higher elastic modulus (E, shown as colorbar) compared to polymeric and 3d-printed architected foams of similar densities. Compared to metallic foams, VACNT foams exhibit a similar amount of energy dissipation but at much lower densities. Among VACNT foams, architected foams outperform non-architected foams in terms of both energy dissipation and elastic modulus. Cylindrically architected VACNT foams exhibit higher energy dissipation at densities similar to non-architected foams, owing to their improved structural stiffness from thin-walled hollow cylinders. Concentric VACNT foams are able to achieve much lower densities without compromising significantly on energy dissipation. Fractal architected foams exhibit intermediate values in the property space, with energy dissipation similar to non-architected foams but at lower densities. In summary, architected VACNT foams outperform conventional

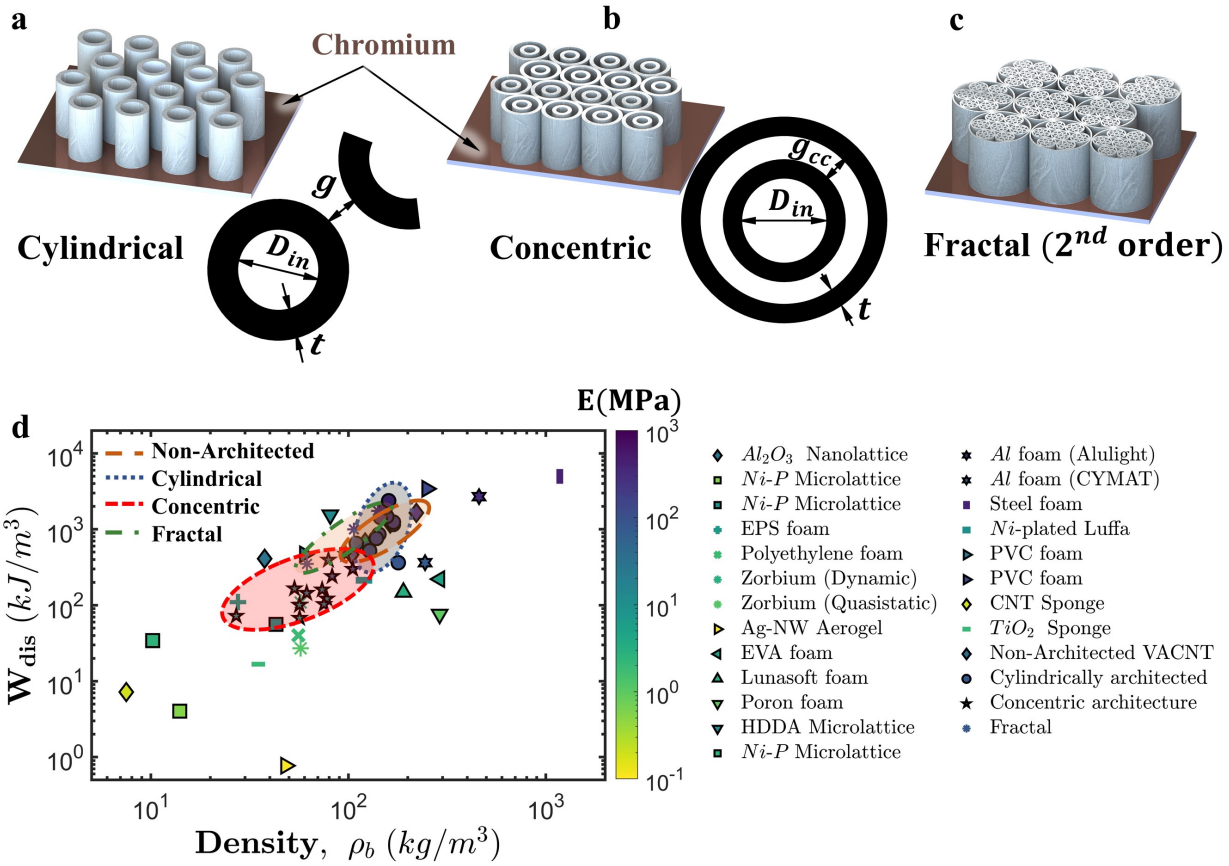

Figure 1.3: (a,b,c) 3D illustrations of architected VACNT foams and their design parameters. (d) Energy dissipated per unit volume of architected and non-architected VACNT foams compared to polymeric, metallic, and other architected foams across literature.

foams, 3D-printed architected foams, and non-architected VACNT foams by exhibiting synergistically improved energy dissipation and modulus while being lightweight. This combination of mechanical properties makes architected VACNT foams highly effective for protective applications in extreme environments. In the subsequent chapters, we will delve deeper into understanding the synthesis-structure-property relationship of VACNT foams, their morphological characterization using Synchrotron X-ray scattering techniques, and theoretical material models.

1.3.3 Research objectives : Hierarchical VACNT foams

1. Investigate the fundamental origin of the preconditioning effect in VACNT foams and similar fibrous materials using synchrotron X-ray scattering and mass attenuation experiments.

2. Investigate the dissipative properties of VACNT foams through stress-relaxation, quasistatic

compression, and dynamic mechanical analysis using a custom-built dynamic mechanical analyzer. Develop a constitutive model to accurately capture the observed behavior in these experiments.

3. Improve the specific mechanical properties of VACNT foams by incorporating various mesoscale architectures using photolithography. Study the morphology and mechanical properties of the resultant architected VACNT foams using quasistatic compression, electron microscopy, and phenomenological models.

4. To develop a scale-free model for shock absorber design, with focus on investigating the role of sample geometry in energy-absorbing pads and its connection with the mechanical properties of foam. The goal is to minimize the peak acceleration imparted to protective objects.

1.4 Non-Hermitian metamaterials

In the preceding section, our focus was on improving the energy absorption in dissipative materials for protective applications. In this section, we delve into a novel area of physics that leverages dissipation as a design element to develop highly sensitive sensors, actuators, and vibration absorbers [25–27]. Non-Hermitian physics is a field that explores the dynamics of dissipative or open systems where energy is not conserved. At the core of non-Hermitian physics lies the concept of Parity-Time (PT) symmetry [28, 29]. Distinct from regular geometrical symmetries such as rotational, translation, and periodicity, PT-symmetry is embedded in the equations of motion. In practice, PT-symmetry in achieved by introducing balanced dissipation (or loss) and amplification (or gain) mechanisms. While dissipation occurs naturally in various material systems (eg. foams, rubbers, VACNTs), gain is created artificially by pumping energy in to the system using feedback control drives.

In Figure 1.4, we illustrate both loss and gain by using the example of a child on a swing. A freely oscillating swing will eventually come to rest due to air resistance. However, if we ignore the air resistance, the swing will keep oscillating indefinitely. In such a case, the only way to stop the swing is by applying an external force that points opposite to the direction of motion. For instance, if the swing is moving away from you, a pulling force will result in slowing it down, and vice versa (Figure 1.4(a)). If this force is applied for a longer duration, always pointing in a direction resisting

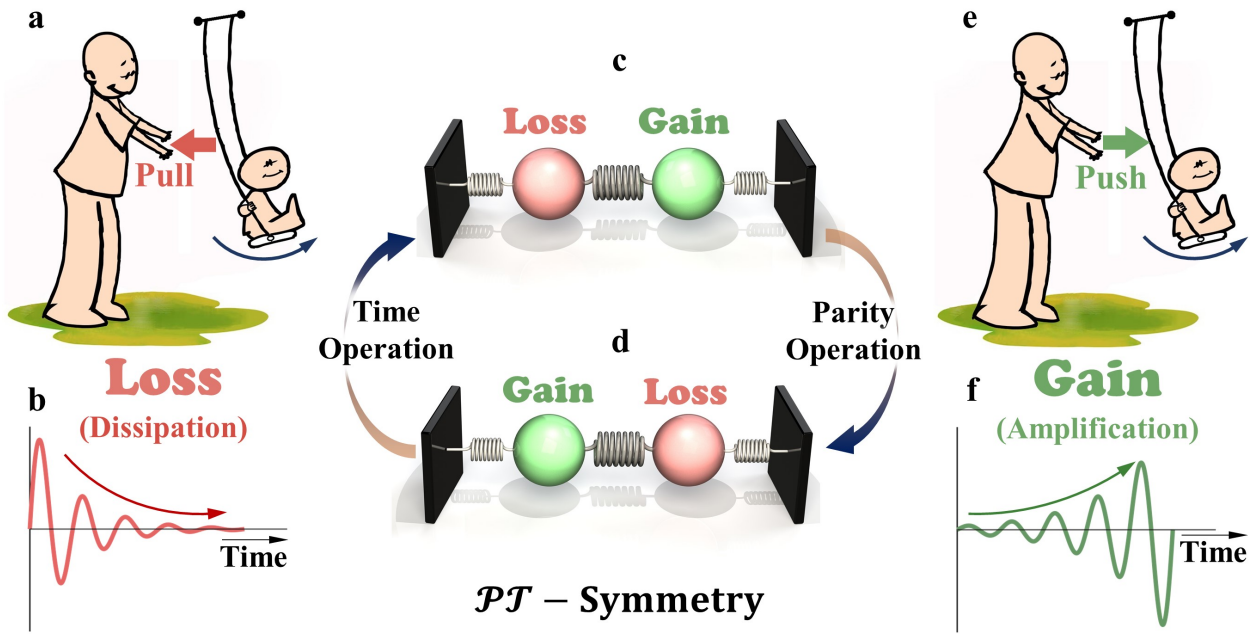

Figure 1.4: (a) An illustration of slowing down a swing (source: Wikimedia) by applying external force (loss). (b) Exponential decay in oscillations due to loss. (c) A coupled oscillators system with balanced gain and loss. (d) Coupled oscillator system after applying the parity operation. (e) An illustration of amplifying swing's oscillations by applying external force (gain). (f) Exponentially growing oscillations with time due to gain.

the motion, the oscillations will exponentially slow down with time (Figure 1.4(b)). In contrast, if the force is applied in the same direction as the velocity (Figure 1.4(e)), the oscillations will grow exponentially with time, resulting in an induced gain (Figure 1.4(f)).

In Figure 1.4(c), we illustrate a coupled spring-mass oscillator system where the left oscillator exhibits loss and the right one has gain. Applying a parity operation ($\mathcal{P}$-Operation) to this system, i.e., switching the positions of the oscillators in space, results in a mirror inversion as shown in Figure 1.4(d). Now, if we perform a time-reversal operation on this system, where gain becomes loss and loss becomes gain, we return back to the original initial system. This demonstrates that the system is Parity-Time symmetric. The principal feature of PT-symmetric systems is the existence of an exceptional point (EP). Any material system that leverages non-Hermiticity and exceptional points to exhibit novel wave phenomena falls into the category of non-Hermitian metamaterials.

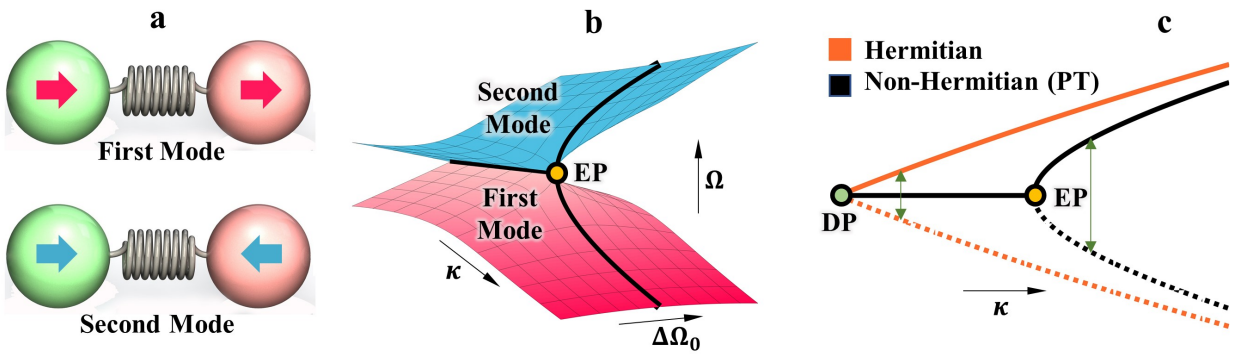

Figure 1.5: (a) Two fundamental modes of a coupled oscillator mass-spring system. (b) Eigenfrequencies of the system as a function of coupling and detuning. (c) Comparison of linear bifurcation at a diabolical point vs. square root bifurcation at an exceptional point.

1.4.1 Exceptional Point

An exceptional point (EP) is a branch-point singularity in the parameter space of a physical system where two distinct vibration modes merge to become degenerate (having the same energy) [26, 28]. For example, in the two-degree-of-freedom coupled spring-mass system shown in Figure 1.4(c), there are two possible vibration modes: an in-phase low-frequency mode (first mode) in which both oscillators move in the same direction (Figure 1.5(a)), and an out-of-phase high-frequency mode (second mode) in which both masses oscillate in opposite directions (Figure 1.5(a)). For balanced gain and loss, these two frequencies will merge to create an exceptional point. In Figure 1.5(b), we plot the natural frequencies (Ω) as a function of the coupling strength between the oscillators (κ) and the detuning ($\Delta\Omega_0$) between the oscillators. At a certain combination of coupling and detuning, both frequencies merge to form an exceptional point (EP).

Exceptional points can be used to create highly sensitive sensors due to the square root behavior of the singularity [25]. In Figure 1.5(c), we compare a Hermitian singularity, also called a Diabolical Point (DP), with a non-Hermitian singularity, i.e., an Exceptional Point. Compared to a linear bifurcation of frequencies at a DP, an EP exhibits a non-linear (square-root) bifurcation, which is much more sensitive to small variations in κ. Any perturbation in κ at the EP will result in a sudden, large bifurcation of the natural frequencies (Figure 1.5(c)), which is advantageous in detecting small environmental variations. Exceptional points have been utilized to develop highly sensitive accelerometers [25], voltmeters [30], and crack detectors in solid materials [31].

In practice, while loss or dissipation is an intrinsic property of various dissipative materials,

gain is induced often by pumping energy into the system from external sources via piezoelectric [32, 33], electroacoustic [34, 35], piezoacoustic [36, 37], non-Foster circuits [38], and electromagnets [39]. Creating gain needs sophisticated, active, positive feedback control circuits, making systems energy expensive, bulkier, and difficult to control each active element . In the subsequent chapters, we will explore both theoretically and experimentally ways to achieve exceptional points in passive systems with purely loss (no gain) [40, 41]. Realizing EPs in passive systems can make implementation more straightforward and integration into devices and structures seamless for engineering applications.

1.4.2 Research objectives : Non-Hermitian Metamaterials

1. Establish a theoretical framework for using viscoelastic materials as non-Hermitian elements to create exceptional points for highly sensitive sensors and actuators.

2. Experimentally achieving an exceptional point in a passive elastodynamic metamaterial and demonstrating its ramifications in achieving an enhancement in applied actuation force.

1.5 Organization and brief overview of thesis

Following is an outline of the content in the chapters that follow this introductory chapter

Chapter 2 : Detailed overview of the materials studied, their fabrication process, and experimental techniques

Chapter 3 : Quasi-static mechanical behavior of non-architected VACNT foams. Synchrotron X-ray scattering experiments to study origin of preconditioning effect. Frictional damping based constitutive model.

Chapter 4 : VACNT foams with cylindrical architectures and resultant improvements in specific mechanical properties.

Chapter 5 : Improved density-dependent scaling in VACNT foams with mesoscale architecture of thin concentric cylinders.

Chapter 6 : Theoretical study on the design of energy absorbing pads such as helmet liners, impact attenuators, and crashworthiness design using dimensional analysis. Studying potential of VACNT foams as protective shock absorbers.

Chapter 7 : Passive non-Hermitian metamaterials. Investigating exceptional points in passive systems using viscoelastic materials.

Chapter 8 : Actuation force amplification in the vicinity of exceptional point.

Conclusion & future-work : Brief summary of research accomplishments and potential future work.

Appendix A Supplementary material related to data correction and data reduction of synchrotron X-ray scattering measurements

Appendix B Supporting data for architected VACNT samples. Derivations of fill-factor and other architectural parameters.

Appendix C Supplementary material for non-Hermitian systems with different kinds of viscoelasticity.

Chapter 2

Materials and Experimental Techniques

2.1 Materials

This section provides an overview of the various materials studied in this thesis. The motivation for including this section is to familiarize the reader with the material systems and the associated jargon that will be frequently used throughout this thesis.

2.1.1 Vertically Aligned Carbon Nanotubes Foams

Vertically aligned carbon nanotube (VACNT) foams, also referred to as VACNT arrays or VACNT forests across the literature, are foam-like materials that are reasonably soft compared to various solid materials but much stiffer than polymeric foams of similar densities. VACNT foams are part of a large system of modern carbonaceous materials made of carbon nanotubes (CNTs), which includes CNT mats, yarns, sponges, and aerogels. Various methods can synthesize carbon nanotubes, such as arc discharge, laser ablation, and chemical vapor deposition (CVD). VACNT arrays of all kinds are synthesized using the CVD process. The fixed catalyst CVD process (FICVD) involves sputter deposition of a layer of iron on a silicon wafer substrate. Iron acts as a catalyst, and CNTs grow on the surface of the silicon wafer, vertically aligned. Ethylene and acetylene are mostly used as the carbon source for the FICVD process. VACNT arrays synthesized using the FICVD process contains mostly single-walled or only a few walled CNTs. Such VACNT arrays are fragile and

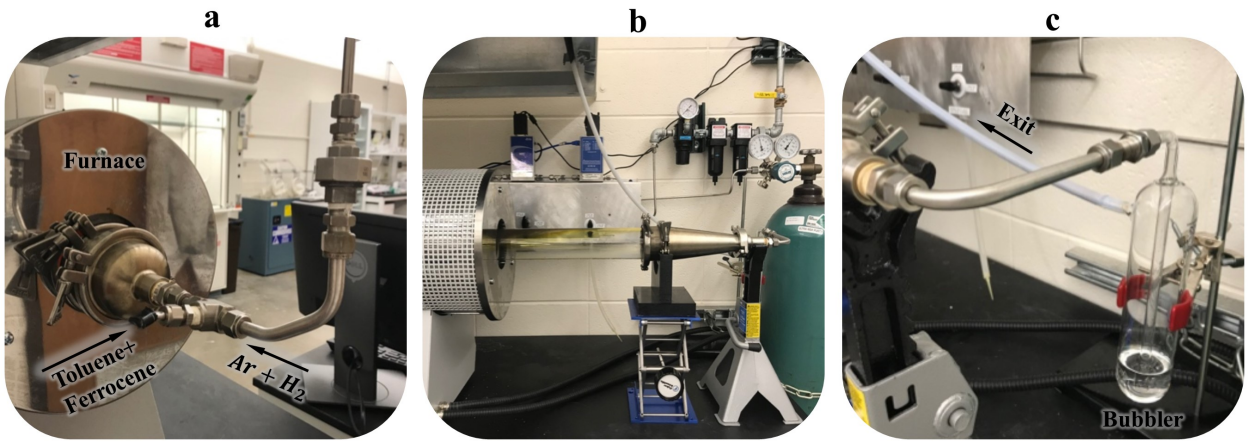

Figure 2.1: (a) Front-end of the CVD synthesis setup showing T-junction. (b) Back-end of the CVD setup showing the glasstube and tri-clamp sanitary fittings. (c) Exit-end with bubbler and exhaust.

have tendency to mechanically disintegrate upon application of external load. FICVD synthesis is primarily used to achieve drawable VACNT arrays, which can be employed to draw CNT yarns and create CNT mats. In contrast, floating catalyst CVD (FCCVD) gives foam-like VACNT arrays that are highly resilient and can withstand mechanical loading without disintegrating. CNTs synthesized using FCCVD are highly multiwalled (> 20) and densely packed. In the FCCVD process, a solution of toluene (carbon source) and ferrocene (catalyst precursor) is used to synthesize CNTs (Figure 1.2).

2.1.1.1 FCCVD Synthesis and Morphology

The FCVVD process mentioned above produces foam-like arrays of freestanding and highly resilient VACNTs suitable for various mechanical applications. To synthesize these arrays, we utilize a custom-built FCCVD synthesis setup (Figure 2.1), which includes a tube furnace (Carbolite Gero CTF12/75/700) capable of reaching a maximum operating temperature of $1200°C$. The CVD enclosure consists of a fused quartz tube with an internal diameter of $50; mm$, inserted inside the furnace and sealed at both ends with custom-made sanitary tri-clamp fittings. At the front end of the tube, a carrier gas mixture of Argon and Hydrogen is supplied (Figure 2.1(a)), which exits from the other end and passes through a glass bubbler filled with deionized water (Figure 2.1(c)) before being released through the exhaust. A luer-lock glass syringe containing a solution of 80 ml of Toluene with dissolved Ferrocene at 0.01 g/ml is connected to the setup, forming a T-junction

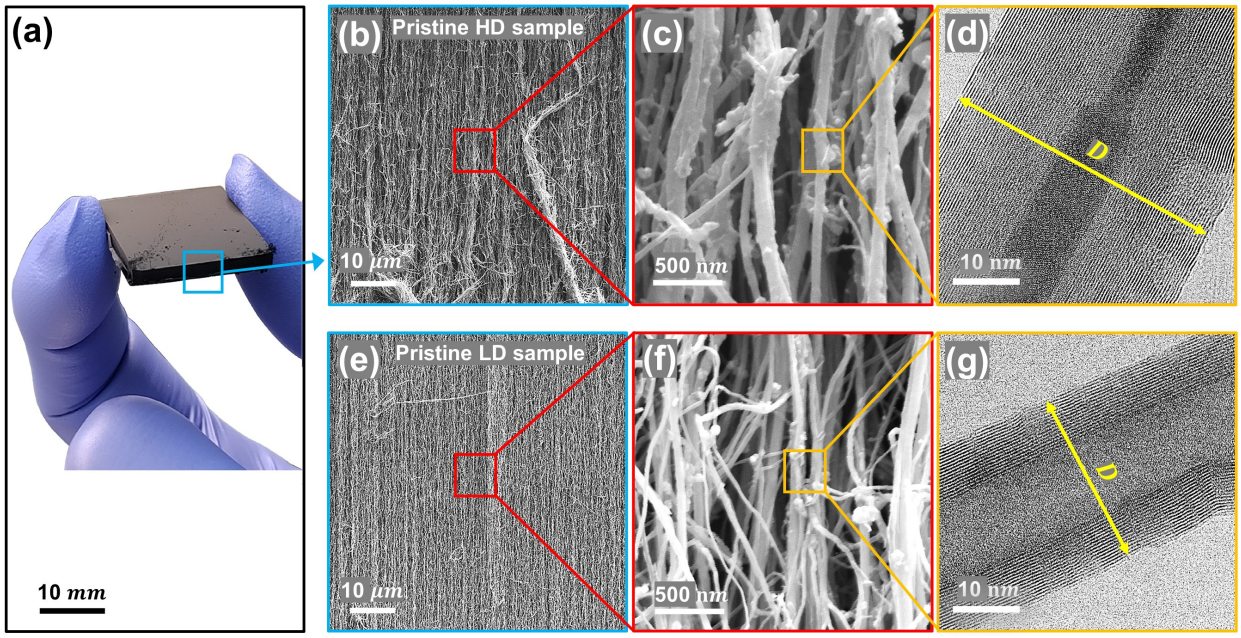

Figure 2.2: (a) A free-standing CVD synthesized VACNT foam sample. Electron microscope images of pristine HD and LD samples showing (b,e)the vertically aligned bundles in mesoscale (SEM) and (c,f) an entangled forest like morphology in microscale (SEM), and (d,g) the multiwall structure of an individual nanotube (TEM). D is the outer-diameter of the MWCNT

at the front end (Figure 2.1(a)). The Toluene solution in the syringe is pushed by a syringe pump (NE-1000) at 0.75 ml/min and mixes with the flowing carrier gas mixture, entering the furnace heated to 827°C. Inside the furnace, CNTs grow on a p-type 1×1 inch silicon wafer substrate placed in the peak heating zone of the Furnace.

The bulk mechanical properties of VACNT foams can be tailored by varying different process parameters in FCCVD [17, 42, 43]. The bottom-up growth nature of FCCVD synthesis leads to a hierarchical, anisotropic structure with mass density and stiffness gradients along the height [14, 44, 45]. By varying the carrier gas concentration, the nanostructure, morphology, and the density of the VACNTs can be tailored [14, 17]. A mixture of 5% H_2 and 95% Ar results in samples with high bulk density (HD) of 0.209 ± 0.014 g/cm^3, while 20% H_2 and 80% Ar results in samples with low bulk density (LD) of 0.097 ± 0.019 g/cm^3. Additionally, the morphology can also be tailored by varying the concentration of catalyst precursor (i.e., Ferrocene) and the injection rate of Toluene solution [46].

The VACNT film on the substrate can grow occasionally up to a thickness of 3 mm, but on average, it ranges between 1.5 mm and 2 mm. The synthesized VACNT film is then scraped off

from the substrate and cut into small pieces using a biopsy punch for SEM imaging and mechanical characterization. Figure 2.2 shows the multilengthscale structural hierarchy of two different types of VACNT foam samples. The SEM and TEM images at the top (Figure 2.2(b,c,d)) represent a VACNT foam sample synthesized using 5% H_2, whereas the bottom images (Figure 2.2(e,f,g)) represent the 20% H_2 sample. Clearly, the morphology is visually distinctive, with the 20% H_2 sample exhibiting CNTs with a comparatively smaller outer diameter (Figure 2.2(f)) as well as fewer walls (Figure 2.2(g)).

2.1.2 Viscoelastic Materials

In this thesis, we present the mechanical property characterization of various viscoelastic materials such as PDMS, natural rubber, and various polyurethane foams. This section provides a brief overview of viscoelastic materials and their mechanical properties. Viscoelastic materials are dissipative materials that exhibit a time delay in their mechanical response [47]. Unlike elastic materials, where the stress response of the material follows in-phase with any change in the applied deformation, viscoelastic materials exhibit a delayed response. In response to an applied constant strain that is held constant for a long time, the stress in a viscoelastic material undergoes a slow decay (exponential or power-law), a process called stress-relaxation. Similarly, viscoelastic materials exhibit creep in strain in response to an applied and maintained constant stress.

$$\sigma(t) = E \times \epsilon(t) \quad \text{(Elastic Materials)} \tag{2.1}$$

$$\sigma(t) = \int_0^t E(t-\tau)\frac{d\epsilon}{d\tau}\,d\tau \quad \text{(Viscoelastic Materials)} \tag{2.2}$$

For elastic materials, stress is directly proportional to strain and elastic modulus, expressed as $\sigma = E\epsilon$ for uniaxial stress or $\sigma_{ij} = C_{ijkl}\epsilon_{kl}$ in three dimensions. In contrast, for viscoelastic materials, the time-varying stress is calculated using the Boltzmann integral, which relates stress to time-varying strain and the material's transient relaxation modulus. In practice, the relaxation modulus can be measured by applying strain in the form of a Heaviside step function ($\epsilon(\tau) = \epsilon_0\mathcal{H}(\tau)$) and recording the stress. The time-dependent relaxation modulus can then be calculated by dividing the stress response by the applied strain as follows

$$\sigma(t) = \int_0^t E(t-\tau)\epsilon_0 \frac{d\mathcal{H}}{d\tau}\, d\tau \tag{2.3}$$

The derivative of a Heaviside step function is a Dirac-delta function (Ω)

$$\sigma(t) = \int_0^t E(t-\tau)\epsilon_0 \Omega\, d\tau \tag{2.4}$$

$$\sigma(t) = E(t)\epsilon_0 \quad \rightarrow \quad E(t) = \frac{\sigma(t)}{\epsilon_0} \tag{2.5}$$

$$E(t) = E_\infty + E_t e^{-t/\tau} \ \text{(Exponential)} \ , \ E(t) = E_\infty + E_t t^{-\alpha} \ \text{(Power-Law)} \tag{2.6}$$

Similarly, the stress in response to an applied steady-state sinusoidal strain of frequency ω and amplitude ϵ_d can be calculated as follows

$$\sigma(\omega, t) = (E' + iE'')\epsilon_d e^{i\omega t} \tag{2.7}$$

where E' and E'' are the frequency-dependent storage and loss moduli of the viscoelastic material, respectively. The storage modulus and loss modulus are the real and imaginary parts, respectively, of the complex Fourier transform of the relaxation modulus ($E(t)$). The expressions for the frequency-dependent storage and loss moduli can vary depending on whether the relaxation modulus follows an exponential or power-law decay. The majority of viscoelastic materials studied in this thesis exhibit power-law viscoelastic behavior. To characterize these materials, we conducted stress-relaxation and quasistatic compression experiments using a commercial load-frame, the Instron Electropulse E3000. Additionally, we built and calibrated a custom dynamic mechanical analyzer to measure the frequency-dependent storage and loss moduli.

2.2 Experimental Techniques

In this thesis, we utilize a variety of commercial, as well as custom-built, experimental techniques to study the morphology of materials and characterize their mechanical properties. This section aims to familiarize the reader with the experimental methodology and provide details on the instrumentation used.

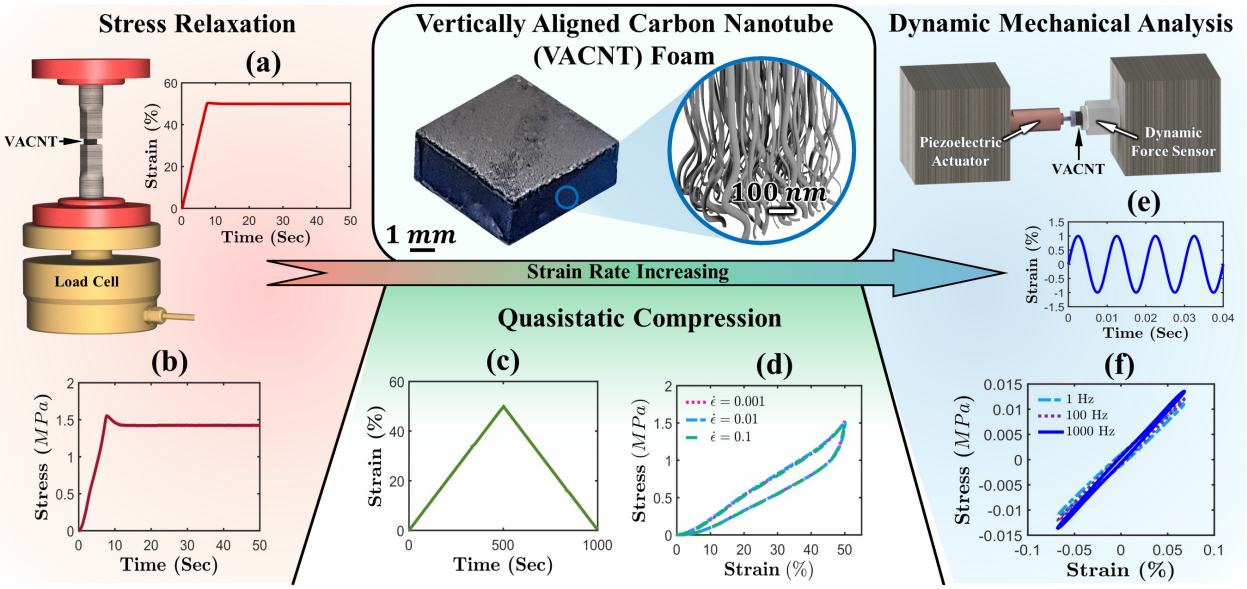

Figure 2.3: (a) Monolithic VACNT foam sample. (b) A schematic showing vertically aligned and entangled morphology of CNTs. (c) Stress-relaxation and compression testing setup. (d,e) Applied strain and stress response in relaxation experiment. (f,g) Quasistatic ramp strain and stress-strain curves for two orders of strain rates. (h) Custom-built DMA setup. (i,j) Applied sinusoidal strain and stress-strain curves for different frequencies.

2.2.1 Stress Relaxation

To perform stress-relaxation experiments, we use a commercial load-frame, the Instron Electropulse E-3000, with a 250 N load cell for soft samples like PDMS and polymeric foams, and a 5 kN load cell for stiffer samples such as VACNT foams. In these experiments, we apply a compressive strain at a constant strain rate in the form of a ramp up to a desired strain value and then hold it constant for 30 to 60 minutes (Figure 2.3(a)). Ideally, to achieve a perfect stress-relaxation curve, the strain should be applied in the form of a Heaviside function. However, due to inertia in the moving platens, there is a limit on the fastest ramp rate achievable in practice. Thus, during the ramping up of the strain, the material already starts to relax, affecting the accuracy of the measurement. The inertia also causes the strain to overshoot initially before settling down to the desired specified strain (Figure 2.3(a)). Generally, researchers trim the ramp and overshoot parts and consider the data afterwards as the relaxation curve. While this approach does not affect the long-term relaxation modulus, it does affect the transient term and the relaxation time. To accurately predict a material's relaxation modulus, the effect of the ramp and overshoot must be modeled and subtracted from the measured data.

2.2.2 Quasistatic Compression

We conducted quasistatic compression experiments to measure the modulus, energy absorption, and energy dissipation of various materials, including VACNT foams, polymeric foams, and elastomers. Quasistatic compression is ideally an ultra-slow strain-rate experiment; however, any strain rate below 0.01 s^{-1} is considered quasistatic. In these experiments, we apply strain in the form of a ramp with a constant strain rate to achieve the desired maximum compression strain (Figure 2.3(c)). Subsequently, we unload the material with the same constant strain rate until the strain returns to zero. Quasistatic compression experiments provide an estimate of the overall modulus of the material, energy dissipation (area under the loading-unloading hysteresis curve), and the peak load that the material can bear (Figure 2.3(d)). During unloading, the stress can reach zero before the unloading is complete, which occurs when the material cannot fully recover or does not have enough time to recover. The residual plastic strain gives an estimate of the percentage strain recovery. Additionally, for foam materials, the maximum compression strain before the onset of densification can also be measured from the quasistatic stress-strain response.

2.2.3 Dynamic Mechanical Analysis

Dynamic mechanical analysis (DMA) is an experimental technique used to measure the frequency-dependent storage and loss moduli of viscoelastic materials. Unlike stress-relaxation and quasistatic compression testing, DMA imparts higher strain rates during material testing. Instead of applying a ramp strain at a constant rate, DMA involves applying sinusoidal strain at a certain amplitude and frequency. This allows for the measurement of storage and loss moduli as a function of both amplitude and frequency. Commercial DMA instruments typically use servo-hydraulics and linear motor actuators to move a piston for applying deformation to materials. However, the frequency range achievable with these instruments is limited to around 100 Hz due to the size and inertia of the instruments. To achieve frequencies in the kHz range, we developed a custom dynamic mechanical analyzer using a preloaded encased piezoelectric actuator and a dynamic force sensor (Figure 2.3(e,f)). The piezoactuator, consisting of a stack of piezocrystals, can achieve frequencies up to 2 kHz. However, there is a tradeoff between frequency and amplitude—the maximum amplitude decreases from 45 microns at 1 Hz to 2 microns at 2 kHz, which is still sufficient for measuring

dynamic properties of thin samples (approximately 1 mm thick).

To measure the storage and loss moduli as a function of frequency, we perform a frequency sweep. For each frequency, we apply a sinusoidal voltage of a fixed amplitude to make the actuator vibrate at that frequency, with the amplitude in microns determined by the calibration factor (Figure 2.3(e)). The flat tip of the actuator compresses and decompresses the material, while the force sensor measures the resultant force response of the sample. For a linear viscoelastic material, the force signal will also be a sine wave but phase-shifted compared to the strain. The tangent of this phase difference, or $\tan(\delta)$, represents the damping factor of the material. To reliably measure $\tan(\delta)$, we supply 20 cycles of a sine signal to the actuator, then trim off 5 cycles from the start and end, and take the average of the middle 10 cycles to get the final hysteresis curve (Figure 2.3(f)).

For an applied dynamic strain $\epsilon(t) = Re(-i\epsilon_d e^{i\omega t}) = \epsilon_d \sin(\omega t)$, where $i = \sqrt{-1}$, ϵ_d is the dynamic strain amplitude, and ω is the cyclic frequency, the stress signal is given as follows

$$\sigma(\omega, t) = Re\left(-i(E' + iE'')\epsilon_d e^{i\omega t}\right) \tag{2.8}$$

$$\sigma(\omega, t) = \epsilon_d(E' \sin(\omega t) + E'' \cos(\omega t)) \tag{2.9}$$

$$\sigma(\omega, t) = \epsilon_d\sqrt{E'^2 + E''^2}\left(\frac{E'}{\sqrt{E'^2 + E''^2}}\sin(\omega t) + \frac{E''}{\sqrt{E'^2 + E''^2}}\cos(\omega t)\right) \tag{2.10}$$

$$\frac{E''}{E'} = tan(\delta) \tag{2.11}$$

$$\sigma(\omega, t) = \epsilon_d\sqrt{E'^2 + E''^2}\,(\cos(\delta)\sin(\omega t) + \sin(\delta)\cos(\omega t)) \tag{2.12}$$

$$\sigma(\omega, t) = \epsilon_d\sqrt{E'^2 + E''^2}\sin(\omega t + \delta) \tag{2.13}$$

$$\sigma(\omega, t) = \epsilon_d E^* \sin(\omega t + \delta) \tag{2.14}$$

where E^* is the dynamic modulus. In experiments, dynamic modulus can be measured by dividing the measured stress amplitude by the applied strain amplitude. The storage and loss moduli can we expressed as functions of dynamic modulus and loss tangent as follows

$$E' = E^* \cos(\delta) \quad , \quad E'' = E^* \sin(\delta) \tag{2.15}$$

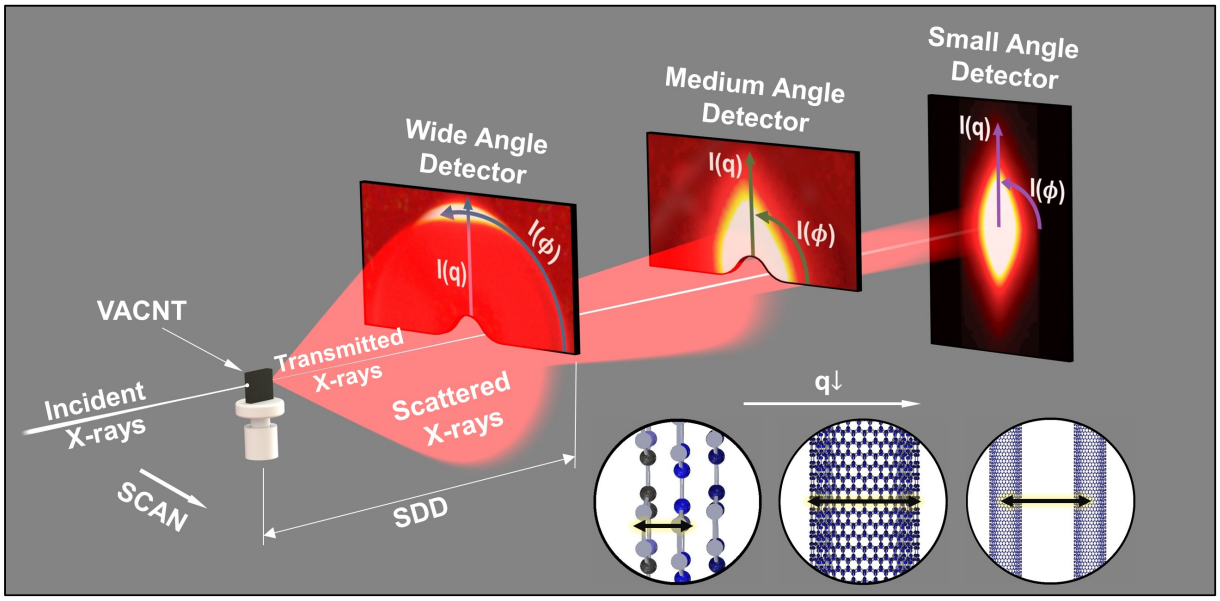

Figure 2.4: DND-CAT's triple area detector system, refer [48] for more details on accurate detectors' configuration. 2D X-ray scattering patterns on WAXS, MAXS and SAXS detectors with corresponding probing length scales are shown. SDD is sample to detector distance, which is smallest for WAXS and largest for SAXS.

2.2.4 Synchrotron X-ray scattering and mass attenuation experiments

To quantitatively characterize the morphology and the deformation-induced hierarchical structural changes in VACNT foams, we performed synchrotron X-ray scattering and mass attenuation measurements at beamline 5-IDD of the DND-CAT at the Advanced Photon Source (APS). Compared to laboratory-scale X-ray scattering sources, a synchrotron X-ray source provides ample scattering for shorter exposure times due to its high intensity and focused monochromatic beam. Figure 2.4 illustrates the triple-detector beamline 5-IDD at the DND-CAT with a VACNT foam sample mounted in the path of the beam. The high-intensity beam strikes the sample's lateral face (surface parallel to the CNTs growth direction) and elastically scatters. X-rays interacting with different feature sizes in the hierarchy of the VACNT foams preferentially scatter at certain angles, and their constructive interference creates anisotropic high-intensity scattering patterns on the WAXS, MAXS, and SAXS detectors. These angles can be calculated from the lengthscale d and X-ray wavelength λ using Bragg's law:

$$n\lambda = 2d\sin(\theta) \tag{2.16}$$

where n is the order of the diffraction and θ is the scattering angle. The magnitude of scattering vector can be expressed as follows

$$q = \frac{4\pi}{\lambda}\sin(\theta) \quad , \quad q = \frac{2\pi}{d} \tag{2.17}$$

Depending on the range of q, the X-ray scattering process can be categorized into wide-angle X-ray scattering (WAXS), medium-angle X-ray scattering (MAXS), and small-angle X-ray scattering (SAXS). The WAXS detector (with the largest q) probes the smallest length scales in VACNT foams, such as the interwall spacing in multi-walled carbon nanotubes (MWCNTs) and the sp^2 bonded carbon in folded graphitic sheets of individual walls. MAXS and SAXS probe the diameter distribution and inter-nanotube spacing between CNTs.

To study the variation in morphology along the height of the VACNT sample, we recorded the scattering patterns on all three detectors by moving the sample in steps of 50 μm along the direction of CNTs' vertical alignment. Various pieces of information about the morphology, such as the vertical alignment of CNTs, crystallite size, and nanoscale strain, can be extracted from the scattering patterns. Measuring these parameters after compressing the sample up to a certain strain and then comparing them to those recorded for pristine samples can provide insights into deformation-induced structural changes on different length scales.

To characterize the density gradient of VACNT foams, we measured the mass attenuation of X-rays using photon-counting detectors placed in the path of the X-ray beam. An upstream detector measured the intensity of X-rays incident on the sample, while a downstream detector measured the intensity of X-rays exiting the sample. The local average mass density of CNTs encountered by X-rays while traversing through the sample can be calculated using the Beer-Lambert law [15]. Each VACNT sample is scanned along its thickness to measure local mass density as a function of height while also collecting the scattering patterns on WAXS, MAXS, and SAXS detectors for each scan location.

Chapter 3

Non-architected VACNT Foams (Preconditioning effect and Constitutive model)

This chapter is adopted from the following publications

Gupta, A., Griesbach, C., Cai, J., Weigand, S., Meshot, E. R., & Thevamaran, R. (2022). Origins of mechanical preconditioning in hierarchical nanofibrous materials. Extreme Mechanics Letters, 50, 101576.

Author Contributions : AG synthesized VACNT samples, performed compression testing, analyzed the data, and prepared the figures. CG and JC assisted in electron microscopy, SW performed the synchrotron experiments, RT and EM conceived the project, and AG and RT wrote the paper with inputs from everyone.

(Under preparation) Gupta, A., Maheswaran, B., Jaegersberg, N., Chawla, K., Thevamaran, R. (2024) Fibers that remember: Memory of loading history and origin of dynamic softening in soft fibrous material with progressive friction.

Author Contributions : AG performed mechanical characterization experiments, conceived the model, designed setup and performed the wave slowdown experiments, BM assisted in wave slowdown experiments, KC synthesized the samples, and RT conceived the project.

In this chapter, we discuss the quasistatic compression behavior of non-architected VACNT foams and investigate the fundamental origins of various properties observed during mechanical testing. VACNT foams exhibit preconditioning effect that influences the maximum energy a VACNT foam sample can absorb under repetitive loading. The preconditioning effect is an initial softening in the stress-strain response of a fibrous material due to applied repetitive compressive loading-unloading cycles. While there are numerous interpretations and phenomenological models for the preconditioning effect in the literature, there is a lack of consensus on its fundamental origin in VACNTs and similar fibrous materials. Additionally, we investigate rate-independent mechanical behavior in VACNT foams and develop a friction damping based constitutive model.

3.1 Preconditioning Effect

3.1.1 Introduction

Stress-induced softening of a material during repeated loading-unloading cycles, especially in the first few cycles–called the preconditioning effect–is found in several engineering and biological materials [49–53]. A broadly studied preconditioning effect is the Mullins effect–found in carbon-black-filled rubbers under large deformation–which exhibits a constitutive behavior that is dependent on the previously encountered maximum load during cyclic loading [54, 55]. The preconditioning effect is thought to originate from microstructural changes that occur during loading-unloading cycles, for example, the reorganization of collagen fibers in biological materials [56]. A pressure history dependent strain-softening response under cyclic loading observed in rat's left ventricular myocardium is hypothesized to arise from the damage occurring in elastic components–e.g. changes in collagen fiber structure–rather than viscous tissue components [50]. Preconditioning due to morphology changes and fracture of fibrin network in human blood clot samples is also observed as a function of multicycle compression and decompression [57]. All material systems exhibiting preconditioning effects show softening during the first few cycles though the source of preconditioning can vary from material to material. Various physical interpretations such as polymer chain disentanglement, molecule slipping, and network rearrangement have been proposed for preconditioning in synthetic elastomers [55]. Yet, there is a lack of consensus on the fundamental origins of the preconditioning effects in various material systems because of the lack of directly measured microstructural evi-

dences. Direct study of agencies causing preconditioning will help develop better physical-based models rather than a behavior-based phenomenological modeling.

Strong preconditioning effects have also been observed in vertically aligned carbon nanotube (VACNT) foams [58–60]–a compelling material system that is touted for its superior mechanical properties relevant to extreme protective applications in impact and vibration mitigation. They have a hierarchical structure with features spanning broad lengthscales from a few angstroms to several millimeters. Collectively interacting, intertwined multi-walled carbon nanotubes–a concentric nanoscale tubular system made of sp^2 carbon structure–form a forest-like morphology in the microscale which organize in vertically aligned bundles in mesoscale to create the macroscale VACNT foams [13]. This hierarchical organization across nanometer-to-millimeter-lengthscales [13, 14, 17, 61, 62] and the exceptional intrinsic properties of individual CNTs [63–65] give rise to exotic bulk mechanical properties in VACNTs. For example, they are stiff enough to bear static structural loads while also dissipating large amounts of energy through stress-strain hysteresis. This dissipated energy can be greater than two-hundred times that of polymeric foams of comparable density in their first loading-unloading cycle. Still, it then reduces to one-fourth of its initial value upon preconditioning over the first few (~ 5) cycles [14, 66]. VACNTs are thermally stable for operation in extreme temperature ranges from $-196^{\circ}C$ to very high temperatures up to $1000^{\circ}C$, outperforming rubbers in vibration isolation applications [16, 67]. Superior strength, toughness, and flexibility of nanotube bundles can also lead to the development of novel nanoelectromechanical systems (NEMS) based devices and sensors. The use of CNT-based nano-beams in nanoelectromechanical actuators, nanorelays, and nano switches are some of the examples [68–70].

When compressed, the VACNTs deform through sequentially progressive collective buckling of CNT bundles and have the ability to recover almost completely from large strains upon unloading [13, 14, 17, 62]. Progressive buckling is beneficial for protection from blunt impacts because of the increased deacceleration time as well as the sequential strain localization that preserves undeformed rest of the sample in non-preconditioned pristine state for further utility [14]. Due to their large surface-to-volume ratio, CNT interactions are dominated by van der Waal forces. A zipping-unzipping mechanism driven by these van der Waal interactions has been proposed for high hysteretic energy dissipation and viscoelastic behavior [16, 62, 67]. However, the stress-strain hysteresis reduces in the first few cycles through preconditioning and then remains constant over

the next thousands of cycles [13, 59]. This preconditioning effect is hypothesized [60] to originate from the mesoscale rearrangements of CNTs during cyclic compression and has been modeled using multiscale mass-spring models that account for Mullins-like effects [60, 71]. Nevertheless, there is not yet direct experimental evidence to support this hypothesis. Moreover, the reorganization of the mesocale morphology of CNTs occurring to a large extent can result in permanent deformation and affect the bulk strain recovery of the material, which can limit their use in protective applications. While high strain recovery ($> 80\%$) of VACNTs has been reported in several studies [13, 14, 58], poor recovery ($< 50\%$) with large plastic deformation or lack of any recovery has also been commonly observed [62, 72]. While the VACNT foams with high strain recovery are modelled with discrete multiscale mass-spring models having recoverable bi-stable spring elements [71, 73], the VACNT foams that undergo large permanent deformations have been modeled with hardening-softening-hardening continuum plasticity models [74, 75]. Continuum theory for evolution of phase transition–of densified and rarefied phases–with stick-slip kinetic law has also been used recently to describe the mechanical behavior of VACNT foams [76]. The phase transition model is shown to accurately describe the mechanical behavior of VACNT under both uniaxial compression and nanoindentation [77]. Despite having similar deformation dominated by progressive collective buckling, the disparity in recoverability as well as the origins of preconditioning in VACNTs remain elusive partly due to a lack of conclusive multiscale structural characterization.

Here, we show that the preconditioning effects in VACNTs arise not only from the mesoscale morphology evolution, but also from the nanoscale structural changes within individual multiwalled carbon nanotubes (MWCNTs) that occur during compression-induced buckling of the CNTs. We performed synchrotron X-ray scattering experiments on VACNT samples as a function of repeated loading-unloading cycles to investigate their mechanical response with direct structural characterization. Using this non-destructive, bulk material characterization along with high-speed microscopy, scanning electron microscopy (SEM), and transmission electron microscopy (TEM), we further elucidate the structural evolution of VACNTs that lead to preconditioning and permanent deformation. The fundamental insights we provide could enable the design of hierarchically structured materials with less initial preconditioning and high strain recovery that are desirable for their application as protective materials in extreme environments.

Table 3.1: Average thickness, strain recovery and mass density of all HD and LD samples (seven $5 \times 5\,mm$ samples of each type) used in this study.

	High-Density (HD) Samples			Low-Density (LD) Samples		
	Pristine	**1-Cycle**	**6-Cycle**	**Pristine**	**1-Cycle**	**6-Cycle**
Thickness (mm)	1.252±0.070	1.031±0.060	0.989±0.075	0.983±0.044	0.892±0.060	0.839±0.080
Strain Recovery (%)		82.42±2.30	78.96±2.48		90.68±2.71	85.23±4.96
Mass density (g/cm^3)	0.209±0.014	0.254±0.018	0.265±0.018	0.097±0.019	0.108±0.025	0.115±0.029

3.1.2 Materials and Methods

3.1.2.1 VACNT Sample Synthesis

We synthesize the VACNT foams by a floating-catalyst thermal chemical vapor deposition (tCVD) process. Additionally, the bulk mechanical properties of VACNT foams can be tailored by varying different process parameters in tCVD [17, 42, 43]. The bottom-up growth nature of tCVD synthesis leads to a hierarchical, anisotropic structure with mass density and stiffness gradients along the height [14, 44, 45]. Our floating-catalyst tCVD process uses 80 ml solution of ferrocene (catalyst precursor) dissolved in toluene (carbon source) at 0.01 g/ml concentration as the feed-stock. This solution is injected at a 0.75 ml/min rate using a syringe pump into a horizontal tube furnace maintained at $1100\,K$ and atmospheric pressure. The vaporized solution at inlet is carried further down into the furnace tube by a gas mixture of argon and hydrogen flowed at $800\,sccm$. We used two carrier gas concentrations at 5% H_2 ($40\,sccm$) and 20% H_2 ($160\,sccm$) as the nanostructure, the morphology, and the density of the VACNTs can be tailored as functions of the hydrogen concentration in the carrier gas [14, 17] (Figure 3.1). The 5% H_2 results in samples with high bulk density (HD) of $0.209 \pm 0.014\,g/cm^3$, while 20% H_2 results in samples with low bulk density (LD) $0.097 \pm 0.019\,g/cm^3$ (Table 3.1). The VACNTs grow on the surface of a micron-thick thermal-oxide coated silicon substrate placed within the furnace's $200\,mm$ heating zone. At the end of the synthesis, the VACNT foams grown up to $\sim$ 1-1.3 mm thickness (Figure 3.1(a)) are removed from the furnace and cut-extracted from the silicon wafer in 5×5 mm free-standing square pieces using a microtome blade for structural and mechanical characterizations.

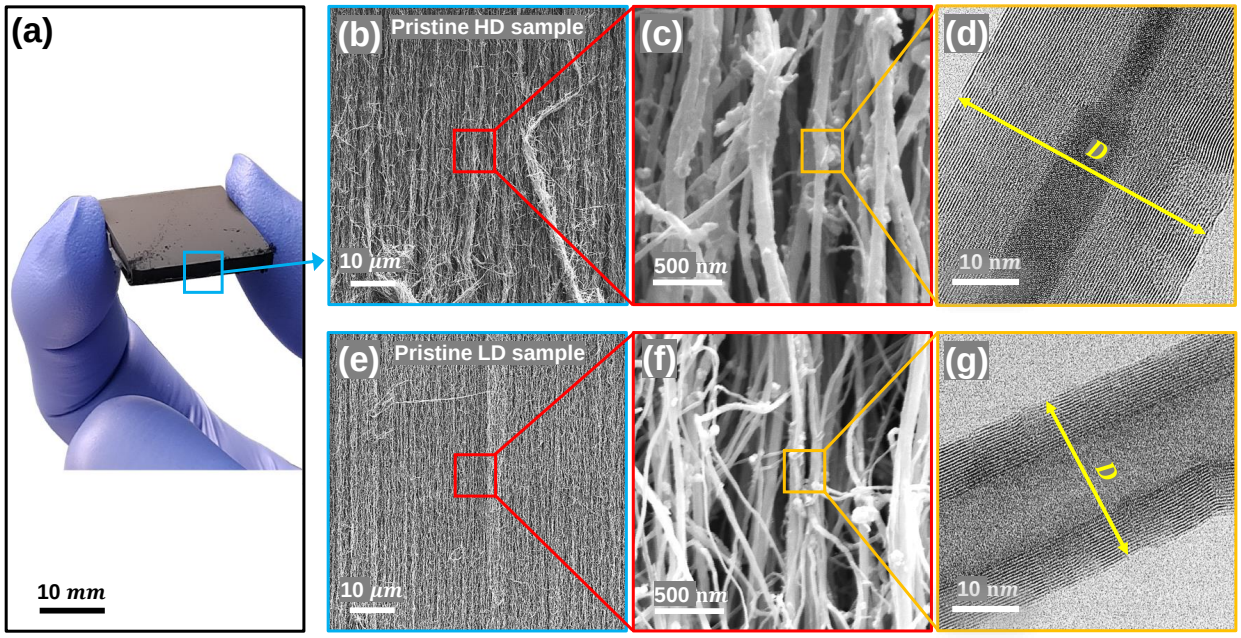

Figure 3.1: (a) A free-standing tCVD synthesized VACNT foam sample. Electron microscope images of pristine HD and LD samples showing (b,e) the vertically aligned bundles in mesoscale (SEM) and (c,f) an entangled forest like morphology in microscale (SEM), and (d,g) the multiwall structure of an individual nanotube (TEM). D is the outer-diameter of the MWCNT.

3.1.3 Quasistatic compression testing

We characterize the stress-strain behavior of VACNT foams by performing quasistatic cyclic compression up to 60% strain at a strain rate of $0.01s^{-1}$ (in TA ElectroForce 3230 and an Instron Electropulse E3000), along with *in situ* high-speed microscopy (a Photron SAZ high-speed camera with K2/KC long distance microscope lens) for visualizing microscale deformations. Upon compression, CNTs undergo collective buckling that initiates at the bottom region, which was adjacent to the substrate during synthesis and sequentially progresses upward as the load is increased. Each collective buckle instability results in a characteristic drop in stress followed by stiffening due to local densification of the buckle fold. In HD samples, the sequential propagation of buckles occurs unidirectionally from the bottom to the top (Figure 3.2(a)), whereas in LD samples, following the initial buckling at the bottom region, buckles are also observed in the top region at higher compressive strains (Figure 3.2(b)). Upon unloading, the sample tends to recover its shape but a portion of the sample at the bottom region remain permanently deformed (Table 3.1). This local permanent deformation causes a slight increase in sample's bulk density as well, particularly during first

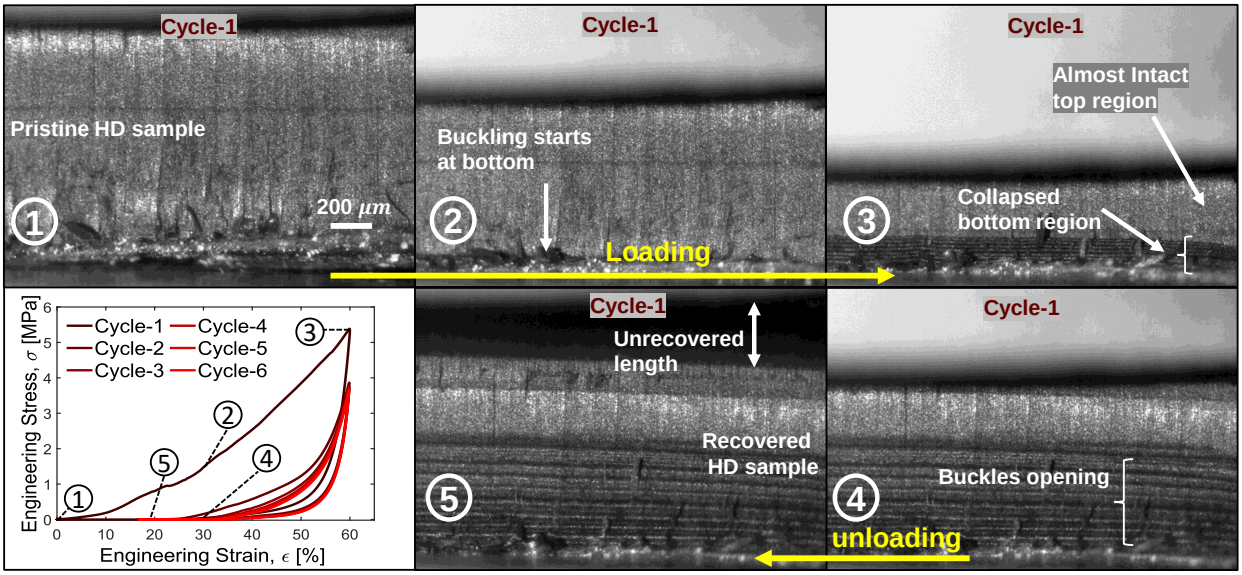

(a)

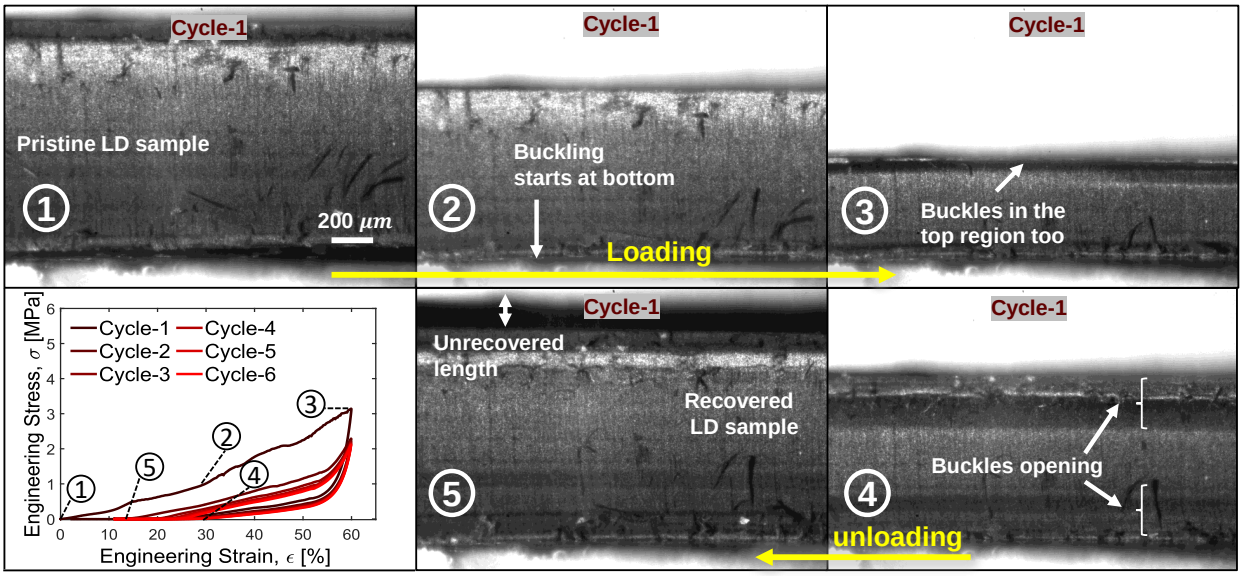

(b)

Figure 3.2: High-speed microscope image sequence of pristine HD (a) and LD (b) sample under cycle compression with respective stress-strain curves shown for first six cycles.

loading-unloading cycle. The sample thicknesses, strain recovery, and bulk mass densities before and after compression are summarized in Table 3.1.

Under cyclic loading, the VACNT foam shows preconditioning in the first few cycles which then reaches a steady-state hysteresis after 5-6 cycles (Figure 3.2). We quantify the effect of preconditioning on the specific energy dissipation for each cycle (energy dissipated per unit mass

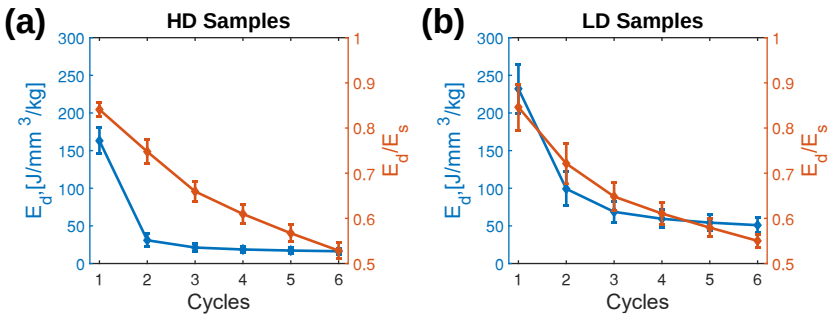

Figure 3.3: Specific energy dissipation and damping capacity (E_d/E_s) during loading-unloading cycle for (a) HD samples and (b) LD samples

and per unit volume). Preconditioning is strong between the first two cycles (∼1/4 for HD samples and ∼1/3 for the LD samples) that decreases afterwards as a steady state is reached (Figure 3.3).

3.1.3.1 Synchrotron X-ray Experiments

To quantitatively characterize the structure of the VACNT foams and investigate the cause of preconditioning, we performed synchrotron X-ray scattering and mass attenuation measurements on the VACNT foam samples at beamline 5-IDD of the DND-CAT [1] at the Advanced Photon Source (APS). We followed an iterative experimental protocol of performing *ex situ* X-ray scattering measurements after detailed mechanical compression experiments to characterize the structural evolution of the VACNT foams as a function of the loading-unloading cycles. For accurate correlation among measurements, samples were mounted precisely in the same orientation following each compression test and scanned in the same direction (bottom to top) at nearly the same location. We designed and 3D printed a multi-sample holder (Figure 3.4(a)) for robust sample handling, repeatable alignment, and high-throughput X-ray scans. This sample holder is mounted on a goniometer stage along the X-ray pathway to facilitate transmission X-ray scattering and mass attenuation measurements (Figure 3.4(a)) [78]. Each sample is scanned from the bottom region–that was adjacent to substrate during synthesis–towards the top at 50 μm scanning steps to characterize its hierarchical structure and local mass density as functions of the sample's height. We used a 9 keV X-ray beam with a 110 μm diameter spot size incident on the sample. Since the VACNT foams have low X-ray absorption at this energy, most of the X-rays are transmitted unscattered. This transmitted primary beam is stopped by a beam stopper while the X-rays that are scattered by

[1] DuPont-Northwestern-Dow Collaborative Access Team

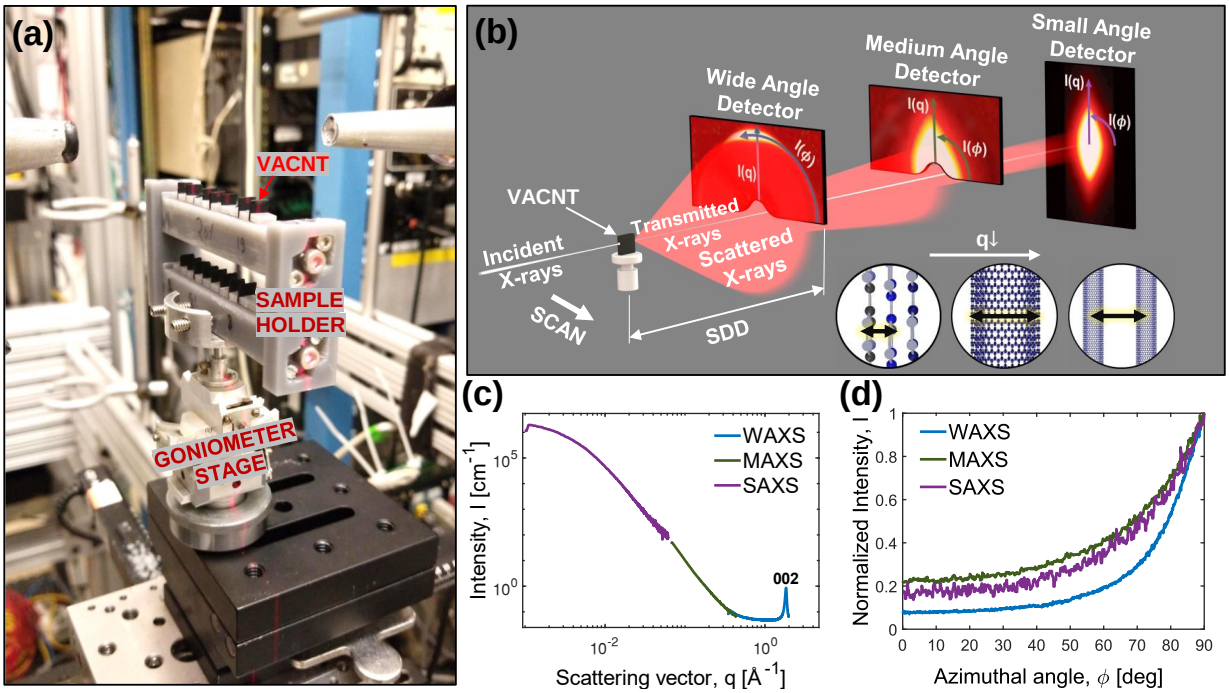

Figure 3.4: (a) X-ray scattering setup - HD and LD samples mounted on sample holder, which is attached to the goniometer stage. (b) DND-CAT's triple area detector system, refer [48] for more details on accurate detectors' configuration. 2D X-ray scattering patterns on WAXS, MAXS and SAXS detectors with corresponding probing length scales are shown. SDD is sample to detector distance, which is smallest for WAXS and largest for SAXS. (c,d) 1D intensity profiles for radial ($I(q)$) and azimuthal integration ($I(\phi)$). The radial integration is done for scattered intensities along polar azimuthal direction (Figure 3.5).

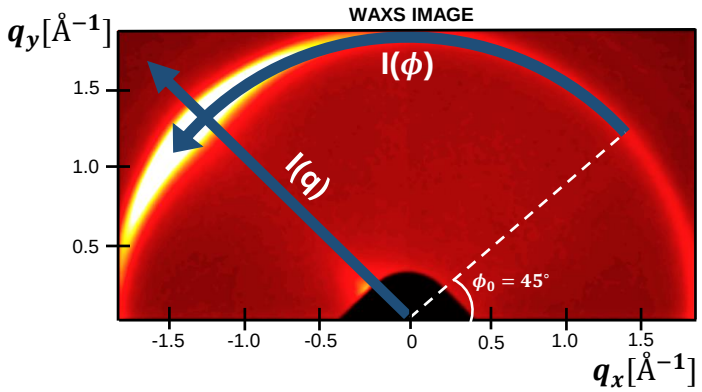

Figure 3.5: Radial (polar) ($I(q)$) and azimuthal ($I(\phi)$) integration on WAXS scattering pattern.

the sample are collected on three planar detectors: a wide angle X-ray scattering (WAXS) detector ($SDD = 201.54\,mm$), a medium angle X-ray scattering (MAXS) detector ($SDD = 1013.93\,mm$), and a small angle X-ray scattering (SAXS) detector ($SDD = 8502.30\,mm$) (Figure 3.4(b)) [48].

The magnitude of the scattering vector (q) as a function of scattering angle (θ) is given by,

$$q = \frac{4\pi}{\lambda} sin(\theta) \tag{3.1}$$

where λ is the wavelength of X-rays. The wavelength of the X-ray beam ($\lambda = 1.3776$Å) is large (less energetic) enough to avoid any inelastic scattering. X-rays interacting with different feature sizes along the hierarchy of the VACNT foams preferentially scatter at certain angles and their constructive interference creates anisotropic high-intensity scattering patterns on the WAXS, MAXS, and SAXS detectors. The higher the anisotropy in the scattering pattern, the higher the vertical alignment of the CNTs in the VACNT foams. For example, a perfectly isotropic sample like powdered CNTs would result in a uniform-intensity circular scattering pattern about the beam's center. The length scale associated with each structural feature can be estimated from the Bragg relation for diffraction:

$$d = \frac{\lambda}{2sin(\theta)} = \frac{2\pi}{q} \tag{3.2}$$

The comprehensive data from WAXS, MAXS, and SAXS detectors allow us to probe length scales ranging from 0.3 nm (WAXS) up to $\sim$ 100 nm (SAXS) (see illustration in Figure 3.4(b)). Integrating the two-dimensional scattering pattern reduces the data into one-dimensional intensity profiles $I(q)$ and $I(\phi)$ (Figure 3.4(c),(d)), where ϕ is the azimuthal angle. $I(q)$ is the sector average of intensity as a function of q integrated at a specific value of ϕ (*i.e.*, $\phi \pm \Delta\phi$), and $I(\phi)$ is the sector average of intensity as a function of ϕ integrated at a specific value of q (*i.e.*, $q \pm \Delta q$) (Figure 3.5).

$$I(q) = \frac{\int_{\phi-\Delta\phi}^{\phi+\Delta\phi} I(q,\phi)\, d\phi}{\int_{\phi-\Delta\phi}^{\phi+\Delta\phi} d\phi} \qquad I(\phi) = \frac{\int_{q-\Delta q}^{q+\Delta q} I(q,\phi)\, dq}{\int_{q-\Delta q}^{q+\Delta q} dq} \tag{3.3}$$

The key feature of our X-ray scattering data is the sharp and slightly asymmetric (002) peak in scattering vector intensity profile $I(q)$ (Figure 3.4(c)), obtained from WAXS detector. This peak reflects the characteristics of the inter-wall spacing of the MWCNTs, i.e. the spacing between the concentric shells within an individual nanotube, which appears at 3.424 ± 0.0036 Å for HD samples and 3.421 ± 0.0052 Å for LD samples in our experiments (compared to 3.37 Å for bulk graphite). The (002) peak corresponds to the maximum intensity region at $\phi = 90°$ (perpendicular to the CNT

alignment direction) in the ring of modulated intensity around the incident beam (Debye-Scherrer ring) (Figure 3.4(b)). Unlike WAXS, we didn't observe any distinct X-ray scattering peaks in MAXS and SAXS. Instead, we observed elongated scattering patterns along the polar q ($\phi = 90°$) direction (Figure 3.4(b)), indicating no long-range order exists in the span of q values probed by MAXS and SAXS detector. This amorphous behavior on higher length scales is likely due to the polydispersity of MWCNT's diameters in VACNT foams.

The azimuthal intensity profile ($I(\phi)$) yields Herman's orientation factor (HOF), which characterizes the alignment of the CNTs in the sample:

$$HOF = \frac{1}{2}\left(3\left\langle cos^2\phi \right\rangle - 1\right) \tag{3.4}$$

$$\left\langle cos^2\phi \right\rangle = \frac{\int_0^{\frac{\pi}{2}} I(\phi) sin(\phi) cos^2(\phi) d\phi}{\int_0^{\frac{\pi}{2}} I(\phi) sin(\phi) d\phi} \tag{3.5}$$

HOF is equal to 1 for perfect vertical alignment of the CNTs, -0.5 for perfect horizontal alignment, and 0 for an isotropic sample with random CNT alignment.

To characterize VACNT foams' density gradient, we measured X-rays' mass attenuation using photon-counting detectors placed in the path of the X-ray beam. An upstream detector measured the intensity of X-rays incident on the sample while a downstream detector measured the intensity of X-rays exiting the sample. The local average mass density of CNTs encountered by X-rays while traversing through the sample can be calculated using Beer-Lambert law. Each VACNT sample is scanned along its thickness to measure local mass density as a function of the height while also collecting the scattering patterns on WAXS, MAXS, and SAXS detectors for each scan location. We developed a MATLAB script for 2D data reduction, HOF computation, and mass density calculations from the X-ray scattering and mass attenuation measurements.

3.1.4 Measuring mass density

While scanning the sample along its thickness, we recorded incident (I_i) and transmitted (I_t) intensities for each scan point. Using Beer-Lambert law, the density is calculated as

$$\rho_{\text{CNT}} = \frac{\ln\left(I_i/I_t\right)}{w(\mu/\rho)} \tag{3.6}$$

where w is the width of the VACNT forest along the X-ray beam and $\frac{\mu}{\rho}$ is the weighted average of mass attenuation coefficient of Iron and Carbon. If the weight fraction of iron is f, then the weighted average mass attenuation coefficient is given as

$$(\mu/\rho) = (1-f) \times (\mu/\rho)_{\text{C}} + f \times (\mu/\rho)_{\text{Fe}} \tag{3.7}$$

where $(\mu/\rho)_{\text{Fe}}$ and $(\mu/\rho)_{\text{C}}$ are mass attenuation coefficients of Iron and Carbon respectively [79]. Using EDS analysis, we found average percentage of Iron to be approximately $7.91 \pm 0.368\%$ and $7.43 \pm 0.074\%$ for HD and LD samples respectively. Mass densities measured using X-ray transmittance, $0.230 \pm 0.014\, gm/cm^3$ for pristine HD samples and $0.123 \pm 0.014\, gm/cm^3$ for prsitine LD samples are found to be very close to the densities measured manually (weighing a sample to estimate its mass and measuring its dimensions for calculating the volume), $0.209 \pm 0.014\, gm/cm^3$ for HD samples and $0.097 \pm 0.019\, gm/cm^3$ for LD sample. X-rays scattered after exiting the sample don't get recorded on the downstream photon-counting detector, resulting in slightly overestimating the density.

3.1.5 Results and Discussion

Both pristine HD and LD VACNT foams we tested exhibit almost linear mass density gradients (Figure 3.6(a,d)) with HD samples having higher gradient of $0.221 \pm 0.023\, g\, cm^{-3} mm^{-1}$ compared to the LD samples that have $0.115 \pm 0.025\, g\, cm^{-3} mm^{-1}$. Additionally, the LD samples' density reaches nearly a constant value at the top region (~ 0.2 mm of the sample thickness) (Figure 3.6(d)). This local mass density distribution and the associated local stiffness could have led to the collective buckle formation in the top region of LD sample in addition to the bottom region at large strains, as shown in Figure 3.2(b). The average mass density of the HD samples ($0.230 \pm 0.014\, g/cm^3$) is higher than that of the LD samples ($0.123 \pm 0.014\, g/cm^3$) because of the larger average outer diameter of the CNTs ($316.9 \pm 137.3\, nm$) and the number of walls (35 ± 19) in HD samples (Figure 3.1(e,h)) compared to the outer diameter ($253.8 \pm 108.8\, nm$) and the number of walls (25 ± 14) of CNTs in LD samples. Also, the average number density (CNTs per unit area) is found to be higher in HD

samples (32% higher). These average densities measured by synchrotron X-ray scattering and mass attenuation are slightly higher than the bulk densities we directly measured from the weight and volume of the samples (Table 3.1). X-rays scattered after exiting the sample do not get recorded on the downstream photon-counting detector, resulting in slightly overestimating the density. The mass density gradient in the samples is a result of the bottom-up CNT growth on the substrate that results in a higher entanglement morphology of the CNTs at the top region compared to less entangled and more vertically aligned CNTs at the bottom region near the substrate. The nature of this CNT morphology is reflected in the HOF of HD samples that characterizes the alignment of the CNTs [14, 45, 80]–the HOF of the pristine HD sample decreases with increasing height (Figure 3.6(b)). The LD samples, on the contrary, has higher waviness than the HD samples (Figure 3.6(e)). The local waviness and corrugations is also evident in the SEM images of the samples (Figure 3.1). Additionally, the LD samples exhibit higher vertical CNT alignment in the top region than the bottom region. The alignment–HOF–of pristine HD and LD samples as a function of the sample height calculated from MAXS and SAXS data also exhibit similar trends as the WAXS (Figure 3.7). This striking correlation reveals how the structural order in the bulk scale emerges from the nanoscale features in a hierarchical fibrous material [81].

The material's structural information lies not only in the scattering intensity distribution but also in the peak position and line width of the one-dimensional sector average intensity profile, $I(q)$. From WAXS, we obtained broad and slightly asymmetric (002) peaks (Figure 3.4(c)). To quantify the peak broadening, we calculated the FWHM (full width at half maximum) of (002) peaks. Peak broadening is considered any deviation from the ideal crystalline lattice's scattering peak–a Dirac delta peak. The primary sources of peak broadening are crystallite-size broadening and lattice-strain broadening. Crystallite-size broadening is a consequence of the distribution of crystallites of various sizes in a sample undergoing X-ray scattering. Lattice-strain broadening arises from non-uniform distortions in the lattice due to crystal defects like dislocations, faulting, twinning, point defects, etc. Pristine samples can have some lattice defects that could further grow in number under bulk deformation.

In our samples, the crystallite size broadening is due to the distribution of MWCNTs of different diameters in HD and LD VACNT samples. If the mean outer diameter is D, the FWHM (Δq_c) due to crystallite size distribution is given by Scherrer equation [82, 83],

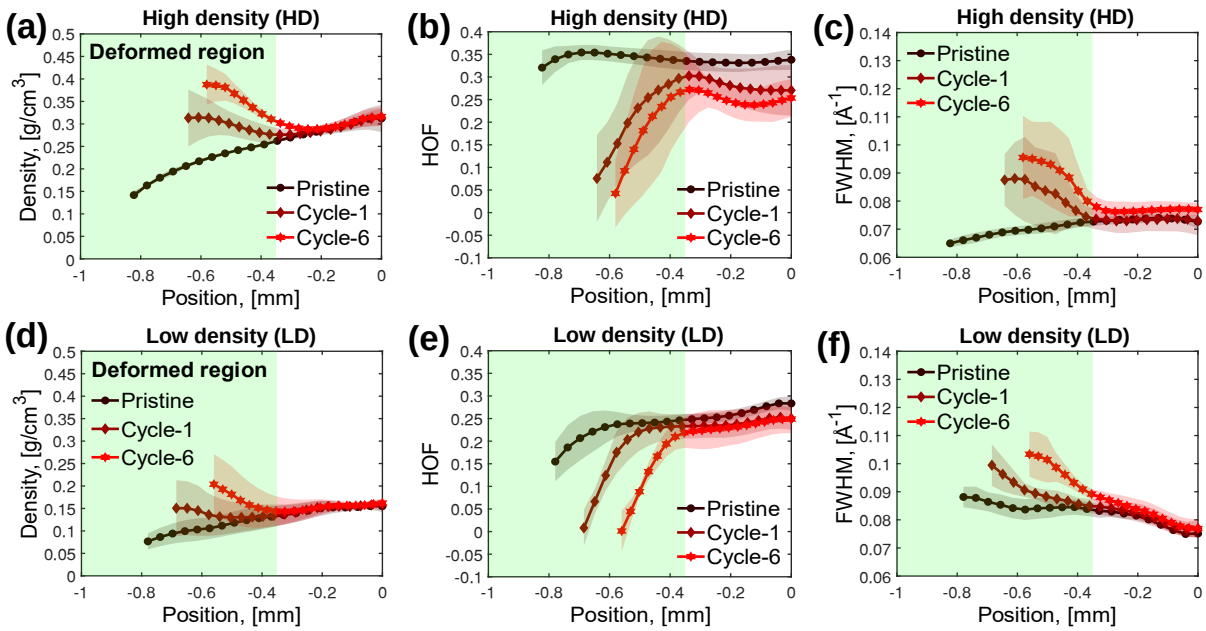

Figure 3.6: (a) Density along samples' thickness for HD samples and (d) LD samples. HOF along the thickness for (b) HD and (e) LD samples calculated from WAXS data. FWHM of polar (002) X-ray scattering peak for (c) HD and (f) LD samples. In figures above, the zero position on X-axis corresponds to top region of VACNT foams, deformed bottom region is highlighted in green color. Each data point in the figures above is the mean value for all HD samples and LD samples (Table 3.1) with shaded region plotted for mean plus-minus one standard deviation.

$$\Delta q_c = \frac{4\sqrt{\pi \ln 2}}{D} \tag{3.8}$$

Using the mean outer diameter of MWCNTs calculated from TEM images of HD (316.9 Å) and LD samples (253.8 Å), the FWHMs from Scherrer equation are $\Delta q_c = 0.0186\,\text{Å}^{-1}$ and $\Delta q_c = 0.0233\,\text{Å}^{-1}$ respectively. But, the FWHM of (002) peak from X-ray scattering of pristine HD and LD samples turned out to be higher than the FWHM calculated from the Scherrer equation. This discrepancy indicates that there is also a significant contribution of strain broadening in total peak broadening. MWCNTs with smaller outer-diameter (few walls) have higher interwall spacing due to more strain (due to higher curvature of the CNTs) in individual rolled graphitic layer. The interwall spacing decreases exponentially with diameter (number of walls > 20) and approaches interlayer distance (3.37Å) of graphite (zero curvature) [83, 84]. Our CVD grown VACNT foams have CNTs with number of walls ranging from single to tens of walls, hence there is distribution of interwall spacing, which results in strain broadening of the (002) peak (Figure 3.4(c)). FWHM

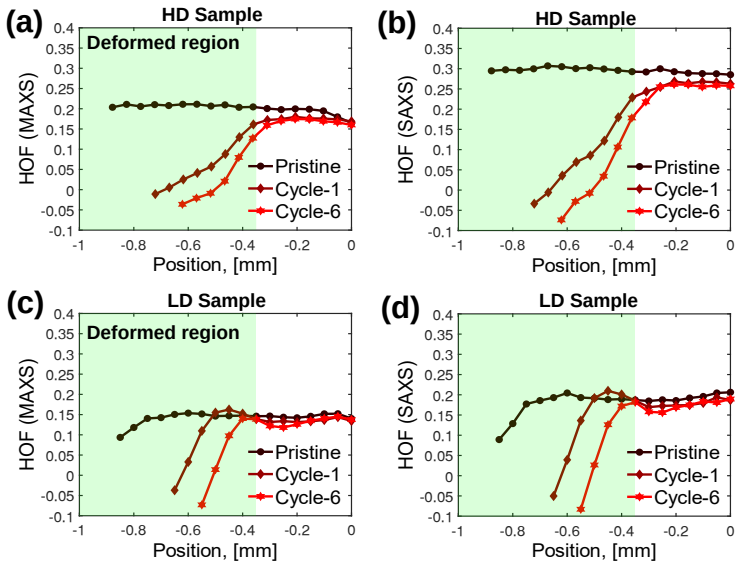

Figure 3.7: (a) HOF(MAXS) (b) HOF(SAXS) for HD sample. (c) HOF(MAXS) (d) HOF(SAXS) for LD sample.

(Δq_s) due to strain broadening of the (002) peak is given by [82]

$$\Delta q_s = 2q\epsilon = 2q\frac{\Delta d}{d} = 4\pi\frac{\Delta d}{d^2} \tag{3.9}$$

where q is the peak position of the (002) peak, ϵ is the effective strain in interwall spacing, Δd is the standard deviation of interwall spacing, and d is the mean interwall spacing. Using interwall spacings calculated from TEM images for pristine HD (3.437 ± 0.047Å) and LD samples (3.481 ± 0.064Å), the FWHMs due to strain broadening are $\Delta q_s = 0.0501\text{Å}^{-1}$ and $\Delta q_c = 0.0664\text{Å}^{-1}$ respectively. Total peak broadening comprising the effect of both crystallite-size broadening and strain broadening is given as follows

$$\Delta q_T = \Delta q_c + \Delta q_s \tag{3.10}$$

Total FWHM for HD samples, $\Delta q_T = 0.0687\text{Å}^{-1}$ and for LD samples, $\Delta q_T = 0.0897\text{Å}^{-1}$ are found to be very close to FWHM of polar (002) peak observed in X-ray scattering experiments $\Delta q = 0.0710 \pm 0.0013\text{Å}^{-1}$ for pristine HD samples and $\Delta q = 0.0822 \pm 0.0026\text{Å}^{-1}$ for pristine LD samples. This agreement indicates that there is very negligible effect of other sources of peak broadening like instrumental broadening.

For pristine HD samples, the FWHM increases with height, following an opposite trend to HOF

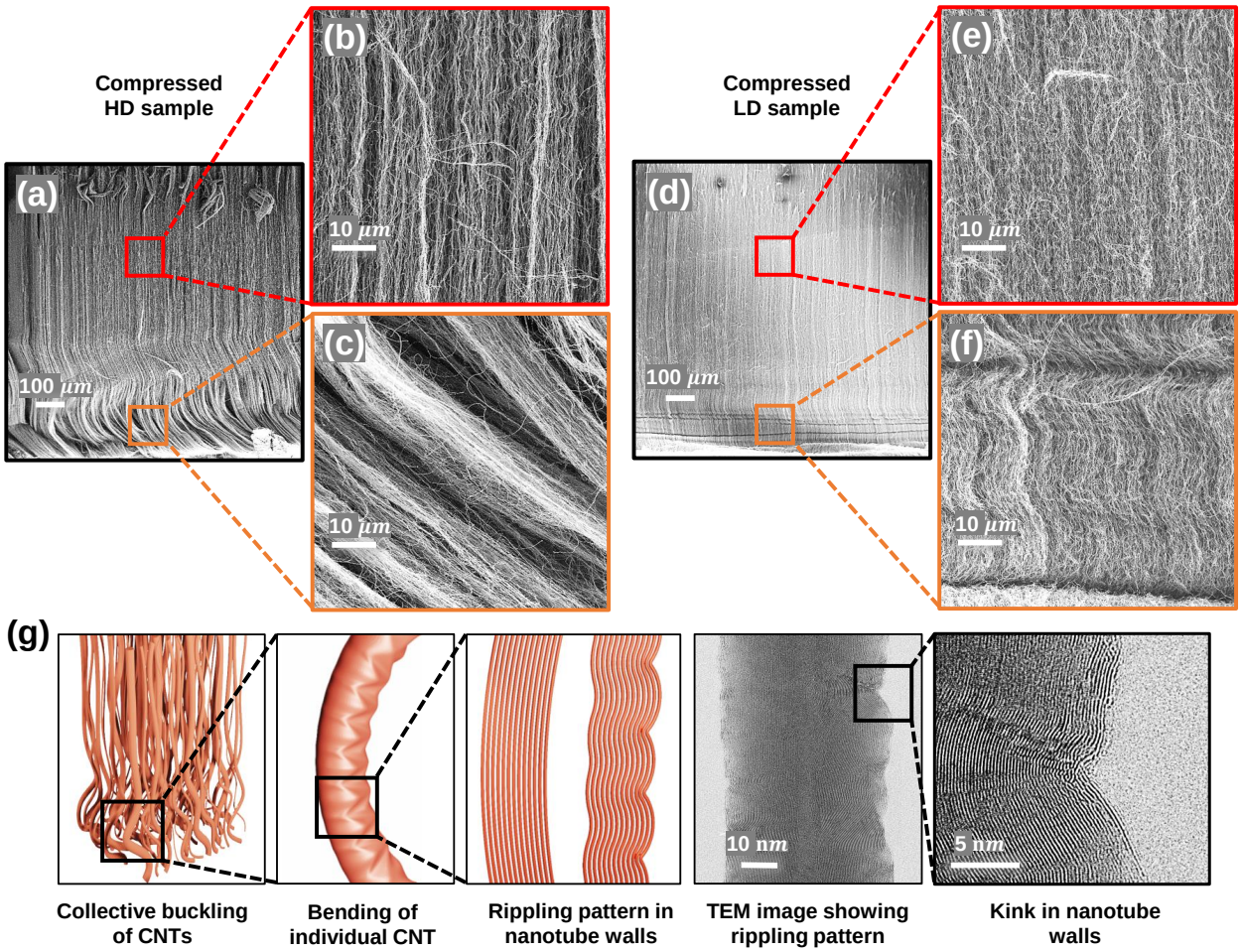

Figure 3.8: (a) An HD sample after six compression cycles. (b) Nearly intact top region of compressed HD sample. (c) Buckled bottom region of compressed HD sample. (d) An LD sample after six compression cycles (e) Nearly intact top region of LD sample. (f) Buckled bottom region of LD sample. (g) Nanoscale deformation mechanism in individual carbon nanotube during collective buckling of CNTs in VACNT foam.

of pristine HD samples. For pristine LD samples, the FWHM decreases with height which also follows an opposite trend to HOF of pristine LD samples. Clearly, regions in VACNT foams with less aligned CNTs have higher FWHM of (002) peak and vice versa. Lesser alignment affects the interwall spacing distribution due to bents and curves in individual nanotubes and hence increases strain broadening.

When the VACNT foams are compressed in consecutive cycles, a clear progressively increasing permanent densification in the bottom region can be seen for both HD and LD samples in the mass density measurements taken after one and six cycles of compression (Figure 3.6(a,d)). In the top region, the mass density is unaffected by compression because of the deformation localization

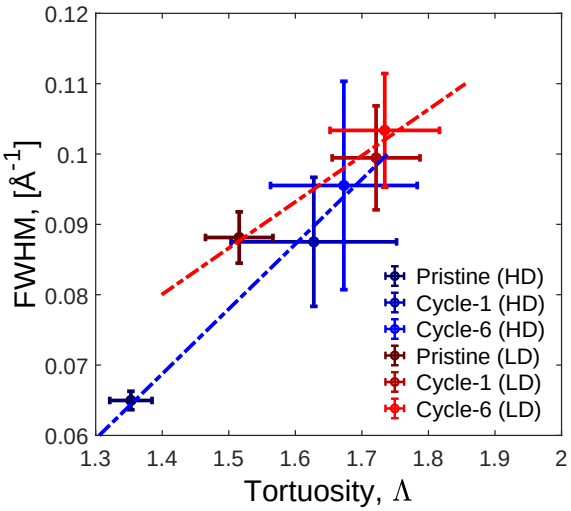

Figure 3.9: FWHM vs. Tortuosity in the deformed (bottom) region of HD and LD samples

mainly occurring in the bottom region. The portion of sample's thickness affected most by compressive strain is highlighted in green as "Deformed region" in Figure 3.6. This local densification results in permanent deformation (nominal strain) in the bulk sample. The substantial portion of densification occurs in the first cycle, reducing the sample thickness by a considerable amount ($\sim 20\%$ for HD and $\sim 10\%$ for LD samples), but it is much smaller for further compression cycles. Densification arising due to collective permanent buckling of nanotubes can be seen in SEM images of six cycles compressed HD and LD VACNT sample (Figure 3.8(a,b,c,d,e,f)). SEM images shown in Figure 3.8 are the sliced cross-section images taken after freezing the VACNT samples using liquid nitrogen to embrittle them and then slicing along their thickness. The morphology of the buckles in the sliced cross-section is different compared to that of the surface buckles shown in Figure 3.2. This internal deformation morphology is representative of the bulk response of the VACNT foams and correlates better with the volumetric X-ray scattering measurements rather than the surface deformation seen in high-speed microscope imaging.

The effect of compression cycles on HOF calculated using WAXS data at (002) peak is shown in Figure 3.6(b,e). Upon compression, the orientation factor reduces across the whole VACNT foam for both HD and LD samples, suggesting that the CNT's initial state in the entire pristine sample is perturbed regardless of the local deformation and densification. The HOF substantially changes at the bottom region with its reduction in the deformed region being gradual for the HD sample and very abrupt for the LD sample. This nature of orientation change is also evident in much larger

lengthscales in respective SEM images of samples compressed to six cycles (Figure 3.8(a,d)).

Similar trends are seen for orientation factors calculated from MAXS and SAXS azimuthal intensity curves (Figure 3.7) indicating the coordinated effect across multiple length scales in the hierarchical VACNT foams. The HOF in the bottom-most region of VACNT foams after compression is even slightly smaller than zero (Figure 3.6(b,e)). This indicates that the CNTs are more horizontally aligned rather than vertically aligned in the densified region following compression.

Similar to what we observed for pristine samples, the correlation between HOF and FWHM remained strong after compression as well. After compression, an increase in FWHM (peak broadening) is observed in the bottom region of samples. The growth in FWHM for the first cycle is substantial, but little further growth is observed for five more cycles (Figure 3.9). This behavior is similar to the drop in specific energy dissipation by VACNT foam with compression cycles, indicating that the origin of preconditioning effect observed in bulk sample's stress-strain response is arising from nanoscale phenomenon causing the broadening of (002) peak. Among the two potential sources of peak broadening–crystallite-size broadening and lattice-strain broadening–the crystallite size broadening can be ruled out because the compression of VACNT foams should not affect the diameter distribution.

Analogous to strain broadening we described for pristine samples, here the reduced orientation as a result of collective buckling of CNTs under macroscale compression of the VACNT foam is leading to additional inhomogeneous nanoscale strain in nanotube walls. Buckling can induce rippling patterns in the walls of nanotubes at high local strains [63, 85]. [86], and [85] reported a Yoshimura-like rippling pattern for nanotubes undergoing buckling. We also observed a similar rippling pattern in TEM images of CNTs from compressed VACNT samples (Figure 3.8(g)). For quantitative assessment, we calculated tortuosity as a function of compression cycles and compared it with FWHM. Buckling increases the tortuosity of nanotubes. Tortuosity is the ratio of the actual length of a CNT to its apparent length. Tortuosity (Λ) as a function of HOF can be written as follows [87]

$$\Lambda = \sqrt{\frac{3}{2 \times HOF + 1}} \tag{3.11}$$

As a function of compression cycles, we observed that FWHM scales linearly with tortuosity

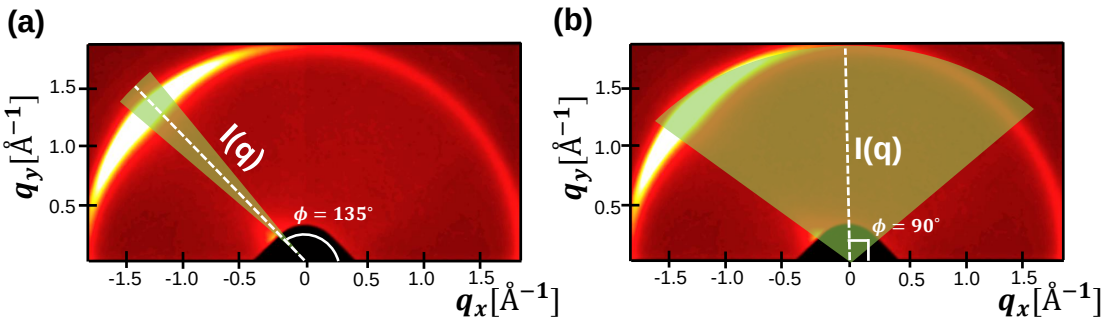

Figure 3.10: Radial Integration methods (a) 10° wedge at $\phi = 135°$ (b) 120° wedge at $\phi = 90°$

(Figure 3.9) in the deformed region of both HD and LD VACNT samples (Figure A.4). Total broadening of the (002) peak in the deformed region can be described by adding an additional strain broadening term due to orientation decay as follows

$$\Delta q_T = \frac{4\sqrt{\pi \ln 2}}{D} + 2q\epsilon + 2q\epsilon_\Lambda \tag{3.12}$$

where ϵ_Λ is directly proportional to change in Λ with compression cycles.

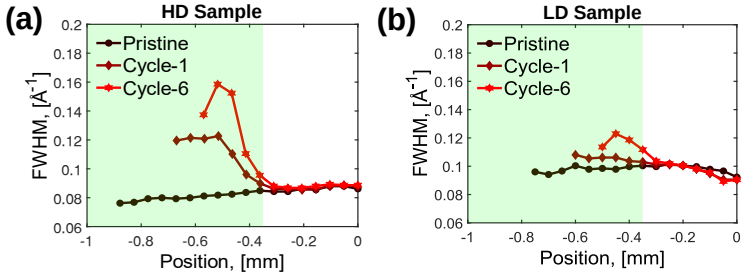

Figure 3.11: Total FWHM of 002 peak (120° wedge at $\phi = 90°$) for (a) HD sample and (b) LD sample

To rule out the possibility that peak broadening is merely a result of redistribution of scattering intensities due to the change in initial orientation of nanotubes, we integrated scattering intensities for the whole azimuthal wedge of 120° degrees (Figure 3.10, Figure 3.11). The peak broadening is still present in the deformed region of both HD and LD samples, confirming that there is permanent nanoscale deformation in the CNTs.

The (002) peaks we obtained in experiments are slightly asymmetric, so we curve-fit the peaks using a weighted sum of two Gaussian components to decouple the effect of compression cycles on each component. (Figure A.2, Figure A.3). We observed peak broadening in both the components,

indicating that the origin of asymmetry is likely due to scattering from sub-population of CNTs with smaller and larger diameters [88].

3.1.6 Conclusions

Using non-destructive X-ray scattering and mass attenuation measurement techniques along with high-speed microscopy and corroborating evidences from electron microscopy, we investigated the effects of compressive cyclic loading on the structure of VACNT foams across their hierarchical length scales. We used two different set of samples, high density samples and low density samples. Due to anisotropy as well as heterogeneity in density and stiffness, the VACNT foams deform through localized sequentially progressive collective buckling of nanotubes. The deformation is localized in the less dense bottom region of the VACNT foams under compression while the top region remains almost intact. We observed a reduction in orientation factor across all lengthscales probed by X-ray scattering in this study, indicating the reduction in vertical alignment of the CNTs upon compression. From the observed broadening of the (002) scattering peak, we show that the preconditioning effect and the permanent deformation occurs in the VACNT foams due not only to the mesoscale reorganization of the CNTs but also to the irreversible nanoscale strain induced on the walls of individual CNTs. This preconditioning effect and permanent strain localization is pronounced in first few cycles and ceases after 5-6 cycles of loading-unloading.

Intriguingly, regardless of the permanent nanoscale strain in CNTs and their mesoscale reorganization, their collective interaction leads to remarkable bulk strain recovery of VACNT foams. This phenomenon that stems from the hierarchical structure provides a beneficial design template for constructing other engineering materials with sustained superior energy dissipation and high strain recovery for applications in extreme environments.

Acknowledgements

We thank Prof. Corinne Henak and Dipul Chawla for their support in compression experiments with TA ElectroForce 323, and Dr. Alex Kvit for TEM. We acknowledge the financial support from the Solid Mechanics program of the Army Research Office (Award number: W911NF2010160). This research used resources of the Advanced Photon Source, a U.S. Department of Energy (DOE) Office

of Science User Facility operated for the DOE Office of Science by Argonne National Laboratory under Contract No. DE-AC02-06CH11357. A portion of this work was performed under the auspices of the U.S. Department of Energy by Lawrence Livermore National Laboratory (LLNL) under Contract DE-AC52-07NA27344.

3.2 Friction damping based constitutive model

VACNT foams are highly dissipative materials that have been extensively studied in the literature using both experimental and theoretical models. Due to their dissipative nature, they are often considered viscoelastic and have been shown to exhibit phenomena such as stress relaxation [89] and complex dynamic modulus [16]. However, these studies have led to erroneous interpretations of the viscoelastic behavior of VACNT foams. For example, an overshoot in strain by the load frame was interpreted as stress relaxation in the study by [89], while hysteretic damping was incorrectly inferred as viscoelasticity in the work by [16] In this section, we present experimental evidence demonstrating that VACNT foams are not viscoelastic and exhibit rate-independent mechanical behavior. Instead of viscoelasticity, VACNT foams exhibit frictional damping, which is governed by van der Waals interactions among nanotubes. Previous studies have also reported strain-rate-independent behavior in VACNT foams, both for quasistatic compression [60] and dynamic mechanical analysis at frequencies up to 100 Hz.

Figure 3.12 shows the mechanical behavior of VACNT foam measured using quasistatic and stress-relaxation experiments performed on a commercial load frame. VACNT foams exhibit no stress-relaxation for a wide range of compressive strains. To apply strain, we ramp up the strain at a constant strain rate and then hold the strain constant. Ignoring the initial overshoot due to the load frame's inertia, the strain is maintained constant in the region highlighted in Figure 3.12(a). In response, the stress also overshoots, but in the shaded region, the stress remains constant for a wide range of relaxation times. Similarly, we observed rate-independent behavior for quasistatic ramp compression, accomplished by applying strain at a constant loading rate and then unloading at the same rate (Figure 3.12(c)). The stress-strain curves obtained for various strain rates overlap, indicating strain-rate-independent behavior (Figure 3.12(d)).

We also observed rate-independent behavior in broadband dynamic mechanical analysis exper-

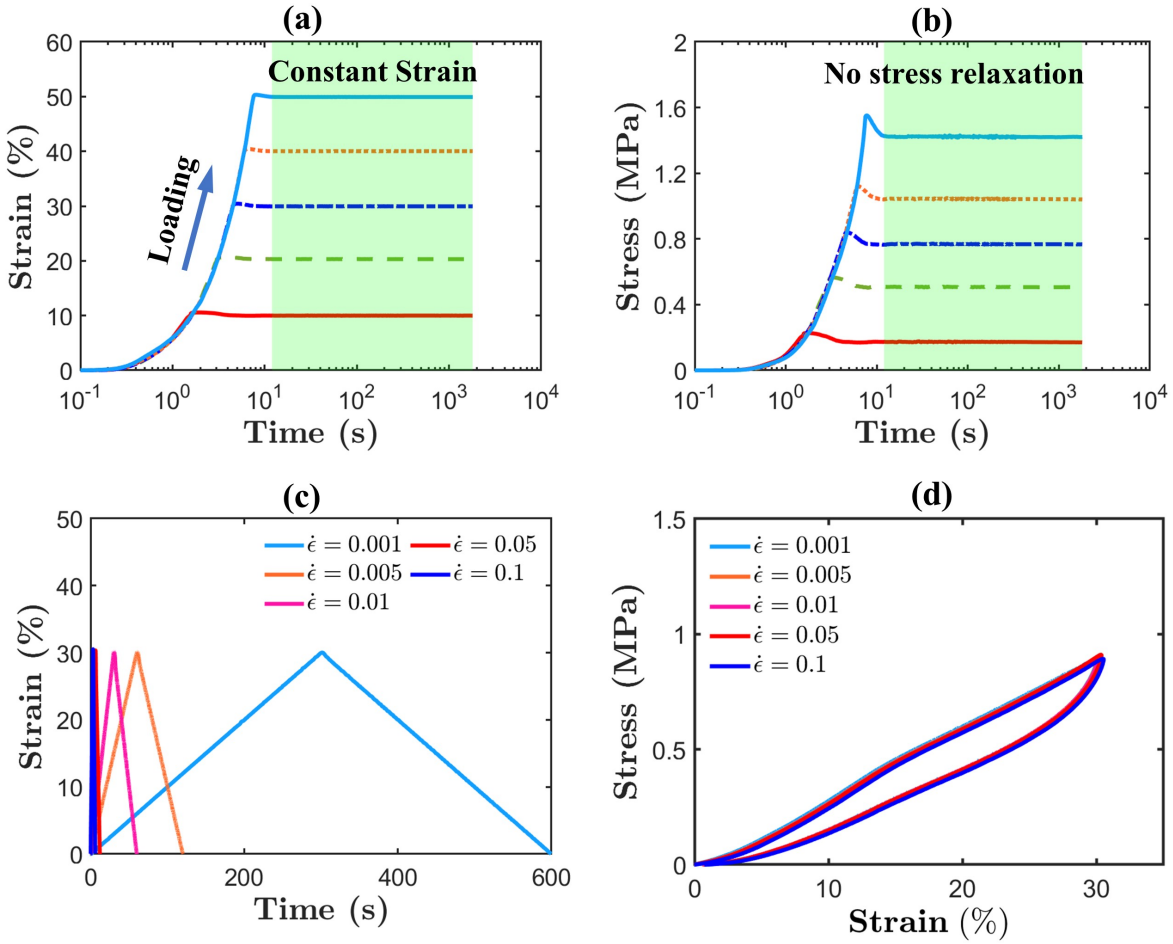

Figure 3.12: (a,b) Applied strain and stress response in relaxation experiment. (c,d) Quasistatic ramp strain and stress-strain curves for two orders of strain rates.

iments. Using our custom-built dynamic mechanical analyzer, we conducted DMA experiments by applying static precompression and then loading the materials with a sinusoidal strain of a particular amplitude and frequency. We performed a frequency sweep and observed a frequency-independent dynamic modulus and loss factor (Figure 3.13(a,b)). Since VACNT foams are not viscoelastic, the characteristic hysteresis curve is not elliptical in shape; rather, the stress and strain signals are in phase with each other at the maxima and minima. Thus, unlike viscoelastic materials, VACNT foams do not have a loss tangent but a loss factor, which is proportional to the ratio of energy dissipated to energy stored. Moreover, the dynamic modulus of VACNT foams is just the ratio of stress amplitude to strain amplitude, with no imaginary part.

We also performed an amplitude sweep and observed a softening effect—a tilt in the stress-

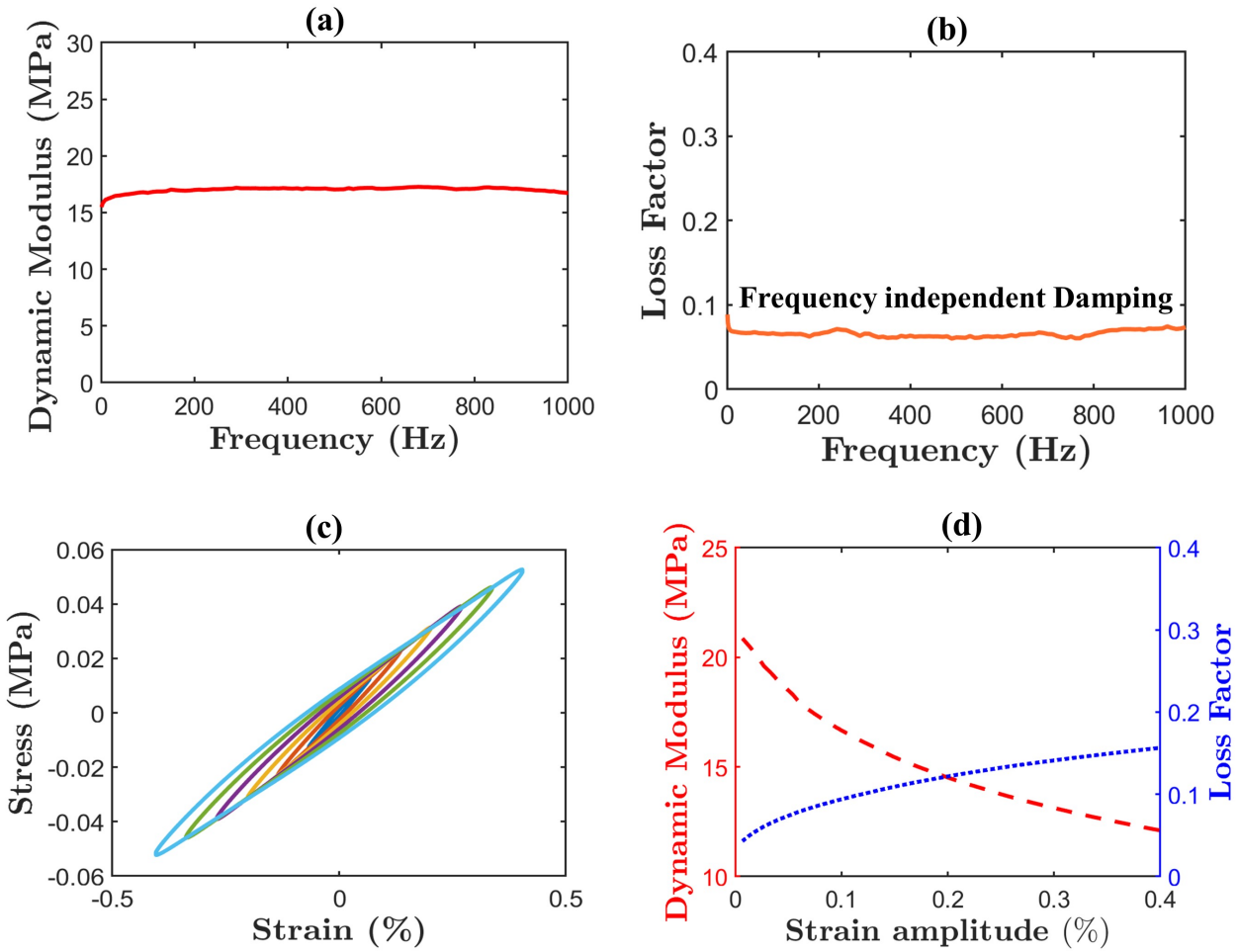

Figure 3.13: (a,b) Frequency dependent dynamic modulus and loss factor measured via DMA. (c,d) Effect of dynamic amplitude on stress-strain hysteresis and dynamic modulus and loss factor.

strain hysteresis as a function of strain amplitude (Figure 3.13(c)), indicating dynamic softening. In Figure 3.13(d), we plot the dynamic modulus as a function of strain amplitude, showing a clear decreasing trend. The loss factor increases as a function of strain amplitude, which is due to a sharper decrease in stored energy compared to dissipation energy. The softening in the dynamic modulus as a function of strain amplitude is called the Payne effect and has been observed in various other filled rubbers and fibrous materials. However, the Payne effect was not known in rate-independent materials before we observed it in VACNT foams.

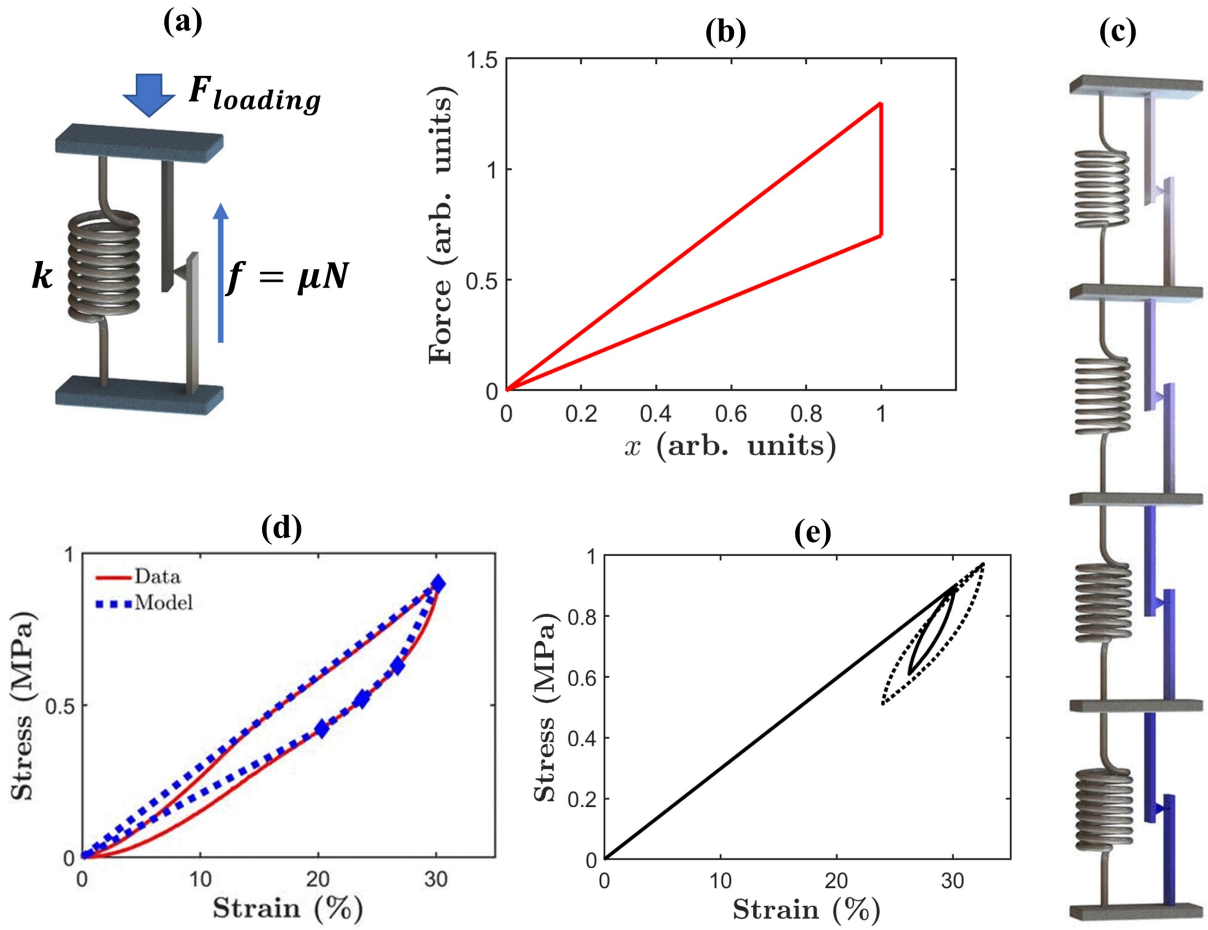

Figure 3.14: (a) Spring and friction elements in parallel combination. (b) Hysteresis for single spring and friction elements in parallel. (c) Multiple springs and friction elements connected in series (d) Experimentally measured stress-strain curve with the friction damping model fit. (e) Friction damping model capturing the Payne effect

3.2.1 Frictional damping model

To explain the rate-independent damping of VACNT foams, some studies have focused on using bi-stable springs to capture the quasistatic stress-strain response [73, 90]. The use of bi-stable springs is motivated by the buckling and snapping of CNT bundles. However, not all VACNT foams exhibit such sudden buckling and collapse, yet they are rate-independent. Additionally, the bi-stable spring-based model cannot capture the Payne effect in VACNT foams. We propose a frictional damping-based model that is rate-independent and effectively captures the Payne effect observed in dynamic mechanical analysis. Similar to viscoelastic models where springs and dashpots are combined to achieve desired properties, we connect a spring in parallel to a friction element

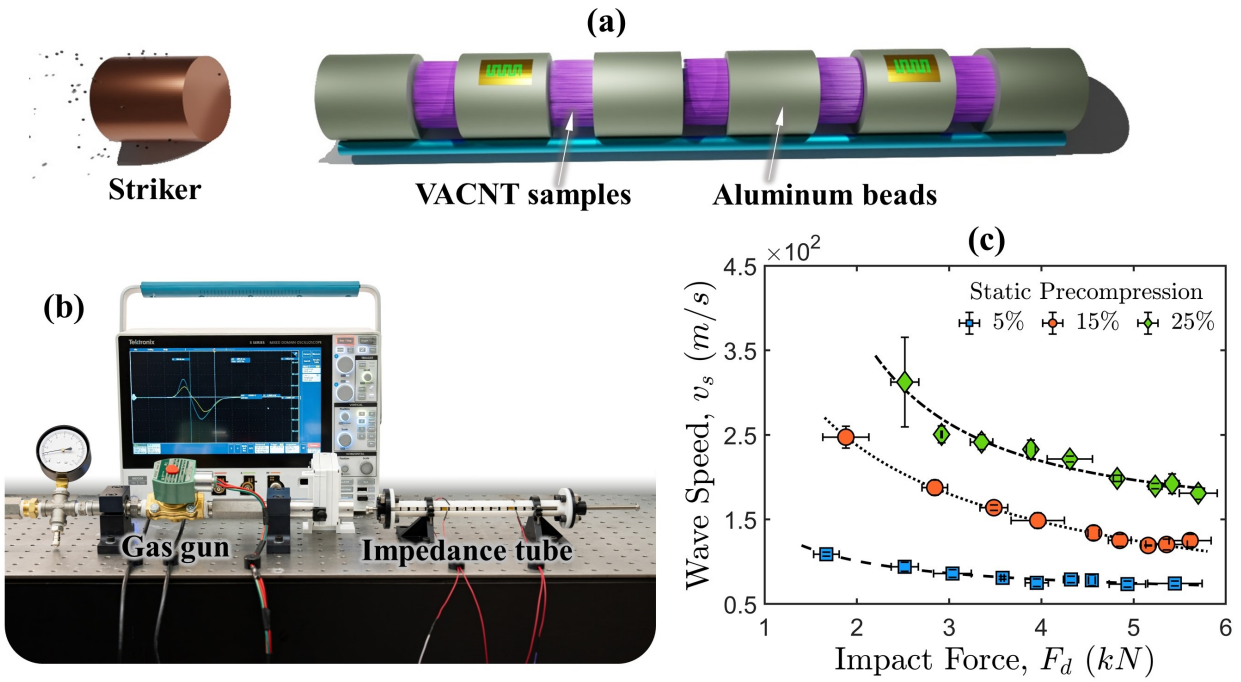

Figure 3.15: (a) Periodic lattice of VACNT and rigid aluminum cylinders (b) Experimental setup consisting of gas gun and impedance tube (c) Wave speed as a function of effective dynamic input force and static precompression strain.

(Figure 3.14(a)). While the spring's force depends on the amount of compression applied, the force in the friction element always opposes relative motion. When a loading force is applied, the spring compresses and the friction element opposes relative motion, adding both forces. During unloading, the friction force direction first switches, resulting in a drop in force, and then unloads. Thus, during unloading, the total force is the spring force minus the friction force, resulting in force-displacement hysteresis (Figure 3.14(b)).

$$F_L = kx + \mu kx \ \text{(Loading)} \quad F_{UL} = kx - \mu kx \ \text{(Unloading)} \tag{3.13}$$

Connecting multiple springs and friction elements with different spring constants and friction coefficients in series allows us to obtain a smooth unloading that captures the stress-strain response of VACNT foam (Figure 3.14(d)). Our model also captures the Payne effect observed in local dynamic mechanical analysis. Figure 3.14(e) shows that a certain amount of static strain is first applied, and then the model is unloaded to a certain amount and loaded back to the same strain level (solid curve), resulting in a local hysteresis loop. The local cyclic loading-unloading follows

the masing rule, where the unloading curve and loading curve are mirror symmetric to each other. If the same local loading and unloading are repeated for a higher amplitude (dashed curve), it results in a bigger hysteresis loop with a smaller dynamic modulus, hence an amplitude-dependent softening.

We leverage the Payne effect to achieve wave slowdown in a periodic lattice of vertically aligned carbon nanotubes (VACNTs) with rigid interlayers of aluminum beads. Our experimental setup consists of an impedance tube with VACNTs and aluminum beads arranged in a periodic fashion (Figure 3.15(a,b)). We applied static precompression using a screw on one side and leave the other end open for applying impulse loading. Using a gas gun, we accelerated a small projectile of aluminum to impact the lattice and send a stress pulse. We measured the pulse velocity using two strain gauges mounted on separate beads in the periodic lattice. Each strain gauge provided a pulse signal, from which we calculated the wave speed using the known distance between the strain gauges. Due to the Payne effect, the wave slows down as a function of impact force. However, with increasing precompression strain on the overall lattice, the wave speeds up, as shown in Figure 3.15(c).

3.2.2 Summary and key findings

We discovered rate-independent mechanical behavior in VACNT foams across a wide range of strain amplitudes and strain rates by conducting stress-relaxation, quasistatic compression, and dynamic mechanical analysis. Additionally, we observed a dynamic softening known as the Payne effect, which is well-known in soft filled rubbers but observed for the first time in a non-viscoelastic material. To explain these observations, we proposed a comprehensive friction-damping-based model that captures both rate-independence and the Payne effect. In a periodic lattice of VACNT foams and rigid aluminum cylinders, we demonstrated an amplitude-dependent slowdown in wave propagation as a result of the Payne effect. This phenomenon has significant potential applications in designing layered composites for shock absorption.

Chapter 4

Superior specific properties in cylindrically architected VACNT foams

This chapter is adopted from the following publication

Chawla, K., Gupta, A., Bhardwaj, A. S., & Thevamaran, R. (2022). Superior mechanical properties by exploiting size-effects and multiscale interactions in hierarchically architected foams. Extreme Mechanics Letters, 57, 101899.
Author Contributions : KC synthesized samples, performed compression testing, and prepared figures. AG performed data analysis, developed phenomenological model and wrote the paper, ASB provided the statistical model. RT conceived and supervised the project and wrote the paper.

In this chapter, we explore methods for improving the mechanical properties of VACNT foams through mesoscale architecture. Although VACNT foams without architecture already demonstrate impressive mechanical properties, the addition of architecture further improves their lightweight and stiffness, thereby enhancing specific density-normalized properties. We present outstanding specific mechanical properties of VACNT foams with diverse architectures, along with phenomenological models.

4.1 Introduction

Exceptional modulus, strength, and toughness with lesser mass density and thermal stability in extreme conditions are critical characteristics of materials that are required in aerospace, automotive, robotics, structural, and defense applications. These qualities, however, are not found together in a conventional material due to the contradictory relationship they have with material's morphology and the different lengthscales of their origin [9, 10, 91]. For example, stiffer materials are typically poor in dissipating energy [92], and high-strength materials generally have lesser toughness [9, 93, 94]. Materials with structural hierarchy have been shown to overcome the limitations on mechanical performance by exploiting superior intrinsic properties of the nanoscale building blocks and their interactions across the structural organization from nano to macroscales to achieve high strength, toughness, and Young's modulus at lightweight than their constituent materials [10, 95, 96]. Multiscale hierarchy and functional property gradients are found in biological materials [12, 97] and have been a source of inspiration to develop synthetic hierarchical materials with functionalities tuned for specific needs [98, 99]. Similarly, architected materials with specific geometries—sometimes referred to as mechanical metamaterials—have also been utilized to achieve superior specific properties and unusual functionalities [100], for example, multistable structures for energy dissipation [101, 102], nacre like structure for improved fracture toughness [9, 98, 103], nanotruss lattices for improved specific stiffness [19, 23, 104, 105], cellular and lattice structures for improved thermal properties [106, 107] and recently PT symmetric fractals for anomalous wave transport [29]. These studies suggest that exploiting the interplay between multitier geometric parameters of an architected design along with structural hierarchy present in a material system like vertically aligned carbon nanotube (VACNT) foams can yield unprecedented bulk properties desirable for protective applications. Additionally, they can serve as versatile design templates for hierarchical materials to achieve synergistic property enhancement and desired functionalities.

Here, we report synergistic improvement in specific elastic modulus, specific energy absorption, and specific compressive strength in architected VACNT foams. The VACNT foams have a hierarchical structure with feature sizes ranging from a few angstroms to several millimeters [13]. The individual CNT's multiwalled structure at the nanoscale along with their entangle forest-like morphology in microscale that further forms into vertically aligned bundles in mesoscale make

them undergo collective sequentially progressive buckling under compressive loading and exhibit bulk strain recovery of over 80% [13, 15]. They also exhibit superior thermal stability of their mechanical properties from -196 to 1000 °C [16]. The hierarchical structure of VACNT foams can be tailored to affect their bulk properties dramatically by varying synthesis parameters [14, 15, 17, 59, 61] and by introducing micropatterned growth process [108–112]. We introduced an additional level of structural hierarchy in our VACNT samples through an architected hexagonally packed lattice of hollow cylinders in mesoscale (in the order of 100 μm) (Figure 4.1). Hollow cylinders provide additional structural rigidity to the samples [113, 114], and the hexagonal pattern allows close packing that enhances interactions among the neighboring cylinders. We design, synthesize, and analyze multiple samples by varying and intermixing the three geometrical parameters—the inner diameter of cylinders (D_{in}), the thickness of cylinders (t), and the gap between the outer walls of neighboring cylinders (g).

To achieve simultaneous improvement in mechanical properties, we used a full factorial design of experiments (DoE) approach with D_{in}, t, and g as our design variables. In contrast to the one variable at a time (OVAT) approach, where changing one variable leave the effect of other variables and their interconnectivity unforeseen, full factorial design allows more comprehensive multivariable study and reveals the correlation between design variables [115]. We choose specific energy absorption (SEA), specific modulus (E^*), and specific peak stress (σ_p^*) calculated from quasistatic stress-strain curve as our response variables (objectives). We observe synergistic improvement in SEA, E^*, and σ_p^* owing to morphology changes due to geometrically-confined CNTs growth (size effects), lateral interactions among adjacent cylinders, and the relationship among design variables revealed by fitted Analysis of Variance (ANOVA) models. Our material transcends the traditional requirements for protective applications and demonstrates a design template for architected materials to achieve desired properties

4.2 Architected Design

We adopt a full factorial design of experiments (DoE) approach to optimize the mechanical performance of microarchitected VACNT foams as a function of the geometric parameters. Figure 4.1 shows electron microscopy images of a VACNT foam sample with hexagonal close-packed cylin-

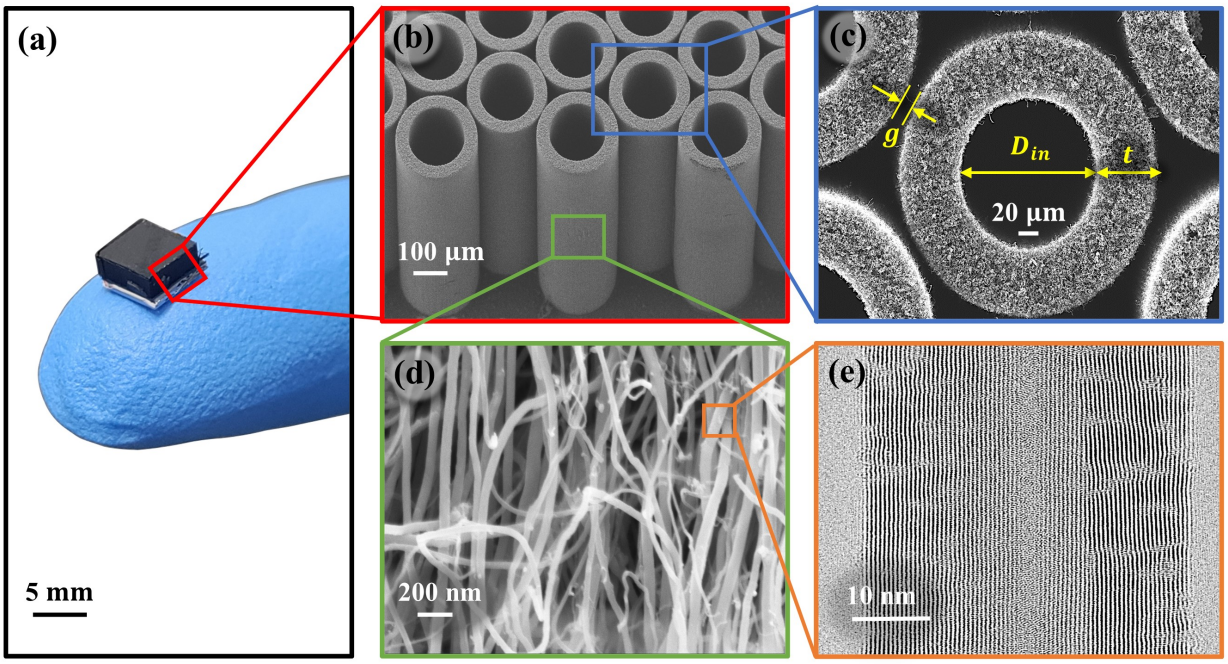

Figure 4.1: (a) CVD synthesized pristine VACNT sample on a 5 mm × 5 mm substrate. (b,c) SEM images showing the mesoscale hexagonally-packed hollow cylinders made of vertically aligned carbon nanotubes; inner diameter (D_{in}) and thickness (t) of a cylinder and the gap (g) between adjacent cylinders are indicated. (d) An SEM image showing the entangled forest-like morphology of vertically-aligned individual CNTs in microscale. (e) A TEM image showing the multi-walled structure of an individual CNT at the nanoscale.

drical architecture synthesized in a floating-catalyst chemical vapor deposition (CVD) process. The multilevel hierarchy is apparent from the continuum-like appearance of structural features at each subsequently larger length scale—a distinction that separates hierarchical materials from conventional materials. To synthesize these samples, we use a floating catalyst CVD method to grow nearly vertically aligned bundles of MWCNTs (Figure 4.1(d,e)) on a photolithographically pre-patterned substrate (See Methods). Synthesized samples reach bulk height of $\sim$ 1.6 mm (Figure 4.1(a)) with a mesoscale cylindrical architecture of cross-sectional dimensions defined by the pre-patterned substrate.

The design variables we adopted for our DoE study—internal diameter (D_{in}), thickness (t), and gap between cylinders (g) are shown in Figure 4.1(c). We synthesized 180 samples with three in each of the 60 different combinations of D_{in}, t, and g listed in Table 4.1. The three tested samples in each unique combination of design variables allow us to characterize any variability in the microstructure of CNTs within cylinders resulting from the CVD synthesis process and me-

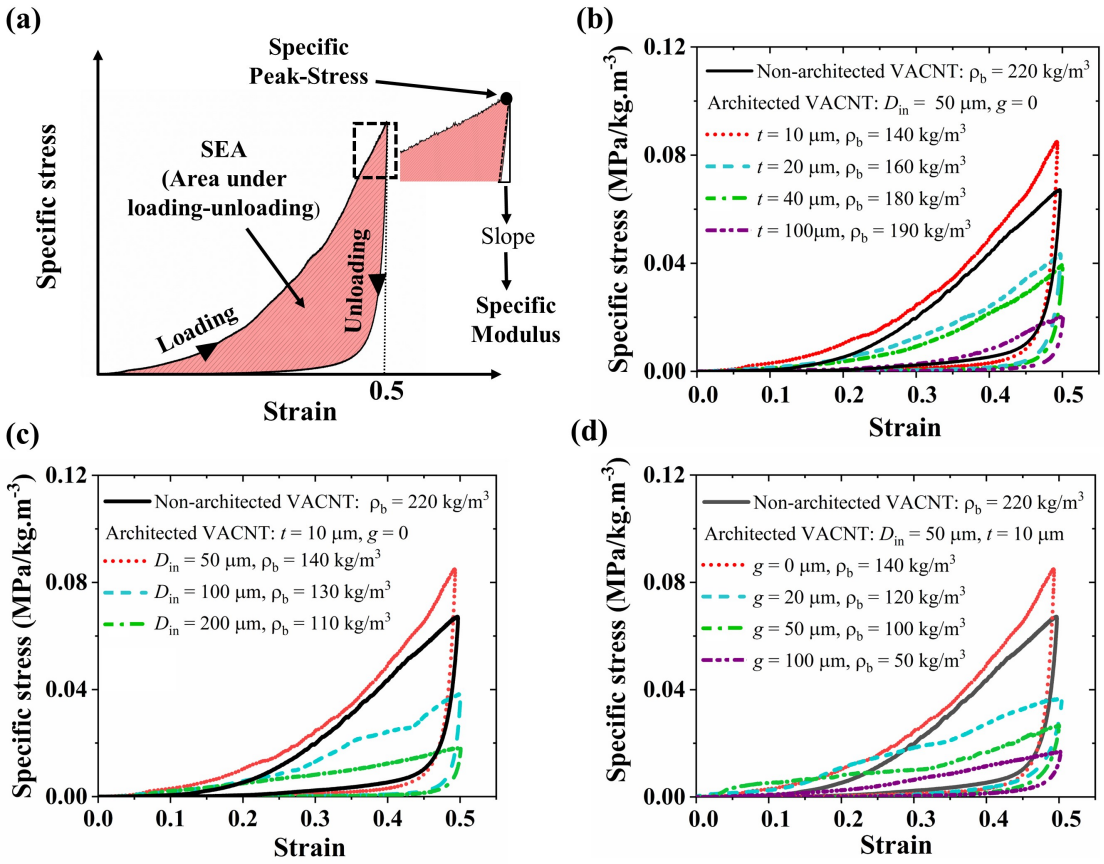

Figure 4.2: (a) Specific stress-strain response of VACNT and mechanical properties—SEA, σ_p^*, and E^*. (b) Specific stress-strain response as a function of t for $D_{in} = 50$ μm and $g = 0$ compared to that of bulk (non-architected) VACNT sample. (c) Specific stress-strain response as a function of D_{in} for $t = 10$ μm and $g = 0$. (d) Specific stress-strain response as a function of g for $D_{in} = 50$ μm and $t = 10$ μm. Stress-strain responses without density normalization are shown in Figure 4.3

chanical testing. These variations are represented by error bars in the data presented in figures. Multiple levels (Table 4.1) considered for each design variable allow us to study both their individual and combined effects on the stress-strain responses and associated mechanical properties. We performed cyclic quasi-static (strain rate: 0.01 sec^{-1}) compressions of up to 50% strain on all samples using an Instron Electropulse E3000 apparatus to characterize the stress-strain behavior. Figure 4.2(a) shows a typical stress-strain response with energy dissipated given by the hysteresis area enclosed by the loading-unloading curves. Protective applications require high specific properties, i.e., higher properties at low densities, so we normalized stress by the bulk density (ρ_b) of the sample to measure the specific stress response with compressive strain (Figure 4.2). We pursue three functional objectives (or response variables) to simultaneously maximize—specific energy

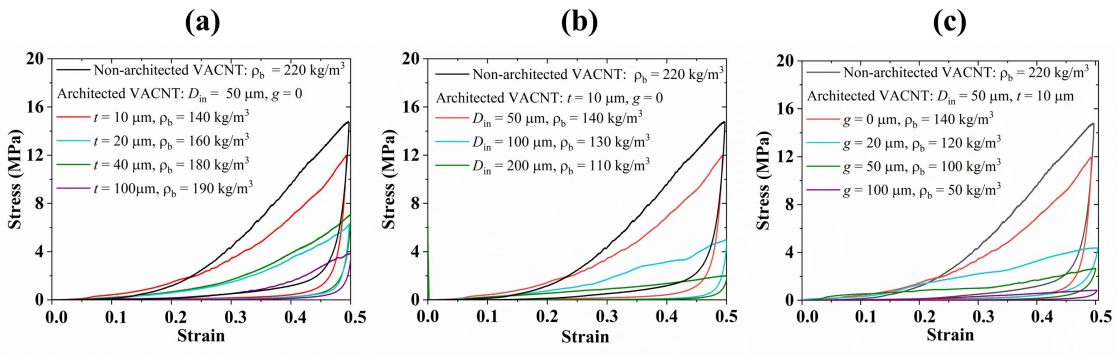

Figure 4.3: (a) Stress-strain curves as a function of t for $D_{in} = 50\mu m$ and $g = 0$ compared to non-architected VACNT sample. (b) Stress-strain curves as a function of D_{in} for $t = 10\mu m$ and $g = 0$. (c) Stress-strain curves as a function of g for $D_{in} = 50\mu m$ and $t = 10\mu m$.

Table 4.1: Design variables and their different levels.

Design variable	**Levels**
D_{in} (μm)	50,100,200
t (μm)	10,20,40,100
g (μm)	0,20,50,100,200

absorption (SEA), specific peak stress (σ_p^*), and specific modulus (E^*)—which are measured from the specific stress-strain curve (Figure 4.2). We measure the SEA from the specific stress-strain hysteresis corresponding to the cyclic compression up to 50% strain, which is much less than the typical densification strain ($\sim 65-70\%$) in VACNTs [13, 14, 17]. σ_p^* indicates the specific compressive stress corresponding to the 50% strain. It should be noted that the compressive strength—the stress at which the material permanently fails—of the VACNT foams is much higher as they have the ability to withstand and near completely recover from 80% or higher strains. E^* denotes the specific modulus typically measured from the elastic unloading of the foam-like materials. We evaluate E^* by calculating the average slope of the unloading curve for the first 30% of unloading in stress.

4.3 Results and discussion

When compressed, VACNT bundles start to buckle in the bottom region (less dense and less stiff region close to the substrate) and then the buckles sequentially propagate upwards [13, 62], causing local densification and nonlinear stiffening—a response typically described by a series of

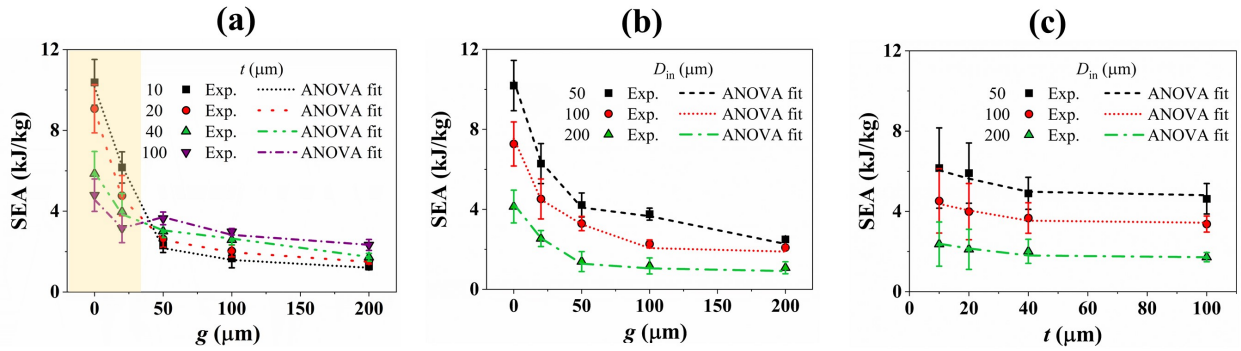

Figure 4.4: Combined effects of design variables $t : g$ (a), $D_{in} : g$ (b), and $D_{in} : t$ (c) on the response variable SEA. In each plot, SEA values are averaged over the third design variable.

bi-stable elements consisting of an unstable phase in between [73, 90] or by hardening-softening-hardening plasticity [74, 77]. This progressive sequential buckling response in VACNTs synthesized by floating-catalyst CVD is strongly governed by the mass density gradient across the height of the samples resulting from synthesis—entangled morphology evolution and increasing CNT population by continuous nucleation of new CNTs as the sample grows lead to the local mass density to increase from the substrate towards the top of the sample [14, 116]. Upon unloading, the sample recovers almost completely, exhibiting an enormous amount of hysteretic energy dissipation—$\sim$ 83% of total energy, corresponding to a damping capacity of 83%. In our architected VACNT samples, the damping capacity of $\sim$ 83% persists for all combinations of D_{in}, t, and g, which suggest that the bulk mechanical performance of VACNT foams can be enhanced by introducing the mesoscale architecture without affecting the damping capacity.

Following the quasistatic compression experiments, we modeled the experimental data using the Analysis of Variance (ANOVA) method to identify the most significant design variables and their interactions. From Figure 4.2(b,c,d), it is clear that individual design variables significantly affect the quasistatic specific stress-strain response of the VACNT foam sample. It is noteworthy that the SEA, σ_p^*, and E^* of architected VACNT foam with $D_{in} = 50$ μm, $t = 10$ μm, and $g = 0$ is even higher than non-architected VACNTs. In Figure 4.4, we plot the SEA to show the effects of different combinations of design variables (in each interaction plot, SEA values are averaged over the third design variable). For lower values of gap, it is noticeable from the shaded region in Figure 4.4(a) that SEA is decreasing with an increase in thickness. However, as the g increases above $g > 40$ μm , the trend reverses such that the higher SEA occurs at higher thicknesses. This

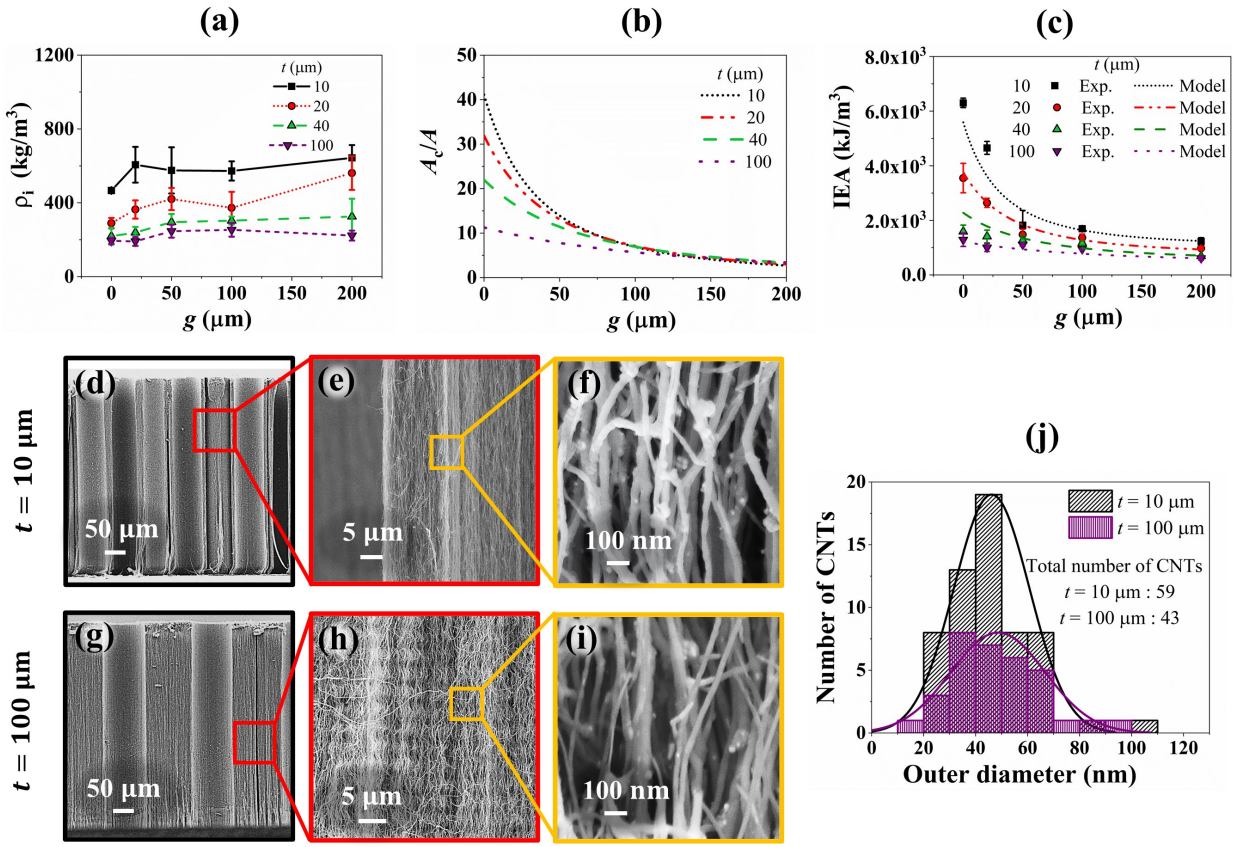

Figure 4.5: Intrinsic density of architected VACNT foams as a function of thickness (t) and gap (g) for $D_{in} = 50\mu$m. (b) Normalized total outer curved surface area of cylinders as a function of gap and thickness for $D_{in} = 50$ μm. (c) Intrinsic energy absorption (IEA) as a function of thickness and gap for $D_{in} = 50$ μm. SEM images of pristine architected VACNT foams with cylinders' thickness $t = 10$ μm (d,e,f) and $t = 100$ μm (g,h,i) for $g = 0$ and $D_{in} = 100$ μm. (j) Distribution of outer diameter of individual MWCNTs measured from SEM images.

interaction between gap and thickness (t : g interaction) for SEA persists for all levels of D_{in}. This trend reversal is arising from competing effects between CNT morphology changes resulting from the size-confined CNT growth (depending on the t) and lateral interactions among adjacent cylinders (depending on both t and g).

To elucidate this intriguing effect, we calculate the intrinsic density (ρ_i) of architected VACNT foams by dividing the measured bulk density (ρ_b) by the fill factor of the cylindrical pattern $\left(\rho_i = \frac{\rho_b}{V_f}\right)$, ρ_i characterizes the mass density of CNTs within the cylinder wall region i.e., excluding the volume associated with hollow and gap regions. Intrinsic density increases with decreasing thickness, signifying the emergence of a size-effect (we found ρ_i converges for $t \leq 10\mu$m). Figure 4.5(a) shows the effect of both gap and thickness on ρ_i. While the gap does not have any

effects, the effect of thickness on ρ_i is clearly evident. Examining the SEM images of samples for two extreme thickness values, i.e., $t = 10\ \mu$m and $t = 100\ \mu$m, a clear difference in morphology is seen (Figure 4.5(d,g)). For $t = 10\ \mu$m, the CNTs are more vertically aligned and packed more densely due to size-confined CVD growth, resulting in higher intrinsic density (Figure 4.5(e,f)) [112]. For $t = 100\ \mu$m, CNTs are wavier and less-dense (Figure 4.5(h,i)). While the average diameter of individual CNTs is similar for $t = 100\ \mu$m and $t = 10\ \mu$m (Figure 4.5(j)), the number density is much higher for $t = 10\ \mu$m, resulting in higher intrinsic density.

In addition to the improvement of properties from aforementioned size-effects, we further enhance the properties by exploiting increased lateral interactions among adjacent mesoscale cylinders. For a particular design thickness, dramatic increase in SEA at smaller gaps is a consequence of this enhanced lateral interactions among adjacent cylinders (Figure 4.4(a)). They also result in an overall increment of specific stress due to constrained deformation of individual cylinders. We hypothesize that the total amount of lateral interactions between cylinders must be proportional to the total cylindrical outer surface area (A_c). In Figure 4.5(b), we plot $\frac{A_c}{A}$ (cylindrical outer surface area normalized by the total cross-sectional area of the sample i.e., $A = 5\text{ mm} \times 5\text{ mm}$) as a function of gap for different values of thickness. To model the combined effects of intrinsic density (arising from size-effect) and lateral interactions, we derive the following expression for SEA (refer to Appendix B for more details),

$$SEA = \frac{1}{\rho_i}\delta \left[\underbrace{2\rho_i}_{\text{Morphology}} + \underbrace{30.29 \left(\frac{A_c}{A}\right)^{1.125}}_{\text{Lateral Interactions}} \right] \tag{4.1}$$

Intrinsic energy absorption (IEA)—energy dissipated (in kJ) normalized by the volume of CNTs (in m^3) (i.e., volume of architected VACNT foam after excluding the volume of empty spaces) is given as,

$$IEA = SEA \times \rho_i = \delta \left[2\rho_i + 30.29 \left(\frac{A_c}{A}\right)^{1.125} \right] \tag{4.2}$$

Where $\delta \approx 0.83 \pm 0.04$ is the damping capacity (ratio of hysteretic energy dissipated in the loading-unloading cycle to the total work done on the material during loading), which we observed to be almost constant with changing architecture. Energy dissipation in VACNT foams is a property

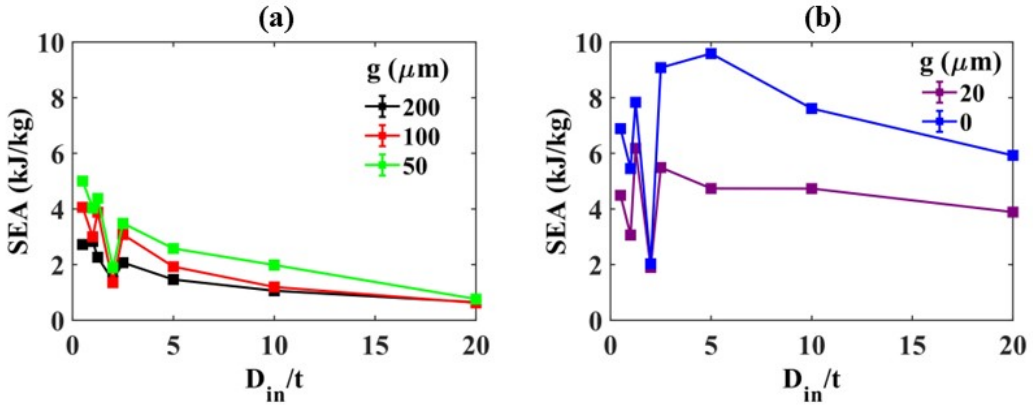

Figure 4.6: SEA as a function of D/t ratio for different gaps (g).

believed to be encrypted in the atomic scale frictional interactions between nanotubes [16, 58, 67, 117]. Thus, damping capacity does not change with mesoscale architecture. The intrinsic density ρ_i is only a function of thickness, whereas A_c is a function of both thickness and gap (for constant D_{in}). For $g \to 0$, the contribution of $\frac{A_c}{A}$ term becomes much larger than ρ_i, causing higher SEA to occur at lesser thickness (Figure 4.5(b)). However, for $g > 100$ μm, the value of $\frac{A_c}{A}$ becomes almost constant (Figure 4.5(b)), and the effect of ρ_i dominates, causing the trend reversal of SEA seen in Figure 4.4(a). In Figure 4.5(c), a good agreement is observed between the experimental data and our model for IEA (Eq. 4.2). Also, there is no trend reversal for IEA, indicating the critical role of intrinsic density in making the order to switch for SEA.

The intrinsic density and lateral interactions also alter the effect of D/t ratio—a dimensionless parameter commonly used to evaluate the load carrying capacity of hollow cylindrical structures towards crashworthy applications. D/t ratio governs the deformation mechanism for compression of cylinders and consequently affects the specific energy absorption. SEA has been reported to decrease with increasing D/t ratio for compression of metallic cylinders [113], fiber reinforced composite cylinders [118], and cylinders embedded in foam matrix [114]. In our samples, when the cylinders are far apart ($g > 40$ μm), the SEA increases with increasing thickness (decreasing D/t ratio) (Figure 4.4(a)), which agrees with the literature. However, the SEA stays almost constant with the D/t ratio when cylinders are tightly packed and undergoing lateral interactions (Figure 4.6).

While the parameter interaction effects of $t : g$ is apparent from Figure 4.4(a), the other potential parameter interactions ($D_{in} : g$, $D_{in} : t$ and $D_{in} : t : g$) are not obvious from Figure 4.4(b) and

Figure 4.4(c). To evaluate the significance of these parameter interactions, we devise a best fit ANOVA model for SEA with significance of terms adjudged by their associated $p-values$. A small $p-value$ (typically less than 0.05) implies that the corresponding parameter interaction term significantly influences the response variable (SEA) [115]. As parsimonious models increase the ease of interpretation, in this work we drop lower level parameter interaction terms if higher level parameter interaction terms are significant. Further, residuals from the fitted model must pass the diagnosis test of normality [119], homoscedasticity [120], and non-correlation [121]. It was observed that residuals from simple ANOVA models failed to pass the diagnosis tests and thus appropriate transformations were applied over the response variable using the renowned Box-Cox transformation [122]. The transformation applied over the response variable helps it to adhere to the assumptions of ANOVA models. Our ANOVA model for response variable SEA is given in Eq. (4.3).

$$\frac{SEA^{0.18}-1}{0.18} = -0.118 + \alpha_{g_j:t_k} + \beta_{D_{in_i}:g_j} \tag{4.3}$$

Table 4.2: ANOVA results for SEA

Source	Sum Square	Df	F	p-value
t : g	18.998	15	22.462	2.2×10^{-16}
D_{in} : g	125.639	14	159.158	2.2×10^{-16}

In the above ANOVA model for SEA, the parameter interaction $D_{in} : g$ also came out to be significant along with $t : g$. In contrast to the $t : g$, $D_{in} : g$ has no trend reversal (Figure 4.4(b)). However, it can be noticed that at $g = 0$, the SEA values are more spaced apart for different D_{in} than for $g = 200\ \mu$m, which could be the reason why $D_{in} : g$ parameter interaction is also significant. The $p-values$ for $t : g$ and $D_{in} : g$ are listed in Table 4.2.

Figure 4.7 shows parameter interaction plots for response variables—specific peak stress (σ_p^*) and specific modulus (E^*). The parameter interaction between thickness and gap is very apparent and shows order switching, similar to that of SEA (Figure 4.7(a,d)). To check the significance of other parameter interactions, we use a similar strategy by formulating a simplified best fit ANOVA model with only higher-level parameter interaction terms. Analysis of residuals from simple ANOVA fits for E^* and σ_p^* also failed to pass the model diagnosis tests. This imply the

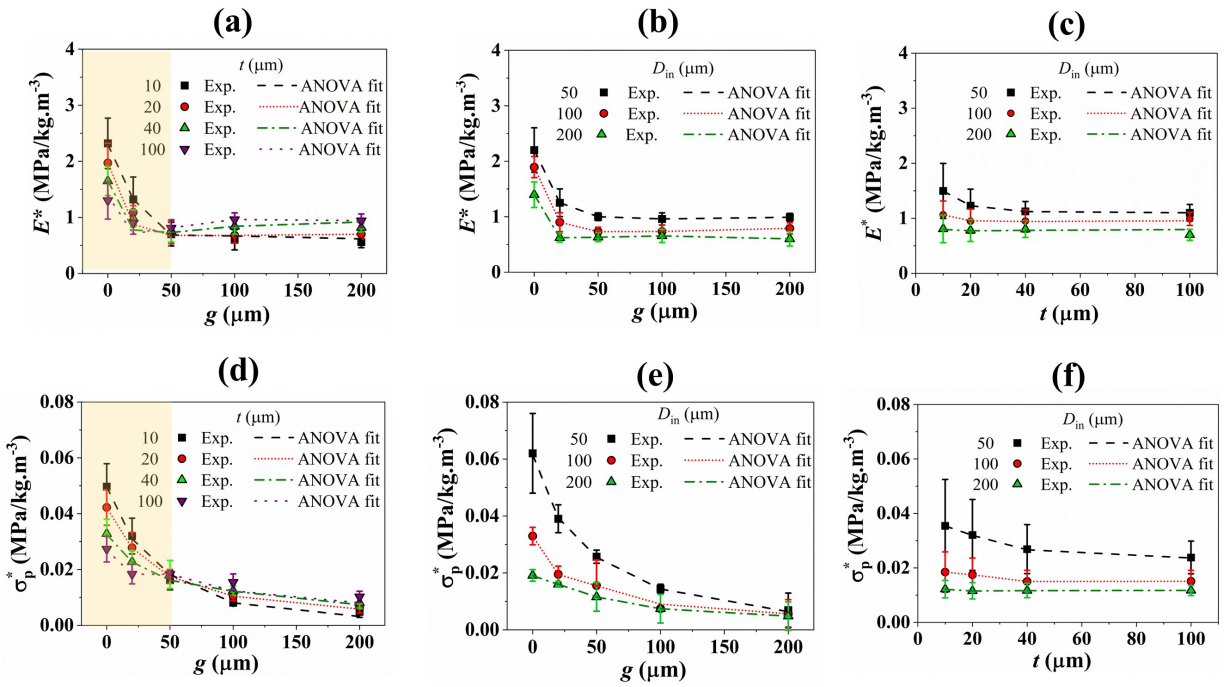

Figure 4.7: Effects of design variable interactions on response variables—(a,b,c) E^* and (d,e,f) σ_p^*

need for appropriate transformations of response variables to better adhere to the assumptions of ANOVA model. In Eq. (4.4), we show the final ANOVA model for E^*. The model implies that a third order parameter interaction $D_{in} : g : t$ is significant and thus all lower level parameter interaction terms are dropped. The reason for significance of third order parameter interaction could be traced to by looking at Figure 4.7(c), which implies high variation in E^* at lower levels of t with respect to D_{in}. The best fit ANOVA model for σ_p^* is given in Eq. (4.5), which has a similar inference as that of E^*. As suggested by Figure 4.7(f), the variation in σ_p^* for lower levels of t with each level of D_{in} is also significant. Thus, the third order parameter interaction term turns out to be significant.

$$\frac{E^{*0.626} - 1}{0.626} = -0.175 + \gamma_{D_{in_i}:g_j:t_k} \tag{4.4}$$

$$\frac{\sigma_p^{*-0.141} - 1}{-0.141} = 1.743 + \phi_{D_{in_i}:g_j:t_k} \tag{4.5}$$

In contrast, for SEA, D_{in} and t don't seem to interact (Figure 4.4(c)), which is also reflected in Eq. (4.3), where the simplified best fit ANOVA model has two second-order parameter interaction terms and cannot be further simplified to achieve the third-order parameter interaction. To investi-

gate the absence of $D_{in} : t$ parameter interaction in SEA data, we derive the following approximate relationship among our three response variables—SEA, σ_p^*, and E^* (refer to Appendix B for more details).

$$SEA = \frac{\delta}{1-\delta} \times \left[\sigma_p^* \left[\frac{2\epsilon_{\max} - \epsilon_m - \epsilon_p}{2}\right] - E^* \left[\frac{(\epsilon_{\max} - \epsilon_m)(\epsilon_{\max} - \epsilon_p)}{2}\right]\right] \tag{4.6}$$

where, $\epsilon_{max} = 0.5$, $0.48 < \epsilon_m < 0.49$ (refer to Appendix B), and ϵ_p is the amount of unrecovered permanent strain measured from the stress-strain response. In Eq. 4.6, the negative sign in the second term indicates that E^* has a contrasting opposite effect on SEA compared to σ_p^*. The absence of parameter interactions between D_{in} and t for SEA is likely due to cancelling of $D_{in} : t$ parameter interaction effects between σ_p^* and E^*. Since the gap dramatically affects σ_p^* more than E^*, the other two parameter interactions are significant for SEA.

It is evident from parameter interaction plots and ANOVA models that we are able to achieve synergistic scaling in SEA, E^*, and σ_p^* as functions of design variables. At the low levels of gap, all three response variables simultaneously maximize for low levels of both thickness and internal diameter. However, at the higher levels of gap, the maximization occurs for higher thickness and lesser diameters. This intriguing interplay among design variables allows drastic tailoring of mechanical properties to achieve lightweight foams for protective applications. In Figure 4.8, we compare specific properties of architected and non-architected VACNT foams from this study with protective foam-like materials found in the literature (all properties calculated from stress-strain responses up to 50% strain, if not provided directly in literature).

Figure 4.8(a) shows the scaling of SEA as a function of bulk density (ρ_b). Compared to non-architected VACNTs, architected VACNTs ($D_{in} = 50\ \mu\text{m}, t = 10\ \mu\text{m}$) exhibit a much steeper scaling, which suggests a better tunability in SEA can be achieved with minimal variation in bulk density. At $\rho_b \approx 150 kg/m^3$, the SEA of architected VACNTs ($g = 0$) exceeds non-architected VACNTs. Similar behavior is seen in Figure 4.8(c) for specific modulus (E^*). In Figure 4.8(b), we compare SEA, ρ_b, and E^* (color-coded in the data points) of architected and non-architected VACNTs with other polymeric, metallic, and architected foams from literature. In addition to SEA, architected VACNTs also exhibit a higher specific modulus (≥ 3 MPa/kg.m^{-3}) compared to non-architected VACNTs (≤ 2 MPa/kg.m^{-3}) and other polymeric foams. While metallic foams (e.g.,

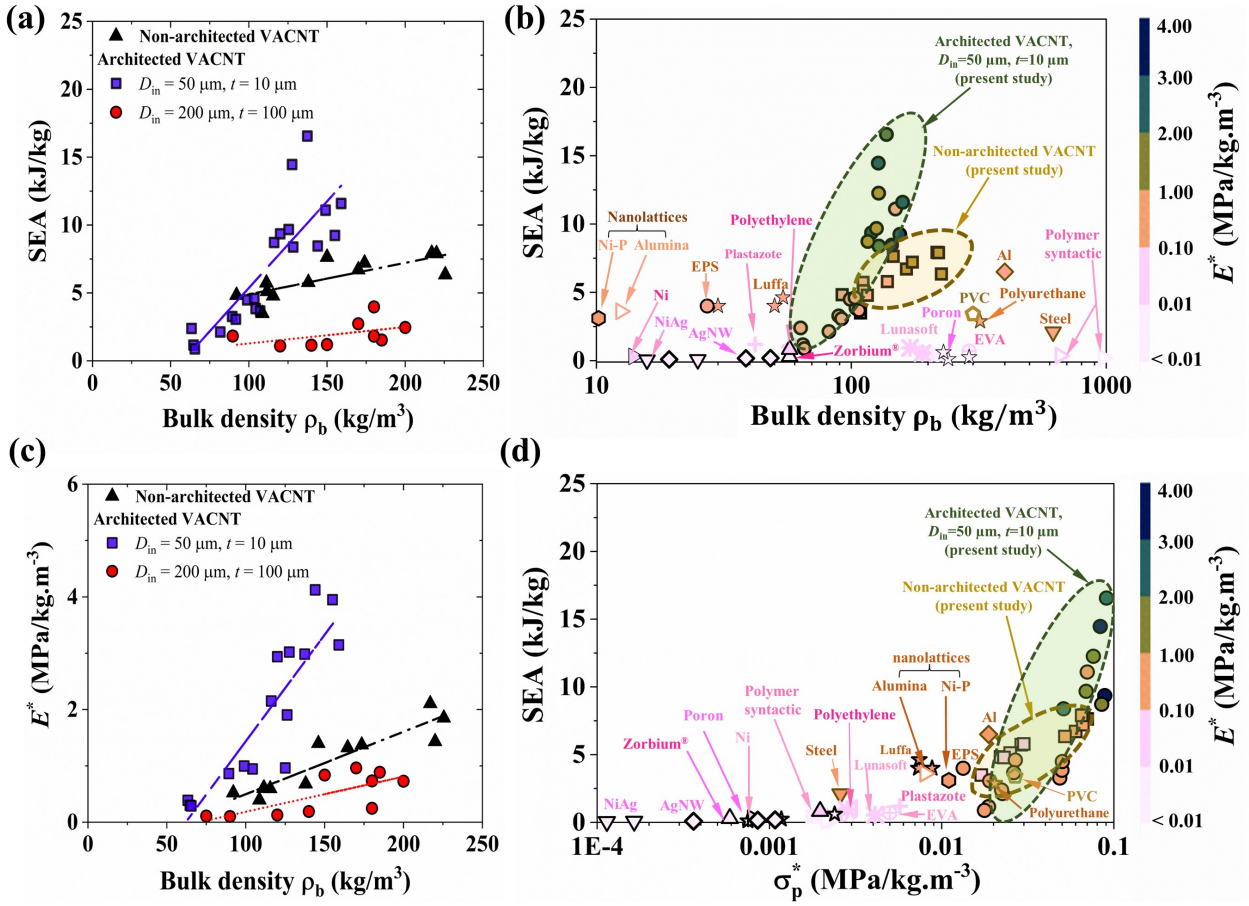

Figure 4.8: (a) Comparison of SEA between architected and non-architected VACNTs; the properties are tailored by varying the gap (g) for a given D_{in} and t in architected VACNT foams and varying the amount of hydrogen during synthesis in non-architected VACNT foams. (b) SEA-bulk density-specific modulus property landscape of architected and non-architected VACNT foams compared with other foams and architected materials [4, 6, 7, 20, 23, 24, 123–128] showing synergistic property enhancement at low density. (c) Comparison of specific modulus between architected and non-architected VACNTs. (d) SEA-specific compressive strength-specific modulus property landscape showing synergistic property enhancement in architected VACNTs compared to all other materials.

steel, aluminum) are competitive in specific modulus, they are much denser and possess lesser SEA. Clearly, architected VACNT foams outperform non-architected VACNT foams, polymeric foams [7, 123, 124], metallic foams [4, 20, 125, 126], and other architected foams [19, 23, 24] by exhibiting simultaneously improved SEA and E^*—two often conflicting properties in materials—while being less dense. Architected VACNTs also achieve high specific compressive strength (σ_p^*), which allows them to withstand loads without failure (Figure 4.8(d)). In addition, architected VACNT foams have a higher range of tailorability of SEA as a function of different design variables. As seen in

Figure 4.8(b), the density and SEA are interdependent in commercial foams. Softer polymeric foams such as polyurethane [6, 123], and polyethylene [124], are less dense and have lesser SEA. Metallic foams such as steel [127], aluminum [128], and nickel exhibit better SEA than polymeric foams but are denser. However, our architected VACNT foams surpass these limitations by exploiting structural hierarchy, size-effects from geometrically-confined CNT growth, and lateral interactions among adjacent mesoscale cylinders. For example, compared to the Zorbium (polyurethane) foams that are currently used in advanced combat helmet liners [6], our architected VACNT foams exhibit $\sim$ 18 times higher SEA, $\sim$ 160 times higher E^*, and $\sim$ 45 times higher σ_p^* at 50% strain and at same quasistatic strain rate. The architected VACNT foams additionally provide exceptional thermal stability [16, 129] of the properties which are not possible with polymeric foams.

4.4 Conclusion

We demonstrated synergistic improvement of specific properties—compressive modulus, compressive strength, and energy absorption—by exploiting structural hierarchy, size-effects, and nanoscale inter-tube interactions in architected VACNTs. Guided by the full-factorial design of experiments (DOE) approach and the statistical analysis of variance (ANOVA) method, we found higher-order interactions among design variable of the mesoscale cylindrical architecture—leading to regimes with synergistically enhanced mechanical properties. We also showed that these intriguing parameter interactions arise from size (thickness)-dependent morphology evolutions of CNTs (number density and alignment) arising from geometrically-confined CVD synthesis and lateral interactions among adjacent cylinders tailored by the gap between them. This unique structure-property relation also disrupts the commonly known effects of D/t ratio on thin-walled structures made of common materials and show us a novel pathway to synergistically enhance mechanical properties. Our architected VACNT foams outperform commercial polymeric, metallic, and other architected foams in terms of energy absorption, modulus, and compressive strength at ultra-lightweight.

Acknowledgements

This research is supported by the U. S. Office of Naval Research under PANTHER program award number N000142112044 through Dr. Timothy Bentley. We also acknowledge partial support from

the Army Research Office award number W911NF2010160 through Dr. Denise Ford. The authors acknowledge the use of facilities and instrumentation at the Wisconsin Centers for Nanoscale Technology (WCNT) partially supported by the NSF through the University of Wisconsin Materials Research Science and Engineering Center (DMR-1720415). We thank all the staff of WCNT, particularly Mr. Quinn Lenord for his assistance in photolithography.

Methods

First, a standard 100 mm diameter (100 crystal orientation) p-type silicon wafer was spin-coated with 10 microns thick S1813 photoresist at 3000 rpm for 30 sec and pre-baked on a hot plate at 110 °C for 45 sec to remove any solvents. After spin coating, the wafer was partially diced through the thickness (30 % of the thickness of the wafer) into 5 mm × 5 mm squares. Next, the diced wafer was exposed to ultra-violet (UV) light through a chrome/soda-lime photomask to transfer the micropattern. The photomask is designed with cylindrical micropatterns of various combinations of D_{in}, t, and g and manufactured by Photo Sciences (Torrance, CA). After 8 sec of exposure with 405 nm UV light (exposure dose of 10 mW/cm^2), the unexposed photoresist is removed in the 30 sec MF321 developer bath. After the developer bath, a 20 nm chromium thin film is evaporated using a metal evaporator. The remaining photoresist (exposed to UV light previously) is removed in an acetone bath, leaving a chromium film on the substrate, which prevents the growth of CNTs in the designated areas on the substrate (inverse of the architecture).

We synthesize architected VACNTs on diced patterned substrates using a floating catalyst thermal chemical vapor deposition (tCVD) process. We use a syringe pump to inject a feedstock solution of ferrocene (catalyst precursor) in toluene (carbon source) ($[w/v] = 0.01$ g/ml) at a rate of 0.8 ml/min into a furnace tube maintained at a temperature of 827 °C (1100K). A mixture of argon (95%) and hydrogen (5%) flowing at 800 sccm carries toluene vapors inside the furnace, where nanotubes grow on the patterned silicon wafer. After synthesis, we remove the architected VACNT film from the furnace and cut it into squares of 5 mm × 5 mm—each square having an architecture with a specific combination of D_{in}, t, and g—for mechanical characterization.

Chapter 5

Disrupting density dependent property scaling in concentric architected VACNT foams

This chapter is adopted from the following publication

Chawla, K., Gupta, A., & Thevamaran, R. (2023). Disrupting Density-Dependent Property Scaling in Hierarchically Architected Foams. ACS nano, 17(11), 10452-10461.

Author Contributions : KC synthesized the samples and performed compression testing, AG performed data analysis, prepared figures, and wrote the paper. RT conceived and supervised the project and wrote the paper.

5.1 Introduction

Recent progress in additive manufacturing and other micro and nanoscale fabrication processes has shifted the attention from conventional cellular foams such as stochastic polymeric and metallic foams to lighter yet stronger micro/nano architected foam materials [23, 24, 130]. Architected materials derive their mechanical properties predominantly from structural features such as micro/nano trusses leading to efficient load transfer across lengthscales for superior strength, toughness, elastic modulus, and energy dissipation at ultra low densities [96, 105]. Architected materials with

efficient structural designs allows us to access untapped regions in material property space and approach theoretical limits of specific properties previously thought unattainable. In particular, ultra-lightweightness in micro lattices [19, 24], improved toughness in ceramic-based architectures [23], strength and stiffness close to theoretical maximum [131, 132], extreme energy dissipation [133], and creating materials with programmable properties [134].

Typically, bulk properties of cellular materials such as elastic modulus and strength scales with the density of the foam as $E \propto \rho^{\alpha}$ and $\sigma_y \propto \rho^{\beta}$ [135]. Architected designs with strong scaling ($\alpha, \beta \geq 2$) of material properties with density are inefficient because a slight decrease in density can result in substantial degradation of the strength and stiffness of the foam [23, 24]. For instance, foams with stochastic structures such as aerogels, sponges, and honeycombs, and other architected materials with bending-dominated deformation mechanism exhibit poor scaling ($\alpha, \beta \geq 2$) leading to a narrow range of tunability in terms of density [136, 137]. In contrast, foam materials with stretch or compression dominated deformation mechanisms exhibit a desirable linear scaling ($\alpha, \beta \approx 1$) with density such that the specific mechanical properties (density normalized properties) will remain constant with the decreasing density [135]. Among architected materials, only a few examples of lightweight architectures have come closer to possess the aforesaid scaling of mechanical properties [24, 138, 139]. Conversely, many natural cellular materials have evolved to become simultaneously strong, tough, and lightweight due to their efficient multilevel hierarchical structure, granting them better scaling with density [12]. Adopting hierarchical architectures in synthetic cellular materials has resulted in lightweight mechanically-effective structures with synergistic improvement in otherwise antagonistic properties [11, 96, 105].

In this work, we report a transformation from a poor higher-order scaling of material properties with density ($\alpha, \beta \approx 3$) to a desirable linear-scaling ($\alpha, \beta \approx 1$) as a function of architecture in hierarchical vertically aligned carbon nanotube (VACNT) foams with a mesoscale architecture of hexogonally close packed thin concentric cylinders (Figure 5.1). The macroscale VACNT foams (sometimes referred to as VACNT arrays or VACNT forests) [13] exhibit a structural hierarchy that spans multiple lengthscales: from the graphitic structure at the atomic scale, tubular multi-walled CNTs (MWCNTs) at the nanoscale, an entangled forest-like morphology of nearly vertically aligned MWCNTs at the microscale [14, 81]. Morphology, resultant bulk density, and elastic stiffness of the VACNT foams can be tailored by varying different synthesis parameters during the floating cata-

lyst chemical vapor deposition (FCCVD) process [15, 17, 46]. FCCVD-synthesized VACNT foams typically have a bulk density close to that of polymeric foams ($\sim 200\ kg/m^3$), which can be further reduced by increasing the hydrogen concentration in the carrier gas during the synthesis [17]. However, due to a strong dependence of the mechanical properties on density ($\alpha, \beta \approx 3$), both strength and stiffness severely degrade as the foam gets lighter [14, 140]. Introducing mesoscale architecture is an another way to tailor the density of VACNT foams [11, 108, 110]. Various mesoscale architectures can be introduced by growing VACNT foams on a photolithographically pre-patterned chromium-coated substrate (see Methods) to reduce the density while improving the structural stiffness. Recently, in architected VACNT foams with a mesoscale architecture of hexagonally close-packed hollow cylinders (Figure 5.2(b)), we demonstrated cylinder's thickness-dependent size effects [11]. Such as improvement in alignment and number density of CNTs with decreasing thickness and lateral interactions between the neighboring mesoscale cylinders leading to a synergistic improvement in mechanical properties. However, we observed a steep scaling law that limits the further drastic reduction in density with enhanced properties. Here, we adopt a hexagonally close packed architecture of multiple thin concentric cylinders—that exploit the thickness-dependent size effect—to optimally harness the improved CNTs morphology and properties. We report a transformation in the deformation mechanism of concentric cylinders from local shell-buckling to global column buckling—governed by a synthesis-structure relationship, leading to an alteration in the density-dependent scaling from strong cubic scaling to an ideal linear scaling.

5.2 Architected Design

In addition to enhancing the bulk properties of the architected foams, such as modulus, strength, and energy dissipation, the choice of architecture also significantly influences the density-dependent scaling of these properties [135]. Utilizing, various structural architectures result in different deformation mechanisms, enabling tailored mechanical performance at low densities. Architected materials with hollow cylinders and tubular structures are known to exhibit a high strength-to-weight ratio and improved crashworthiness due to high bending stiffness and progressive buckling deformation that occur in a stable and controlled manner [11, 19, 23, 141]. We have found that the VACNT foams with mesoscale cylindrical architecture performs better than non-architected

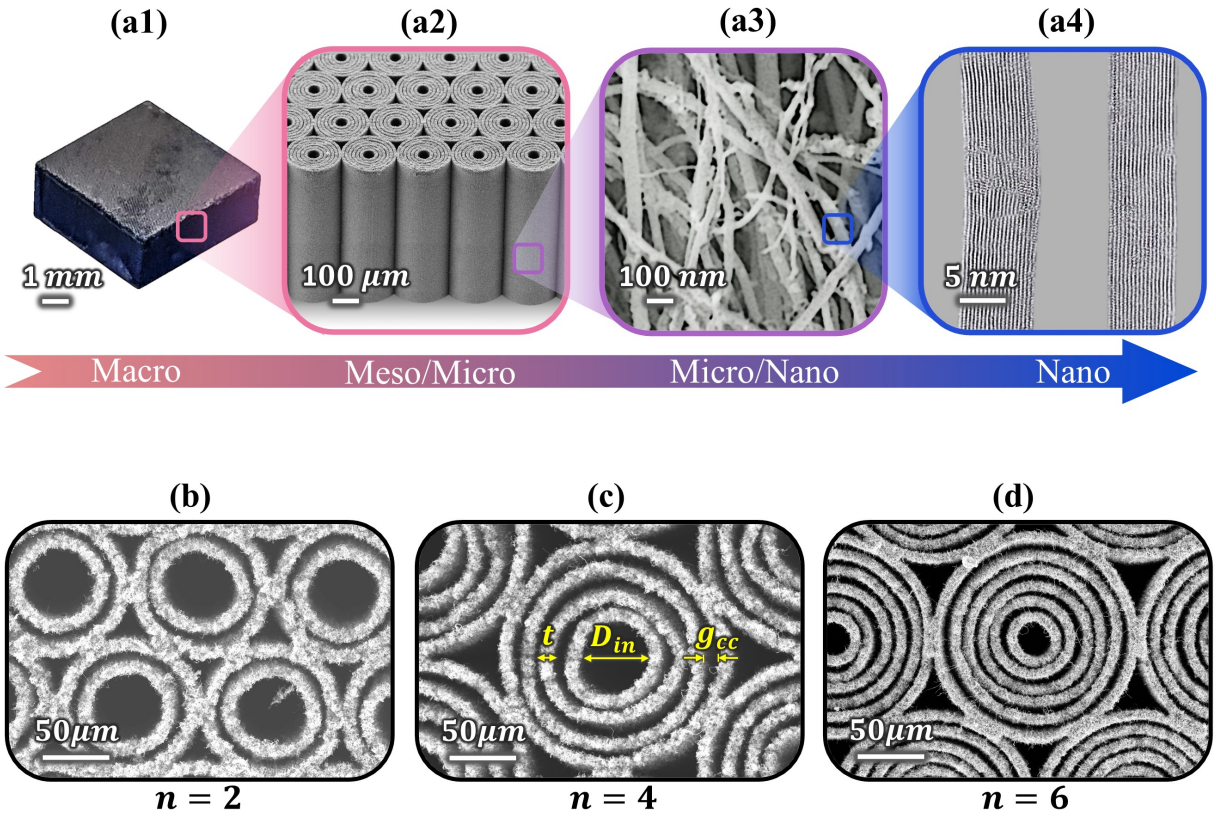

Figure 5.1: (a1) CVD synthesized freestanding architected VACNT foam sample. (a2) SEM image unveiling the mesoscale hexagonally close-packed concentric cylindrical architecture of the foam. (a3) Entangled forest-like morphology of the vertically aligned CNTs at the microscale. (a4) TEM image showing the multi-walled structure of an individual CNT at the nanoscale. SEM images showing the top view of the foams with two (b), four (c), and six (d) concentric cylinders. Internal diameter of the innermost cylinder (D_{in}), thickness of individual cylinders (t), and the gap between the adjacent concentric cylinders (g_{cc}) are indicated (c).

VACNT foams and other polymeric and metallic foams in terms of energy dissipation, stiffness, and strength while being lightweight [11]. Moreover, these properties are highly tunable in response to changing geometrical parameters like wall thickness, internal diameter, and the gap between neighboring cylinders. We found an increment in the number density and observed more vertical alignment in CNTs as the cylinders got thinner ($t \leq 10\ \mu m$)—an apparent size effect that reveals a process-structure relation—which makes the foam simultaneously stiffer, stronger, and more energy dissipative [11]. Additionally, we observed that cylinders with smaller inner diameter ($D_{in} \leq 50\ \mu m$) demonstrate a progressive buckling type deformation mechanism, which leads to higher energy dissipation and improved strain recovery [11]. Building on previous findings, the current study aims to enhance these effects by employing multiple concentric cylinders, thereby

Table 5.1: Design parameters and their different levels

Design Parameter	Levels
D_{in} (μm), t (μm)	50, 10 & 25, 5
g_{cc} (μm)	5, 20, 50
n	2, 4, 6

amplifying inter-cylinder interactions and achieving a tailored deformation mechanism.

In this work, we adopt a mesoscale hexagonally close-packed architecture of thin concentric cylinders (Concentric-VACNT) to further improve the mechanical performance of architected VACNT foams for protective applications. Figure 5.1(a1) shows a pristine CVD synthesized freestanding concentric-VACNT foam sample at the macroscale. Scanning (Figure 5.1(a2,a3)) and transmission (Figure 5.1(a4)) electron microscopy (SEM and TEM) reveal the foam's multi-lengthscale structural hierarchy. A concentric-cylinder architecture at the mesoscale (Figure 5.1(a2)), an entangled forest-like morphology of CNT bundles at the microscale (Figure 5.1(a3)), and the multiwalled structure of an individual CNT at the nanoscale (Figure 5.1(a4)). To investigate the effects of geometry on mechanical properties and to optimize the design, we considered four design parameters—the internal diameter of the innermost cylinder (D_{in}), the wall thickness of the cylinders (t), the gap between the concentric cylinders (g_{cc}), and the number of rings of concentric cylinders (n) (Figure 5.1(b,c,d)). Table 5.1 lists the different levels of design parameters, generating 18 different combinations. We combined $D_{in} = 50\ \mu m$ with $t = 10\ \mu m$ and $D_{in} = 25\ \mu m$ with $t = 5\ \mu m$ to maintain a constant D_{in}/t ratio—a dimensionless parameter used to evaluate the load-bearing capacity of hollow cylindrical structures [141]. The energy dissipation per unit volume of cylindrical tubes increases with decreasing D_{in}/t ratio [11, 141]. Thus, we kept the D_{in}/t ratio in our concentric VACNT foams very low ($D_{in}/t = 5$), equal to the D_{in}/t ratio at which we found the energy dissipation maximum in the cylindrically architected foams [11].

5.3 Results and discussion

We synthesized and characterized a total of 54 concentric-VACNT foam samples, three for each of the 18 different combinations of design parameters (Table 5.1). Testing multiple samples in each architecture allows us to minimize any potential variability from the synthesis process. In figure 5.2(d), we compare the quasistatic stress-strain response of concentric-VACNT foams with non-

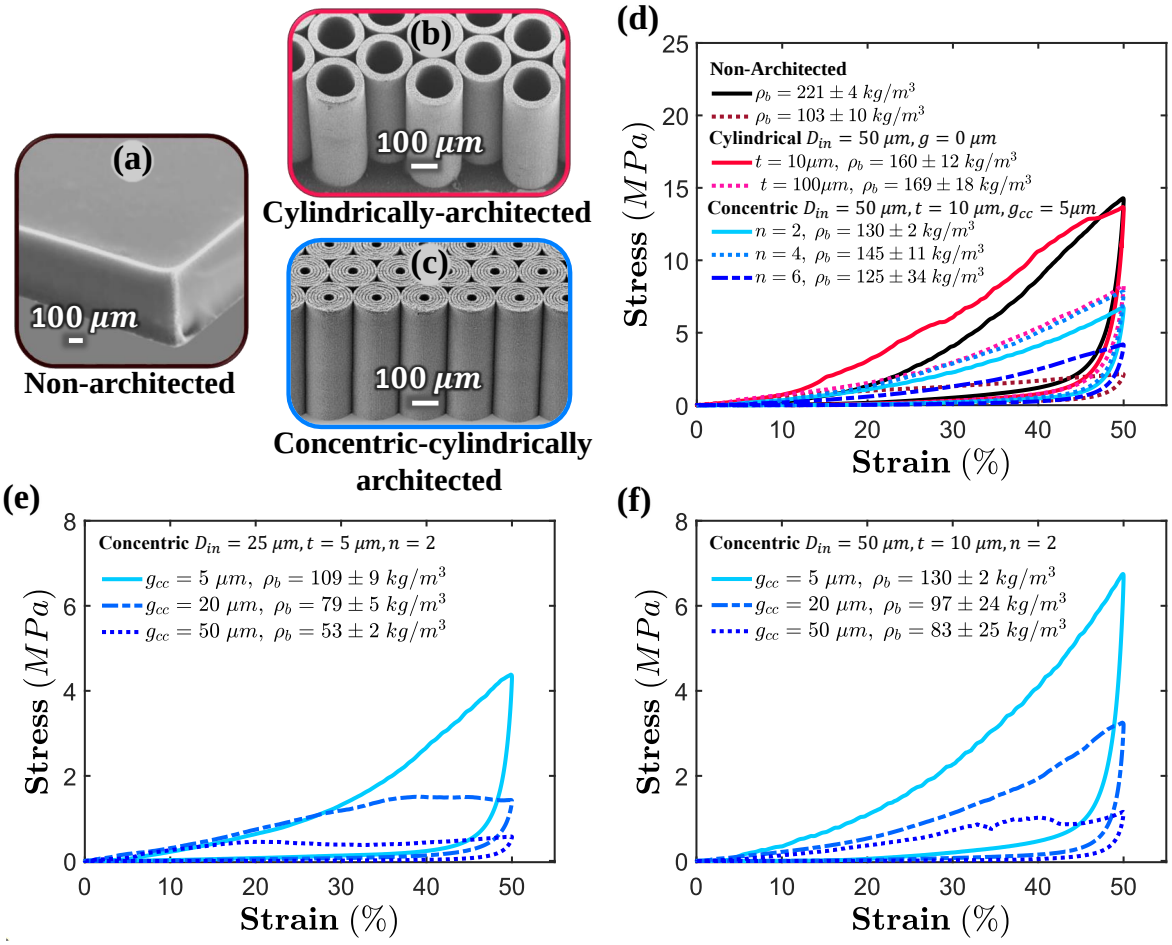

Figure 5.2: SEM images showing the non-architected (a), cylindrically architected (b), and concentric cylindrically architected (c) VACNT foams. (d) Stress-strain responses of concentric-VACNT foams as a function of the number of rings (n) for constant g_{cc}, D_{in}, and t are compared with stress-strain responses of non-architected and cylindrically architected VACNT foams [11]. Stress-strain responses of concentric-VACNT foams as a function of g_{cc} for (e) $D_{in} = 25\ \mu m$, $t = 5\ \mu m$, $n = 2$, and (f) $D_{in} = 50\ \mu m$, $t = 10\ \mu m$, $n = 2$. All stress-strain curves are obtained by compressing the foams up to 50% strain at a quasistatic strain rate of 0.01 s^{-1} (see Methods)

architected and cylindrically architected VACNT foams (Figure 5.2(a,b,c)). Concentric-VACNT foams are lighter and thus exhibit more compliant stress-strain behavior (Figure 5.2(d)). For $n = 2$, the stress-strain response of concentric-VACNT foam is comparable to cylindrically-architected foam ($t = 100\ \mu m$) while being less dense. As the number of rings (n) increases, the stress response of concentric-VACNT foams increases slightly for $n = 4$ and then decreases for $n = 6$, which correlates with the respective bulk densities (ρ_b) of the foams.

While the number of rings (n) imposes only a mild effect, the gap between the concentric rings (g_{cc}) dramatically affects the stress-strain response of concentric-VACNT foams (Figure 5.2(e,f)).

As the gap increases, the material becomes compliant and exhibits a plateau-like region in the stress-strain response, which is accompanied by a sharp decay in bulk-density (ρ_b). We hypothesize that for a smaller g_{cc}, the hollow cylinders being tightly packed undergo shell-buckling resulting in the local densification of buckled folds and nonlinear stiffening of the foam, whereas, for higher g_{cc}, the hollow cylinders undergo column-buckling resulting in softening and formation of a plateau in the stress-strain curves. The presence of a plateau region in the stress-strain curve increases the energy absorption efficiency (EAE) of the foam and makes it perform better in protective applications [8]. Concentric-VACNT foams with $D_{in} = 50\ \mu m$ and $t = 10\ \mu m$ exhibit slightly stiffer and more nonlinear stress-strain responses than foams with $D_{in} = 25\ \mu m$ and $t = 5\ \mu m$, possibly due to the higher bending moment of inertia of cylinders with larger diameters.

To evaluate the mechanical performance of concentric VACNT foams and to compare the effect of different design parameters, we calculate the energy dissipation per unit volume, modulus, and peak stress from the quasistatic stress-strain data. We calculate the energy dissipation per unit volume (W_{dis}) of the foams by computing the area inscribed within the loading-unloading cycle of the stress-strain curves. If the area under the loading curve is W_L, and the area under the unloading curve is W_{UL}, then we can write W_{dis} as follows

$$W_{dis} = W_L - W_{UL} \tag{5.1}$$

Since VACNT foams dissipate energy through internal friction between the nanotubes [16], we hypothesize that approximately half of the total energy dissipated ($W_{dis}/2$) is during loading (compressing the foams), and the other half is while unloading the foam. This assumption is based on rate-independent hysteretic damping that occurs in structured materials [142], which suggests that the internal friction always opposes the relative sliding between slidable interfaces within the material, but its magnitude only depends upon the strain and does not depend upon the direction of loading. During loading, some of the energy is stored as elastic strain energy in the material, which helps the material strain recover during unloading. If the elastic strain energy stored during loading is W_{sto}, we can write the following relation,

$$W_L = W_{sto} + \frac{W_{dis}}{2} \quad or \quad W_{dis} = 2(W_L - W_{sto}) \tag{5.2}$$

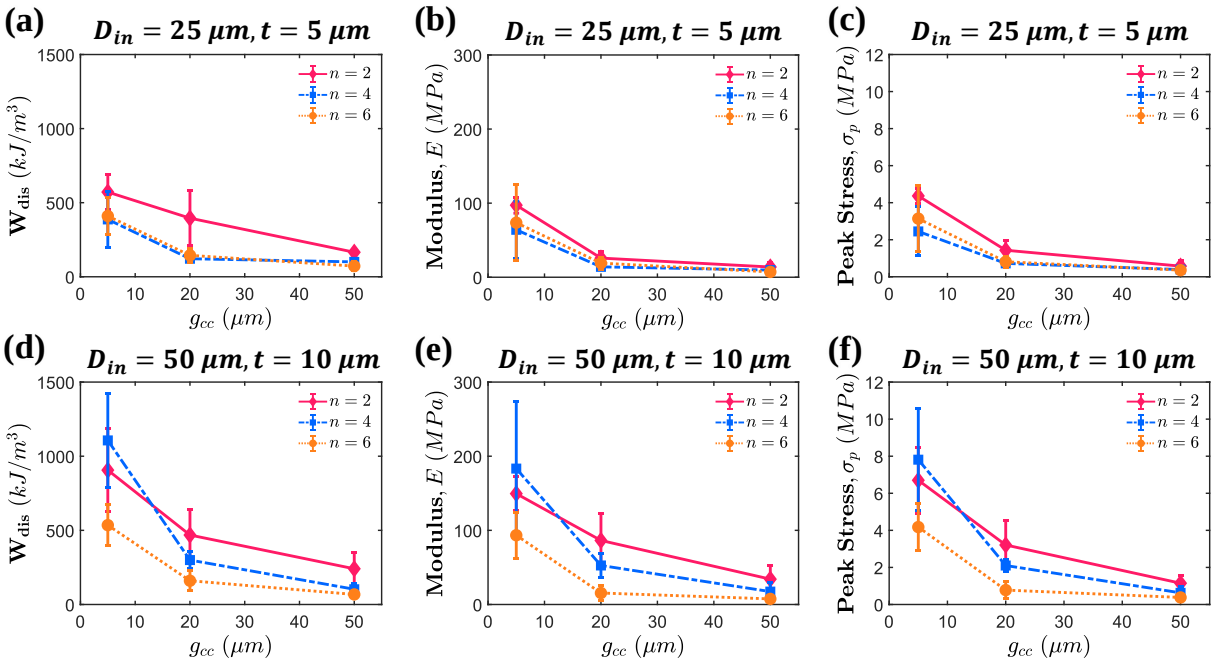

Figure 5.3: Energy dissipated (W_{dis}), modulus (E), and peak stress (σ_p) for concentric-VACNT foams as a function of n and g_{cc} for (a,b,c) $D_{in} = 25\mu m$, $t = 5\mu m$ and (d,e,f) $D_{in} = 50\mu m$, $t = 10\mu m$

Substituting W_{dis} in equation (5.1) yields

$$W_{sto} = \frac{W_L + W_{UL}}{2} = \int_0^{\epsilon_{max}} \left(\frac{\sigma_L + \sigma_{UL}}{2}\right) d\epsilon = \int_0^{\epsilon_{max}} \bar{\sigma}\, d\epsilon \tag{5.3}$$

where ϵ_{max} is the maximum compression strain and $\bar{\sigma}$ is the average of the loading stress (σ_L) and unloading stress (σ_{UL}) at a particular strain.

Equation (5.3) suggests that an average of the loading and the unloading curves is a better measure of the elastic energy stored in the VACNT foam (W_{sto}). Thus, we calculate the elastic modulus of the concentric-VACNT foams (E) by measuring the slope of $\bar{\sigma}(\epsilon)$. Since stress-strain curves are nonlinear, we measured the slope of the curve at 90% of maximum stress (σ_p). To evaluate the compressive strength of the concentric-VACNT foams, we measured the peak stress (σ_p) in the stress-strain curves at 50% strain. Typical densification strain in VACNT foams is $\sim 65\% - 70\%$ [14], so actual compressive strength is much higher than what is measured at 50% strain.

Figure 5.3 shows energy dissipated per unit volume (W_{dis}) in kJ/m^3, elastic modulus (E) in MPa, and peak stress (σ_p) in MPa as functions of g_{cc}, n, D_{in}, and t. In accordance with the stress-

strain responses (Figure 5.2), the concentric-VACNT foams with $D_{in} = 50\ \mu m$ and $t = 10\ \mu m$ are stiffer, dissipates more energy, and exhibit higher peak stress in comparison to the foams with $D_{in} = 25\ \mu m$ and $t = 5\ \mu m$. The number of rings (n) have negligible and inconclusive effect, whereas the effect of the gap between the cylinders (g_{cc}) is apparent. As the gap increases from 5 μm to 20 μm, the bulk density of the foam decreases as well as results in weakening of the cylindrical structure because of decreasing lateral interactions between adjacent cylinders leading to decrease in modulus, peak-stress, and energy dissipation. However, from $g_{cc} = 20\ \mu m$ to 50 μm, the effect is very minimal. To understand this behavior, we investigate the morphology of the CNTs by calculating the intrinsic density (ρ_i) of the concentric-VACNT foams. Intrinsic density is a measure of the density of VACNT cylinders i.e., the density of the foam after excluding all the empty space in the architecture. If the fill-factor of the architecture is V_f, then ρ_i is given by (refer to Appendix B for details)

$$\rho_i = \frac{\rho_b}{V_f} \quad , \quad V_f = \frac{2\pi nt\left[D_{in} + nt + (n-1)g_{cc}\right]}{\sqrt{3}\left[D_{in} + 2nt + 2(n-1)g_{cc}\right]^2} \tag{5.4}$$

In figure 5.4(a), we have plotted ρ_i as a function of g_{cc} for $D_{in} = 50\ \mu m$ and $t = 10\ \mu m$. The intrinsic density increases with g_{cc}, which could be either due to an increase in the average diameter of CNTs or a rise in the number density (number of CNTs per unit area) of CNTs or both. From SEM images, we calculated the average diameter of CNTs, which turned out to be approximately same i.e., $40 \pm 18\ nm$ for $g_{cc} = 5\ \mu m$, $42 \pm 8\ nm$ for $g_{cc} = 20\ \mu m$, and $40 \pm 11\ nm$ for $g_{cc} = 50\ \mu m$. Therefore, ρ_i increases due to a rise in the number density of CNTs, which is noticeable in SEM images as well (Figure 5.4(b,c,d)). As g_{cc} increases, the reduction in fill-factor (V_f) balances the effect of increasing intrinsic density—giving a slow response for higher g_{cc} in figure 5.3. In contrast, the number of rings (n) does not affect the intrinsic density much (Figure 5.4(a)), perhaps due to a slow dependence of V_f on n leading to an inconclusive effect of n on mechanical properties (Figure 5.3) and constitutive response (Figure 5.2(d)).

In the above discussion, we establish that the geometry also affects the morphology of CNTs growing in the architecture. Understanding the dynamics of the CVD growth process will allow us to elucidate this interconnection. Figure 5.4(e) shows an illustration of the floating catalyst CVD growth process of concentric VACNT foams. Concentric-cylinders made of vertically aligned carbon

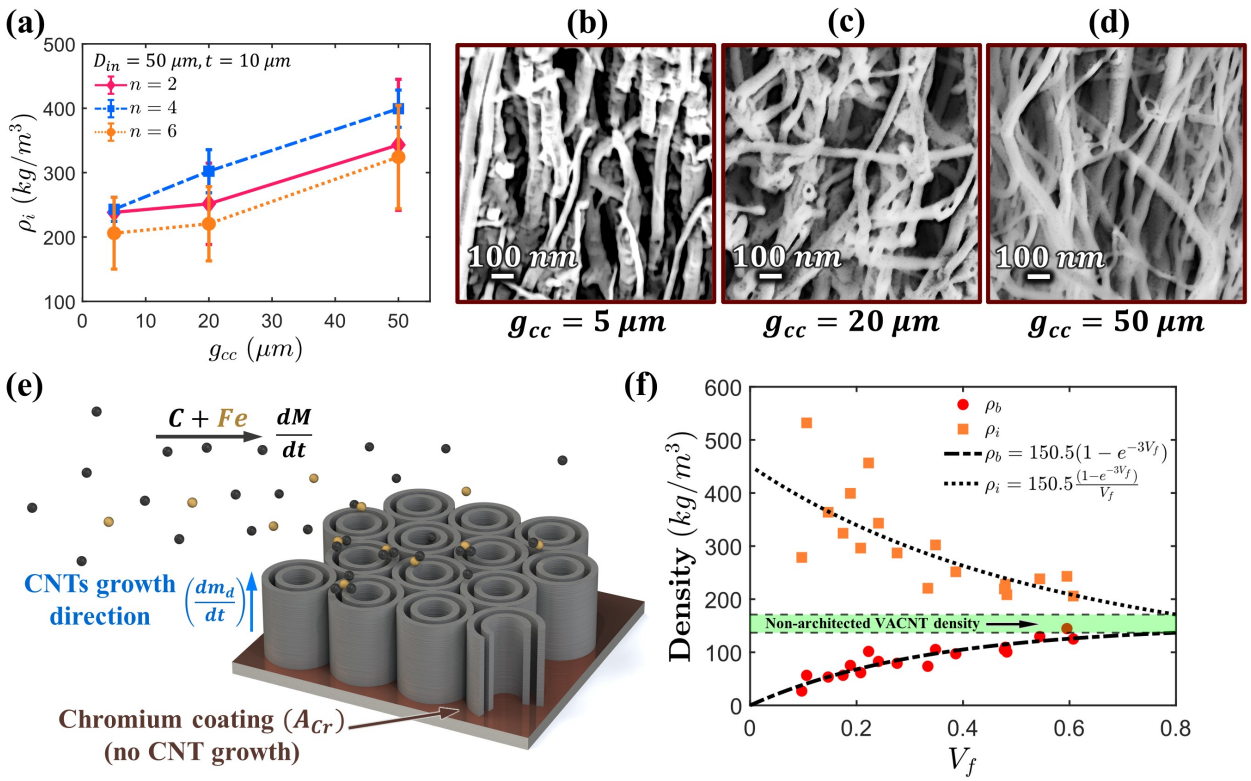

Figure 5.4: (a) Intrinsic density (ρ_i) of concentric-VACNT foams is plotted as a function of g_{cc} and n for $D_{in} = 50\ \mu m$ and $t = 10\ \mu m$. SEM images showing the morphology of CNTs in pristine samples for (b) $g_{cc} = 5\ \mu$m, (c) $g_{cc} = 20\ \mu$m, and (d) $g_{cc} = 50\ \mu$m. (e) Illustration of the growth of concentric VACNT cylinders on a photolithographically pre-patterned chromium-coated silicon wafer substrate. dM/dt is the flux of Carbon and Iron atoms and dm_d/dt is the rate of mass deposition in the form of CNTs. (f) Bulk density (ρ_b) and intrinsic density (ρ_i) of concentric-VACNT foams as a function of fill fraction (V_f).

nanotubes grows on photolithographically pre-patterned chromium-coated silicon-wafer substrate (see Methods). The chromium coating prevents CNTs from growing in those areas. If A is the total area of the substrate and A_{Cr} is the area of chromium coating, then we can write the fill-factor as,

$$V_f = 1 - \frac{A_{Cr}}{A} \tag{5.5}$$

The amount of CNT growth (m_d) on the substrate must be a function of the fill factor (V_f) of the architecture as follows

$$m_d \propto f(V_f) \tag{5.6}$$

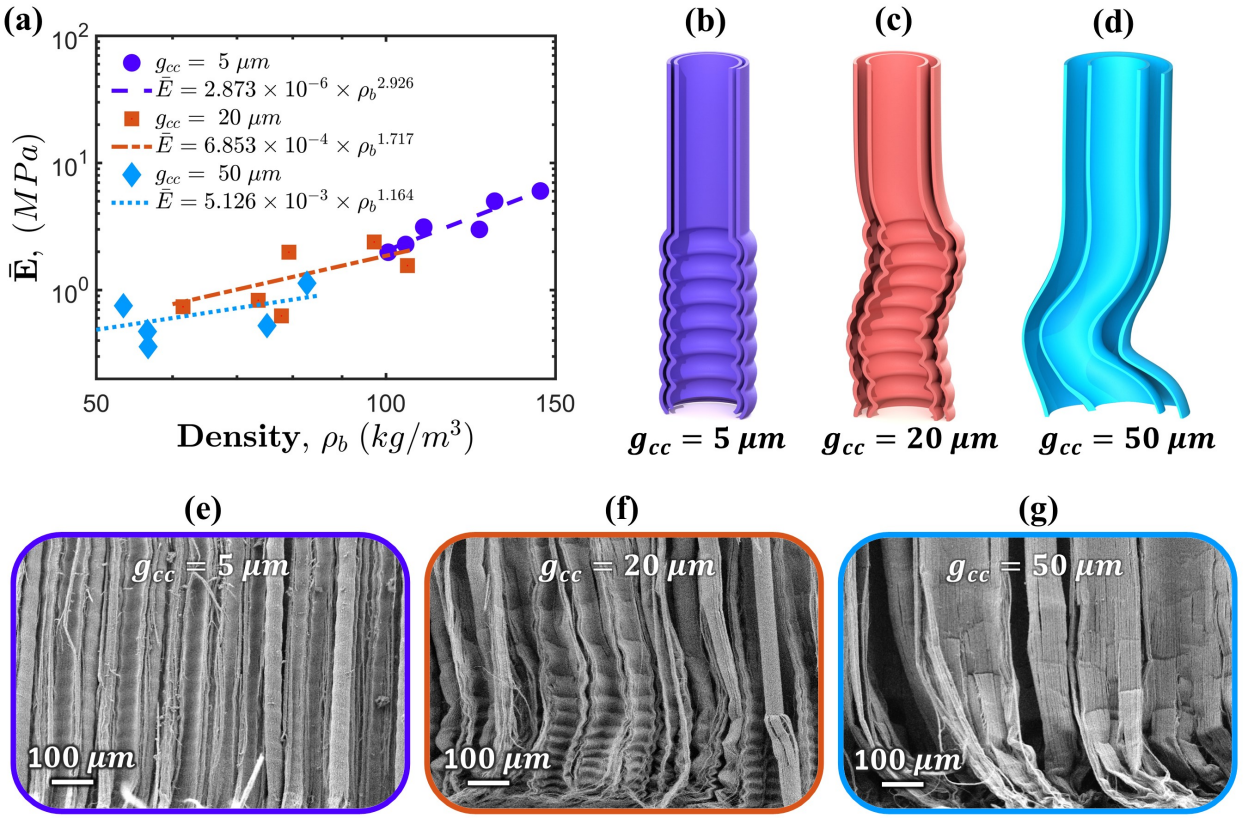

Figure 5.5: (a) Scaling of average modulus ($\bar{E}$) with bulk density (ρ_b) for different g_{cc} in concentric-VACNT foams. (b,c,d) Illustrations of deformation mechanism in individual pairs of concentric cylinders as a function of g_{cc}. SEM images showing the cross-section views of one-cycle compressed concentric-VACNT foams for $D_{in} = 25\ \mu m$, $t = 5\ \mu m$, $n = 2$, and (e) $g_{cc} = 5\ \mu m$, (f) $g_{cc} = 20\ \mu m$, and (g) $g_{cc} = 50\ \mu m$.

The bulk-density (ρ_b) of the sample is given by

$$\rho_b = \frac{m_d}{Ah} = \lambda \frac{f(V_f)}{Ah} \tag{5.7}$$

where h is the height of the foam and λ is a constant of proportionality. If $V_f = 0$ i.e., $A_{Cr} = A$, there won't be any CNT growth ($\rho_b = 0$), whereas if $V_f = 1$ i.e., $A_{Cr} = 0$, CNTs will grow everywhere on the substrate (non-architected VACNTs). Therefore, the bulk density (ρ_b) of concentric-VACNT foams should asymptotically converge to the density of non-architected VACNT foams as $V_f \to 1$. We used the following exponential function to fit the data,

$$\rho_b = \rho_0(1 - e^{-\nu V_f}) \ , \ \rho_0 = \frac{\lambda}{Ah} \ , \ f(V_f) = (1 - e^{-\nu V_f}) \tag{5.8}$$

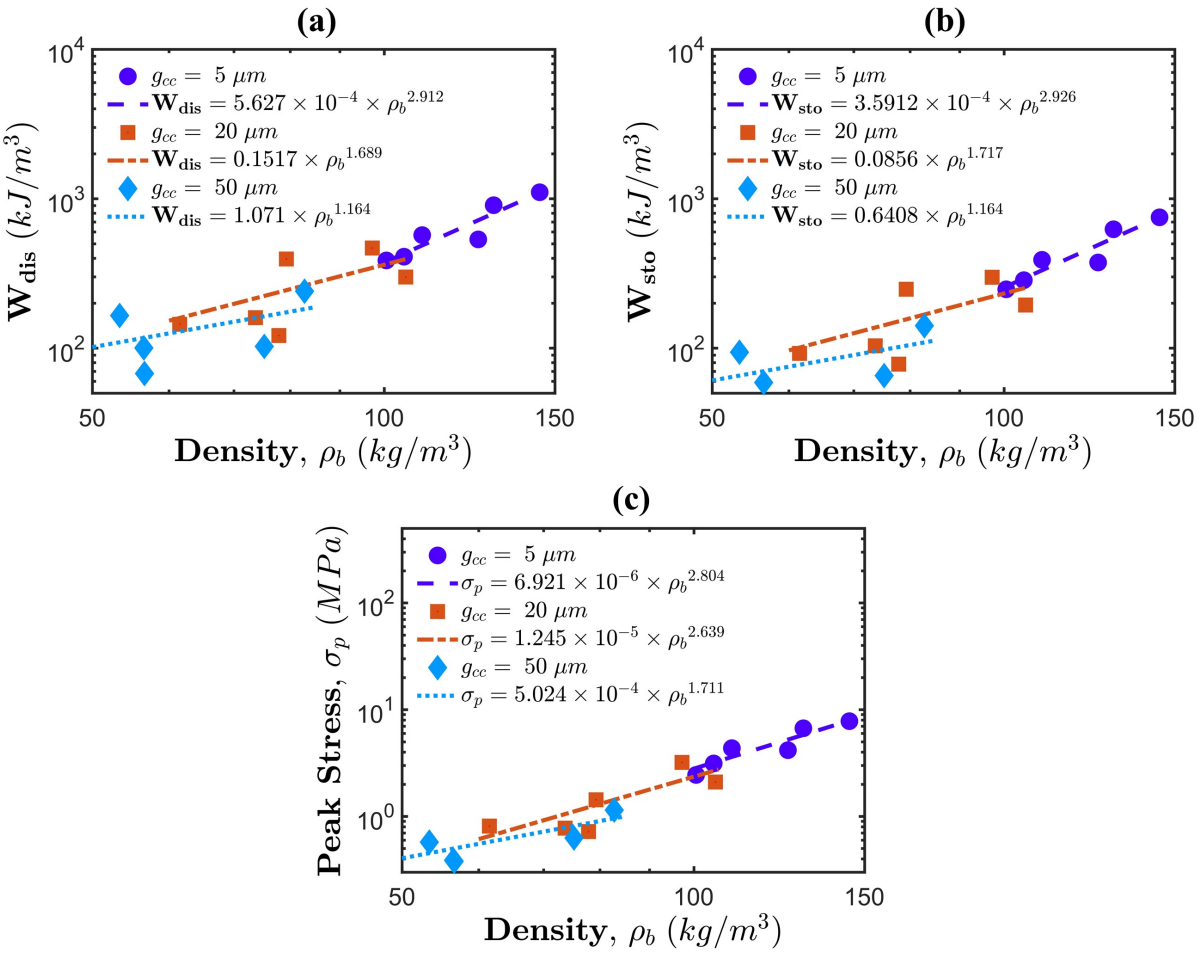

Figure 5.6: Scaling of energy dissipation (a), energy stored (b), and peak stress with density (ρ_b)

The choice of a decaying exponential fitting function here is motivated by the transient population growth dynamic of CNTs that follows an exponential growth curve [87]. By fitting the experimental data with the above equation, we find that $\rho_0 = 150.5\ kg/m^3$ and $\nu = 3$. Illustrated in figure 5.4(f), as V_f increases, both ρ_b and ρ_i converge towards the typical density range of non-architected VACNT foams (if synthesized under similar conditions).

From figure 5.4(f), it is evident that ρ_b and ρ_i are more tunable as functions of V_f for $V_f < 0.4$. For smaller V_f, foams are lighter (less ρ_b) and tend to be softer, but they exhibit higher ρ_i which counterbalances the effect to preserve mechanical properties. Thus, concentric-VACNT foams with smaller V_f, such as those with $g_{cc} = 50\ \mu m$, have better tunability in terms of bulk-density while maintaining similar mechanical performance. To investigate further, we study the scaling laws for average modulus ($\bar{E}$) with bulk density (ρ_b) for different g_{cc} as shown in figure 5.5(a). Average

modulus ($\bar{E}$) denotes the modulus of an equivalent spring that can store the same amount of elastic energy as a VACNT foam. $\bar{E}$ can be calculated from stored energy W_{sto} as follows,

$$\bar{E} = 2\frac{W_{sto}}{\epsilon_{max}^2} \tag{5.9}$$

Concentric-VACNT foams with $g_{cc} = 50\ \mu m$ have the smallest power-law scaling exponent of $\bar{E} \sim \rho_b^{1.164}$ which is better than concentric-VACNT foams with $g_{cc} = 20\ \mu m$ ($\bar{E} \sim \rho_b^{1.681}$) and $g_{cc} = 5\ \mu m$ ($\bar{E} \sim \rho_b^{2.926}$), and other architected foams. Having a moderate scaling of $\bar{E}$ with ρ_b indicates that the foam's density can be drastically reduced without significantly affecting the stiffness (Figure 5.5(a)). We observe similar scaling laws for energy dissipation (W_{dis}), energy stored (W_{sto}), and peak stress (σ_p) with density (ρ_b) (Figure 5.6)

Concentric-VACNT foams with larger g_{cc} have smaller fill-factor but higher intrinsic density (Figure 5.4(f)) in comparison to foams with smaller g_{cc}, which gives better structural stiffness at low densities and thus better scaling. Varying scaling exponent with g_{cc} also alters the deformation mechanism of concentric cylinders. For $g_{cc} = 5\ \mu m$, concentric cylinders undergo local shell-buckling (Figure 5.5(b,e)), causing densification and nonlinear stiffening (Figure 5.2), whereas, for $g_{cc} = 50\ \mu m$, concentric cylinders undergo column-buckling (Figure 5.5(d,g)), resulting in softening of the foam. For $g_{cc} = 20\ \mu m$, concentric-cylinders undergo mixed mode (shell+column) buckling (Figure 5.5(c,f)). SEM images (Figure 5.5(e-g)) of one-cycle compressed samples clearly reveals a variation in the deformation mechanism as a function of g_{cc}.

Varying deformation mechanism with g_{cc} also significantly influences the dimensionless material properties such as foam's damping capacity (δ) and energy absorption efficiency (ψ) given by

$$\delta = \frac{W_{dis}}{W_L} \quad , \quad \psi = \frac{W_L}{\sigma_p \epsilon_{max}} \tag{5.10}$$

Damping capacity is a measure of the percentage of total energy dissipated by a foam within the loading-unloading cycle. Materials with higher damping capacity exhibit smaller coefficient of restitution against impact thus are better at stopping speeding projectiles. On the other hand, energy absorption efficiency (EAE) is the ratio of energy absorbed by a foam up to a particular strain to the energy absorbed by an equivalent ideal absorber. An efficient foam can absorb impact energy without exerting significant forces on the entity being protected. Both damping capacity

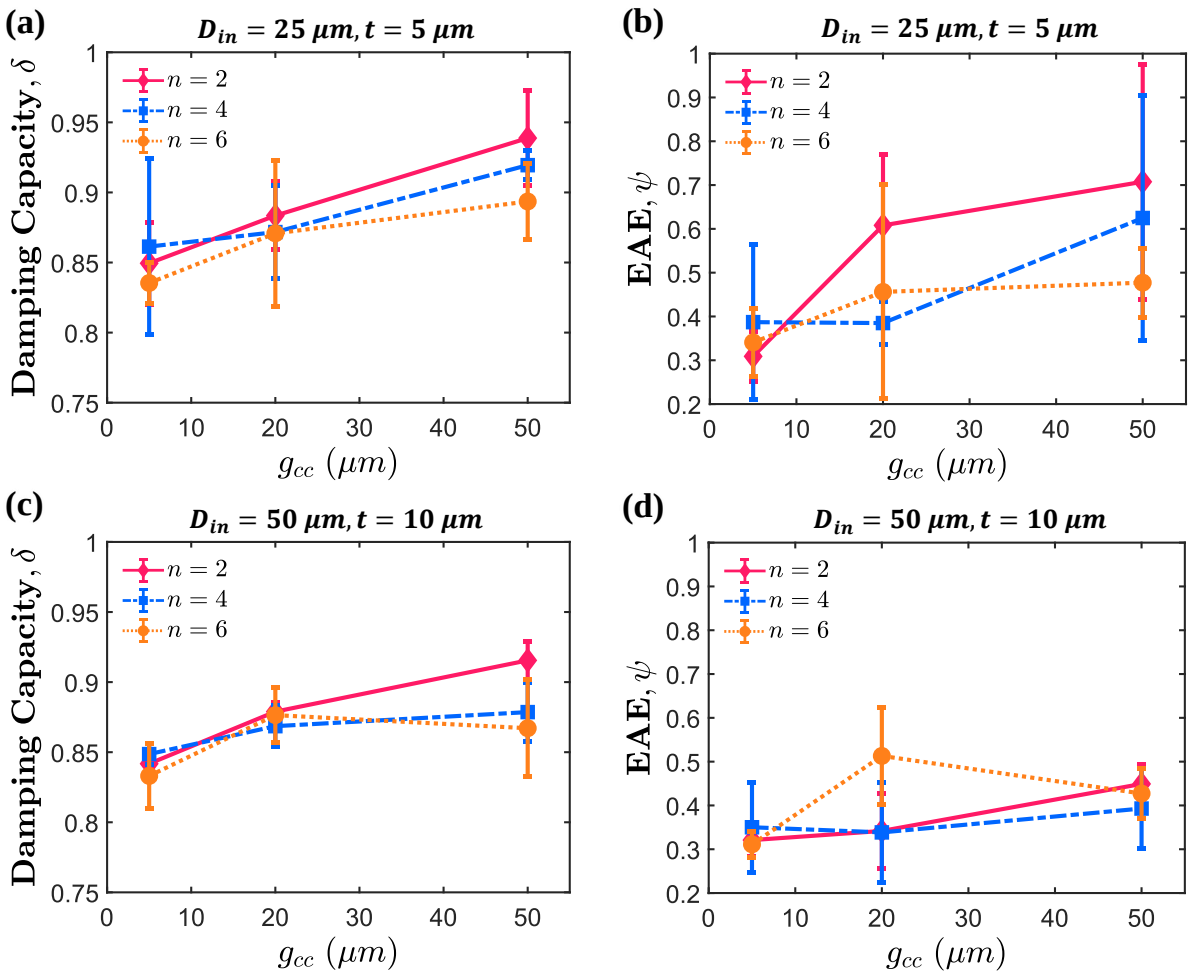

Figure 5.7: Damping capacity (δ) of concentric-VACNT foams plotted as a function of g_{cc}, number of rings (n), and internal diameters (a) $D_{in} = 25\ \mu m$, $t = 5\ \mu m$ and (c) $D_{in} = 50\ \mu m$, $t = 10\ \mu m$. Energy absorption efficiency (ψ) of concentric-VACNT foams plotted as a function of g_{cc}, number of rings (n), and internal diameters (b) $D_{in} = 25\ \mu m$, $t = 5\ \mu m$ and (d) $D_{in} = 50\ \mu m$, $t = 10\ \mu m$.

and EAE are dimensionless parameters and range between $0 < \delta, \psi < 1$. However, even for the same material, these parameters can take vastly different values. The EAE is solely influenced by the shape of the loading curve in the constitutive stress-strain response, whereas the damping capacity is determined by the shapes of both the loading and unloading curves. For example, materials with nonlinear stress-strain response in loading can have a large damping capacity but a lower EAE due to higher peak stress (σ_p). In concentric-VACNT foams, we observe a similar characteristic. For foams with $D_{in} = 50\ \mu m$ and $t = 10\ \mu m$, the EAE is smaller than that for foams with $D_{in} = 25\ \mu m$ and $t = 5\ \mu m$ (Figure 5.7(b,d)) while the damping capacity is almost the same (Figure 5.7(a,c)). For $D_{in} = 25\ \mu m$, $t = 5\ \mu m$, and $g_{cc} = 50\ \mu m$, the EAE and damping

capacity of concentric VACNT foams ($\psi = 66 \pm 23$ %, $\delta = 90 \pm 3$ %) exceeds non-architected ($\psi = 42 \pm 11$ %, $\delta = 79 \pm 2$ %) and cylindrically architected foams ($\psi = 37 \pm 4$ %, $\delta = 85 \pm 3$ %).

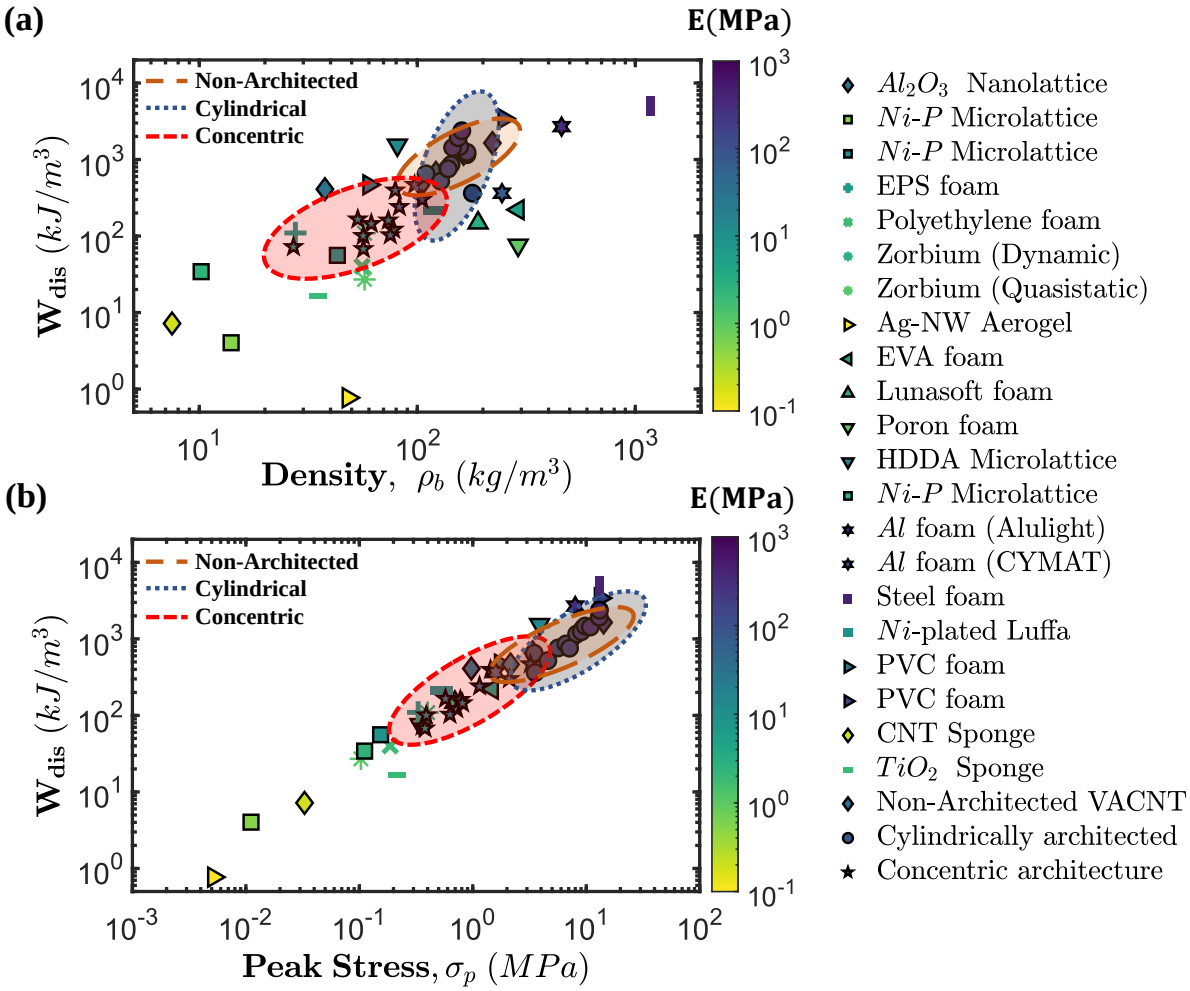

Figure 5.8: Property landscapes representing the relations between W_{dis}, ρ_b, σ_p, and E for concentric-VACNT foams (this work), non-architected VACNT foams [11], cylindrically architected VACNT foams [11], polymeric foams [6, 7], metallic foams [19–22], various sponges [4, 143, 144], and other micro/nano architected foams [23, 24].

As a function of g_{cc}, we observe simultaneous improvement in damping capacity and EAE, owing to softening in the stress-strain responses (Figure 5.2(c,d)) induced by the transition of the deformation mode from shell buckling to column buckling. Synergistic improvement in damping capacity and EAE for concentric VACNT foams with higher g_{cc} makes them superior for protective applications. Table 5.2 summarizes how each design parameter discussed in the manuscript thus far affects all of the mechanical properties considered. It is evident that g_{cc} holds the highest significance among design parameters, while the number of rings (n) has minimal impact on the

mechanical properties. By combining the design parameters in an optimal way, architected foams can be generated with properties that are tailored to meet specific requirements.

Table 5.2: A summary of how different design parameters impact various mechanical properties, with an upward arrow (↑) representing a proportional effect, a downward arrow (↓) representing an inversely proportional effect, and a tilde sign (∼) conveying little to no effect.

	ρ_b	ρ_i	$\bar{E}, W_{dis}, \sigma_p$	ψ	δ
D_{in}, t	↑	↓	↑	↓	∼
g_{cc}	↓	↑	↓	↑	↑
n	∼	∼	↓	∼	∼

While concentric VACNT foams with higher g_{cc} proved to be better in terms of damping capacity, EAE, and density-dependent scaling of mechanical properties, they are also competitive with other foams in terms of energy dissipation at lightweight. In Figure 5.8, we compare the mechanical properties of concentric VACNT foams (for $g_{cc} = 50\ \mu m$ and $20\ \mu m$) with cylindrically architected VACNT, non-architected VACNT, polymeric, metallic, and other architected foams found in literature. Concentric VACNT foams are lighter and exhibit a moderate scaling of energy dissipation with density as compared to a much steeper scaling in non-architected and cylindrically architected VACNT foams. Moderate scaling enables a significant reduction in foam density without compromising its ability to dissipate energy, making it suitable for protective applications at a lightweight. However, a steeper density-dependent scaling may have practical value in certain engineering contexts. In scenarios where absolute energy dissipation takes precedence over cushioning effect, and a higher modulus is preferred, such as in ballistic and crashworthy applications, the samples with steeper scaling could still be useful.

Concentric VACNT foams are lighter, stiffer and on par with polymeric foams in dissipating energy. While metallic foams are stiffer and dissipates more energy per unit volume than VACNT foams, they are denser and undergo brittle failure. In contrast, VACNT foams are more resilient, exhibit super-compressibility and demonstrate strain recovery close to 90% (Figure 5.9). Other architected materials such as ceramic and metallic micro/nanolattices are lighter and have proportionally small energy dissipation and modulus. They also exhibit steeper density dependent scaling and experience fatigue failure. In contrast, VACNT foams are fatigue resistant and can survive thousands of loading-unloading cycles without failure [58]. Additionally, VACNT foams are thermally stable from very low temperatures to very high temperatures [16] which makes them

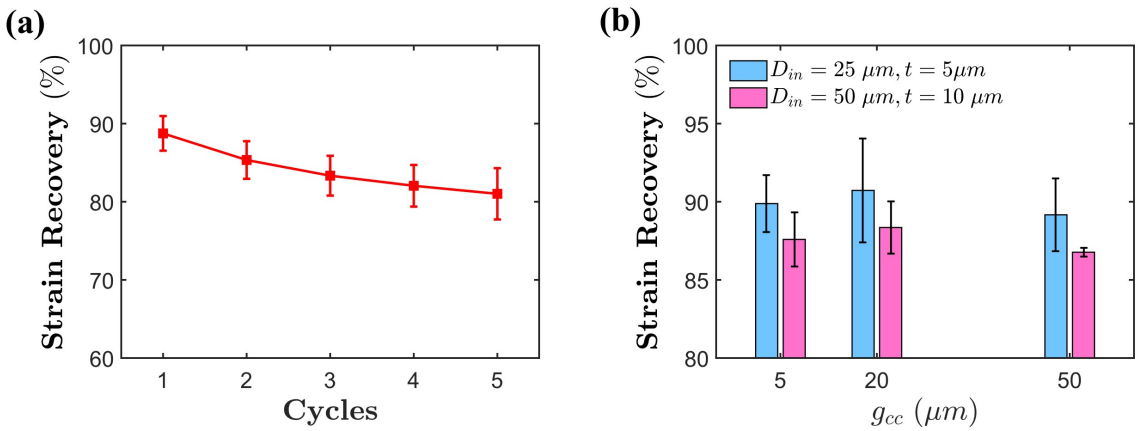

Figure 5.9: Strain recovery as a function of compression cycles. (b) Strain recovery averaged over n as a function of g_{cc}, D_{in}, and t

ideal for applications in harsh environments.

5.4 Conclusion

We report a highly desirable linear scaling of average elastic modulus and energy dissipation with density in ultra-lightweight vertically aligned carbon nanotube foams with a mesoscale architecture of hexagonally close packed thin concentric cylinders. We observe a geometry-dependent alteration in the morphology and deformation mechanism, leading to a damping capacity of $\sim 95\%$ and energy absorption efficiency of $\sim 70\%$. Our architected VACNT foams performs better than polymeric foams and lattice materials in terms of stiffness and strength at lightweight. Our foam material exhibits higher toughness compared to metallic foams and has the ability to recover almost entirely ($\sim 90\%$) from being crushed to extreme compressive strains. In contrast, metallic foams tend to fail in a brittle manner with minimal elastic recovery. We envision applications of our material in lightweight structural batteries, vibration mitigation, and energy absorbing protective gears for military, sportsmen, and construction workers.

5.5 Methods

Creating Micropatterns: To create the micropatterns on the substrate, we used photolithographic techniques. First, we spin coated a standard 100 mm diameter (500 μm thickness) p-type silicon wafer (100 crystal orientation) with a 10 μm thick layer of photoresist (S1813) at 3000 rpm

for 30 seconds and pre-baked it on a hot plate at $383K$ for 45 seconds to remove any solvents. After spin coating, we partially diced the wafer through the thickness (30% of the thickness) into 5 $mm \times 5$ mm squares. Next, we exposed the diced wafer to ultra-violet (UV) light through a chrome/soda-lime photomask with concentric-cylindrical micropatterns (manufactured by Photo Sciences, Torrence, CA). After 8 seconds of exposure with 405 nm UV light at an exposure dose of 80 mJ/cm^2, we removed the unexposed photoresist in a MF321 developer bath for 30 seconds. After the developer bath, we coated the wafer with a 20 nm thin film of Chromium at a deposition rate of 0.5 Å$/s$ using a metal evaporator. After chromium coating, we removed the remaining photoresist (exposed to UV light previously) in an acetone bath for 30 seconds, leaving only a chromium film on the substrate, which prevents the growth of CNTs in the designated areas on the substrate (inverse of the architecture).

CVD synthesis: We use a floating catalyst thermal chemical vapor deposition process (tCVD) to synthesize VACNT foams in a fused-quartz tube with an internal diameter of 50 mm heated at 1100 k inside a horizontal tube furnace (Carbolite CTF 12 & TZF 12 wire wound tube furnace) at atmospheric pressure. We use a syringe pump (NE-1000 one channel programmable syringe pump) to inject a 80 ml solution ($[w/v] = 0.01$ g/ml) of ferrocene (catalyst precursor) in toluene (carbon source) at a rate of 0.8 ml/min into the quartz tube. A carrier gas mixture flowing at 800 $sccm$ of Argon (95% *or* 760 $sccm$) and hydrogen (5% *or* 40 $sccm$) with flow rates controlled by individual mass-flow controllers (MKS G-series GE50A) carries the vapors of toluene and ferrocene inside the furnace. Before starting the synthesis process, a photolithographically prepatterned substrate is placed inside the quartz tube at the furnace's peak heating zone. Carbon nanotubes then grow vertically aligned on this substrate during the synthesis process. After the toluene-ferrocene solution is depleted and syringe pump stops, we switch off the flow of hydrogen and continue the flow of Argon for another 30 minutes, while waiting for the furnace to cool down. After the furnace temperature drops below $400°C$, we proceed to open the quartz tube fixtures and remove the architected VACNT film from the furnace and cut it into squares of 5 $mm \times 5$ mm—each square having an architecture with a specific combination of D_{in}, t, g_{cc}, and n for mechanical characterization.

Quasistatic compression testing: To evaluate the effect of different design parameters on mechanical properties, we performed quasistatic cyclic-compression testing to measure the constitu-

tive stress-strain response. We use an Instron Electropulse E3000 with a 5 kN load cell to compress the samples up to 50% strain at a quasistatic strain-rate of 0.01 s^{-1}. When compressed, bundles of MWCNTs undergo sequential progressive buckling guided by the intrinsic stiffness and density gradient induced by the CVD (chemical vapor deposition) synthesis process. When unloaded, the buckles open like springs to strain recover the foam from compression strains of up to 90%. In the loading-unloading cycle, VACNT foams dissipates huge amount of energy, exhibiting a damping capacity of nearly 90%.

Acknowledgement

This research is supported by the U. S. Office of Naval Research under PANTHER program award number N000142112044 through Dr. Timothy Bentley. We also acknowledge the award number W911NF2010160 from the solid mechanics program of the U.S. Army Research Office through Dr. Denise Ford. The authors acknowledge the use of facilities and instrumentation at the Wisconsin Centers for Nanoscale Technology (WCNT) partially supported by the NSF through the University of Wisconsin Materials Research Science and Engineering Center (DMR-1720415).

Chapter 6

Dimensional analysis guided design of shock absorbers

This chapter is adopted from the following publication

Gupta, A., Chawla, K., & Thevamaran, R. (Submitted). Embracing Nonlinearity and Geometry: A dimensional analysis guided design of shock absorbing materials
Author Contributions : A.G. performed the theoretical analysis, performed the experiments on polymeric foams, analyzed the data, and prepared the figures. K.C. synthesized the VACNT foam samples and performed the quasistatic compression testing. R.T. conceived and supervised the project. A.G. and R.T. wrote the paper.

In this chapter we study design of shock absorbers for protective applications using a dimensional analysis approach. Shock absorbers in protective applications must absorb the kinetic energy of impacts while minimizing the acceleration experienced by the protected entity. This dual objective demands careful consideration of not only the constitutive response of the material, but also the design of energy-absorbing pad's geometry—a role that has largely been ignored in the pursuit of enhancing the mechanical properties of protective materials. Our dimensional analysis-guided framework enables the design of thin and lightweight energy absorbing materials to reliably absorb the given kinetic energy while limiting acceleration and compressive strain within desired limits. Guided by this design framework, we demonstrate optimal protective performance in hierarchically architected VACNT foams. Our scale-free kinematic design framework enables the design of novel

architected materials and bridges the necessary gap between their measured mechanical properties and the critical design considerations in practical engineering applications.

6.1 Introduction

Energy-absorbing materials permeate our lives, from soft polymeric foams used in helmet liners [145, 146], packaging [147], and seat cushions, to crushable metallic foams employed in ballistic impact attenuators [148, 149], automotive buffers, and planetary landers [150]. Those protective foams must absorb the kinetic energy from impacts and undesirable vibrations while limiting the forces and accelerations imparted on the protected objects [1, 147]. Compared to stochastic foams, architected foams demonstrate superior modulus, strength, and energy absorption at comparable or lower densities [130]. This indicates better specific properties or density-normalized properties, achieved through architectural design of the lattice unit cells [131, 151–153]. The pursuit of achieving specific mechanical properties near the theoretical limits has resulted in several advancements [131, 132], including ultra-stiff micro-lattices [19, 24], nanolattices with high mechanical strength [131, 154], high energy-absorption of supersonic projectiles [133], and fracture resilience in hierarchical [58, 105] and woven architectures [155]. While the field of architected materials is thriving with advancements on improving specific mechanical properties, the role of the sample geometry of the energy absorbing material and its interplay with the mechanical properties towards meeting critical performance criteria has been overlooked. For example, it is well understood that helmet liners designed to prevent traumatic brain injury during extreme sports or combat require not only high specific energy absorption capacity but also the ability to limit peak accelerations below a critical value [146, 156].

This interplay between the intrinsic properties of the foam and the protective layer's geometry is governed by three important mechanical properties of foams: relative density ($\bar{\rho}$), the scaling of relative modulus with relative density ($\bar{E} \propto \bar{\rho}^{\alpha}$), and the characteristic shape of the stress-strain response. The relative density, which is the ratio of the foam's bulk density (ρ) to the density of its solid counterpart (ρ_s), controls the compressibility of the foam. A porous foam with a low relative density can be compressed to larger strains before reaching the densification regime beyond which the stress rapidly increases, diminishing the foam's effectiveness. The relative modulus ($\bar{E}$) of all

cellular materials has been observed to scale with relative density ($\bar{E} \propto \bar{\rho}^{\alpha}$). The scaling exponent (α) is determined by the morphology and the deformation mechanism and typically falls within the range $1 < \alpha < 3$ [2, 18, 24]. A linear scaling exponent ($\alpha = 1$) is generally desirable because it allows achieving higher modulus and greater specific energy absorption without significantly increasing the foam's density [24, 151]. The protective performance of the foams also depends on the characteristic shape of the stress-strain response (Figure 6.1(d)). Foams with a plateau-like sublinear stress-strain response are typically considered desirable, allowing absorption of a given amount of energy at a lower stress levels. A desirable protective foam, hence, should exhibit high porosity, a near-linear scaling of modulus with density, and a plateau-like sublinear stress-strain curve.

Traditionally, foams exhibiting properties similar to those mentioned above are considered suitable for nearly all protective applications. Contrary to this belief, we report that foams with steeper scaling ($\alpha > 1$) and nonlinear stress-strain behavior can be beneficial in achieving compact and lightweight energy-absorbing pads. Using a streamlined kinematic model and dimensional analysis, we derive guidelines for geometric design and discover optimal mechanical properties resulting in the thinnest and lightest energy absorbing foam pads. Guided by these derived criteria, we design, synthesize, characterize, and demonstrate optimal performance in hierarchically architected vertically aligned carbon nanotube (VACNT) foams.

Using photolithography, we introduced an additional level of structural hierarchy in VACNT foams by creating mesoscale patterns [11, 18, 110]. Incorporating various geometries of mesoscale patterns opens a broad range of tunability in relative density, constitutive response, and density-dependent scaling of mechanical properties. Our hierarchical architecture design of VACNT foams yields optimal pad geometries subjected to imposed constraints on peak acceleration and maximum compression strain. For example, a bio-inspired higher-order fractal architecture and a sparsely packed cylindrical architecture exhibiting nonlinear stress-strain response enable protective pads with minimum mass. On the other hand, a concentric cylinder architecture with sublinear plateau-like stress-strain response results in more thin and compact protective pads. Our design framework and its effective demonstration on the hierarchically architected VACNT foams provide a comprehensive approach to designing architected materials for superior performance. Our work provides guidance on achieving enhanced protective performance with imposed constraints on geometric and

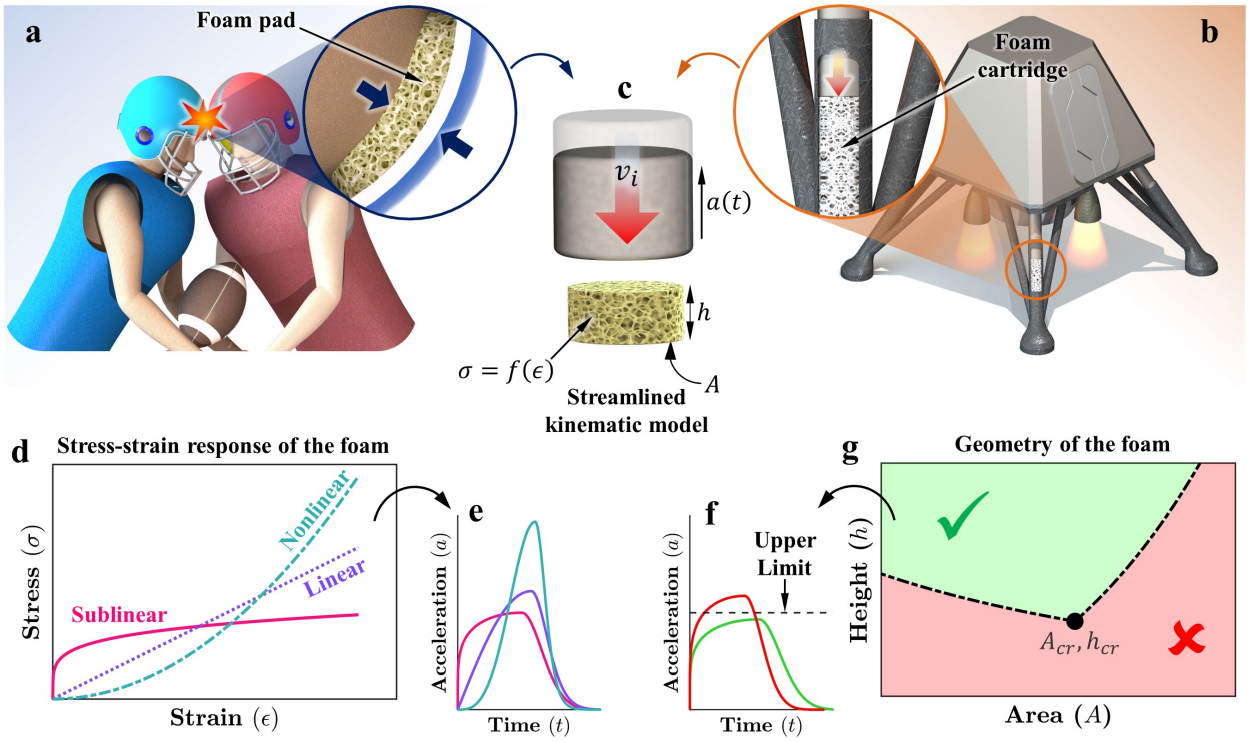

Figure 6.1: (a) An illustration of a collision in sports, where sudden acceleration can cause Traumatic Brain Injury (TBI). Inset: A comfort pad in a helmet absorbing kinetic energy. (b) An illustration of a spacecraft lander with struts consisting of aluminum honeycomb foam cartridges absorbing residual kinetic energy at touchdown. (c) A streamlined kinematic model showing a mass traveling at velocity v_i and coming to rest by impacting a foam pad. (d,e) Various types of stress-strain curves seen in cellular materials and their effect on the impact acceleration vs. time curves. (f,g) A design map for the thickness and cross-sectional area of foam to keep the peak acceleration and peak strain below desired limits

physical properties within the vast material design space offered by machine learning [134, 157] and statistical design of experiments [11].

6.1.1 The foundation of the design framework

Energy-absorbing pads can take various geometries depending on the application, such as a flat comfort pad in helmet liners (Figure 6.1(a)) or a long cylindrical cartridge in planetary landers (Figure 6.1(b)). In all cases, during an impact, the foam is compressed in the direction of impact, absorbing kinetic energy while minimizing the imparted load and recoil. The impact scenarios depicted in Figure 6.1(a,b) can be described by the simplified equation of motion corresponding to an impacting mass m compressing the protective foam with an initial impact velocity (v_i) resulting in swift acceleration (retardation) to rest (Figure 6.1(c)). Assuming that the foam compresses

uniformly within an area A and height h, the force acting on the mass during acceleration will be equivalent to the magnitude of force developed in the foam, as follows:

$$m\frac{d^2x}{dt^2} = mg - \sigma_L A, \tag{6.1}$$

with the initial conditions:

$$x|_{t=0} = 0 \ , \ \left.\frac{dx}{dt}\right|_{t=0} = v_i \tag{6.2}$$

where x is the compression in the foam, t represents time, g is the acceleration due to gravity, and σ_L is the stress response of the foam, with the subscript L indicating that the foam is being loaded (compressed) by the impact. We describe the constitutive stress-strain response of the foam by an empirical power law equation [158] as follows

$$\sigma_L = E_L \epsilon^{\lambda_L} \tag{6.3}$$

where E_L is an elastic modulus, and the exponent (λ_L) governs the shape of the constitutive stress-strain response. By varying λ_L, various stress-strain curves, such as those exhibiting sublinear ($\lambda_L < 1$), linear ($\lambda_L \approx 1$), and nonlinear ($\lambda_L > 1$) behaviors, can be modeled for parametric analysis. Integrating equation (6.3) up to a compression strain ϵ_{max}, we obtain the expression for energy absorption per unit volume (W_L) as follows,

$$W_L = E_L \frac{\epsilon_{max}^{\lambda_L+1}}{\lambda_L + 1} \tag{6.4}$$

In the above expression, W_L is inversely related to $\lambda_L + 1$. This suggests that for a nonlinear stress-strain response ($\lambda_L > 1$), the energy absorbed will be significantly smaller than that of a sublinear stress-strain response ($\lambda_L < 1$), which is not true for real materials [159]. Generally, materials with nonlinear stress-strain response absorb either a similar amount or more energy up to the onset of densification strain [18, 159]. To account for the effect of λ_L, we scale the power law expression in equation (6.3) by multiplying with $(\lambda_L + 1)^\beta$ (Figure 6.2) as follows:

$$\sigma_L = E_L(\lambda_L + 1)^\beta \epsilon^{\lambda_L} \tag{6.5}$$

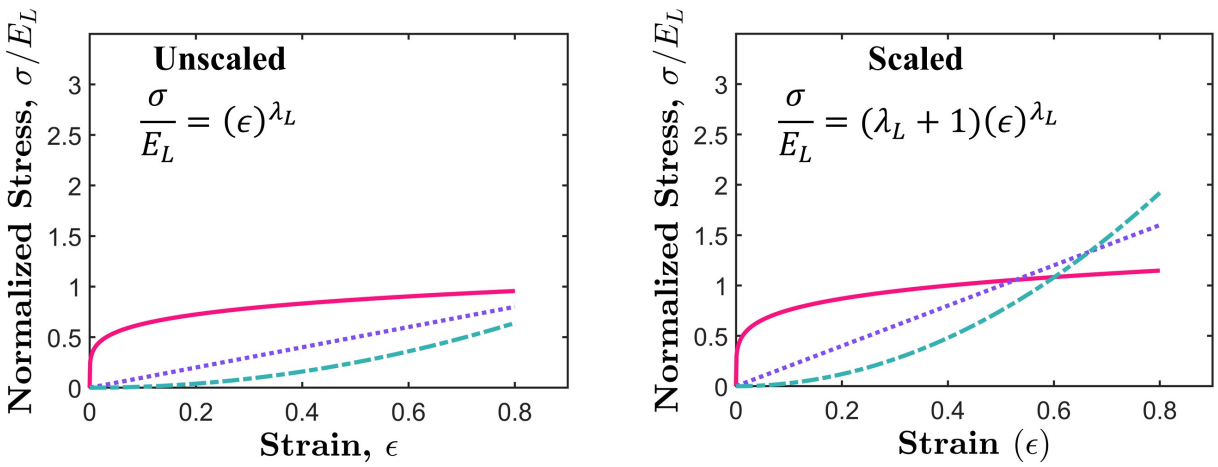

Figure 6.2: Unscaled stress-strain curves as a function of λ_L for empirical power-law. Stress-strain curves adjusted by multipplying $(\lambda_L + 1)^{\beta}$ ($\beta = 1$ above) to counter the effect of λ_L

where the exponent $\beta \geq 1$ determines the relative difference in modulus among a set of foams with various λ_L values. As shown in Figure 6.3(a), the power law equation captures the experimentally measured stress-strain response up to the onset of densification (indicated by red dots)—all measured at the same 0.01 s^{-1} strain rate—fairly well for different open-cell elastomeric foams. These power-law fits yield the effective modulus ($E_L(\lambda_L + 1)^{\beta}$) of the foam and a dimensionless exponent (λ_L) that describes the shape of the stress-strain curve. The strain at the onset of densification, also called critical strain (ϵ_c), is where the energy absorption efficiency of the foam reaches the maximum, beyond which it declines rapidly [160]. The critical strain (ϵ_c) is slightly smaller than the actual densification strain (ϵ_d) where the slope of the stress-strain curve becomes almost vertical [1]. While a foam does keep absorbing more energy for $\epsilon_c < \epsilon < \epsilon_d$, the transmitted force rises sharply making foam ineffective. Hence, a foam's performance is characterized based on the amount of energy it can absorb before the onset of densification ($\epsilon < \epsilon_c$). We measured the critical strain of different polymeric foams using the energy absorption efficiency method [160] and observe a linear relationship ($\epsilon_c = 0.66 - 2\bar{\rho}$) between the critical strain and the relative density of the foam (Figure 6.3(b)). Noteworthy is that this linear fit extrapolates to $\bar{\rho} \to 0.33$ for $\epsilon_c \to 0$, which matches the relative density of foams reported in literature which do not have a plateau region and exhibit densification immediately after the linear elastic regime [1]. In addition to the critical strain, the modulus of the foam also depends on the relative density as mentioned in the introduction:

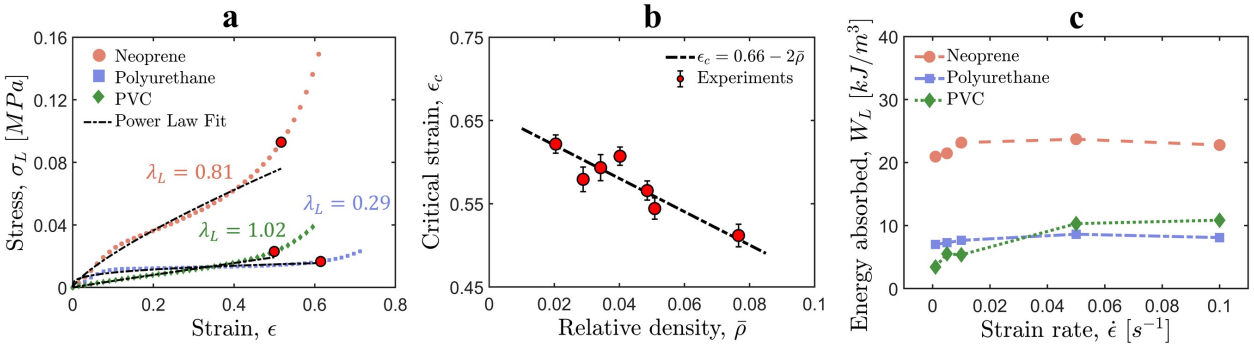

Figure 6.3: (a) Quasistatic stress-strain curves, measured experimentally at a strain rate of 0.01 s^{-1}, for various open-cell polymeric foams, fitted with a power-law model up to the critical strain (indicated by red dots). (b) Critical strain (or onset-to-densification strain) of different polymeric foams plotted as a function of their relative densities. (c) Energy absorbed per unit volume of different foams, measured up to the critical strain, plotted against the strain rate.

$$\frac{E_L}{E_s} = c_1 \left(\frac{\rho}{\rho_s}\right)^{\alpha} \tag{6.6}$$

Here, E_s and ρ_s represent the modulus and density, respectively, of the solid material utilized in foam fabrication, α denotes a scaling exponent that is a function of the foam's morphology and deformation mechanism, and c_1 is a constant of proportionality [3]. Utilizing equation (6.6), the stress-strain relationship for the foam can be expressed as,

$$\sigma_L = c_1(\lambda_L + 1)^{\beta} E_s \, (\bar{\rho})^{\alpha} \, (x/h)^{\lambda_L}, \tag{6.7}$$

where x/h represents the compressive strain ($\epsilon = x/h$). The stress response in equation (6.7) is independent of the strain rate while the most polymeric and elastomeric foams are strain-rate sensitive. This rate dependency is generally incorporated into constitutive models by multiplying a rate-dependent viscous damping term to the elastic term [161]. However, we observe that the specific energy absorbed—the area under the stress-strain curve up to the critical strain—as a function of the strain rate we measured experimentally on various open-cell elastomeric foams show only a mild strain-rate effect with it initially increasing and then becoming almost constant (Figure 6.3(c)). While some foams exhibit rate dependency up to much higher strain rates, their response eventually stabilizes [162]. Moreover, our VACNT foams exhibit rate-independent behavior from quasistatic to very large strain rates [16, 60]. Therefore, adding a rate-dependent term in

equation (6.7) is not worth considering. To make our modeling scale-free, we establish the following dimensionless variables:

$$\bar{x} = x \times \frac{a_c}{v_i^2} \quad , \quad \bar{t} = t \times \frac{a_c}{v_i} \quad , \quad \bar{h} = h \times \frac{2a_c}{v_i^2} \quad , \quad \bar{A} = A \times \frac{E_s}{ma_c} \tag{6.8}$$

Here, a_c represents the maximum acceleration limit that the protected object should not exceed. This limit depends on the object's structural resilience or physiological tolerance, for example, the allowable peak acceleration in the case of traumatic brain injury prevention [163]. By substituting the dimensionless variables (Equation (6.8)) and stress-strain relation (Equation (6.7)) into equation (6.1) and equation (6.2), we arrive at the following dimensionless governing equation and dimensionless initial conditions:

$$\frac{d^2\bar{x}}{d\bar{t}^2} - \frac{g}{a_c} = -c_1\bar{A}(\lambda_L + 1)^{\beta}\,(\bar{\rho})^{\alpha}\left(2\bar{x}/\bar{h}\right)^{\lambda_L} \tag{6.9}$$

$$\bar{x}|_{t=0} = 0 \quad , \quad \left.\frac{d\bar{x}}{d\bar{t}}\right|_{t=0} = 1 \tag{6.10}$$

Usually $a_c \gg g$, so the term (g/a_c) can be ignored [164]. When the impacting mass accelerates to rest from initial velocity v_i as the foam absorbs all its kinetic energy, the maximum compression $(\bar{x}_{max})$ experienced by the foam can be calculated as follows:

$$\left(2\frac{\bar{x}_{max}}{\bar{h}}\right)^{\lambda_L+1} = \frac{\lambda_L + 1}{c_1\bar{A}\bar{h}(\lambda_L + 1)^{\beta}(\bar{\rho})^{\alpha}} \tag{6.11}$$

The magnitude of acceleration will also reach its peak when the compressive strain in the foam reaches its maximum. From equation (6.9), the expression for maximum acceleration can be obtained as,

$$\left|\frac{d^2\bar{x}}{d\bar{t}^2}\right|_{max} = c_1\bar{A}(\lambda_L + 1)^{\beta}\,(\bar{\rho})^{\alpha}\left(\frac{2}{\bar{h}}\bar{x}_{max}\right)^{\lambda_L} \tag{6.12}$$

By substituting $\bar{x}_{max}$ from equation (6.11), we obtain the following expression for the magnitude of peak acceleration:

$$\left|\frac{d^2\bar{x}}{d\bar{t}^2}\right|_{max} = \left(c_1\bar{A}(\lambda_L+1)^{\beta}\,(\bar{\rho})^{\alpha}\right)^{1/(\lambda_L+1)} \times \left(\frac{\lambda_L+1}{\bar{h}}\right)^{\lambda_L/\lambda_L+1} \tag{6.13}$$

Our objective is to minimize both the mass and the thickness of the foam required to absorb the kinetic energy of the impact while ensuring that the magnitude of the maximum acceleration (a_{max}) stays below the desired limit (a_c) and the maximum compressive strain (ϵ_{max}) remains below the critical strain (ϵ_c).

$$\epsilon_{max} = \frac{x_{max}}{h} \leq \epsilon_c \quad \rightarrow \quad \frac{\bar{x}_{max}}{\bar{h}} \leq \frac{\epsilon_c}{2} \tag{6.14}$$

$$a_{max} = \left|\frac{d^2x}{dt^2}\right|_{\max} \leq a_c \quad \rightarrow \quad \left|\frac{d^2\bar{x}}{d\bar{t}^2}\right|_{\max} \leq 1 \tag{6.15}$$

By substituting equation (6.11) and equation (6.13) into equation (6.14) and equation (6.15), respectively, we obtain the following constraints on $\bar{h}$ for a given value of dimensionless foam area $\bar{A}$ and parameters describe the foam's mechanical properties $(c_1, \lambda_L, \alpha, \bar{\rho}, \epsilon_c, \beta)$

$$\bar{h} \geq \frac{(\lambda_L+1)^{1-\beta}}{c_1\bar{A}(\bar{\rho})^{\alpha}(\epsilon_c)^{\lambda_L+1}} \quad (\epsilon_{max} \leq \epsilon_c) \tag{6.16}$$

$$\bar{h} \geq (\lambda_L+1)^{\left(1+\frac{\beta}{\lambda_L}\right)}(c_1\bar{A})^{1/\lambda_L}(\bar{\rho})^{\alpha/\lambda_L} \quad (a_{max} \leq a_c) \tag{6.17}$$

The above two inequalities can be solved to obtain the constraints on both $\bar{h}$ and $\bar{A}$ as follows:

$$\bar{h} \geq \bar{h}_{cr} \;\;,\;\; \bar{h}_{cr} = \frac{\lambda_L+1}{\epsilon_c} \tag{6.18}$$

$$\left(\frac{\bar{h}}{\bar{h}_{cr}}\right)^{\lambda_L} \times \bar{A}_{cr} \geq \bar{A} \geq \left(\frac{\bar{h}_{cr}}{\bar{h}}\right) \times \bar{A}_{cr} \;\;,\;\; \bar{A}_{cr} = \frac{1}{c_1(\lambda_L+1)^{\beta}\epsilon_c{}^{\lambda_L}\bar{\rho}^{\alpha}} \tag{6.19}$$

The above inequalities suggest that, to maintain the peak acceleration and maximum compression strain within the desired limits (Equation (6.16)), the thickness of the foam must exceed a critical thickness $\bar{h}cr$, which depends on the material properties. Conversely, the cross-sectional area can vary within a range determined by the ratio $\bar{h}/\bar{h}_{cr}$ and a critical area $\bar{A}_{cr}$. For the limiting

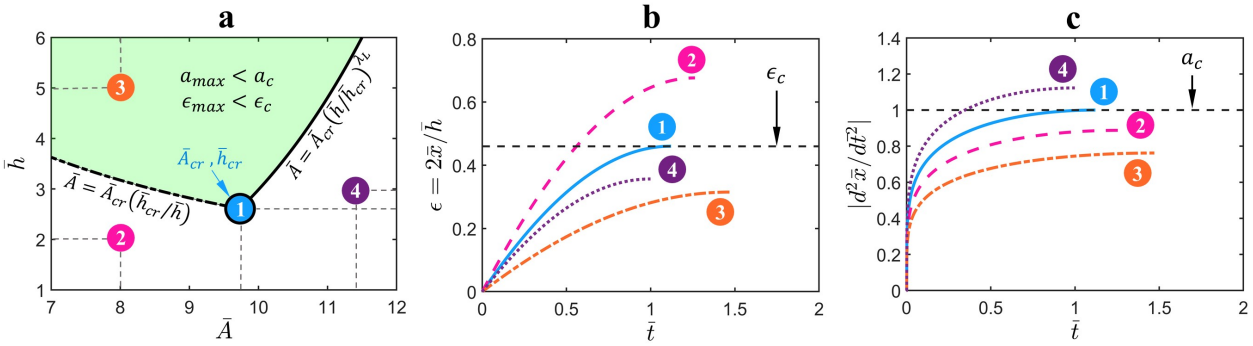

Figure 6.4: (a) Geometric design space showing constraints on dimensionless thickness ($\bar{h}$) and dimensionless area ($\bar{A}$). In the shaded region, both peak acceleration and peak strain will remain below the desired limits for any combination of $\bar{A}$ and $\bar{h}$, while absorbing the given kinetic energy of impact. (b) Compressive strain in the foam during impact as a function of dimensionless time ($\bar{t}$). The maximum limit on strain (critical strain, ϵ_c) is indicated by a black dashed line. (c) Dimensionless acceleration as a function of dimensionless time. The limit on maximum acceleration is shown by a black dashed line (a_c).

case of $\bar{h} = \bar{h}_{cr}$, $\bar{A}$ must exactly be equal to $\bar{A}_{cr}$. The flexibility in selecting $\bar{A}$ and $\bar{h}$ provides design freedom for addressing different challenging applications with geometric constraints on shock absorbers. In Figure 6.4(a), we illustrate such combinations in a shaded region bounded by the upper and lower limits of $\bar{A}$ for an example $\bar{A}_{cr}$ and $\bar{h}_{cr}$ calculated from a certain set of material parameters ($\alpha = 1$, $\lambda_L = 0.2$, $\beta = 1$, $\bar{\rho} = 0.1$, $c_1 = 1$, $\epsilon_c = 0.66 - 2\bar{\rho}$). All combinations of $\bar{A}$ and $\bar{h}$ that fall within the green-shaded region will ensure that the peak acceleration and peak compressive strain remain below the desired limits while the entire kinetic energy due to impact is absorbed by the foam. To validate this, we select four different combinations of $\bar{A}$ and $\bar{h}$, as marked in Figure 6.4(a), for which we solve the time-domain differential equation (Equation (6.9)). In Figure 6.4(b) and Figure 6.4(c), we plot strain and dimensionless acceleration, respectively, as functions of dimensionless time. At the critical point ($\bar{A} = \bar{A}_{cr}, \bar{h} = \bar{h}_{cr}$), the peak acceleration and the maximum strain exactly match the set upper limits a_c and ϵ_c. For points (2) and (4), one of the conditions is not satisfied, whereas for point (3), which lies in the shaded region, both conditions are satisfied.

6.1.2 Thickness and mass minimization

As shown in the previous section, for a given set of material parameters ($\alpha, \lambda_L, \beta, \bar{\rho}, c_1$), the thickness of the foam ($\bar{h}$) must be greater than the critical thickness ($\bar{h}_{cr}$), while the cross-sectional area ($\bar{A}$)

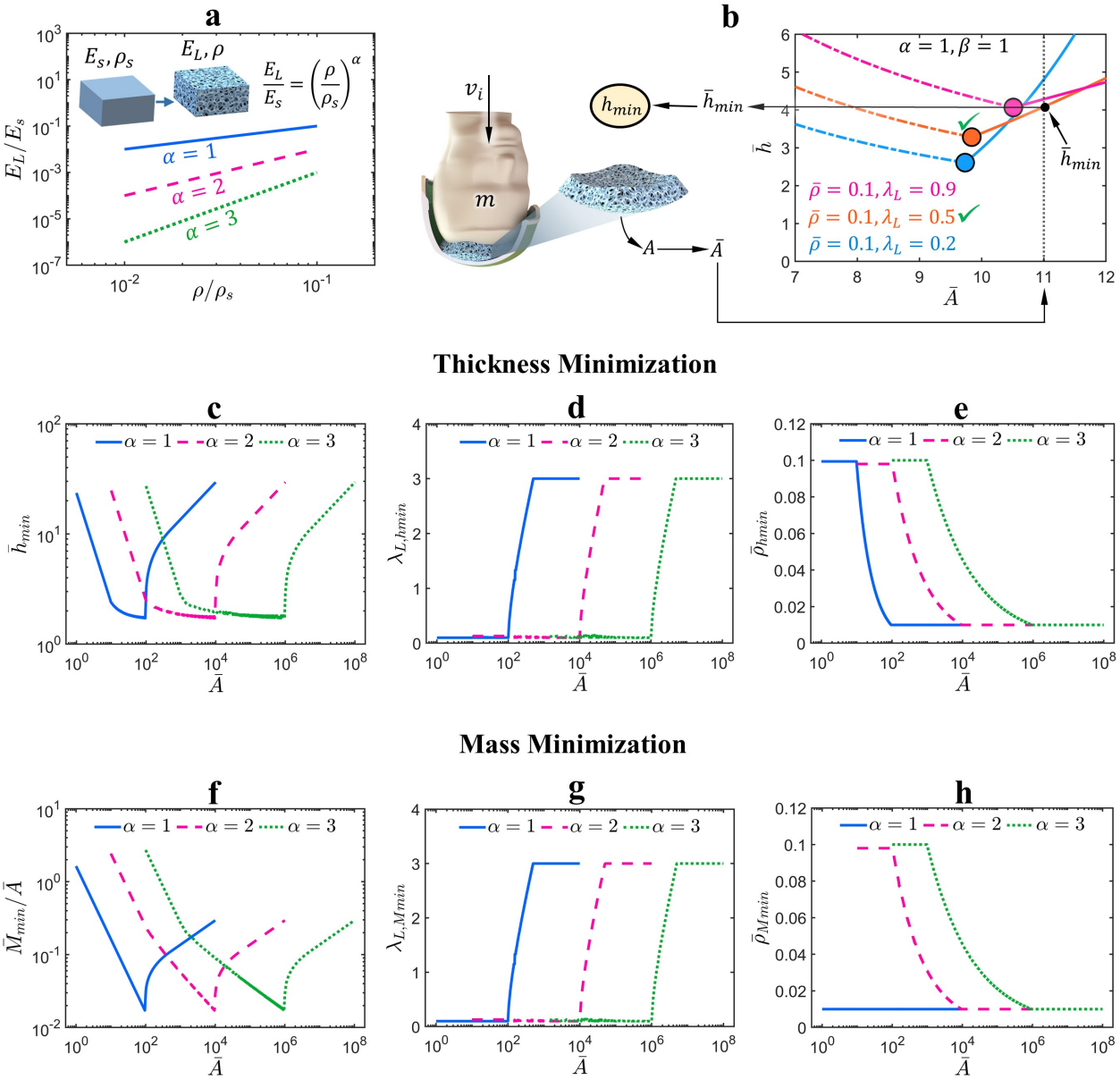

Figure 6.5: (a) Scaling of the relative modulus with the relative density. (b) Determining the minimum possible thickness for a protective foam pad of a known area $\bar{A}$ from a given set of foam material parameters; inset shows a surrogate head-helmet system undergoing impact. (c) Minimum thickness as a function of area for material parameters $0.01 < \bar{\rho} < 0.1$, $0.1 < \lambda_L < 3$, and $1 < \alpha < 3$. (d,e) Values of λ_L and $\bar{\rho}$ corresponding to the minimum thickness. (f) Minimum mass per unit area as a function of area for material parameters $0.01 < \bar{\rho} < 0.1$, $0.1 < \lambda_L < 3$, and $1 < \alpha < 3$. (g,h) Values of λ_L and $\bar{\rho}$ corresponding to the minimum mass per unit area.

can fall within a broad range defined by a lower and an upper limit (Equation (6.19)) in order to limit peak acceleration and maximum compressive strain while entirely absorbing the kinetic energy of impact. These bounds on cross-sectional area depend on the ratio $\bar{h}/\bar{h}_{cr}$, such that the higher

the ratio, the broader the range. Thus, any desired cross-sectional area ($\bar{A}$) within the permissible range can be achieved by proportionally scaling the thickness. We can use this property to identify an optimal set of material parameters that will minimize the thickness of a protective foam given a specific cross-sectional area, for absorbing a given kinetic energy of impact.

To this end, we consider a foam with density ρ and modulus E_L made of a solid material with density ρ_s and modulus E_s. As the relative modulus scales with relative density (Figure 6.5(a)), we explore three different scaling exponents (α) that are commonly found in cellular materials literature: a linear scaling ($\alpha = 1$) that is typically associated with a stretch-dominated deformation mechanism of the foam's micro-structure [2], a quadratic scaling ($\alpha = 2$) observed in bending-dominated deformation mechanisms [19], and cubic scaling ($\alpha = 3$) which has been observed in foams with stochastic micro-structure [140]. Values of α greater than 3 are exceedingly rare [165]. While certain efficient architectures demonstrate $\alpha \approx 1$ [151], values of α less than 1 have not been reported. We assume that the relative density varies between $\bar{\rho} = 0.01$ and $\bar{\rho} = 0.1$, which is typical for open-cell foams [1] and approximately the range for which we measured the critical strain of various open-cell polymeric foams (Figure 6.3(b)). The measured critical strain (ϵ_c) follows a linear relationship with relative density, as shown in Figure 6.3(b). Additionally, we assume that λ_L ranges from $\lambda_L = 0.1$ (indicative of a highly sublinear stress-strain response resembling a Heaviside function) to $\lambda_L = 3$ (indicative of a highly nonlinear stress-strain response) (Figure 6.1(d)).

The workflow to achieve minimum thickness for a given cross-sectional area is illustrated in Figure 6.5(b) using an example of a head-helmet system undergoing a blunt impact, similar to that of a drop tower test for evaluating helmet performance. Here, m represents the effective mass of the head-helmet system, while v_i denotes the impact velocity. While the foam liner—often in combination with an additional soft layer for comfort—inside the helmet undergoes much more complex deformation [166], the direct impact shown in Figure 6.5(b) leads to axial compression of the foam liner that absorbs kinetic energy. For the cross-sectional area A of the pad that experiences direct impact, the corresponding dimensionless area can be calculated using equation (6.8). The Figure 6.5(b) illustrates the process of obtaining the minimum thickness ($\bar{h}_{min}$) for a given $\bar{A}$ ($\bar{A} = 11$ in this example), indicated by a black dotted vertical line. Here, we consider three different $\bar{h}_{cr}$ values and their corresponding $\bar{A}_{cr}$ values (represented as colored dots in Figure 6.5(b)), which were obtained for $\bar{\rho}$, λ_L, and α within the parameter space we considered ($0.01 < \bar{\rho} < 0.1$,

$0.1 < \lambda_L < 3$, $\alpha = 1, 2, 3$). For each dot, when $\bar{h}$ is scaled, the lower and upper limits of permissible $\bar{A}$ are depicted by dashed and solid lines, respectively. The solid lines extend to our target $\bar{A} = 11$, intersecting the vertical dotted line at different locations. Among the three dots, the orange dot corresponding to $\bar{\rho} = 0.1$ and $\lambda_L = 0.5$ results in the minimum thickness ($\bar{h}_{min}$). This dimensionless minimum thickness can be converted to dimensional minimum thickness (h_{min}) using the known parameters v_i and a_c to fabricate a compact foam pad (Equation (6.8)). Let's denote the $\bar{\rho}$ and λ_L corresponding to the minimum thickness as $\bar{\rho}_{hmin}$ and $\lambda_{L,hmin}$, respectively. The chosen energy absorbing foam must have a relative density equal to $\bar{\rho}_{hmin}$ and a stress-strain response with $\lambda_L = \lambda_{L,hmin}$ to achieve the minimum thickness.

Similarly, all possible pairs of $\bar{h}_{cr}$ and $\bar{A}_{cr}$ within the range of material parameters ($0.01 < \bar{\rho} < 0.1$, $0.1 < \lambda_L < 3$, $\alpha = 1, 2, 3$) can be compared for a given $\bar{A}$ to determine the absolute minimum thickness. In Figure 6.5(c), we plot the absolute minimum thickness as a function of $\bar{A}$ obtained for material parameters $\bar{\rho}$, λ_L, and α, varying within the range we assumed, while $\beta = 1$ is fixed. As $\bar{A}$ increases, $\bar{h}_{min}$ counters $\bar{A}$ and decreases initially to maintain the volume of the foam nearly constant for energy absorption, reaching a minimum, and then sharply rises to prevent the effective stiffness ($E_L A/h$) of the foam pad from becoming too large. The descending portion is governed by the constraint on $\bar{h}$ set in equation (6.16), whereas the ascending portion is governed by equation (6.17) (Figure 6.6). The two effects balance each other in the middle to generate a flat region with a nearly constant $\bar{h}_{min}$. For smaller cross-sectional areas ($\bar{A} < 100$), linear scaling ($\alpha = 1$) results in the smallest thickness, whereas for $\bar{A} > 10^4$, cubic scaling is better. This suggests that linear scaling results in a compact-sized foam pad for applications with space limitations in terms of area, such as a foam cartridge in landing struts (Figure 6.1(b)). On the other hand, cubic scaling performs better when more area has to be covered with foam, such as helmet liners and packaging applications.

Figure 6.5(d,e) show optimized parameters corresponding to the minimum thickness $\bar{h}_{min}$. A small value of λ_L initially leads to a lower value of $\bar{h}_{cr}$ (Equation (6.18)). Therefore, it's not surprising that for a smaller cross-sectional area, the thickness is minimized for $\lambda_{L,hmin} = 0.1$. In contrast, for higher $\bar{A}$, the minimum thickness occurs for $\lambda_{L,hmin} = 3$. Notice the power exponent λ_L in the upper limit of $\bar{A}$ in equation (6.19), which allows for attaining significantly higher $\bar{A}$ without scaling $\bar{h}$ by a large amount. This demonstrates the utility of foams with a nonlinear stress-strain

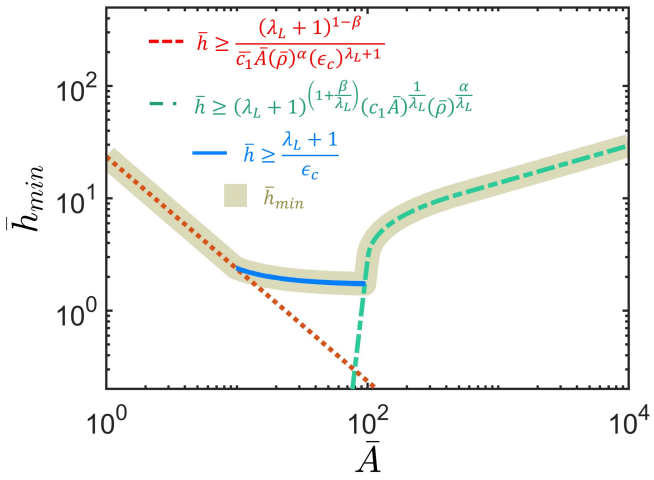

Figure 6.6: Contributions of three constraints derived for $\bar{h}$ on the minimum thickness $\bar{h}_{min}$

curve ($\lambda_L > 1$), which contradicts the conventionally held belief that foams should always exhibit a sublinear response with a plateau of nearly constant stress. The relative density ($\bar{\rho}_{hmin}$) on the other hand follows an opposite trend. A higher relative density for a small $\bar{A}$ provides stiffness to the foam pad, whereas a low relative density, which results in a large critical strain ($\epsilon_c = 0.66 - 2\bar{\rho}$), limits $\bar{h}_{cr}$ (equation (6.18)) for large $\bar{A}$. It is worth mentioning that $\bar{h}_{min}$ and $\bar{A}$ are dimensionless; therefore, their magnitudes in Figure 6.5(c) are not to scale. Their magnitudes are meaningful only when converted back to their dimensional form using equation (6.8). Moreover, since we made our equations scale-free by rendering them dimensionless beforehand, any variation in the external factors such as v_i, m, and a_c will only scale up or scale down $\bar{A}$ and $\bar{h}$ in Figure 6.5(c) without changing the trend of the curves. For example, setting a lower value of a_c, which is akin to increasing the factor of safety, will make $\bar{A}$ larger for a constant A (Equation (6.8)), affecting only the selected $\bar{h}_{min}$ (Figure 6.5(c)) along with the associated $\lambda_{L,hmin}$ and $\bar{\rho}_{hmin}$.

Minimizing thickness and making a foam pad compact in size doesn't always guarantee minimum possible mass. The mass depends on both the volume and the relative density. The dimensionless mass can be calculated using the following equation

$$\bar{M} = \bar{\rho}\bar{A}\bar{h} \tag{6.20}$$

The above mass can be minimized and the resultant optimal material parameters can be obtained by using the similar methodology we implemented earlier for $\bar{h}_{min}$ (Figure 6.5(b)). Since

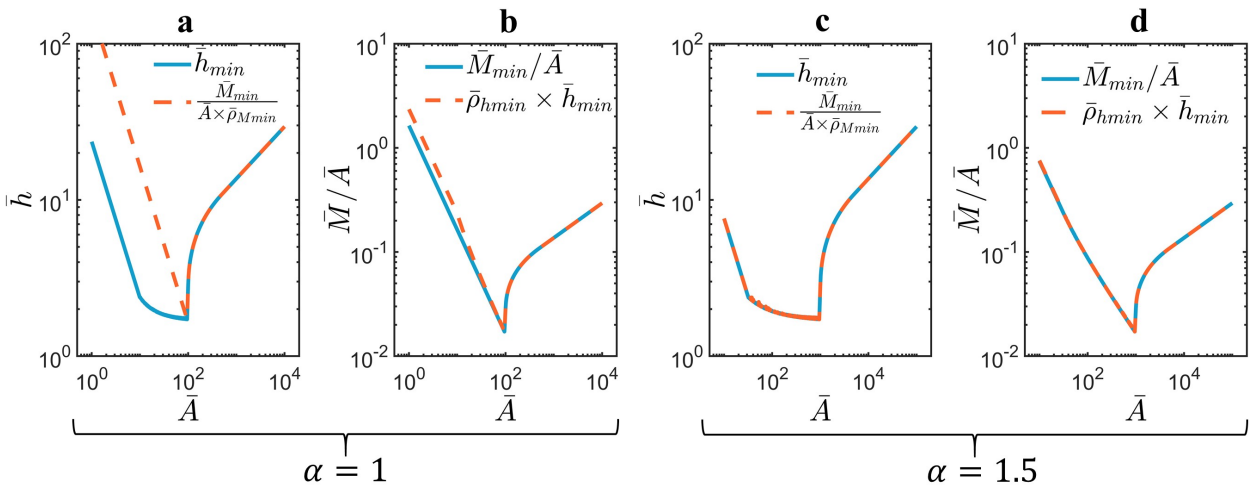

Figure 6.7: (a) Comparison of the absolute minimum thickness with the thickness associated with the minimum mass for $\alpha = 1$. (b) Comparison of the absolute minimum mass per unit area with the mass per unit area associated with the minimum thickness for $\alpha = 1$. (c) Comparison of the absolute minimum thickness with the thickness associated with the minimum mass for $\alpha = 1.5$. (d) Comparison of the absolute minimum mass per unit area with the mass per unit area associated with the minimum thickness for $\alpha = 1.5$.

mass scales with area, we have plotted the minimum mass per unit area ($\bar{M}_{min}/\bar{A}$) in Figure 6.5(f). The trend is similar to $\bar{h}_{min}$: linear scaling ($\alpha = 1$) performs better for a small cross-section area, whereas cubic scaling is better when overlaying a larger area with foam. In Figure 6.5(g,h), we plot the optimized parameters $\lambda_{L,Mmin}$ and $\bar{\rho}_{Mmin}$ corresponding to minimum mass. For $\alpha = 2$ and $\alpha = 3$, both $\lambda_{L,Mmin}$ and $\bar{\rho}_{Mmin}$ exactly match $\lambda_{L,hmin}$ and $\bar{\rho}_{hmin}$ respectively which suggest that both mass and thickness are simultaneously minimized. However, for $\alpha = 1$, while λ_L still matches, the relative densities are different. $\bar{\rho}_{Mmin}$ remains constant at 0.01, which is the smallest relative density we considered. This occurs because for $\alpha = 1$, the $\bar{\rho}^{\alpha-1}$ term vanishes from the critical mass, which is defined as follows:

$$\bar{M}_{cr} = \bar{\rho}\bar{A}_{cr}\bar{h}_{cr} = \frac{1}{c_1(\lambda_L+1)^{\beta-1}\epsilon_c{}^{\lambda_L+1}\bar{\rho}^{\alpha-1}} \tag{6.21}$$

While ϵ_c is a function of relative density, it is maximum for $\bar{\rho} = 0.01$ (Figure 6.3(b)), thus minimizes $\bar{M}_{cr}$.

To summarize, a nonlinear scaling of relative modulus with relative density allows for the simultaneous minimization of both the mass and thickness of the foam. In contrast, for linear scaling ($\alpha = 1$), minimizing one disregards the other, not allowing both objectives to be simultaneously

achieved. We can witness this by comparing the absolute minimum thickness ($\bar{h}_{min}$) with the thickness corresponding to the minimum mass, expressed as follows:

$$\bar{h}_{min} \quad \text{vs.} \quad \bar{h} = \frac{\bar{M}_{min}}{\bar{A} \times \bar{\rho}_{Mmin}} \tag{6.22}$$

Figure 6.7(a) illustrates that for $\alpha = 1$, minimizing the mass has unintentionally resulted in a much higher thickness. Similarly, minimizing the thickness leads to a slightly higher mass, as shown in Figure 6.7(b). For $\alpha \geq 1.5$, both mass and thickness are simultaneously minimized (Figure 6.7(c,d)).

6.1.3 Architected VACNT Foams

The underlying assumption behind the minimization problem we pursued in the previous section was that the material parameters, such as $\bar{\rho}$, λ_L, and α, are independent of each other. In reality, they exhibit some inter-dependency, and not all possible combinations can occur, especially in stochastic polymeric and metallic foams. For example, a nonlinear stress-strain response (where $\lambda_L > 1$) is usually observed in foams with large relative densities. In contrast, architected foams offer versatility in the design space and allow independent tunability of different mechanical properties. The vertically aligned carbon nanotube (VACNT) foams with mesoscale architecture are particularly interesting because of their hierarchical structure that can be tailored to achieve broad range of properties. In previous works, we have reported tunability in density-dependent scaling, specific modulus, and relative density by introducing a mesoscale architecture in VACNT foams synthesized via the floating catalyst chemical vapor deposition process [11, 18]. The non-architected VACNT foams themselves exhibit exceptional modulus and energy absorption comparable to metallic foams, while their densities, compressibility, and strain-recovery are similar to polymeric foams [13]. These exceptional properties arise from a hierarchical structure with features across various length scales. Multi-walled CNTs (MWCNTs) at the nanoscale (Figure 6.8(d)), a random forest of entangled CNTs at the microscale (Figure 6.8(c)), and a structure of nominally vertically aligned CNTs at the mesoscale (Figure 6.8(b)) all culminate in a monolithic, seemingly solid foam at the macroscale (Figure 6.8(a)). We introduced an additional level of structural hierarchy at the mesoscale by synthesizing VACNTs on a photo-lithographically prepatterned silicon wafer sub-

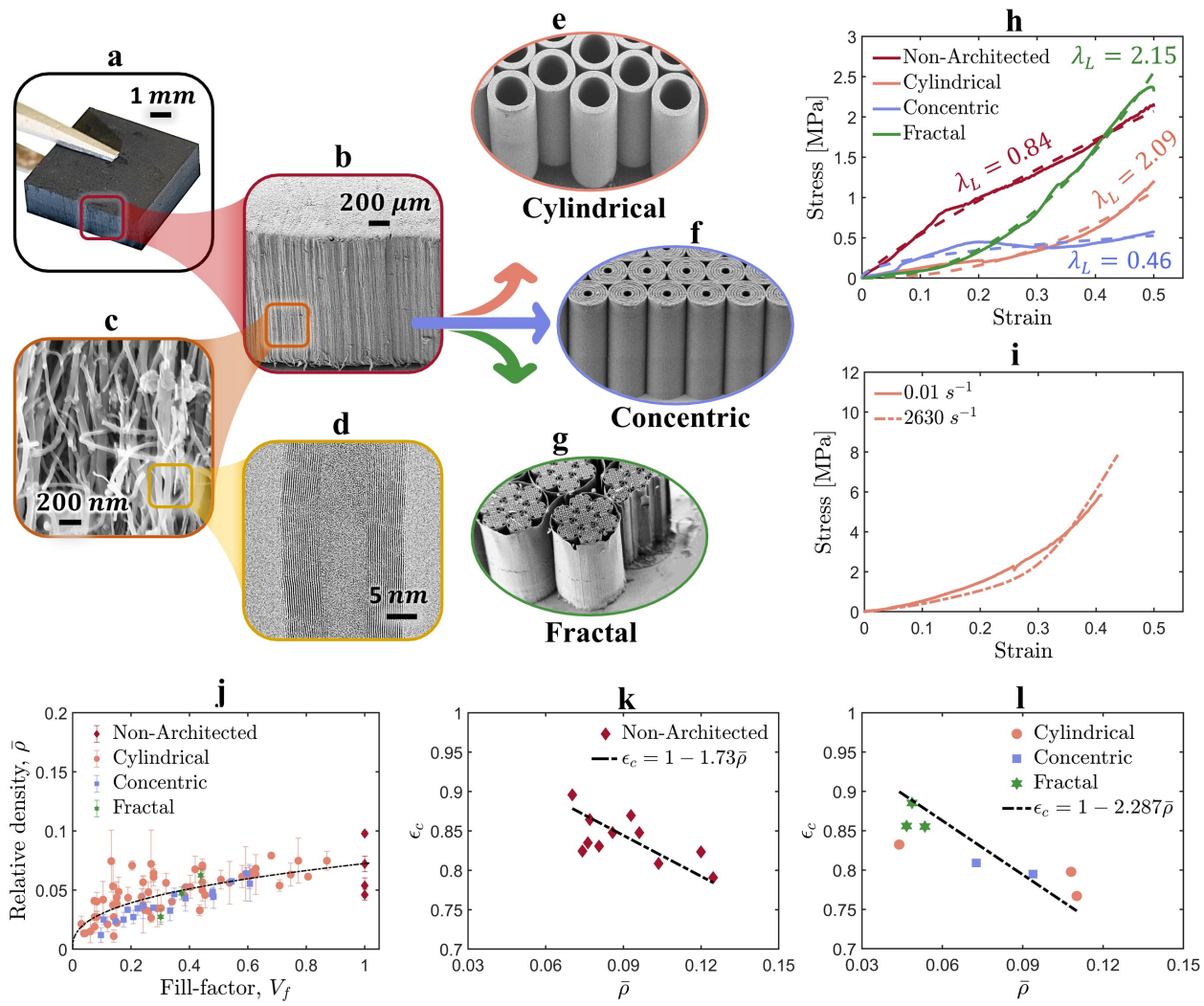

Figure 6.8: (a,b,c,d) Hierarchical vertically aligned carbon nanotube foam with structural length-scales spanning from nanometers to millimeters. VACNT foams with mesoscale architecture having hexagonal close-packed arrays of cylinders (e), concentric cylinders (f), and self-similar fractal (g). (h) Representative experimentally measured quasistatic stress-strain responses of non-architected and architected VACNT foams along with the corresponding power law models. (i) Strain-rate independency of stress-strain response of cylindrically architected VACNT foams across five orders of strain rates. (j) Relative density of various non-architected and architected VACNT foam samples as a function of the fill-factor of the architecture (V_f). (k) Critical strain of non-architected VACNT foams as a function of relative density. (l) Critical strain of architected VACNT foams as a function of relative density.

strate. We selectively deposit chromium in areas where we do not want CNTs to grow (the inverse of architecture), allowing growth only in the region defined by the architecture [18]. Figure 6.8 illustrates SEM images of three different mesoscale architectures: a hexagonally packed cylindrical architecture (Figure 6.8(e)), a concentric cylinder architecture (Figure 6.8(f)), and a self-similar

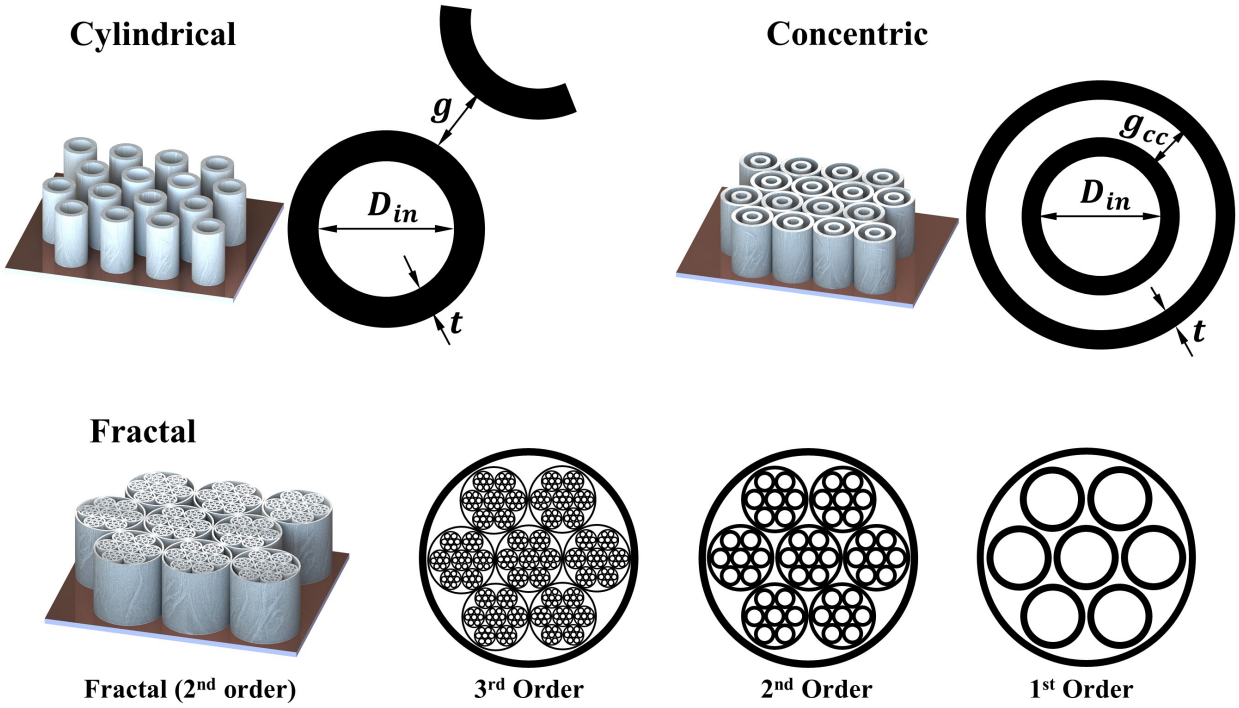

Figure 6.9: Illustrations of various architected VACNT foams

fractal architecture (Figure 6.8(g)).

Figure 6.8(h) shows representative experimentally measured quasistatic (strain-rate of 0.01 s^{-1}) stress-strain responses of non-architected VACNT foam as well as architected foams, including the corresponding power law models (dashed curves). As shown, architected VACNT foams enhances the range of values of λ_L, which was limited to nearly linear $\lambda_L \approx 1$ for non-architected foams, to sublinear ($\lambda_L < 1$) and nonlinear ($\lambda_L > 1$). The shape of the stress-strain curve or the value of λ_L depends on the specific architectural parameters that elicit specific deformation mechanism of cylinders within the architecture. For example, in concentric cylinder architecture (Figure 6.8(f)), a column buckling of cylinders with larger gap between the concentric cylinders results in a sublinear stress-strain curve, whereas a progressive shell buckling of cylinders with smaller gap results in a nonlinear stiffening stress-strain response [18]. Moreover, the stress-strain responses of both architected and non-architected VACNT foams are strain-rate independent (Figure 6.8(i)) up to very large strain rates [16, 60, 111]. In Figure 6.8, the stress-strain responses of a cylindrically architected VACNT foam we tested at quasistatic and dynamic strain rates, reveals almost no effect of strain rate. This strain-rate independence and the richness of material parameter space makes VACNT foams an ideal material system for us to demonstrate the effectiveness of our model

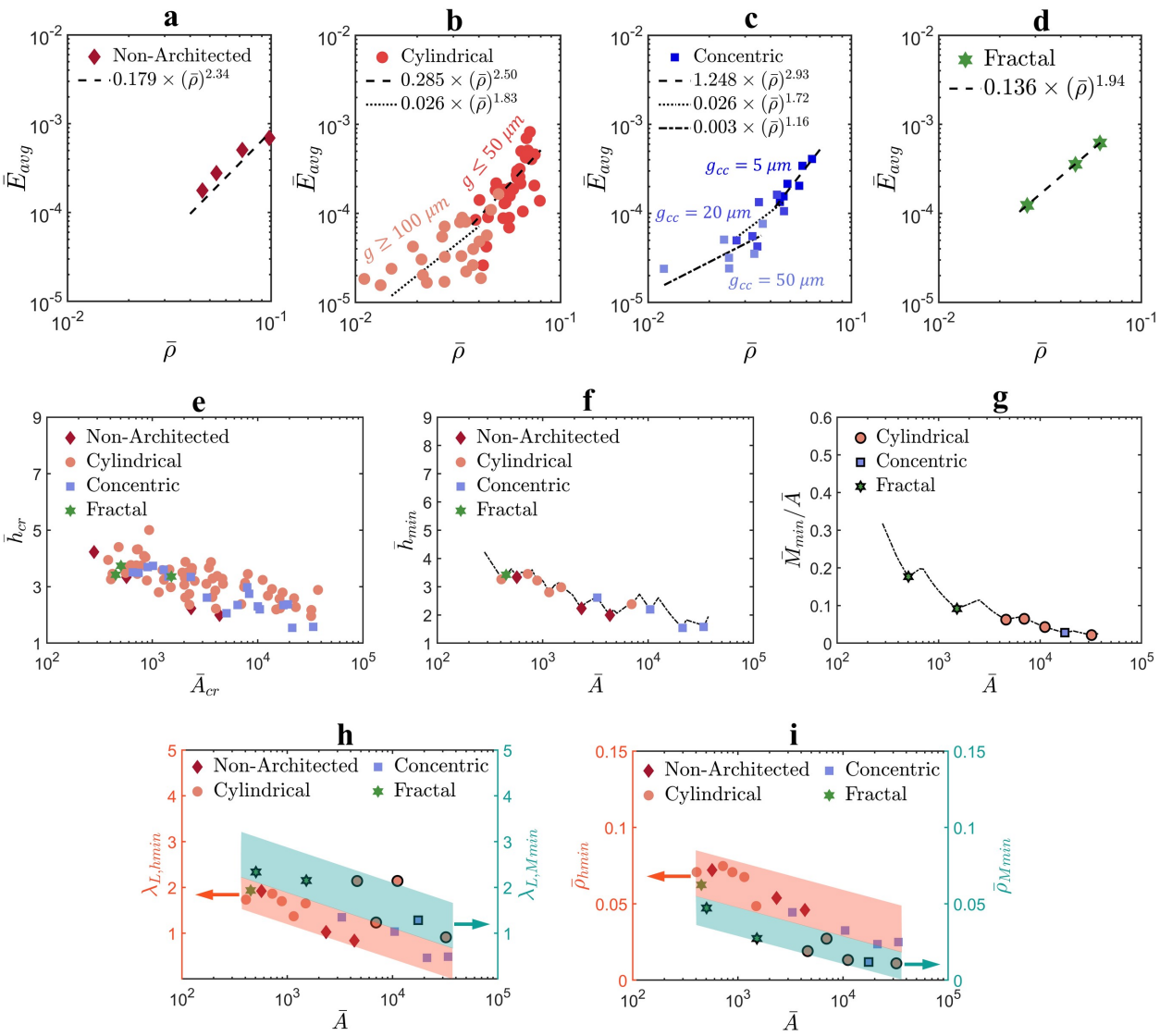

Figure 6.10: Scaling of normalized average modulus with relative density of non-architected (a), cylindrical (b), concentric (c), and fractal architectures (d). (e) Critical thickness vs. critical area of all VACNT foams. Minimum thickness (f) and minimum mass per unit area (g) as a function of dimensionless area. (h) $\lambda_{L,hmin}$ compared to $\lambda_{L,Mmin}$. (i) $\bar{\rho}_{hmin}$ compared to $\bar{\rho}_{Mmin}$

in real materials.

We synthesized multiple samples in each architecture category by varying the dimensions of architectural features. For example, by varying the inner diameter (D_{in}), wall-thickness (t_w), and gap (g) between the cylinders in cylindrically architected foams, we synthesized 60 different types of samples [11]. In concentric architecture, we varied the inner gap and the number of rings of concentric cylinders, resulting in a total of 18 samples [18]. For fractal architecture, we synthesized 3 types of samples with different orders of self-similarity (Figure 6.9). Moreover, we repeated the

synthesis of each kind of sample three times and averaged the mechanical properties to account for any variability in the samples of a given architecture.

We calculated the relative density ($\bar{\rho}$) by dividing the bulk density (ρ) of VACNT foams by the density of highly packed CNTs ($\rho_s \sim 2.26\ g/cm^3$) [167]. In Figure 6.8(j), we plotted the relative densities of all VACNT foams as a function of the fill-factor (V_f) of the architectures (see Appendix-B for derived expressions of V_f for different architectures). It is evident that the relative density is adjustable as a function of fill-factor and exhibits a wide range across samples, from $\bar{\rho} = 0.01$ to $\bar{\rho} = 0.1$. As the fill-factor approaches 1, the relative density of architected VACNT foams asymptotically approaches the relative density of non-architected VACNT foams. Similar to polymeric foams in Figure 6.3(b), we measured the critical strain ϵ_c of both non-architected and architected VACNT foams using the energy absorption efficiency method [160]. For both types of foams, the critical strain ϵ_c varies linearly as a function of $\bar{\rho}$ with a slope of approximately 2, which is typically observed in crushable metallic foams [1].

We observe a wide range of density dependent scaling of elastic modulus among different architectures. In Figure 6.10(a,b,c,d), we plot average relative modulus ($\bar{E}_{avg}$) of VACNT foams as a function of relative density, where $\bar{E}_{avg}$ is a dimensionless modulus calculated from the experimentally measured stress-strain response of VACNT foams. $\bar{E}_{avg}$ is a measure of the elastic energy stored in the foam during compression. Unlike E_L, $\bar{E}_{avg}$ is normalized by $\lambda_L + 1$, thus it scales more consistently with relative density. As a function of loading modulus E_L and λ_L obtained from power-law fits, the expression of $\bar{E}_{avg}$ is given as follows

$$\bar{E}_{avg} = \frac{E_L}{E_s} \times (\lambda_L + 1)^{\beta-1} \epsilon_p^{\lambda_L - 1} \times (2 - \delta) \tag{6.23}$$

where, E_s is the elastic modulus of highly densely packed CNTs ($E_s \sim 15\ GPa$) [168], ϵ_p is the peak compression strain applied while measuring the stress-strain response, and δ is the damping capacity—a ratio of hysteretic energy dissipated in the loading-unloading cycle divided by the area under the loading curve [18]. For non-architected and fractal-architected, the scaling is nonlinear with scaling exponent $\alpha = 2.34$ and $\alpha = 1.94$ respectively. However, for cylindrically-architected and concentric cylinder architectures, the scaling is tunable as a function of the external gap between the cylinders and the internal gap between the concentric cylinders respectively.

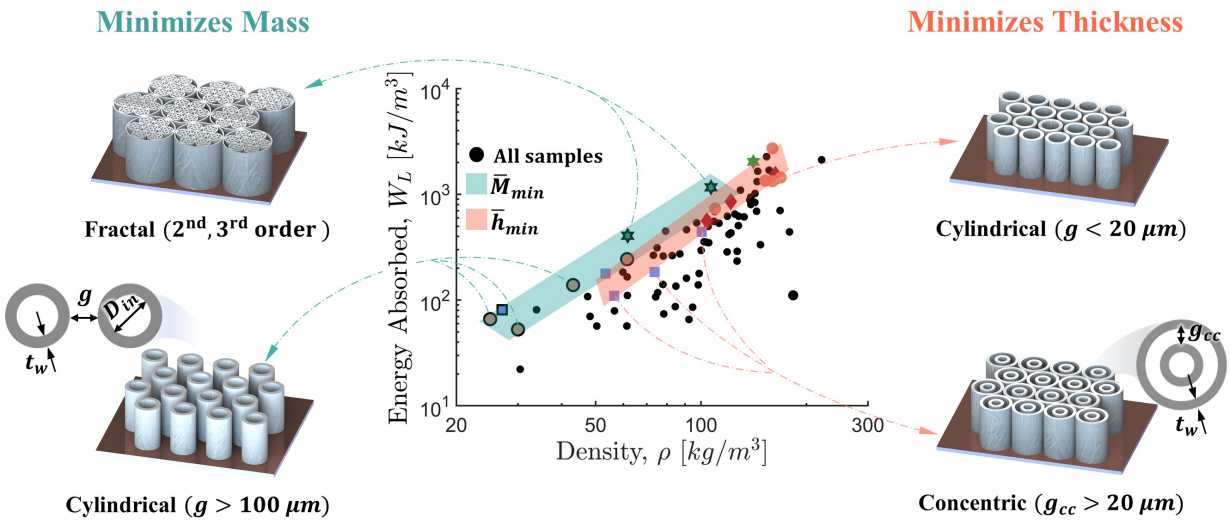

Figure 6.11: Volumetric energy absorption as a function of density for all the VACNT foam samples. The data points for samples that minimizes mass are shown with black outline. The illustration of the architectures of different VACNT samples that outperform others are also shown

Using the measured material parameters $(\bar{\rho}, \lambda_L, E_L)$ we calculated dimensionless critical thickness and critical area which are plotted in Figure 6.10(e). To identify the VACNT foam samples that will result in minimum thickness, we implemented the framework that we demonstrated earlier in Figure 6.5(b). In the thickness minimization process, starting with 85 samples, we were able to condense down to 14 samples that will result in minimum thickness for a given area $(\bar{A})$ lying in the range shown in Figure 6.10(f). Similarly, we identified VACNT foam samples that will result in minimum mass for a given $\bar{A}$. For minimum mass, we were able to condense down to 7 samples which all turned out to be architected VACNT foams, because of the comparatively large relative densities associated with non-architected VACNT foams. In Figure 6.10(h), we compare λ_L corresponding to minimum thickness $(\lambda_{L,hmin})$ with minimum mass $(\lambda_{L,Mmin})$. The data points corresponding to $\lambda_{L,Mmin}$ are plotted with black outline to distinguish from $\lambda_{L,hmin}$. The data points seem to form distinctive bands with $\lambda_{L,hmin}$ forming a band of lower overall values compared to $\lambda_{L,Mmin}$. In contrast, for relative density, $\bar{\rho}_{Mmin}$ values form a band of lower overall values compared to $\bar{\rho}_{hmin}$ (Figure 6.10(i)). In summary, a higher $\bar{\rho}$ and a sublinear λ_L are favourable to achieve minimum thickness whereas a smaller $\bar{\rho}$ and a nonlinear λ_L are needed to achieve minimum mass.

In Figure 6.11, we present a plot showing volumetric energy absorption versus density, where

we have isolated the best-performing VACNT samples from a total of 85 samples. The samples that minimize thickness ($\bar{h}min$) are represented by colored markers, while data points for samples that minimize mass ($\bar{M}min$) are depicted with the same markers but with black borders. All other samples are shown using solid black dots.

The samples corresponding to $\bar{M}_{min}$ and $\bar{h}_{min}$ form two distinct bands in the top region of the scatter plot, demonstrating maximum energy absorption for a given density. The architectures corresponding to the majority of samples lying in these bands are illustrated along with their geometric design parameters. For $\bar{M}_{min}$, the samples include higher-order fractal (2nd and 3rd order) and sparsely packed cylindrically architected samples (with $g > 100\ \mu m$) due to their low densities and high energy absorption capabilities. On the other hand, samples associated with $\bar{h}_{min}$ include tightly packed cylindrical architected and non-architected samples due to their highest energy absorption. Additionally, sparsely ($g_{cc} > 20\mu m$) packed concentric cylindrically architected foams are present due to their sublinear stress-strain response (Figure 6.10(h)) and consequently lower critical thickness ($\bar{h}_{cr}$) (see Equation (6.18)). While a lot of samples, other than the optimal ones, lying in the $\bar{h}_{min}$ band exhibit considerably high energy absorption at a given density, their λ_L are too large to minimize thickness.

In our theoretical calculations, we achieved simultaneously minimized thickness and mass for a large range of λ_L and $\bar{\rho}$ varying independently. In VACNT foams, there seems to be a slight interdependence between λ_L and $\bar{\rho}$ (Figure 6.10(h)), resulting in only one type of sample—a cylindrically architected foam with $D_{in} = 50\ \mu m$, $t_w = 20\ \mu m$, and $g = 100\ \mu m$ that simultaneously minimizes both thickness and mass. However, using novel hierarchical graph network based machine-learning methods to design architectures can potentially result in a broadened parameter space, allowing for independent tunability of λ_L and $\bar{\rho}$. Such independent tunability can possibly lead to simultaneous thickness and mass minimization in various types of architectures.

6.1.4 Summary and key findings

In conclusion, our study highlights the pivotal role of a foam pad's geometry in determining the mechanical performance. By employing a simplified kinematic model and dimensional analysis, we established constraints on the cross-sectional area and thickness of foam pads with known mechanical properties. These constraints ensure that both the maximum compressive strain within

the foam and the maximum acceleration experienced by the protected object remain below desired limits. Using these constraints as a design framework, we identified the mechanical properties necessary for achieving the thinnest, lightest, or a combination of both in foam pads for a given cross-sectional area. Contrary to prevailing beliefs, our findings suggest that foams with stress-strain curves lacking a plateau of constant stress but instead exibiting a nonlinear stress-strain response can lead to both thin and lightweight foam pads—that are critical to many extreme protective applications. Using our non-dimensional design framework, we demonstrate optimal designs in hierarchically architected VACNT foams with cylindrical, concentric cylindrical, and fractal architectures. Our generalized design framework can be applied to any architected and stochastic foams with known mechanical properties to design compact and lightweight energy absorbing pads for diverse protective applications by identifying the best-performing architectures from a multitude of options.

Acknowledgement

This research is supported by the U.S. Office of Naval Research under PANTHER program award number N000142112044 through Dr. Timothy Bentley as well as the award number W911NF2010160 from the solid mechanics program of the U.S. Army Research Office through Dr. Denise Ford. The authors acknowledge the use of facilities and instrumentation at the Wisconsin Centers for Nanoscale Technology (WCNT) partially supported by the NSF through the University of Wisconsin Materials Research Science and Engineering Center (DMR-1720415). We thank Bhanugoban Maheswaran for performing the high strain rate compression experiments on the architected VACNT foam samples using a custom-built Kolsky bar apparatus. We also acknowledge Team Wendy for sending us their Zorbium soft and hard polyurethane foams to compare their mechanical properties with our VACNT foams.

Chapter 7

Exceptional points in passive dynamical systems

This chapter is adopted from the following publication

Gupta, A., & Thevamaran, R. (2023). Requisites on material viscoelasticity for exceptional points in passive dynamical systems. Journal of Physics: Materials, 6(3), 035011.
Author Contributions : AG performed theoretical analysis and experiments. RT supervised the project. AG and RT wrote the paper.

In this chapter, we discuss strategies to design non-Hermitian elastodynamic metamaterials with sharp exceptional point (EP) bifurcations using viscoelastic materials.

7.1 Introduction

Using non-Hermitian singularities such as the exceptional points (EPs) to control wave dynamics is emerging as a new paradigm to develop novel elastodynamic [29, 169–173] and acoustic [34, 35, 174–176] metamaterials with unusual functionalities like unidirectional invisibility [34, 176], asymmetric mode switching [177, 178], frequency-pure asymmetric transmission [174], enhanced sensitivity [25, 171], and enhanced emission [40]. Unlike the geometric symmetries—e.g., rotational, translational, and periodicity—present in phononic crystals and acoustic metamaterials [179–183], non-Hermitian systems utilize parity and time reversal symmetries (PT-symmetry) [184] induced

by spatially distributed gain and loss mechanisms [29, 171, 173].

While a plethora of research has studied EPs and their applications in PT-symmetric systems with balanced gain and loss, entirely passive (with no gain) systems with differential-loss have also been shown to exhibit exceptional points [40, 169, 174, 185, 186]. Loss or dissipation is often found as an intrinsic property of materials, whereas gain is induced often by pumping energy into the system from external sources via piezoelectric [32, 33], electroacoustic [34, 35], piezoacoustic [36, 37], non-Foster circuits [38], and electromagnets [39]. Creating gain needs sophisticated, active, positive feedback control circuits, making systems energy expensive, bulkier, and difficult to control each active elements [33, 38, 39, 187]. Realizing EPs in passive systems can make implementation more straightforward and integration into devices and structures seamless for engineering applications.

EPs are branch point singularities in the parameter space of a physical system where eigenvalues and corresponding eigenvectors coalesce and become degenerate [188, 189]. In contrast to degeneracy points in Hermitian Hamiltonians (diabolic points), where the bifurcation is linear, EPs exhibit higher-order bifurcations [27, 190] (Figure 7.1). Any perturbation in the vicinity of an exceptional point results in a bifurcation of degenerate eigenvalues in the orthogonal direction (orthogonal bifurcation), making EPs very sensitive to external interference. The sensitivity of EPs has been exploited in developing hypersensitive gyroscopes [191, 192], nanoparticle sensors [27, 171, 190, 193], and accelerometers [25, 194]. However, achieving a similar level of sensitivity in passive non-Hermitian systems is challenging regardless of their other utility such as in enhancing emissivity at the proximity to the EPs [40]. Unlike sharp orthogonal EP phase transition in PT-symmetric systems, bifurcations in passive non-Hermitian systems exhibit an approximate transition with an avoided crossing of eigenmodes [169, 195, 196].

In this chapter, we report material design considerations for realizing EPs with sharp bifurcation in a passive non-Hermitian metamaterial in elastodynamic framework. Such a metamaterial can be realized by constituent elements containing a coupled mechanical oscillators (dimer) having differential loss. Incorporating a resonant element with a viscoelastic material for the dissipative component while the other resonator being an elastic conservative element will allow introducing non-Hermiticity to the metamaterial. Until now, the theoretical investigations to realize exceptional points (EPs) in coupled mechanical oscillators with passive differential damping have predominantly been limited to employing springs and viscous dashpots as a means to introduce non-Hermiticity

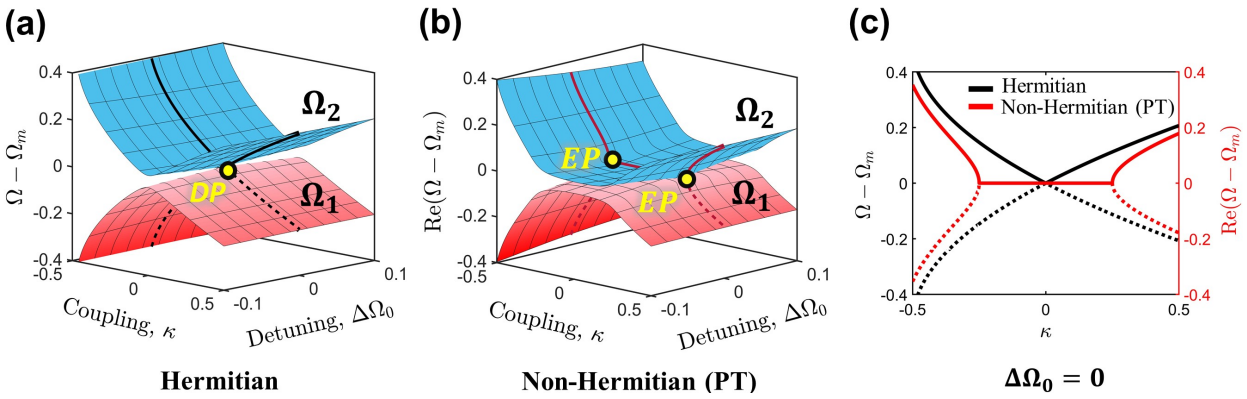

Figure 7.1: (a) Linear bifurcation of eigenvalues Ω_1 and Ω_2 at a diabolical point (DP) in a coupled resonators system described by a 2×2 Hermitian Hamiltonian. Where, κ is the coupling between the resonators, $\Delta\Omega_0$ is the frequency detuning between the resonators, and Ω_m is the mean of natural frequencies $\left(\Omega_m = \frac{\Omega_1+\Omega_2}{2}\right)$. (b) Square root bifurcation of eigenvalues at an exceptional point in a non-Hermitian coupled oscillators system with PT-symmetry. (c) Comparison of bifurcation diagrams between Hermitian and Non-Hermitian (PT) for $\Delta\Omega_0 = 0$. Introducing gain and loss in Hermitian system results in splitting of one DP into two EPs.

[195, 197, 198]. Nevertheless, the springs and dashpots inadequately capture the physical characteristics exhibited by the majority of real viscoelastic materials such as common rubbers and polymeric foams. While numerous plastics, rubbers, and foams exhibit viscoelasticity that can be described by different viscoelastic models, not every viscoelastic material will lead to a non-Hermitian metamaterial with a clear EP. The inherent-coupling between the storage and loss moduli (i.e. the real and imaginary parts of the complex dynamic modulus) by the Kramers-Kronig relation [47, 199] makes the experimental realization a significant challenge and require a judicial design [40]. We investigate different viscoelastic material models in comparison to a coupled oscillator model consisting of differential structural damping and formulate requisites on frequency-dependent loss tangent to achieve a sharp EP bifurcation that is critical for exploiting its hypersensitivity to system parameters. Our findings will guide the experiments [40] on achieving sharp EPs in systems containing viscoelastic materials to create non-Hermiticity. Because the governing non-Hermitian Hamiltonian of our system is mathematically similar to all other bimodal physical systems, our results can be applied broadly to other fields of physics as well.

This chapter has the following structure: We first discuss general rate independent frictional (structural) damping and compare the occurrence of EPs in a coupled oscillators dimer for PT-symmetric case with balanced gain and loss and passive non-Hermitian case with differential loss.

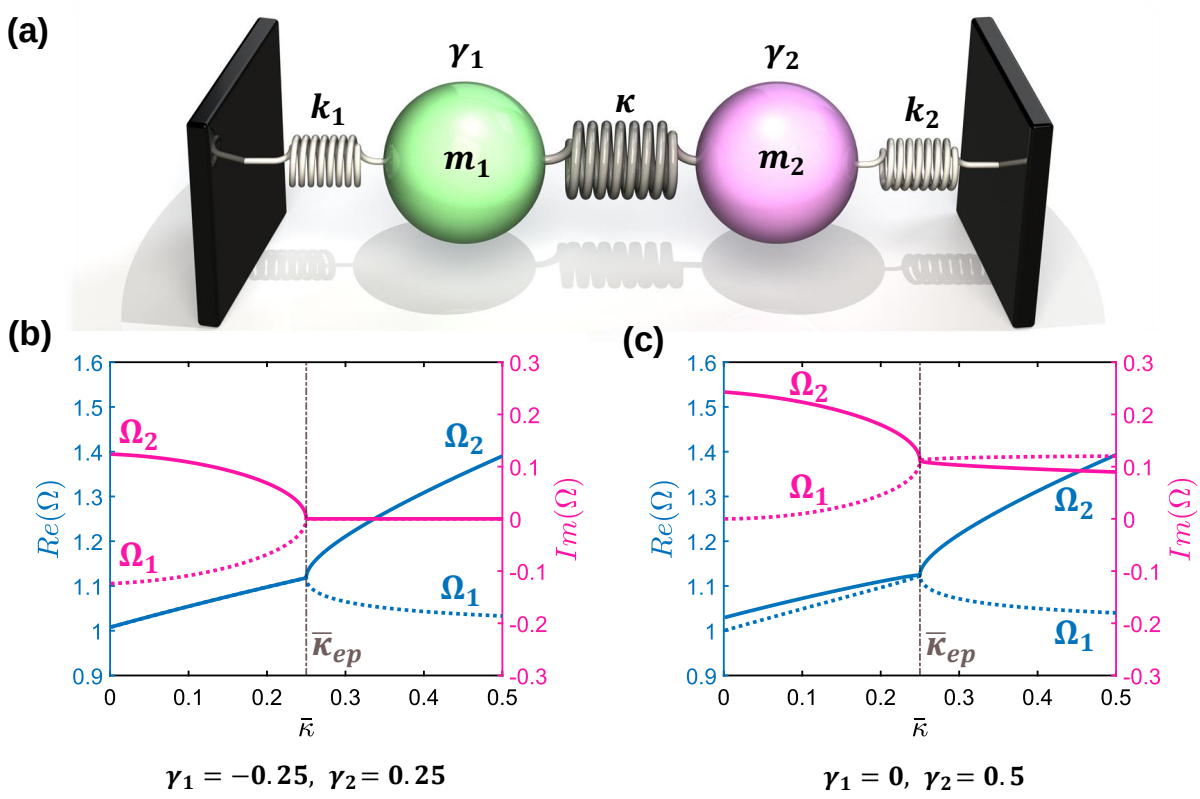

Figure 7.2: (a) A coupled oscillator dimer with differential damping, the green oscillator is less damped than the purple oscillator. (b) Real and imaginary parts of natural frequencies for balanced gain and loss (PT symmetric). (c) Real and imaginary parts of natural frequencies for noLoss-Loss differential damping case (passive non-Hermitian).

In the following sections, we revisit the basics of viscoelastic materials to test the feasibility of using them in creating non-Hermiticity. We individually analyze three different viscoelastic material models to identify the best suited viscoelastic material to create a passive elastodynamic metamaterial that support the formation of an EP. Finally, we report experimentally measured dynamic properties of viscoelastic elastomers—polydimethylsiloxane (PDMS), polyurethane rubber, natural rubber, and polyurethane foam and demonstrate a concept experimental design to achieve EPs.

7.2 Coupled oscillators with differential frictional damping

Discrete coupled oscillators exhibit two individual vibration modes, one in-phase and one out-of-phase. For Hermitian systems, the resonant frequencies of these modes are real and distinct. However, these modes begin interacting with each other when appropriate damping is introduced, resulting in an exceptional point (EP) degeneracy.

The most common source of damping in structures is Coulomb friction, which opposes the relative motion between surfaces. A coupled oscillators system with frictional damping is shown in Figure 7.2(a). Two oscillators of masses m_1 and m_2 and Hookean springs of stiffnesses k_1 and k_2, respectively are mounted on rigid walls and coupled together by another Hookean spring of stiffness κ. Frictional forces of magnitudes $\gamma_1 N_1$ and $\gamma_2 N_2$ are resisting the motion of m_1 and m_2 respectively. Where γ_1, γ_2 are coefficients of friction and N_1, N_2 are the contact forces. The governing equations of motion for the oscillators can be written as

$$m_1\ddot{x_1} + k_1 x_1 + (\gamma_1 N_1) \times sgn(\dot{x_1}) + \kappa(x_1 - x_2) = 0 \tag{7.1}$$

$$m_2\ddot{x_2} + k_2 x_2 + (\gamma_2 N_2) \times sgn(\dot{x_2}) + \kappa(x_2 - x_1) = 0 \tag{7.2}$$

where $x_1(t)$ and $x_2(t)$ are the instantaneous positions of m_1 and m_2 oscillators respectively, and sgn is the signum function, e.g., $sgn\,(\dot{x}_1) = \frac{\dot{x}_1}{|\dot{x}_1|}$. In a system with Coulomb damping, free vibrations undergo a gradual linear decay in oscillations, but it is not possible to arrive at a steady-state solution. Thus, we consider structural damping by assuming $N_1 = k_1 x_1$ and $N_2 = k_2 x_2$, which means that the friction force is due to the structural (or hysteretic) damping property of the spring's constituent material. Considering steady state solutions for x_1 and x_2 i.e., $x_1(t) = X_1 e^{i\omega t}$ and $x_2(t) = X_2 e^{i\omega t}$ which gives $sgn\,(\dot{x}_1) = \frac{i\omega X_1}{|i\omega X_1|} = i = \sqrt{-1}$, where, X_1 and X_2 are the complex amplitudes of vibration of the two individual oscillators. Unlike viscous damping, structural damping is rate-independent. It is usually found in metals, where it arises due to crystal defects and internal friction from grain boundary sliding.

Assuming $m_1 = m_2 = m$ and $k_1 = k_2 = k$ for symmetry, and $\omega_0 = \sqrt{\frac{k}{m}}$, $\Omega = \frac{\omega}{\omega_0}$, and $\bar{\kappa} = \frac{\kappa}{k}$ for making the parameters dimensionless, final equations of motion in matrix form can be written as

$$\begin{bmatrix} -\Omega^2 + 1 + i\gamma_1 + \bar{\kappa} & -\bar{\kappa} \\ -\bar{\kappa} & -\Omega^2 + 1 + i\gamma_2 + \bar{\kappa} \end{bmatrix} \begin{Bmatrix} X_1 \\ X_2 \end{Bmatrix} = 0 \tag{7.3}$$

$$[\mathcal{H}]\,\{\psi\} = 0 \tag{7.4}$$

For non-trivial solutions of eigenvalues (Ω) and eigenvectors $\{\psi\}$, substituting the determinant

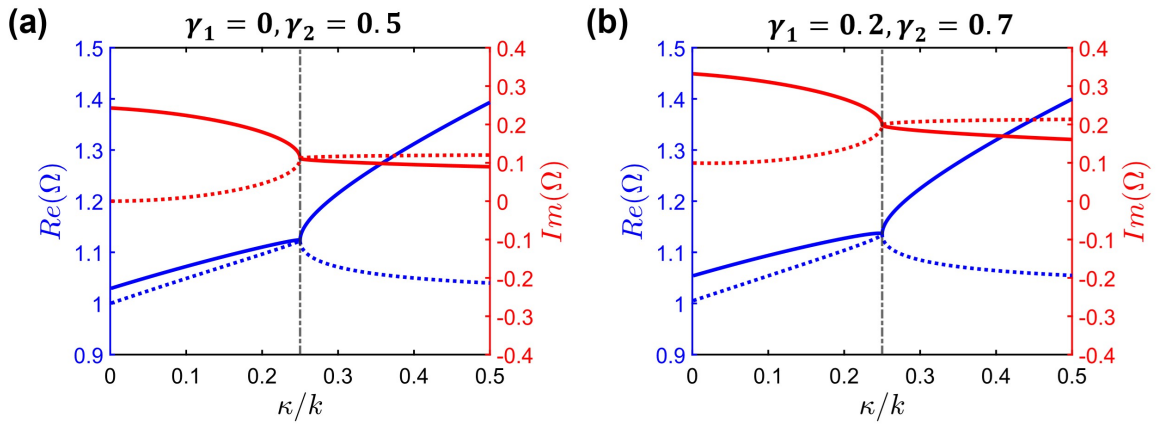

Figure 7.3: Real and imaginary parts of eigenfrequencies for coupled oscillators with differential structural damping. The vertical dotted line represents the location of the exceptional point

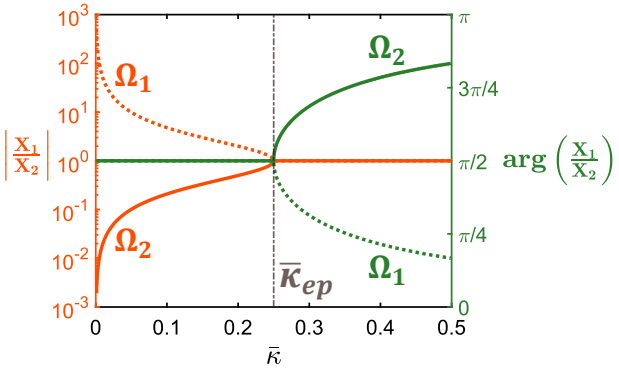

Figure 7.4: (a) Magnitudes and phases of eigenvectors corresponding to both natural frequencies of coupled oscillators dimer with differential structural damping ($\gamma_1 = 0,\ \gamma_2 = 0.5$).

of $[\mathcal{H}]$ equal to 0 yields,

$$\Lambda(\Omega) = \Omega^4 - (2 + i(\gamma_1 + \gamma_2) + 2\bar{\kappa})\,\Omega^2 + 1 + i\,(\gamma_2 + \gamma_1) + i\,(\gamma_1 + \gamma_2)\,\bar{\kappa} + 2\bar{\kappa} - \gamma_1\gamma_2 = 0 \qquad (7.5)$$

Solving the above equation yields the two complex natural frequencies of the system, Ω_1 and Ω_2. In Figure 7.2, we plot the real and the imaginary parts of Ω_1 and Ω_2 as functions of normalized coupling ($\bar{\kappa}$) for both PT-symmetric (Figure 7.2(b)) and passive non-Hermitian (differential loss only) cases (Figure 7.2(c)). To balance the gain and the loss in the PT-symmetric case, we consider $\gamma_1 = -\gamma$ and $\gamma_2 = \gamma = 0.25$. As the coupling increases, an EP emerges at $\bar{\kappa}_{ep} = \gamma$ (refer to Appendix C for derivation). In the passive non-Hermitian case with no gain, we consider the simplest differential-loss condition (zero loss-loss) by assuming $\gamma_1 = 0$ and $\gamma_2 = \gamma = 0.5$. Figure 7.3

shows other cases of differential loss. In such a system, the EP appears at $\bar{\kappa}_{ep} = \frac{\gamma}{2}$ (refer to Appendix C for detailed derivation). Noteworthy is the sharp and orthogonal bifurcation at the EP. Here, sharpness and orthogonality are characterized by a zero gap between the complex natural frequencies i.e., $|\Omega_1 - \Omega_2| = 0$ and a slope of $\tan^{-1}\left(\frac{\partial\Omega}{\partial\bar{\kappa}}\right) \approx \pi/2$ at the EP—which implies that an infinitesimal variation in $\bar{\kappa}$ will result in a large splitting of frequencies (i.e. Ω_2-Ω_1), suitable for highly sensitive EP-based sensors. It is worth highlighting that, unlike the PT-symmetric case (Figure 7.2(b)), where eigenfrequencies are real in the exact-phase ($\bar{\kappa} > \bar{\kappa}_{ep}$) and complex in the broken-phase ($\bar{\kappa} < \bar{\kappa}_{ep}$), eigenfrequencies in the passive non-Hermitian case are always complex. Thus, the Hamiltonian for the passive non-Hermitian case does not need to satisfy the pseudo-Hermitian condition to exhibit an exceptional point [200]. We also observe a similar bifurcation in corresponding eigenvectors $\psi = [X_1/X_2, 1]$ (Figure 7.4) for the passive non-Hermitian case, a hallmark feature of EPs. At the EP, the magnitude of eigenvectors $\left|\frac{X_1}{X_2}\right| \approx 1$ and phase difference $arg\left(\frac{X_1}{X_2}\right) \approx \pi/2$ for both the modes, which suggest that the modes are degenerate. Conclusively, we have shown a viable pathway to realizing an EP degeneracy in a passive (with no gain) physical system with differential loss. Despite the simplicity, the above system with differential structural damping exhibits a sharp EP degeneracy in a 2×2 Hamiltonian system similar to coupled optical waveguides [201], LCR circuits [202], acoustic cavities [203], microwave cavities [204], and quantum harmonic oscillators [205].

7.3 Viscoelastic solids as dissipative elements

While structural damping is the simplest model for material damping, it is not the most common type of damping present in engineering materials that are used in applications requiring damping. Usually, engineering materials exhibit viscous damping, which is intrinsically connected to materials' elastic properties, making the materials viscoelastic [47, 199]. In contrast to structural damping, where the stiffness and damping parameters $(k_1, k_2, \gamma_1, \gamma_2)$ are constants, viscoelastic materials are rate dependent. Viscoelastic materials distinctively exhibit a time decaying relaxation modulus ($E(t) = E_\infty + E_t(t)$) whose Fourier transform gives a complex dynamic modulus with frequency dependent real and imaginary parts ($E_d(\omega) = E'(\omega) + iE''(\omega)$). The real part $E'(\omega)$ is called the storage modulus, which is associated with the amount of elastic energy that the material

Table 7.1: Relaxation and dynamic moduli of KV solid, SLS and KVFD solid.

	Kelvin-Voigt (KV)	**Standard Linear Solid (SLS)**	**Kelvin-Voigt fractional derivative (KVFD**
Relaxation Modulus	$E_\infty + \eta\hat{\delta}(t)$	$E_\infty + E_t e^{-\frac{t}{\tau}}$	$E(t) = E_\infty + \eta\frac{1}{\Gamma(1-\alpha)}t^{-\alpha}$
Dynamic Modulus	$E_\infty + i\omega\eta$	$E_\infty + E_t\frac{\omega^2\tau^2}{1+\omega^2\tau^2} + iE_t\frac{\omega\tau}{1+\omega^2\tau^2}$	$E_\infty + \eta\omega^\alpha\left(\cos\left(\frac{\pi}{2}\alpha\right) + i\sin\left(\frac{\pi}{2}\alpha\right)\right)$

stores under deformation. The imaginary part $E''(\omega)$ is called the loss modulus, which is associated with the energy that the material dissipates under cyclic loading. The ratio $\tan(\delta) = \frac{E''(\omega)}{E'(\omega)}$, known as the loss-tangent, is a quantitative measure of the damping capacity of a viscoelastic material.

To realize the non-Hermitian metamaterial, we replace the structurally damped spring of the coupled oscillators model with a viscoelastic material of dynamic modulus $E_d(\omega)$, cross-sectional area A, and length L (Figure 7.7(a)). The resultant dynamic stiffness of the material is given by $k_d(\omega) = E_d(\omega)\frac{A}{L}$. The modified governing equations for the non-Hermitian metamaterial with viscoelastic damping elements in frequency domain can be written as,

$$-\Omega^2 X_1 + X_1 + \bar{\kappa}(X_1 - X_2) = 0 \tag{7.6}$$

$$-\Omega^2 X_2 + \frac{k_d(\Omega)}{k}X_2 + \bar{\kappa}(X_2 - X_1) = 0 \tag{7.7}$$

where X_1 and X_2 are complex amplitudes, $\bar{\kappa} = \frac{\kappa}{k}$, $\Omega = \frac{\omega}{\omega_0}$, $\omega_0 = \sqrt{\frac{k}{m}}$, and k is the stiffness of Hookean spring (non-lossy) as shown in Figure 7.7(a).

We investigate three different models of viscoelastic materials in comparison: the Kelvin-Voigt (KV) model, the Standard Linear Solid (SLS), and the Kelvin-Voigt fractional derivative (KVFD) model. The relaxation moduli and the corresponding frequency-dependent dynamic moduli of the three viscoelastic materials are listed in Table 7.1.

7.3.1 Kelvin-Voigt (KV) materials

Kelvin-Voigt is the simplest model of a viscoelastic solid. It consist of a spring and a newtonian dashpot in parallel combination (Figure 7.7(b)). Under sinusoidal loading, the complex dynamic

modulus of the KV solid is given by

$$E_d = E_\infty + i\omega\eta \tag{7.8}$$

where, E_∞ is the modulus of the spring, η is the viscous damping coefficient and ω is the frequency of the dynamic load. Notably, KV materials exhibit a frequency-independent storage modulus (E_∞) and a loss modulus ($\omega\eta$) that is linearly dependent on frequency. Assuming $k = E_\infty \frac{A}{L}$ for symmetry in real part of stiffness and $\frac{A}{L}\frac{\eta}{m\omega_0} = \gamma$ as the dimensionless damping coefficient, the governing equations can be written in matrix form as follows

$$\begin{bmatrix} -\Omega^2 + 1 + i\Omega\gamma_1 + \bar{\kappa} & -\bar{\kappa} \\ -\bar{\kappa} & -\Omega^2 + 1 + i\Omega\gamma_2 + \bar{\kappa} \end{bmatrix} \begin{Bmatrix} X_1 \\ X_2 \end{Bmatrix} = 0 \tag{7.9}$$

Here, we first consider the PT-symmetric case ($\gamma_1 = -\gamma, \gamma_2 = \gamma$). To balance with loss, the gain must also be linearly dependent on frequency. Physical example of such gain is self-excitation of spring-block on a moving conveyor due to velocity-dependent friction coefficient [206]. On putting the determinant of the Hamiltonian matrix in Eq. 7.9 equal to zero and solving for Ω, we observed a sharp EP at $\bar{\kappa}_{ep} = \frac{1}{2}(\gamma^2 + 2\gamma)$ (Figure 7.5(a,b)) [195], with eigen frequencies very similar to the PT-symmetric case in structural damping (Figure 7.2(b)). For the passive non-Hermitian case ($\gamma_1 = 0, \gamma_2 = \gamma$), the real and imaginary parts of the complex natural frequencies Ω_1 and Ω_2 are plotted as functions of $\bar{\kappa}$ in Figure 7.7(b). Contrary to the structural damping case, the passive non-Hermitian metamaterial made of a KV material does not exhibit a sharp EP bifurcation. Instead, we observe a region of approximate transition [195, 196] where the modes gradually bifurcate. In this region, we identify that for a particular coupling of $\bar{\kappa}_c \approx \frac{1}{4}\left(\frac{2}{5}\gamma^2 + 2\gamma\right)$ (Figure 7.5(c,d)), the eigenfrequencies make the closest approach without merging such that the gap between them i.e., $|\Omega_1 - \Omega_2|$ is minimum (Figure 7.5(c)). We hypothesize that the indistinct EP transition observed here (Figure 7.7(b)) is due to a strong linear dependence of $\tan(\delta)$ on the frequency, i.e., to achieve a sharp EP bifurcation, $\tan(\delta)$ should converge to a constant value as a function of frequency (Figure 7.6). Strong dependence of $\tan(\delta)$ on frequency in KV solid is associated with dirac delta function ($\hat{\delta}(t)$) in the transient part of the relaxation modulus (Table 7.1), which indicates that material relaxes abruptly at $t = 0$ and does not relax further afterwards ($\hat{\delta}(t > 0) = 0$). To test our hypothesis of the effect of frequency dependent $\tan(\delta)$, we next investigate SLS and KVFD

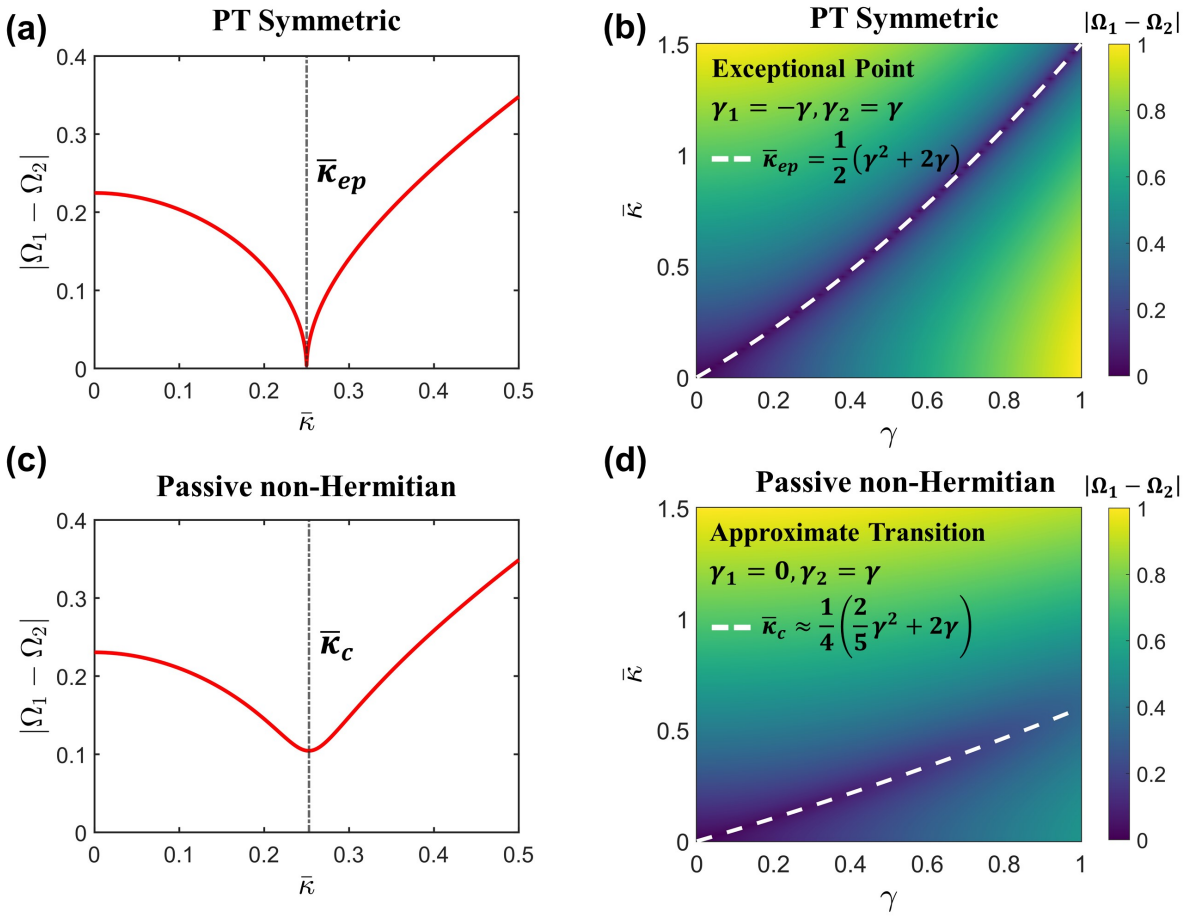

Figure 7.5: Magnitude of the difference between the complex eigenfrequencies as a function of normalized coupling for PT symmetric ($\gamma = 0.225$) (a) and passive non-Hermitian case ($\gamma = 0.458$) (c). Magnitude of the difference between the complex eigenfrequencies (colorbar) as a function of the coupling $\bar{\kappa}$ and the damping parameter γ for PT-symmetric system (b) with balanced Kelvin-Voigt gain and loss and passive non-Hermitian system (d) with differential loss. The relationship between $\bar{\kappa}_{ep}$ (location of the exceptional point) and γ for PT-symmetric case and $\bar{\kappa}_c$ (location of the closest approach) and γ are shown using white dashed lines.

viscoelastic solids, which undergo stress relaxation for longer durations.

7.3.2 Standard Linear Solid (SLS) materials

The SLS is a viscoelastic material model consisting of a spring connected in parallel to a Maxwell element (a spring and a dashpot in series) as shown in Figure 7.7(c). The relaxation modulus of SLS decays exponentially with time, and corresponding storage and loss moduli are both frequency-dependent (Table 7.1). Assuming E_∞ and E_t as the moduli of springs, η as the damping coefficient of the dashpot and $\tau = \frac{\eta}{E_t}$ as the relaxation time, the dynamic modulus can be written as,

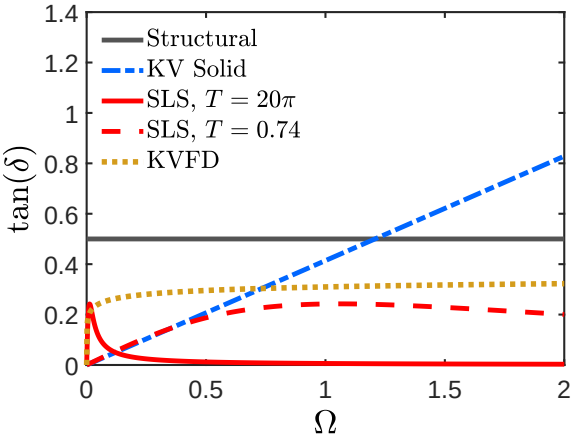

Figure 7.6: (a) Loss tangent ($\tan(\delta)$) as a function of frequency for structural damping ($\gamma = 0.5$), KV solid ($\gamma = 0.41$), SLS $\left(\frac{k_\infty}{k} = 0.81, \frac{k_t}{k} = 0.50, T = 20\pi\right)$, SLS $\left(\frac{k_\infty}{k} = 0.81, \frac{k_t}{k} = 0.50, T = 0.74\right)$ and KVFD solid $\left(\frac{k_\infty}{k} = 0.25, \frac{\gamma}{k} = 0.80, \alpha = 0.25, \omega_0 = 1315\pi\right)$

$$E_d(\omega) = E_\infty + E_t \frac{\omega^2\tau^2}{1+\omega^2\tau^2} + iE_t \frac{\omega\tau}{1+\omega^2\tau^2} \tag{7.10}$$

Assuming $k_\infty = E_\infty \frac{A}{L}$, $k_t = E_t \frac{A}{L}$, $\Omega = \frac{\omega}{\omega_0}$, $\omega_0 = \sqrt{\frac{k}{m}}$, and $T = \omega_0\tau$ (dimensionless relaxation time), the normalized dynamic stiffness can be written as,

$$\frac{k_d(\Omega)}{k} = \frac{1}{k}\left(k_\infty + k_t \frac{\Omega^2 T^2}{1+\Omega^2 T^2} + ik_t \frac{\Omega T}{1+\Omega^2 T^2}\right) \tag{7.11}$$

Since it is physically not possible to create gain and maintain symmetry in materials systems with the real part of modulus also frequency dependent, from here onwards, we only investigate passive non-hermitian systems with differential loss (noLoss-Loss). On substituting Eq. (7.11) in Eqs. (7.6,7.7) and solving for Ω, we obtain two resonant frequencies Ω_1, Ω_2. The real and imaginary parts of Ω_1 and Ω_2 are plotted in Figure 7.7(c). In this case, we didn't observe any EP formation for all reasonable values of material parameters. An EP only starts to appear when T is very small ($T < 1$), which is physically not possible. In Figure 7.6, comparison of $\tan(\delta)$ for $T = 20\pi$ and $T = 0.74$ indicates that, for shorter relaxation times, the $\tan(\delta)$ has a plateau like regime and is almost constant for $\Omega \approx 1$ resulting in the formation of an exceptional point (Figure 7.12). However, for longer relaxation times, the $\tan(\delta)$ quickly decays to almost zero, making the imaginary part of the dynamic modulus so small to show any effect. Supposedly, a material model representing a

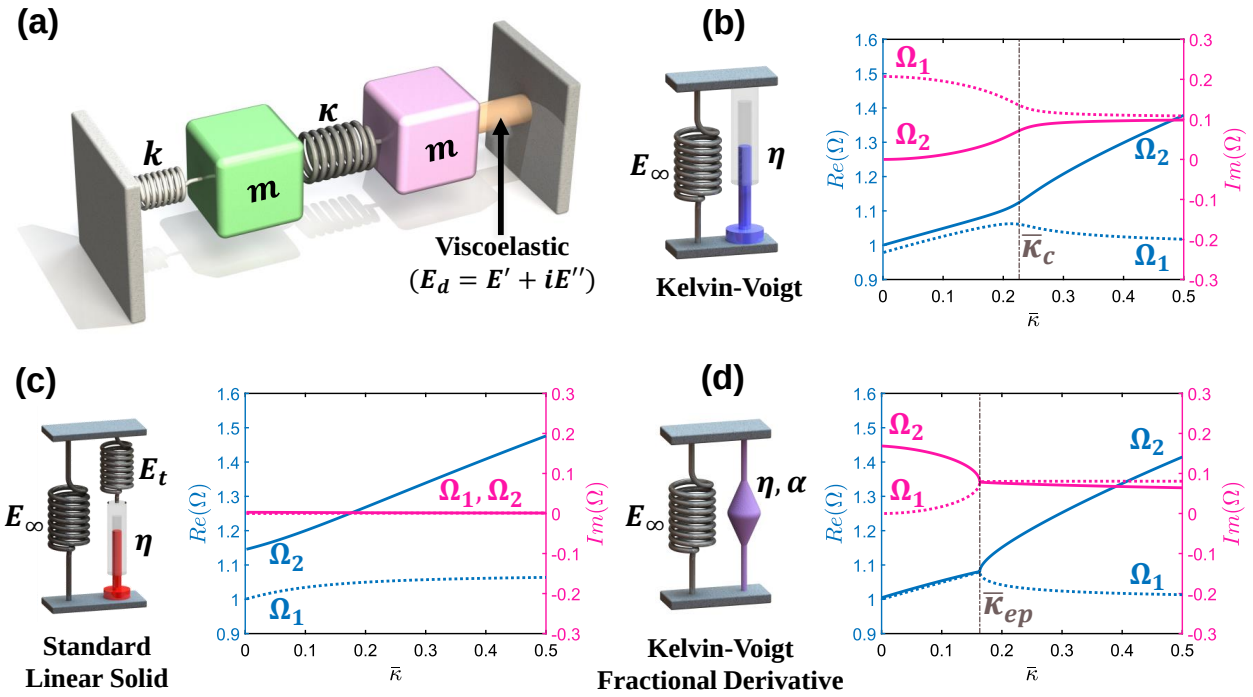

Figure 7.7: (a) Coupled oscillators dimer with differential loss achieved by a Hookean spring of stiffness k and a viscoelastic material of dynamic modulus E_d, cross-sectional area A and length L. Physical representations and corresponding plots of real and imaginary parts of natural frequencies for (b) KV solid ($\gamma = 0.41$), (c) SLS $\left(\frac{k_\infty}{k} = 0.81, \frac{k_t}{k} = 0.50, T = 20\pi\right)$, and (d) KVFD solid $\left(\frac{k_\infty}{k} = 0.25, \frac{\gamma}{k} = 0.80, \alpha = 0.25, \omega_0 = 1315\pi\right)$ as functions of coupling.

weighted sum of multiple relaxation times—both short and long—will resolve this issue. Usually, experimental measurements of relaxation modulus of viscoelastic materials are best described by a prony series, a sum of exponentials physically represented by the generalized Maxwell (GM) model [207–209]. The GM model is similar to SLS model with multiple Maxwell elements connected in parallel, resulting in a discrete spectrum of relaxation times [47, 199]. Relaxation modulus $E(t)$ and dynamic modulus $E_d(\omega)$ for the GM model can be written as,

$$E(t) = E_\infty + \sum_{m=1}^{M} E_m e^{-\frac{t}{\tau_m}} \tag{7.12}$$

$$E_d(\omega) = E_\infty + \sum_{m=1}^{M} \left(E_m \frac{\omega^2 \tau_m^2}{1 + \omega^2 \tau_m^2} + i E_m \frac{\omega \tau_m}{1 + \omega^2 \tau_m^2} \right) \tag{7.13}$$

However, fitting these many terms to experimental data is neither practical nor desirable. So, a power law relaxation function $(E(t) = E_\infty + E_\alpha t^{-\alpha})$ is generally used for materials which relaxes

over a large spectrum of relaxation times [210–213]. For sufficient number of terms, the prony series (7.12) is approximately equivalent to a shifted power law relaxation function $E(t) = E_\infty + E_\alpha(t + t_l)^{-\alpha}$ ($t_l \geq 0,\ 0 < \alpha < 1$) as follows (more details in Appendix B),

$$E_\infty + E_\alpha(t + t_l)^{-\alpha} = E_\infty + \frac{E_\alpha}{\Gamma(\alpha)} \int_0^\infty \left(e^{-\frac{t_l}{\tau}} \frac{1}{\tau^{\alpha+1}} \right) e^{-\frac{t}{\tau}} d\tau \tag{7.14}$$

where Γ is the gamma function. Eq. (7.14) can be converted into an approximate discrete sum using trapezoidal rule as follows

$$E_\infty + E_\alpha(t + t_l)^{-\alpha} \approx E_\infty + \sum_{m=1}^{M\to\infty} E_m e^{-\frac{t}{\tau_m}} \tag{7.15}$$

$$E_m = \frac{E_\alpha}{\Gamma(\alpha)} \begin{cases} 0.5 \times e^{-\frac{t_l}{\tau_m}} (\tau_m)^{-(\alpha+1)} \times (\tau_{m+1} - \tau_m) & m = 1 \\ 0.5 \times e^{-\frac{t_l}{\tau_m}} (\tau_m)^{-(\alpha+1)} \times (\tau_{m+1} - \tau_{m-1}) & 1 < m < M \\ 0.5 \times e^{-\frac{t_l}{\tau_m}} (\tau_m)^{-(\alpha+1)} \times (\tau_m - \tau_{m-1}) & m = M \end{cases} \tag{7.16}$$

where, $\tau_m = \tau_1, \tau_2, \tau_3 ..... \tau_M$ are relaxation times and E_m are corresponding coefficients of a discrete relaxation spectrum $\hat{H}(\tau)$ given by [47]

$$\hat{H}(\tau) = \sum_{m=1}^{M} \tau E_m \hat{\delta}(\tau - \tau_m) \tag{7.17}$$

Eqs. (7.15, 7.16) suggests that instead of using prony series, the simpler power-law relaxation modulus can be used to model realistic viscoelastic materials [212, 214–216]. Physical representation of power-law relaxation is the Kelvin-Voigt fractional derivative (KVFD) model. Thus, in the next section, we investigate the possibility of achieving an EP using KVFD solid as the non-Hermitian element.

7.3.3 Kelvin-Voigt fractional derivative (KVFD) materials

The KVFD solid is similar to the KV solid with a springpot replacing the dashpot. Springpot represents an interpolation between a spring and a dashpot. For an applied strain ϵ, the stress response of a springpot will be $\sigma = \eta \frac{d^\alpha \epsilon}{dt^\alpha}$, where, $0 \leq \alpha \leq 1$, with $\alpha = 1$ indicating a dashpot and $\alpha = 0$ indicating a spring. The KVFD model we have consider here consists of a sprintpot

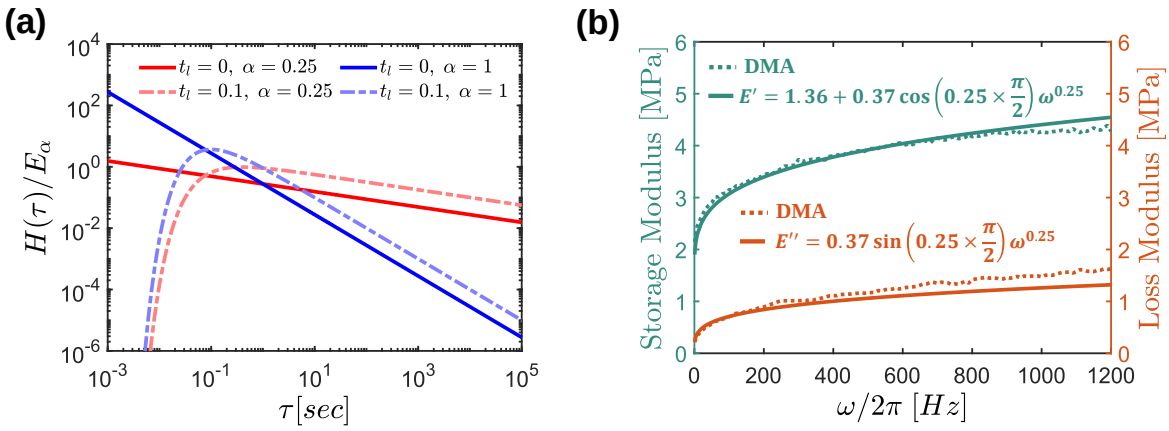

Figure 7.8: (a) Normalized relaxation spectrums for different combinations of t_l and α. (b) Experimentally measured storage and Loss modulus of Polydimethylsiloxane (PDMS) as functions of excitation frequency by performing the dynamic mechanical analysis (DMA). Best-fit power-law curves indicate that PDMS follows the KVFD model.

connected in parallel to a spring (Figure 7.7(d)). Usually one or two springpots in parallel are sufficient to accurately model both transient and dynamic behavior of a viscoelastic material [214].

The relaxation modulus of KVFD solid obeys a power-law decay as follows,

$$E(t) = E_\infty + E_\alpha t^{-\alpha}\,, \quad E_\alpha = \frac{\eta}{\Gamma(1-\alpha)}. \tag{7.18}$$

Sometimes, a more general function—shifted power law ($E(t) = E_\infty + E_\alpha(t+t_l)^{-\alpha}$) is used to avoid the divergence of the transient term at $t = 0$. From Eq. (7.14), we can extract the relaxation spectrum $H(\tau)$ as follows

$$E_\infty + E_\alpha(t+t_l)^{-\alpha} = E_\infty + \int_0^\infty H(\tau)\, e^{-\frac{t}{\tau}}\, \frac{d\tau}{\tau}\,, \quad H(\tau) = \frac{E_\alpha}{\Gamma(\alpha)} e^{-\frac{t_l}{\tau}} \frac{1}{\tau^\alpha} \tag{7.19}$$

In contrast to GM model (7.17), relaxation spectrum for power law model (7.19) is continuous. In Figure 7.8(a), the normalized relaxation spectrum of the power law ($H(\tau)/E_\alpha$) is plotted as a function of relaxation time for different combinations of α and t_l. For $\alpha = 1$ and $t_l = 0$ (KV solid), shorter relaxation times are more dominant as compared to longer, which is the reason why KV solid undergoes an abrupt relaxation at $t = 0$. For $t_l > 0$ (shifted power law), the relaxation spectrum peaks at $\tau = t_l/\alpha$, but decays in both directions from the peak. For $t_l = 0$ and $\alpha = 0.25$ (KVFD), both shorter and longer relaxation times dominate. The effect of such relaxation behavior

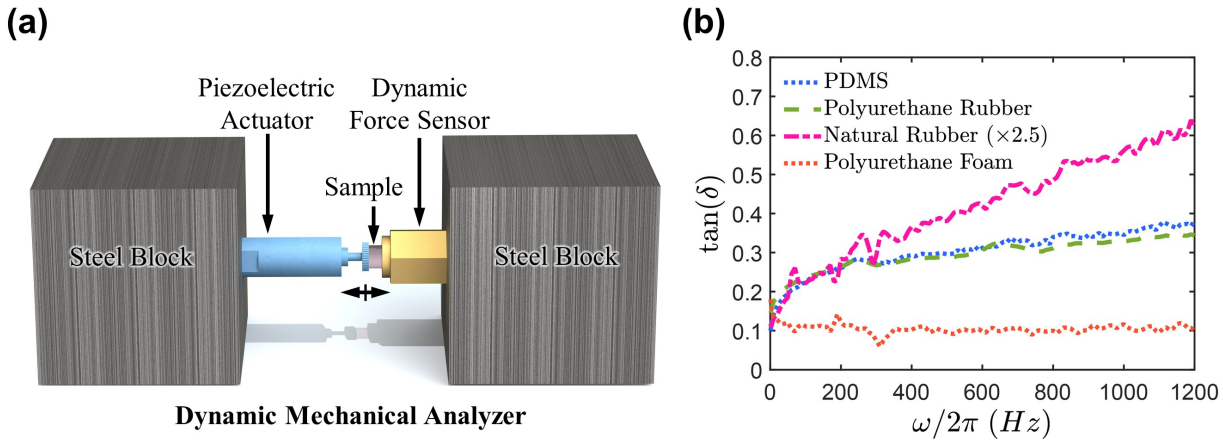

Figure 7.9: (a) Custom built dynamic mechanical analyzer consisting of a piezoelectric actuator (P841.10 Physik Instrumente) and a dynamic ICP force sensor (PCB 208C01) (b) Comparison of frequency-dependent loss-tangent between PDMS, Polyurethane rubber, Natural rubber, and Polyurethane foam. To provide a better comparison, we scale the loss tangent of natural rubber by 2.5 times.

can be observed in the loss-tangent (Figure 7.6), which stays almost constant for higher frequencies, making KVFD materials a potential choice for achieving EPs.

The normalized dynamic stiffness (Table 7.1) for the KVFD solid shown in Figure 7.7(d) can be written as,

$$\frac{k_d(\Omega)}{k} = \frac{1}{k}\left(k_\infty + \gamma\Omega^\alpha \cos\left(\frac{\pi}{2}\alpha\right) + i\gamma\Omega^\alpha \sin\left(\frac{\pi}{2}\alpha\right)\right) \tag{7.20}$$

where $k_\infty = E_\infty \frac{A}{L}$, $\gamma = \eta{\omega_0}^\alpha \frac{A}{L}$, $\Omega = \frac{\omega}{\omega_0}$ and $\omega_0 = \sqrt{\frac{k}{m}}$. Substituting Eq. (7.20) in Eqs. (7.6,7.7) and solving for Ω gives two converging solutions, Ω_1 and Ω_2. Figure 7.7(d) shows the real and imaginary parts of both natural frequencies undergoing a sharp EP bifurcation. The characteristics of bifurcation near the EP for KVFD material are similar to the structural damping case described earlier (Figure 7.10). Analogous to strcutural damping, for KVFD, $tan(\delta)$ is almost constant and coverges to $\tan\left(\frac{\pi}{2}\alpha\right)$ as $\Omega \to \infty$. This verifies our hypothesis that for a sharp EP bifurcation to occur, the $\tan(\delta)$ should not diverge with frequency and should stay almost constant in the frequency range of interest. It is important to note that although exceptional points (EPs) are single-frequency phenomena, the occurrence of sharp bifurcation relies on the behavior of $\tan(\delta)$ in the surrounding frequency range. Remarkably, compared to structural damping, which is rarely observed in engineering materials, many soft polymers and biological materials exhibit viscoelastic

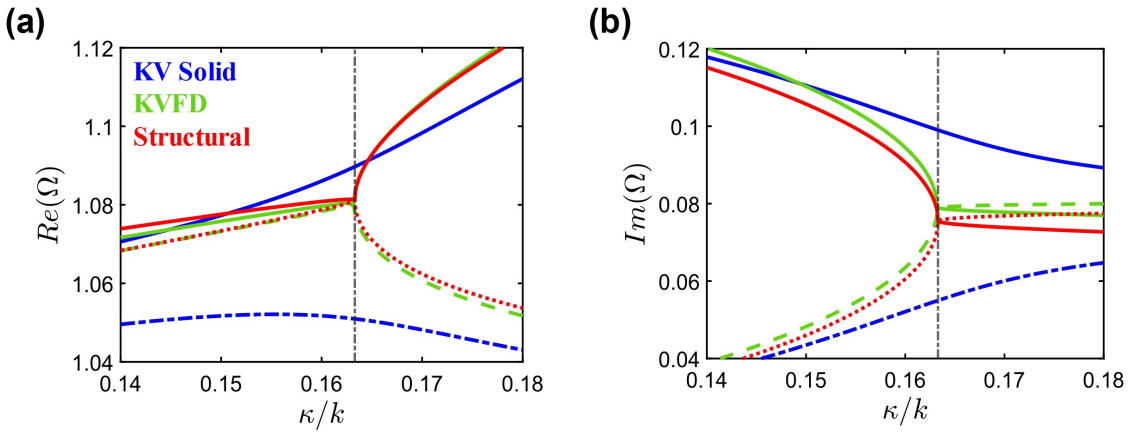

Figure 7.10: Comparison of real (a) and imaginary (b) parts of eigenfrequencies (zoomed-in view of the degeneracy region) for coupled oscillators with Kelvin-Voigt, Kelvin-Voigt fractional derivative, and structurally damped solid as the dissipative element.

behavior that is best described by fractional derivative models. Figure 7.8(b) shows the storage and loss modulus of PDMS (Sylgard 184, 1:20 ratio of curing agent to liquid elastomer) that we measured experimentally by performing the dynamic mechanical analysis (DMA) on our custom built dynamic mechanical analyzer (Figure 7.9(a)). It strongly follows the KVFD model with parameters $\alpha = 0.25$, $E_\infty = 1.36$, $\eta = 0.37$ (refer to Appendix C for details on DMA).

In Figure 7.9(b), we compare the frequency-dependent loss tangent of PDMS, polyurethane rubber, natural rubber, and polyurethane foam that we measured using DMA. PDMS and polyurethane rubber display a gradual dependence on the frequency, while polyurethane foam exhibits no dependence of $\tan(\delta)$ on frequency. Both of these characteristics are suitable for creating a sharp exceptional point. However, natural rubber demonstrates a strong dependence on frequency, making it unsuitable for the intended purpose. Therefore, the utilization of elastomers such as PDMS and polyurethane rubber, as well as foams like polyurethane foam, in passive non-Hermitian systems enables the realization of sharp EPs experimentally. However, it should be noted that the low elastic modulus of foams leads to a lower ratio of elastic stiffness to the mass of the oscillator. Consequently, the usage of foams in non-Hermitian systems will be limited to very low-frequency ranges. Furthermore, the densification of the foam under significant compression strains causes a steep increase in modulus due to nonlinearity. This situation presents challenges in preserving the parity symmetry within the stiffness matrix. In our previous work, we experimentally demonstrated an EP in a passive dynamical system with PDMS serving as the damping component [40].

The occurrence of EP in experiments is highly sensitive to even the slightest variations in the symmetry of the real part of the stiffness. Therefore, it is essential to precisely characterize the frequency-dependent storage and loss modulus of the viscoelastic material. To achieve this, we conducted precise measurements of the PDMS's frequency-dependent storage and loss modulus using our custom-built dynamic mechanical analyzer (see Figure 7.9(a) and Appendix C). To conduct DMA experiments, we initially apply a static precompression stress to secure the sample and carry out local sinusoidal small-strain dynamics to measure the dynamic mechanical properties. It is noteworthy that, due to potential nonlinearities, the storage and loss modulus can vary based on the initial precompression. Therefore, when experimentally characterizing the EP, the precompression stress applied to the system must be identical to the stress applied to the viscoelastic material (PDMS in our case) for measuring the frequency-dependent storage and loss modulus. In contrast to prior studies focusing on enhanced sensitivity, in this study, we demonstrated that the actuation forces (emissivity) can be amplified at the proximity to the EPs [40]. Notably, a two fold enhancement of the applied force is achieved using entirely passive dissipative non-Hermitian system, when it operates near the EP compared to far away from EP.

In experiments, the real and imaginary parts of eigenfrequencies can be characterized by measuring the frequency response of the system under sinusoidal excitation. Figure 7.11(a) shows our model system under forced vibration with the left boundary being driven by applying a sinusoidal displacement $u(t) = Ue^{i\omega t}$. The two oscillators are coupled together by a tunable spring whose stiffness can be adjusted to change the coupling. The required differential-damping is achieved by a Hookean spring of stiffness k (no-Loss) and a PDMS cylinder of area A, length L, and dynamic modulus E_d (Loss) (Figure 7.8(b)).

We assume, $m = 4.635\ g$, $A = 28.27\ mm^2$ (6 mm diameter) and $L = 1.95\ mm$. For the known dynamic stiffness of PDMS ($k_d = \frac{E_d A}{L}$), we estimated the corresponding required optimal stiffness of Hookean spring (k) by minimizing the gap between the resonant frequencies ($|\omega_1 - \omega_2|$) such that the bifurcation at EP is sharpest (Figure 7.11(b)). Theoretically calculated, real (ω_r) and imaginary parts (ω_i) of resonant frequencies are plotted in Figure 7.11(c, d) in the parameter space of κ and k. For $k = 79.12\ kN/m$, the gap between the two natural frequencies approaches almost zero at the EP, which is an indication of a sharp bifurcation. Figure 7.11(e) shows the theoretical frequency response of the second oscillator, a sharp bifurcation of a single narrow resonant peak at

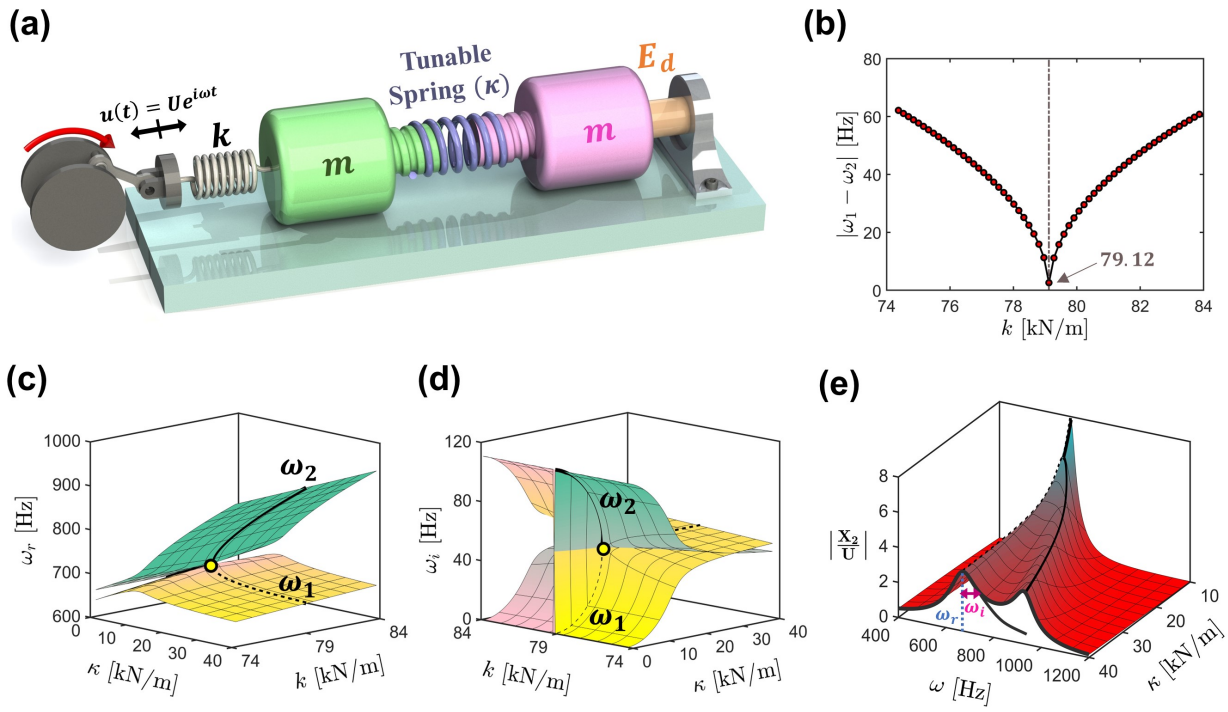

Figure 7.11: (a) Coupled oscillators with driven left boundary by a sinusoidal actuation. The oscillators are coupled together by a spring of tunable stiffness. (b) Absolute gap between eigen frequencies at the EP is minimized by selecting a Hookean spring of optimal stiffness. (c, d) Real (ω_r) and imaginary parts (ω_i) of natural frequencies (ω_1, ω_2) are plotted against coupling for various values of k. A sharp exceptional point appears for optimized value of k. (e) For the optimized system, normalized forced vibration amplitude of second oscillator is plotted as a function of frequency for a range of values of coupling. At each coupling, real and imaginary parts of eigen frequencies can be estimated by fitting the resonance pulse and identifying its peak position and pulse width at $1/\sqrt{2}$ of pulse height respectively.

low couplings ($\kappa < \kappa_{ep}$) into two broad peaks of same linewidth at higher couplings ($\kappa > \kappa_{ep}$). From the frequency response, the real part of resonant frequencies can be estimated from the position of resonant peaks and the imaginary part by measuring the half-width of the peak at $1/\sqrt{2}$ of peak height (Figure 7.11(e)).

7.4 Conclusion

In this work, we investigated the viability of achieving sharp orthogonal EP branch-point singularities in passive non-Hermitian systems with viscoelastic materials serving as the dissipative component. Using a coupled oscillators as the model system, we compared different viscoelastic solids with the general rate-independent hysteretic damping to identify the requisites on frequency-

dependent dynamic properties for the creation of an elastodynamic metamaterial that support the formation of an EP. We show that for an EP to form, the loss-tangent of viscoelastic material should stay almost constant in the frequency range of operation—a characteristic encoded in the relaxation spectrum of the material. Our work provides a critical framework to design passive (without gain) non-Hermitian systems by using viscoelastic materials for realizing non-Hermiticity. It paves the way for the development of passive non-Hermitian devices for sensing, actuation, and energy-harvesting.

Acknowledgements

We acknowledge the financial support from the Solid Mechanics program of the U.S. Army Research Office (award number: W911NF2010160) and the Dynamics, Controls, and System Diagnostics program of the National Science Foundation (NSF-CMMI-1925530). We also acknowledge the support of Dr. Jizhe Cai in fabricating PDMS samples.

Effect of relaxation time in SLS model on eigen frequencies

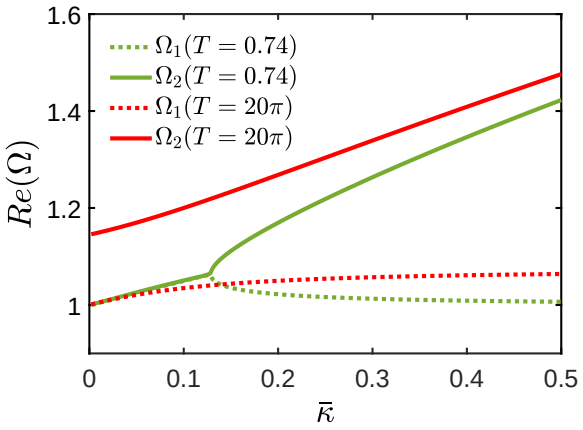

Figure 7.12: Real part of natural frequencies for $T = 0.74$ and $T = 20\pi$

Equivalence of generalized Maxwell model and Kelvin-Voigt fractional derivative model

Kelvin-Voigt fractional derivative (KVFD) model undergoes power-law stress relaxation in the time-domain, whereas the generalized Maxwell model is a sum of decaying exponentials. A power law decay can be converted to an approx sum of weighted exponentials as follows

Consider the following Laplace transform ($\mathcal{L}(f(x)) \rightarrow F(s)$)

$$\mathcal{L}\left(\frac{e^{cx}x^{\alpha-1}}{\Gamma(\alpha)}\right) = \frac{1}{(s-c)^{\alpha}} \tag{7.21}$$

$$\frac{1}{(s-c)^{\alpha}} = \frac{1}{\Gamma(\alpha)}\int_0^{\infty} e^{cx}x^{\alpha-1}e^{-sx}dx \tag{7.22}$$

Changing variables $s \rightarrow t$ and $c \rightarrow -t_l$ ($t_l > 0$)

$$(t+t_l)^{-\alpha} = \frac{1}{\Gamma(\alpha)}\int_0^{\infty} e^{-t_l x}x^{\alpha-1}e^{-tx}dx \tag{7.23}$$

Multiplying E_α and adding E_∞ on both sides

$$E_\infty + E_\alpha(t+t_l)^{-\alpha} = E_\infty + \frac{E_\alpha}{\Gamma(\alpha)}\int_0^{\infty} e^{-t_l x}x^{\alpha-1}e^{-tx}dx \tag{7.24}$$

Changing variable $x \rightarrow \frac{1}{\tau}$

$$E_\infty + E_\alpha(t+t_l)^{-\alpha} = E_\infty + \frac{E_\alpha}{\Gamma(\alpha)}\int_0^{\infty}\left(e^{-\frac{t_l}{\tau}}\frac{1}{\tau^{\alpha}}\right)e^{-\frac{t}{\tau}}\left(\frac{1}{\tau}d\tau\right) \tag{7.25}$$

Dynamic Mechanical Analysis

We perform dynamic mechanical analysis (DMA) using our custom-built dynamic mechanical analyzer, which consists of a preloaded piezoelectric actuator (Physik Instrumente P841.10) and a dynamic force sensor (PCB 208C01) (Figure 7.9(a)). To conduct DMA experiments, we first attach the sample between the actuator and the force sensor and apply a static precompression strain to

hold the sample in place. Using a MATLAB script and an NI data acquisition board, we supply a sinusoidal input voltage with a specific frequency and amplitude to the actuator. The resulting vibration of the actuator's tip causes a sinusoidal compression and decompression of the sample. The dynamic force sensor measures the sinusoidal force response of the sample. The tangent of the phase shift between the transient force and displacement signals represents the loss tangent of the material. We perform a frequency sweep from 0.1 Hz to 1200 Hz to calculate the loss tangent as a function of excitation frequency.

Chapter 8

Actuation enhancement at EP

This chapter is adopted from the following publication

Gupta, A., Kurnosov, A., Kottos, T., & Thevamaran, R. (2023). Reconfigurable enhancement of actuation forces by engineered losses in non-Hermitian metamaterials. Extreme Mechanics Letters, 59, 101979.

Author Contributions : AG performed the numerical simulations and designed, fabricated, performed the experiments, analyzed the data, and prepared the figures. AK performed the theoretical analysis, TK proposed the theoretical concept and RT conceptualized the experimental design. TK wrote the paper with input from all authors.

This chapter focuses on the experimental realization of exceptional point in passive elastic system of coupled oscillators with viscoelasticity and its ramification in achieving an enhancement of applied actuation force with constant Q-factor.

8.1 Introduction

Unusual wave phenomena associated with phononic crystals and locally resonant metamaterials have been utilized for various engineering applications from tunable acoustic bandgaps [179, 181] to wave rectification [180], cloaking [217], and non-reciprocal and topological wave guides [218, 219]. On the other hand, the unveiled wealth of underlying mathematical structures of the non-Hermitian wave systems [220, 221] and their utilization in new technologies have flourished over the

last few years. The non-Hermitian notions have influenced various areas of physics and engineering such as optics and photonics [26, 188], RF and microwaves [177, 222, 223], optomechanics [224], acoustics [35, 174], physics of cold atoms [225], magnonics [226, 227], and most recently elastodynamics [29, 169–173]. Consequently, new concepts have been developed and realized in these frameworks. Examples include a loss-induced transparency [228], unidirectional invisibility [229], asymmetric transport with frequency purity [174], parity-time-symmetric lasers [230, 231], hypersensitive sensors [27, 190, 232–234], etc. Many of these phenomena are reliant on the existence of EPDs. Their implementation requires judicious design of attenuation (and/or amplification) and impedance profiles that lead to enhanced wave-matter interactions.

As opposed to many of these previous studies that emphasized the topology of the eigenfrequency surfaces in the parameter space near an EPD, here we exploit phenomena intimately related to the eigenvector coalescence at EPDs [221] and its ramifications in the shape of the Local Density of States (LDoS). The latter has recently attracted a lot of attention in the optics framework [235–242]. Specifically, it was theoretically argued that a direct consequence of such eigenbasis collapse is an anomalous emissivity enhancement of a source when it is brought at the proximity of an environment (e.g., a cavity) featuring EPDs. The underlying physics of emissivity enhancement of a source due to a surrounding environment is known as Purcell effect and has been initially developed in the framework of quantum electrodynamics [243]. It described the modification of the spontaneous emission rate of a quantum source by changing its environment via manipulation of the local density of states (LDoS) of the quantum system. The latter information is imprinted in the Green's function that describes the surrounding environment. Interestingly, this same physics is intimately connected with one of the most fundamental rules of quantum mechanics: The Fermi's Golden Rule (FGR) [244] which links emission rates to the LDoS of the system. Elucidating the Purcell physics from this angle allows for expanding its applications to various wave systems where cavity manipulation can be employed to tailor the LDoS of the environment to which a source is coupled. Purcell effect has benefitted numerous technologies such as nano-optical spectroscopy, nanolasing, quantum information processing, energy harvesting, emission enhancement of sound and elastodynamic sources, etc [245–251]. An investigation, therefore, of non-Hermiticity and EPDs and their ramifications in FGR and Purcell physics constitutes a dual benefit: on a fundamental level, it will provide us a deeper understanding of the connection between engineered impedance and one of

the basic rules, i.e., FGR, while on the technological level, it will allow us to exploit the effects of non-Hermitian spectral singularities like EPDs to enhance the emissivity of mechanical sources.

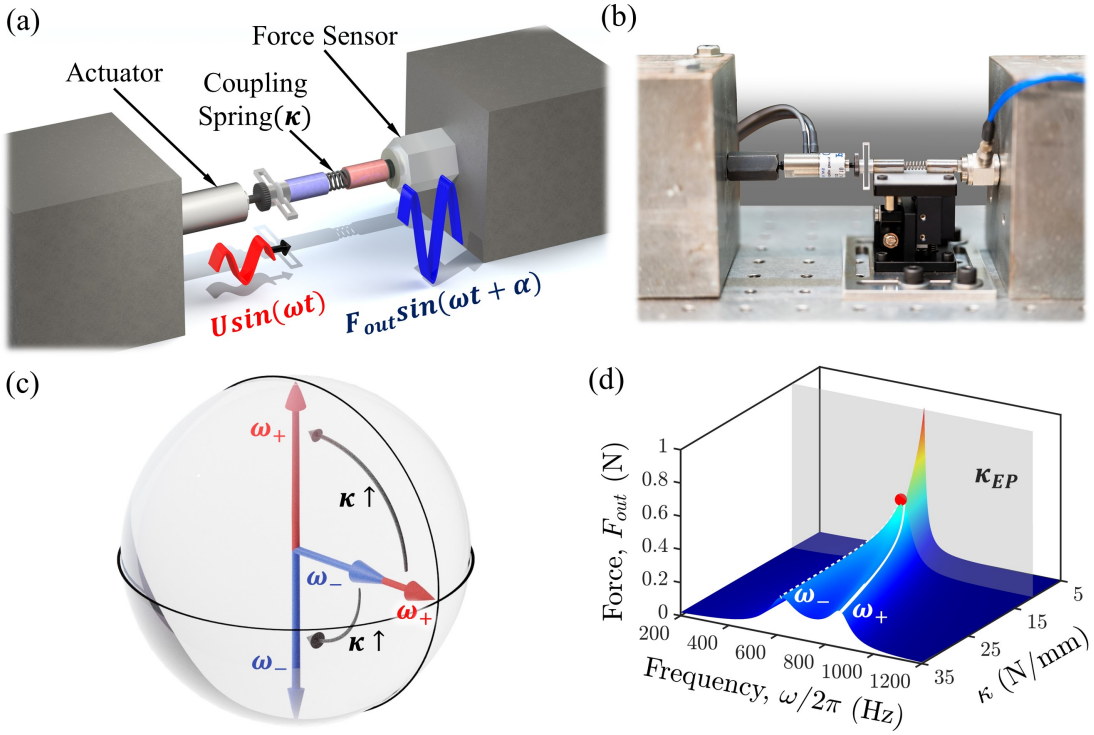

Figure 8.1: (a) A schematic and (b) a photograph of the experimental setup used in this study showing a non-Hermitian metamaterial consisting of two coupled resonators with one made of a Hookean aluminum spring and the other made of a viscoelastic material (PDMS) with controlled crosslinking. This metamaterial is mounted between a piezoelectric actuator (forced boundary condition) and a dynamic force sensor with an applied static precompression and supported by a low-friction Teflon surface mount. A frequency sweep is performed by applying a sinusoidal displacement excitation $U\sin(\omega t)$ (U is amplitude and ω is frequency) on the left side (undamped resonator/mass). The exerted force $F_{out}\sin(\omega t + \alpha)$, ($F_{out}$ is force amplitude and α is phase lag) is measured on the right side for various coupling spring stiffnesses (κ). (c) The eigenmodes of the non-Hermitian system are skewed and become degenerate at the exceptional point corresponding to a critical coupling $\kappa = \kappa_{EP}$. (d) Theoretically predicted reaction force amplitude as a function of excitation frequency (ω) and coupling (κ). The force exerted on the force sensor is twice as large in the proximity of the EPD (red dot) as compared to when metamaterial is operating away from the EPD, i.e., with higher coupling spring stiffness ($\kappa >> \kappa_{EP}$).

8.2 Results and Discussion

To this end, we have designed a two-mode cavity made by a non-Hermitian elastodynamic metamaterial consisting of two coupled resonant elements with differential damping (or non-proportional

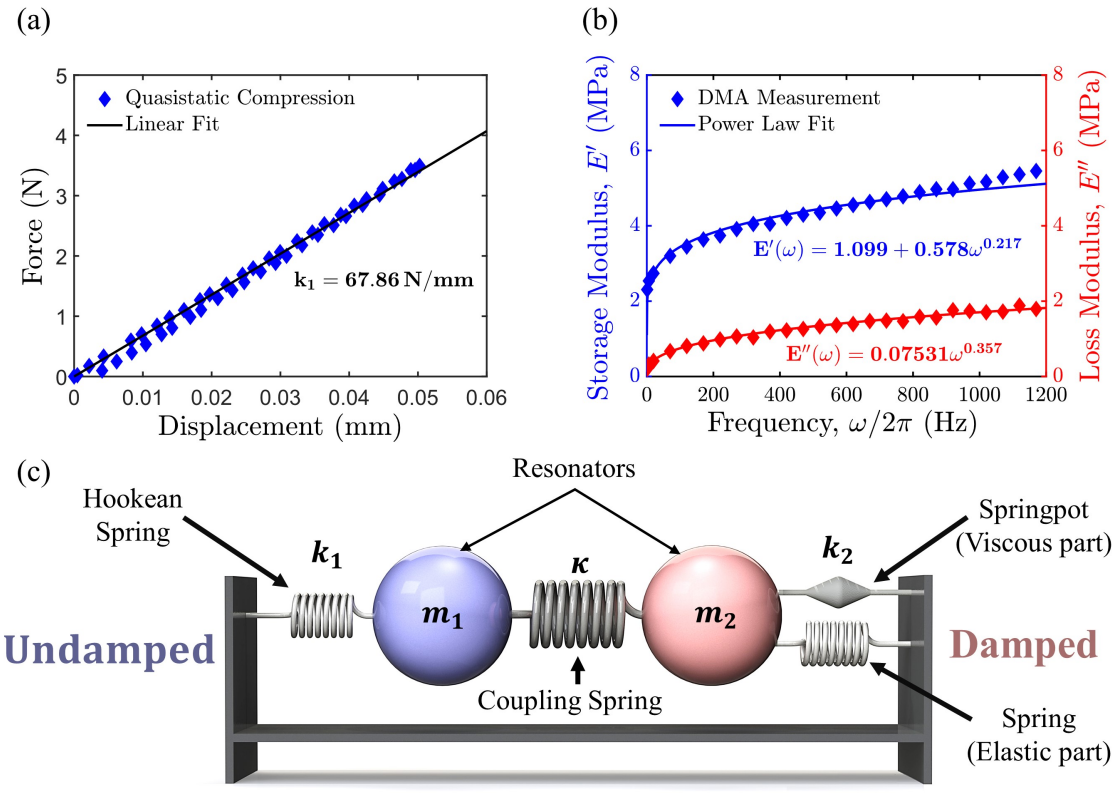

Figure 8.2: (a) Force vs. Displacement of the compliant aluminum Hookean spring ($F = k_1 x_1$). (b) Dynamic mechanical analysis (DMA) of frequency-dependent storage and loss moduli of PDMS and corresponding power law fits. (c) Conceptual design of non-Hermitian coupled resonators with differential damping under fixed boundary condition. Viscoelastic material (damped component) is represented by a parallel combination of an elastic spring and a springpot, where k_2 is the complex dynamic stiffness of the viscoelastic material. Undamped component is represented by a Hookean spring of stiffness k_1. Damped and undamped components are coupled together by a coiled spring of spring constant κ.

damping) between them (Figure 8.1(a,b)). The damped ($m_2 = m = 4.635\ g$) and the undamped ($m_1 = m$) resonators (masses) are coupled by a coiled Hookean spring of stiffness κ, see Figure 8.1(a,b). When the Hookean coupling strength between the two resonators acquires a critical value, the system exhibits an EPD associated with a coalescence of its eigenmodes (Figure 8.1(c)) and the corresponding eigenfrequencies (Figure 8.1(d)). Beyond this critical coupling, the eigenfrequencies bifurcate into two resonant modes with approximately the same constant linewidths (Figure 8.1(d)). Linewidth is a measure of the spectral width of a resonance peak—characterized by the half-width of the resonance force peak at $1/\sqrt{2}$ of the peak's height. It is equal to the imaginary part of the complex eigenfrequency. In this domain, a constant-amplitude dynamic force

applied on the undamped resonator side of the metamaterial results in an actuation force—i.e., the force exerted by the damped resonator side of the metamaterial onto the dynamic force sensor—whose amplitude is controlled by the coupling strength between the two masses without any deterioration of force-signal quality. The input force is enhanced by 6.4 times at the proximity of an EPD compared to the 3.2 times enhancement produced by the same cavity-source system when the metamaterial does not support an EPD, see Figure 8.1(d) and Figure 8.5. A relation between the actuation force and the dissipative power from the viscous element allows to employ a mapping between electrodynamics and elastodynamics: a monochromatic source (actuator) emits light into a "dark"mode, i.e., non-radiative mode (undamped resonator), which is coupled to a "bright"mode (damped resonator). At some critical coupling the emission power (dissipative power) from the "bright"mode experiences a four-fold enhancement, related to a two-fold enhancement of the exerted actuation force. This phenomenon cannot be explained by conventional Purcell physics as the cavity quality factor remains constant. Its origin is traced back to the coalescence of supermodes (eigenvectors of the coupled resonators system) near the EPD. It is reflected in a narrowing of the Green's function that describes the metamaterial—and consequently its LDoS—which acquires a square Lorentzian line-shape whose peak has a fourfold enhancement with respect to the peak of a single resonance. Our proof-of-principle metamaterial system promotes a new class of nano-indenters, atomic force microscopes and robotic-actuators.

To achieve differential damping between the two resonant elements of the metamaterial, we have designed and fabricated two types of springs: a compliant aluminum spring with specifically designed stiffness for the undamped component and a viscoelastic Polydimethylsiloxane (PDMS) for the damped component (Figure 8.2(a,b)). For the undamped component, we fabricated a lightweight aluminum spring (T6-6061), whose geometry was designed using finite element modeling such that the spring does not yield plastically under static pre-stress. Its effective stiffness allows for an EPD to form as we vary the coupling between the two elements. Quasistatic and dynamic mechanical analysis of the aluminum spring (Figure 8.2(a)) indicates that it follows Hooke's law with a spring constant $k_1 = 67.86\ N/mm$ as designed, resulting in a natural frequency of $\omega_0 = \sqrt{k_1/m} \approx 609\ Hz$ for the undamped resonator. We fabricated the PDMS films with different amounts of crosslinking, which was controlled by varying the percentage of the curing-agent (5 to 10% wt.) to tailor its dynamic modulus and loss-tangent. Then, 6 mm diameter cylindrical specimens were

cutout and preconditioned through five quasistatic compressive loading-unloading cycles up to 30% strain to remove any potential variations in the constitutive response of the pristine material. We used an optimal cylindrical specimen—a softer PDMS with large loss-tangent identified from the material's storage and loss moduli measured by dynamic mechanical analysis (DMA)—as the damped spring component of the metamaterial. The DMA was performed by first applying a 10% static precompression strain to the cylindrical PDMS specimens and then harmonically exciting them with a piezoelectric actuator (Physik Instrumente P841.10) at prescribed strain amplitudes and at frequencies ranging from 1 Hz to 1200 Hz while measuring the response force by a dynamic force sensor (PCB 208C01). The measured amplitude and phase lag between the actuation and the dynamic force signal were then used to calculate the frequency-dependent storage ($E'(\omega)$) and loss ($E''(\omega)$) moduli. We precisely calibrated our custom-built DMA setup by measuring the damping properties of different materials with known loss-tangents such that any phase lag occurring due to the force sensor and the actuator at higher frequencies is corrected for in the measurements. Also, the actuator and the force sensor in our setup are orders of magnitude stiffer than the materials and metamaterial we tested. Hence, any effect due to their deformation on the measurements is negligible. The measured storage and loss moduli were then fitted using power-law functions (see Figure 8.2(b)). The fits were used for the numerical modeling as well as the design of the metamaterial. We model the dynamics of the metamaterial by the following integro-differential equations

$$m_1\ddot{x}_1(t) = -k_1\left[x_1(t) - x_0(t)\right] - \kappa\left[x_1(t) - x_2(t)\right] \tag{8.1}$$

$$m_2\ddot{x}_2(t) = -\sigma(t)A - \kappa\left[x_2(t) - x_1(t)\right] \tag{8.2}$$

Assuming $E(t)$ is the relaxation modulus and $\epsilon(t)$ is the axial strain in PDMS, then $\sigma(t)$ is given by the Boltzmann superposition integral as follows

$$\sigma(t) = \int_0^t E(t-\tau)\frac{d\epsilon(\tau)}{d\tau}d\tau \tag{8.3}$$

Above equations describes two coupled masses m_1, m_2 with displacements $x_1(t)$, $x_2(t)$ respectively. The Hookean spring constant of the aluminum spring is k_1, and $x_0(t) = U\sin(\omega t)$ is the

displacement prescribed by the actuator, while $F_{\text{out}} = -\sigma(t)A$ is the force exerted on the mass m_2 with $A(= 28.274\ mm^2)$ and $\sigma(t)$ being the cross-sectional area and the stress response of the PDMS specimen respectively. After taking the Fourier transform, Eqs. (8.1,8.2) in the frequency domain takes the form

$$-m\omega^2 x_1(\omega) + k_1 x_1(\omega) + \kappa\left[x_1(\omega) - x_2(\omega)\right] = k_1 U \tag{8.4}$$

$$-m\omega^2 x_2(\omega) + \kappa\left[x_2(\omega) - x_1(\omega)\right] + \sigma(\omega)A = 0 \tag{8.5}$$

where $\sigma(\omega)$ is the dynamic stress amplitude which can be expressed as a function of frequency dependent storage (E') and loss modulus (E'') as follows

$$\sigma(\omega) = [E'(\omega) + iE''(\omega)]\epsilon(\omega) \quad , \ i = \sqrt{-1} \tag{8.6}$$

where $\epsilon(\omega) = x_2(\omega)/h$ is the dynamic strain amplitude and $h(= 1.948\ mm)$ is the height of the PDMS specimen. Assuming $k_2(\omega) = (A/h)[E'(\omega) + iE''(\omega)]$ is the effective dynamic stiffness, Eq. (8.5) can be rewritten as follows

$$-m\omega^2 x_2(\omega) + \kappa\left[x_2(\omega) - x_1(\omega)\right] + k_2(\omega)x_2(\omega) = 0 \tag{8.7}$$

In our metamaterial design, the real part of the effective stiffness of the PDMS specimen $(E'(\omega)(A/h))$ is approximately equal to the Hookean spring's stiffness (k_1) in the frequency range of our experiment, which makes the natural frequency of both damped and undamped oscillators (when they are not coupled together) roughly the same (zero detuning). The imaginary part $(E''(\omega)(A/h))$ behaves similarly to the real part because they are causally linked via the Kramers-Kronig relations due to their common origin—Fourier transform of a time-dependent relaxation modulus [92]. Both storage and loss modulus stay almost constant in the frequency range of our experiment (Figure 8.2(b)), thus keeping the differential damping constant. In systems with an independent source of dissipation, the damping factor can be tuned to tailor the location of the exceptional point [29, 252]. However, in our case, damping (E'') and stiffness (E') are connected. Thus, our system exhibits constant differential damping and zero detuning with coupling as the tunable parameter.

Eqs. (8.4,8.7) can be written in matrix form as follows

$$\left\{ -\omega^2 \underbrace{\begin{bmatrix} m & 0 \\ 0 & m \end{bmatrix}}_{\mathbf{M}} + \underbrace{\begin{bmatrix} k_1+\kappa & -\kappa \\ -\kappa & \kappa+\mathcal{R}e\left(k_2(\omega)\right) \end{bmatrix}}_{\mathbf{K}} + i \underbrace{\begin{bmatrix} 0 & 0 \\ 0 & \mathcal{I}m\left(k_2(\omega)\right) \end{bmatrix}}_{\mathbf{C}} \right\} \begin{Bmatrix} x_1(\omega) \\ x_2(\omega) \end{Bmatrix} = \begin{Bmatrix} k_1 U \\ 0 \end{Bmatrix} \tag{8.8}$$

where **M**, **K**, and **C** are the mass, stiffness, and damping matrices. Noteworthily, the damping matrix (**C**) doesn't commute with the stiffness (**K**) and mass (**M**) matrices, which suggests that our system exhibits non-proportional damping [253]. The corresponding eigenfrequencies $\omega_\pm$ of the metamaterial are found by solving the characteristic equation associated with Eqs. (8.4,8.7). Figure 8.3(a,b) shows the real and imaginary parts of $\omega_\pm$ as functions of the stiffness κ of the coiled coupling spring. A critical coupling, κ_{EP} enforces an EPD, a coalescence of the resonant frequencies, $\omega_- = \omega_+ = \omega_{EP}$, as well as the corresponding eigenvectors. As the coupling stiffness κ is increased above κ_{EP} the modes separate from one another, i.e. $\omega_-^R \equiv \mathcal{R}e\left(\omega_-\right) \neq \mathcal{R}e\left(\omega_+\right) \equiv \omega_+^R$, while their linewidths remain approximately the same, i.e. $\omega_-^I \equiv \mathcal{I}m(\omega_-) \approx \mathcal{I}m(\omega_+) \equiv \omega_+^I$ (see Methods). Our modeling is further validated by a direct comparison with the measured eigenvalues (see Methods), see Figure 8.3(a,b).

We further evaluate the mechanical power dissipated from mass m_2, which takes the form (see Methods)

$$P_d(\omega) = \frac{\omega}{2\pi} \mathrm{W_d} = \Phi_e \cdot \xi(\omega) \quad , \; \xi(\omega) = \frac{2\omega}{\pi} \mathcal{I}m(G_{11}(\omega)) \tag{8.9}$$

where $W_d(\omega) = Ah \int_0^{2\pi/\omega} \sigma(t) \frac{d\epsilon}{dt} dt = (\pi A h) E''(\omega) |\epsilon(\omega)|^2$ is the dissipated energy per cycle [92], $\Phi_e = \frac{\pi}{4} \frac{F_{in}^2}{m}$ depends only on the equivalent input force from the actuator $F_{in} = k_1 U$ acting on the mass $m_1 = m$, and $G_{11}(\omega)$ is the element of the Green's function that describes the system of Eqs. (8.4,8.5)

The Eq. (8.9) establishes a connection between the power dissipated by the elastodynamic metamaterial shown in Figure 8.1(a,b) and the Purcell physics of quantum optics. The analogies become clearer once we interpret the imaginary part of the Green's function $\xi(\omega)$ as the LDoS of the

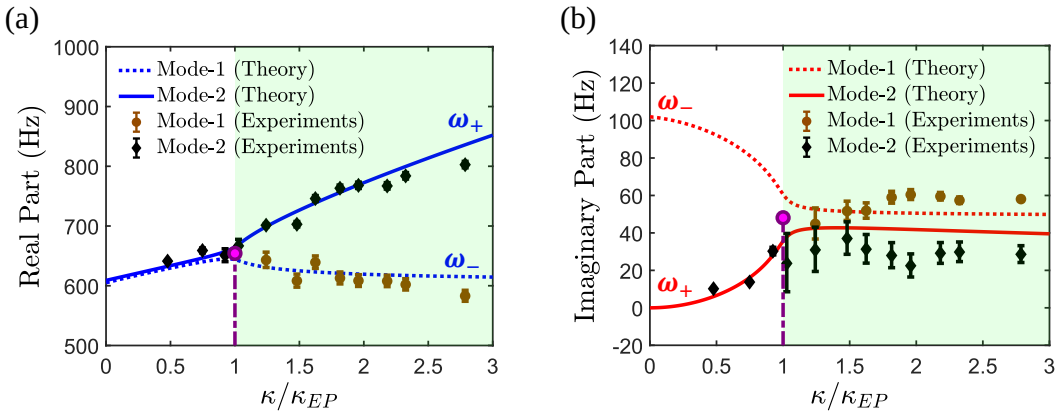

Figure 8.3: (a) The real part (peak position) and (b) the imaginary part (half of peak width at $1/\sqrt{2}$ of peak height) of resonant frequencies ($\omega_\pm$) vs. coupling strength, obtained by a modal curve-fitting of the experimentally measured force spectra (Figure 8.4(a)). The solid and dotted lines are the results of the simulations with the model described by Eqs. (8.4,8.5) where dispersion effects are considered. The Hookean spring constant was taken to be $k_1 = 67.86\ N/mm$.

mechanical resonant cavity formed by the metamaterial, and the piezoelectric actuator that excites the system as an emitter placed in the proximity of this cavity. Then the mechanical power emitted by the metamaterial is the analogue of the emissive power in the quantum optics framework. In the latter framework, Purcell realized that the spontaneous emission rate of a quantum emitter is enhanced (or suppressed) by appropriately engineering its surrounding environment, and therefore, the LDoS [243].

Further theoretical progress can be made by assuming that the storage and loss moduli take a constant value in the frequency range of our experiments which are $E' = \frac{k_1 h}{A} = 4.675\ MPa$ and $E'' = 1.5235\ MPa$ (see Methods). This approximation is justified by the slow frequency dependence that the PDMS exhibits, see Figure 8.2(b). Under this approximation, the critical coupling is $\kappa_{EP} = \frac{A}{2h}E''$, and for $\kappa \geq \kappa_{EP}$ the two resonant modes exhibit approximately the same decay rate $2\omega_\pm^I \approx \Gamma \equiv \frac{A}{2mh\omega_0}E''$ (Figure 8.3(b)). In this case $\xi(\omega)$ becomes

$$\xi(\omega) = \frac{1}{\pi}\frac{\Gamma\cdot\omega_0\cdot(\kappa/m)^2\omega}{\left(\omega^2-\omega_0^2\right)^2\left(\omega^2-\omega_0^2-2\kappa/m\right)^2+\left(2\Gamma\omega_0\right)^2\left(\omega^2-\omega_0^2-\kappa/m\right)^2} \tag{8.10}$$

where $\omega_0 = \sqrt{k_1/m}$. Because at the proximity of the EPD the two eigenfrequencies degenerate at $\omega_\pm^R = \omega_{EP} \approx \omega_0\sqrt{1+\Gamma/\omega_0} \approx \omega_0$ (see Methods), one naturally expects that $\xi(\omega)$, and subsequently $P_d(\omega)$, will also be modified. To better understand the consequence of EPD on them, we

first evaluate $\xi(\omega)$ in the vicinity of $\omega \approx \omega_{EP}$. From Eq. (8.10), we get that

$$\xi_{\mathrm{EP}}(\omega) \approx \frac{1}{2\pi} \frac{(\Gamma/2)^3}{\left[(\omega-\omega_{\mathrm{EP}})^2+(\Gamma/2)^2\right]^2} \tag{8.11}$$

corresponding to a square-Lorentzian—as opposed to the more traditional Lorentzian line-shape characterizing the LDoS away from an EPD. In the other limiting case of $\kappa >> \kappa_{EP}$, the two resonant frequencies $\omega_{-}^{R} \approx \omega_0$ and $\omega_{+}^{R} \approx \sqrt{\omega_0^2+(2\kappa/m)}$ (see Methods) are well separated from each other. In this case one can approximate Eq. (8.10) as a sum of two Lorentzians centered at $\omega_{\pm}$ and having the same linewidth Γ. Specifically, we have

$$\xi_{\infty}(\omega) \approx \frac{1}{8\pi} \sum_{\pm} \frac{\Gamma/2}{\left(\omega-\omega_{\pm}^{R}\right)^2+(\Gamma/2)^2} \tag{8.12}$$

which can be used as a reference for measuring the effects of EPD in the power emission. At this point, it is instructive to introduce the rescaled dissipated power $\mathcal{P}\left(\omega_e\right)=P_d\left(\omega_e\right)/P_d^{\infty}\left(\omega_{\pm}^{R}\right)$ where $P_d^{\infty}\left(\omega_{\pm}\right) \equiv \frac{\pi}{2}\Phi_e \cdot \xi_{\infty}\left(\omega_{\pm}\right)$ and $\omega_e=\omega_{\pm}^{R}$ is the frequency of the actuation force which is considered to be monochromatic and at resonant frequency. Substituting Eqs. (8.11) and (8.12) back in the general expression for the emissivity Eq. (8.9), we deduce that $\mathcal{P}(\omega_e=\omega_{EP})=4$. A more careful analysis indicates that $\mathcal{P}(\omega_e=\omega_{EP})$ might be slightly larger/smaller than a factor of four, i.e., $\mathcal{P}(\omega_e=\omega_{EP}) \approx 4+\mathcal{O}\left(\frac{\Gamma}{\omega_0}\right)+\mathcal{O}\left(\frac{\kappa}{k_1}\right)$, where $\frac{\Gamma}{\omega_0} << 1$; $\frac{\kappa}{k_1}<1$.

The enhanced dissipated power due to the four-fold enhancement of the peak of $\xi(\omega)$ is also reflected in the actuation force emitted from the metamaterial and measured by the dynamic force sensor attached to the m_2-resonator. The latter is written in the form $F_{\mathrm{out}}(t)=F_{\mathrm{out}}(\omega_e)\sin(\omega_e t+\alpha)$, where ω_e is the driving frequency of the actuator. At the same time, the emitted force amplitude $|F_{\mathrm{out}}(\omega_e)|$ is

$$\left|F_{\mathrm{out}}\ \left(\omega_e\right)\right| \equiv \mathrm{A}\left|\sigma\left(\omega_e\right)\right| = \sqrt{\frac{2A\left(\left|E'\left(\omega_e\right)\right|^2+\left|E''\left(\omega_e\right)\right|^2\right)}{h\omega_e E''\left(\omega_e\right)} P_d\left(\omega_e\right)} \tag{8.13}$$

where we have expressed the stress function as $\sigma(\omega)=[E'(\omega)+iE''(\omega)]\epsilon(\omega)$ and subsequently we have used Eq. (8.9) to express the strain in terms of the emitted power as $|\epsilon(\omega)|=\sqrt{4P_d(\omega)/\left(\pi E''Ah\right)}$. From Eq. (8.13) we can further estimate the force amplification factor

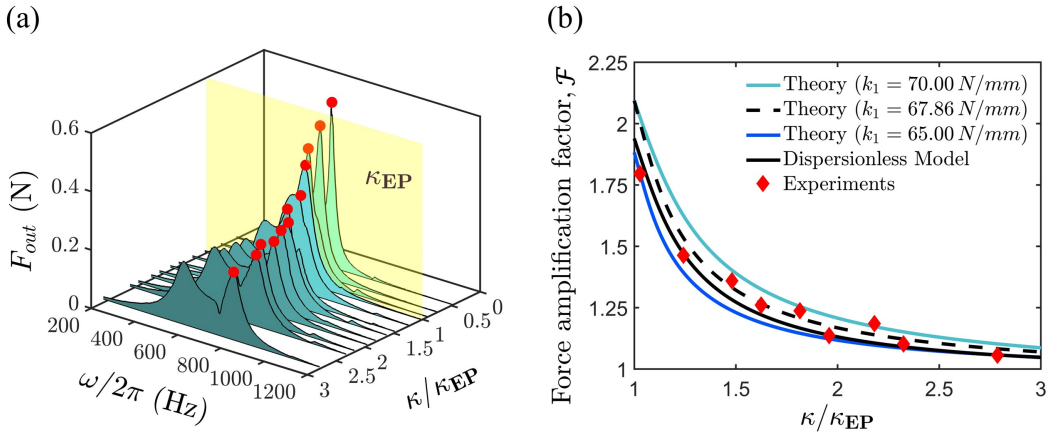

Figure 8.4: (a) Frequency-swept force amplitude measured experimentally for various coupling spring stiffnesses. Splitting of a single sharp peak into two broad peaks can be observed as coupling increases. (b) Emitted force amplification factor $\mathcal{F}(\omega_{\pm})$ vs. the rescaled coupling. The experimental data are indicated in filled diamonds. The solid black line indicates the results of the dispersionless modeling with $k_1 = 70\ N/mm$. Black dashed line indicate the results of the simulation of model Eqs. (8.4,8.5) for $k_1 = 67.86\ N/mm$—corresponding to best fit model. Curves corresponding to $k_1 = 70\ N/mm$ and $k_1 = 65\ N/mm$ represent the upper and lower uncertainty bounds of data fitting in Figure 8.2. A two-fold enhancement is observed in all cases.

$\mathcal{F}(\omega_e) \equiv \frac{F_{\text{out}}(\omega_e)}{F^{\infty}_{\text{out}}(\omega^R_{\pm})} = \sqrt{\mathcal{P}(\omega_e)}$, which for κ_{EP} and driving frequency $\omega_e = \omega_{EP}$ is $\mathcal{F}(\omega_e = \omega_{EP}) = 2$. We point out that the force amplification factor $\mathcal{F}(\omega_e)$ indicates an additional enhancement relative to the typical Purcell force enhancement occurring in the actuating force $F^{\infty}_{\text{out}}(\omega^R_{\pm})$ (Figure 8.5) for the same metamaterial-source configuration when the metamaterial does not support an EPD.

We have tested the validity of the above predictions by direct measurements of the emitted actuation force amplitude (Figure 8.4(a)) for various coupling stiffness κ versus the driving frequency ω_e (see Methods). From these data we extracted the force amplification factor $\mathcal{F}(\omega_e = \omega_{\pm})$ and report it as a function of the coupling stiffness κ normalized by the coupling stiffness corresponding to the EPD, κ_{EP}, in Figure 8.4(b). The experimental data confirm the above theoretical predictions very well. In the same figure, we also report the force amplification factor calculated numerically from Eqs. (8.4,8.5). From these equations, we extracted the frequency-dependent displacement amplitude $x_2(\omega)$ using the dispersion characteristics of the stress function, which is related to the strain in viscoelastic material as $\epsilon(\omega) = x_2(\omega)/h$. Using the definition of $|F_{\text{out}}(\omega)|$ in Eq. (8.13), we have calculated $\mathcal{F}(\omega_e = \omega^R_{\pm})$ for three different k_1 constants to evaluate the robustness of the observed two-fold enhancement. In the same figure, we also report the theoretical results of the

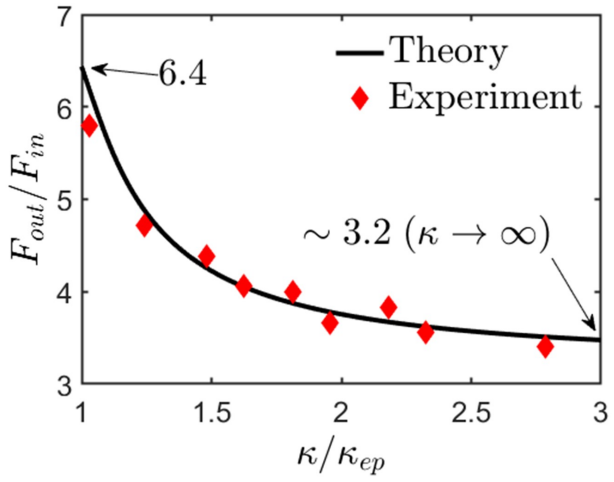

Figure 8.5: Boosting of Purcell Enhancement factor. The input force enhancement of 3.2 due to Purcell effect is observed when the metamaterial is far from EPD, which is boosted to 6.4 when the system is at the proximity to EPD.

non-dispersive model (solid black line). All curves confirm the two-fold enhancement in exerted actuation force at the proximity of the EPD with respect to the actuation force value corresponding to large coupling constants where a standard cavity-enhancement Purcell effect occurs.

8.3 Conclusion

In conclusion, we have demonstrated experimentally and analyzed theoretically an enhancement in the exerted actuation force and the emitted mechanical power by a non-Hermitian elastodynamic cavity—a metamaterial consisting of undamped and damped resonators. It occurs when the actuation source is coupled only to the undamped resonator (a "dark"mode) while the emission is measured on the viscoelastic element (the "bright"mode). The origin of this enhancement has been traced to the reorganization of the super-modes of the metamaterial in the proximity of an EPD. Our experiments pave the way for understanding the ramifications of non-Hermiticity and EPD engineering in the manipulation of the Purcell factor of narrow-band emitters. Additionally, while coupled oscillators and periodic structures have been extensively studied in vibroacoustics under various scenarios, our work provides a unique metamaterial design pathway that utilizes differential damping as a design element to realize exceptional point degeneracies experimentally and demonstrates a novel phenomenon of enhanced emission at constant quality factor. Our work

paves the way to an unexplored realm of physics in non-Hermitian systems and their potential in various applications, such as a new class of indenters for material hardness measurements [251] or enhanced reconfigurable actuators in robotics.

Methods

Experimental Methods for Spectral Measurements. We have used the same setup that we used for the DMA measurement of the PDMS for spectral measurements of the non-Hermitian metamaterial. The non-Hermitian metamaterial is supported by a low-friction Teflon surface and a static precompression force equivalent to the one used for measuring the storage and loss moduli of PDMS is applied. Since PDMS is slightly nonlinear, the precompression of PDMS should be consistent so that the storage and loss moduli remain the same as the one used for numerical modeling. A sinusoidal actuation of constant displacement amplitude at driving frequencies ranging from 10 Hz to 1200 Hz was applied on the left side of the non-Hermitian metamaterial, and the steady-state emitted force amplitude was measured at the fixed right end. The coupling stiffness between the resonators was varied by changing the coupling springs. A sharp resonant peak is observed in the reaction-force frequency spectrum for low coupling, see Figure 8.4(a). As the coupling increases, the single sharp peak splits into two broad damped peaks, indicating the departure from an EPD. The peak position (real part of frequencies) and linewidth (imaginary part of frequencies) were extracted via a modal curve-fitting of the experimental data.

Evaluation of the storage and loss moduli for the dispersionless model. In the dispersionless approximation, the storage and loss moduli of the damped spring (PDMS) were assumed to be frequency independent. The storage modulus is approximated to be $E' = \frac{h}{A}k_1 = 4.675\text{MPa}$, to match the real part of stiffness of the damped spring with the undamped spring. The dispersionless complex stiffness (k_2) is given by $k_2 = (E' + iE'')\,\frac{A}{h} = E'(1 + i\tan(\delta))\frac{A}{h}$, where $tan(\delta) = E''/E'$ is the dispersionless loss tangent of the damped spring. The value of $tan(\delta) \approx 0.326$ has been chosen such that the EPD forms at the same coupling as in dispersive model i.e., $\kappa_{ep} = 10.95N/mm$. Using this information, we have evaluated the loss moduli to be $E'' = 1.5235\ MPa$

Error bars calculations. We estimated maximum variation in measurements of k_1 (Δk_1) and

$k_2\,(\Delta k_2)$ and calculated the resultant errors in the resonant frequencies (ω_+, ω_-) using the relation

$$\Delta\omega_\pm = \frac{1}{2m\omega_\pm}\frac{\Delta k_2\left(m\omega_\pm^2 - \kappa - k_1\right) + \Delta k_1\left(m\omega_\pm^2 - \kappa - k_2\right)}{\left(2m\omega_\pm^2 - 2\kappa - k_1 - k_2\right)} \tag{8.14}$$

Spectral properties of the elastodynamic metamaterial under dispersionless approximation. We have found that a good description of the experimental data is obtained by considering that the storage and loss moduli take a constant value in the frequency range of our experiment (dispersionless approximation). Specifically, we have evaluated these two quantities at frequency $\omega_* \approx 700$ Hz such that $E'(\omega_*) \equiv k_1 h/A$. In this case, the corresponding $E' \approx 4.67$MPa while $E'' \approx E''(\omega_*) = 1.50$MPa. Under this approximation we have that $k_2 = (A/h)\,[E' + iE'']$ and the resonant frequencies $\omega_\pm = \omega_\pm^R + i\omega_\pm^I$ of the system of Eqs (8.4, 8.5) in the main text are the solutions of the secular equation

$$\left[\omega_\pm^2 - \omega_0^2 - (\kappa/\mathrm{m})\right]\left[\omega_\pm^2 - \omega_0^2 - (\kappa/\mathrm{m}) + 2\mathrm{i}\Gamma\omega_0\right] - (\kappa/\mathrm{m})^2 = 0. \tag{8.15}$$

Our experiment operates in the domain of $\kappa \geq \kappa_{EP} \equiv m\Gamma\omega_0, \left(\omega_0 = \sqrt{k_1/m}\right)$ where the solutions of Eq (8.15) take the form

$$\omega_\pm^R = \left(\left[\omega_0^2 + (\kappa/\mathrm{m}) \pm \sqrt{(\kappa/\mathrm{m})^2 - \Gamma^2\omega_0^2}\right]^2 + \Gamma^2\omega^2\right)^{1/4}\cos(\varphi/2) \tag{8.16}$$

$$\omega_\pm^I = \left(\left[\omega_0^2 + (\kappa/m) \pm \sqrt{(\kappa/m)^2 - \Gamma^2\omega_0^2}\right]^2 + \Gamma^2\omega^2\right)^{1/4}\sin(\varphi/2) \tag{8.17}$$

$$\tan\varphi = \frac{\omega_0\Gamma}{\omega_0^2 + (\kappa/m) \pm \sqrt{(\kappa/m)^2 - \Gamma^2\omega_0^2}} \tag{8.18}$$

indicating that for $\kappa = \kappa_{EP}$, the modes are degenerate (exceptional point degeneracy). We have further confirmed the formation of an EPD by analyzing the corresponding eigenvectors. These are given by the following expression

$$\Psi_\mp = \frac{1}{\sqrt{2}}\left(\frac{\kappa}{m}\right)^{-1}\begin{bmatrix} -i\Gamma\omega_0 \mp \sqrt{(\kappa/m)^2 - \Gamma^2\omega_0^2} \\ (\kappa/m) \end{bmatrix}, \tag{8.19}$$

demonstrating a degeneracy at $\kappa_{EP} = m\Gamma\omega_0$

Further progress can be made by realizing that $\tan\varphi \ll 1$. The latter inequality is imposed by the physical conditions $\omega_0\Gamma \leq (\kappa/\mathrm{m}) \ll \omega_0^2, \Gamma \ll \omega_0$ which dictate our experimental set-up. Using these conditions, we can simplify Eqs. (8.16,8.17, 8.18) to the following forms

$$\omega_{\pm}^{R} \approx \omega_0 \left[1 + (\kappa/\mathrm{k}_1) \pm \sqrt{(\kappa/\mathrm{k}_1)^2 - (\Gamma/\omega_0)^2}\right]^{1/2} \tag{8.20}$$

$$\omega_{\pm}^{I} \approx \frac{1}{2} \frac{\Gamma}{\left[1 + (\kappa/\mathrm{k}_1) \pm \sqrt{(\kappa/\mathrm{k}_1)^2 - (\Gamma/\omega_0)^2}\right]^{1/2}} \tag{8.21}$$

Let us first evaluate the eigenfrequencies of the metamaterial in the limit of $(\Gamma/\omega_0) \ll (\kappa/k_1) \ll 1$ where the last inequality always applies in our experiments. From Eqs. (8.20, 8.21) we get that $\omega_{-}^{R} \approx \omega_0$ and $\omega_{+}^{R} \approx \omega_0\sqrt{1 + 2\,(\kappa/k_1)}$ while for the linewidths we have $\omega_{\pm}^{I} \approx \frac{1}{2}\Gamma(1 + \mathcal{O}\left(\frac{\kappa}{k_1}\right))$. From the same equations we find that when $(\kappa/\mathrm{k}_1) = (\Gamma/\omega_0)$ (corresponding to stiffness $\kappa_{EP} = m\omega_0\Gamma = \frac{A}{2h}E''$) the eigenvalues become degenerate (see discussion above). Notice that the condition $(\kappa/m) = \omega_0\Gamma$ is equivalent to the relation $(\kappa/\mathrm{k}_1) = (\Gamma/\omega_0)$. At EPD the eigenfrequencies Eqs. (8.16, 8.17, 8.18) of the metamaterial can be simplified using Eqs. (8.20, 8.21) to

$$\omega_{\pm}^{R}\big|_{EP} = \omega_{EP} \approx \omega_0 \left[1 + \frac{\Gamma}{\omega_0}\right]^{1/2} \approx \omega_0 \tag{8.22}$$

$$\omega_{\pm}^{I}\big|_{EP} \approx \frac{1}{2} \frac{\Gamma}{[1 + (\Gamma/\omega_0)]^{1/2}} \approx \frac{\Gamma}{2}, \tag{8.23}$$

where for the right-hand side of Eqs. (8.20, 8.21) we have used the physical constraint that $(\kappa/\mathrm{m}) \ll \omega_0^2 \rightarrow \kappa/\mathrm{k}_1 \ll 1$. We have also confirmed that the same EPD condition is applicable for the case of eigenvectors of the couple mass system of Eqs. (8.1, 8.2). Specifically, Eq. S19 becomes $\psi_+ = \psi_- = \frac{1}{\sqrt{2}} \begin{bmatrix} -i \\ 1 \end{bmatrix}$ indicating a relative phase of $\pi/2$ between the two components of the degenerate eigenvector (Figure 8.6).

The validity of these approximations has been checked against the numerical results presented in the main text that have considered the dispersion characteristics of the storage and loss moduli. The comparison is shown in Figure 8.7 where we report $\omega_{\pm}^{R,I}$, versus the stiffness κ, using the approximate expressions of Eqs. (8.22, 8.23) together with the outcomes of the exact numerics

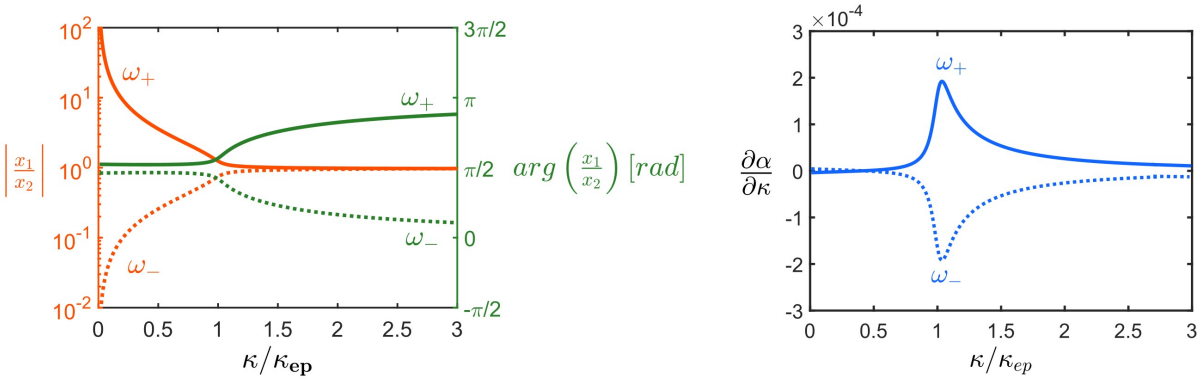

Figure 8.6: Eigen vectors. Ratio of amplitude of oscillators ($|x_1/x_2|$) and phase difference between them ($\arg(x_1/x_2)$) are plotted as a function of normalized coupling for both the modes $\omega_\pm$ (Left). Phase sensitivity as a function of normalized coupling (Right).

and the measurements. It is also noteworthy that, strictly speaking, due to dispersion effects, our designed metamaterial shows a quasi-EPD degeneracy. Nevertheless, for all practical purposes this quasi-degeneracy is sufficient for observing all novel features characterizing systems with EPD.

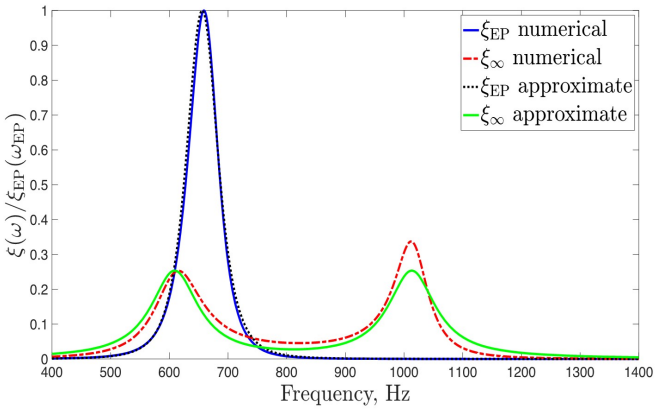

Figure 8.7: Two representative cases corresponding to spring stiffness of $\kappa = \kappa_{EP} = 10.95$kN/m (dashed black and solid blue lines) and $\kappa = \kappa_\infty = 60$kN/m (dashed red and solid green lines). The green and blue solid lines correspond to the approximate expressions Eq. (8.11) and Eq. (8.12). The red dashed-dotted and black-dashed lines correspond to the numerical evaluation of $\xi(\omega)$ via Eq (8.4,8,5) where the dispersion characteristics of E' and E'' are taken into consideration. The parameters used in the plot are $k_1 = 67.87kN/m$, $h = 1.95mm$, $A = 28.3mm^2$, $m = 4.6g$, and $\omega_0 = \sqrt{k_1/m} = 2\pi \times 609\ rad/s$. In the case of dispersionless modeling $E' = k_1 h/A = 4.67MPa$ and $E'' = 1.50MPa$ while the critical coupling has been estimated to be $\kappa_{ep} = 10.95kN/m$. All the data are normalized by the maximum value $\xi_{EP}(\omega_{EP})$. The slightly larger deviation of the approximate result Eq. (8.12) (green solid line) from the numerical data (red dash-dotted line) at the higher frequency ω_+ is expected because the ratio $(\kappa/k_1) = 0.88$ is barely satisfying the condition $\kappa/k_1 < 1$ for the chosen $\kappa_\infty = 60$kN/m

General expression for dissipated power: The averaged (over one driving cycle) dissipated power is given by the expression

$$P_d(\omega) = \frac{\omega}{2\pi} W_d = \mathrm{Ah}\,\frac{\omega}{2\pi}\int_0^{2\pi/\omega} \sigma(\mathrm{t})\frac{\mathrm{d}\epsilon}{\mathrm{dt}}dt \tag{8.24}$$

where W_d is the dissipated energy per cycle. This choice of definition guaranties that the elastic component will not contribute to the final calculation since the work done by conservative forces is zero along a close loop. For the evaluation of $P_d(\omega)$ we use the following relations

$$\epsilon(\mathrm{t}) = |\epsilon(\omega)|\sin\omega\mathrm{t}, \quad \sigma(\mathrm{t}) = |\sigma(\omega)|\sin(\omega\mathrm{t}+\delta), \quad \sin\delta(\omega) = \frac{E''(\omega)}{\sqrt{|E'(\omega)|^2 + |E'(\omega)|^2}}, \tag{8.25}$$

where we have also introduced the loss-tangent $\tan\delta(\omega) \equiv E''(\omega)/E'(\omega)$. These equations allow us to express Eq. (8.25) in the form

$$P_d(\omega) = \mathrm{Ah}\,\frac{\omega}{2\pi}|\epsilon(\omega)|^2\sqrt{|E'|^2 + |E''|^2}\int_0^{2\pi/\omega} \omega\sin(\omega t+\delta)\cos\omega t dt \tag{8.26}$$

$$= \mathrm{Ah}\,\frac{\omega}{2}E''(\omega)|\epsilon(\omega)|^2 = \frac{0}{2h}A''(\omega)\,|x_2(\omega)|^2 \tag{8.27}$$

where we used the stress-strain relation in the frequency domain $\sigma(\omega) = [\mathrm{E}'(\omega) + \mathrm{iE}''(\omega)]\,\epsilon(\omega)$ and the fact that $\epsilon(\omega) = \mathrm{x}_2(\omega)/h$. Therefore, the task at hand is to evaluate the displacement of the second mass $x_2(\omega)$ and by substituting in Eq. (8.27) evaluate the average dissipated power $P_d(\omega)$. To this end, we rewrite Eqs. (8.1, 8.2) in a matrix form as

$$\left(\hat{\mathcal{J}}\omega^2 - \hat{\mathcal{L}}\right)\psi = \mathrm{s} \tag{8.28}$$

where

$$\hat{\mathcal{L}}(\omega) = \begin{bmatrix} \frac{\mathrm{k_1}}{\mathrm{m}} + \frac{x}{\mathrm{m}} & \frac{x}{\mathrm{m}} \\ \frac{x}{\mathrm{m}} & \frac{\mathrm{A}}{\mathrm{mh}}\mathrm{E}'(\omega) + \frac{x}{\mathrm{m}} + \mathrm{i}\frac{\mathrm{A}}{\mathrm{mh}}\mathrm{E}''(\omega) \end{bmatrix}, \quad \psi = \begin{bmatrix} \mathrm{x}_1(\omega) \\ \mathrm{x}_2(\omega) \end{bmatrix}, \quad s = \begin{bmatrix} -\frac{\mathrm{k_1}}{\mathrm{m}}\mathrm{U} \\ 0 \end{bmatrix} \tag{8.29}$$

and $\hat{\jmath}$ is the identity 2×2 matrix. The solution of Eq. (8.29) is then

$$\psi = \hat{\mathcal{G}}\mathrm{s}; \quad \hat{\mathcal{G}} = \frac{1}{\det\left((\omega^2 - \mathcal{L}\right)} \begin{bmatrix} \omega^2 - \frac{A}{mh}E'(\omega) - \frac{\kappa}{m} - i\frac{A}{mh}E''(\omega) & -\frac{\kappa}{m} \\ -\frac{\kappa}{m} & \omega^2 - \frac{k_1}{m} - \frac{\kappa}{m} \end{bmatrix}, \tag{8.30}$$

where $\hat{g} \equiv \left(\hat{\jmath}\omega^2 - \hat{L}\right)^{-1}$ is the Green's function that describes the dynamics of the metamaterial. Consequently, the displacement $x_2(\omega)$ becomes

$$|\mathrm{x_2}(\omega)|^2 = \left|(\hat{\mathcal{G}}\mathrm{s})_2\right|^2 = |G_{21}|^2 \mid \mathrm{s_1}|^2 = \frac{(\kappa/\mathrm{m})^2 \left(\mathrm{k_1/m}\right)^2 |\mathrm{U}|^2}{\left|\det\left(\hat{\jmath}\omega^2 - \hat{\mathcal{L}}\right)\right|^2}, \tag{8.31}$$

It could be shown that $\left|\det\left(\hat{\jmath}\omega^2 - \hat{\mathcal{L}}\right)\right|^2 \mathrm{Im}\, G_{11} = \frac{\mathrm{A}}{\mathrm{mh}}\mathrm{E}''(\omega)\left(\frac{\mathrm{k}}{\mathrm{m}}\right)^2$ which allows us to establish the following important equality between matrix elements of the Green's function

$$\mathrm{Jm}\left(G_{11}\right) = \frac{\mathrm{A}}{\mathrm{mh}}\mathrm{E}''(\omega)\left|G_{21}\right|^2 \tag{8.32}$$

Combining Eqs. (8.27,8.31,8.32), we finally get that the dissipation power can be expressed as in Eq. (8.9) where $\xi(\omega) = \frac{2\omega}{\pi}\,\mathrm{Im}\,\mathrm{G_{11}}$ has dimensions of density of states.

LDoS Analysis in the two limiting cases, Eq 8.11 and Eq 8.12

Using the definition of$\xi(\omega) = \frac{2\omega}{\pi} J\ \mathrm{m}G_{11}(\omega)$ from Eq. (8.9) and the expression for the Green's function of the metamaterial (see Eq. (8.30)), we can now deduce Eq. (8.10). Specifically, $\xi(\omega)$ takes the form

$$\xi(\omega) = \frac{1}{\pi}\frac{\Gamma\omega_0(\kappa/\mathrm{m})^2\omega}{\left[\omega^2 - \omega_0^2\right]^2\left[\omega^2 - \omega_0^2 - 2(\kappa/\mathrm{m})\right]^2 + (2\Gamma\omega_0)^2\left[\omega^2 - \omega_0^2 - (\kappa/\mathrm{m})\right]^2} \tag{8.33}$$

The two limiting cases corresponding to the shape of $\xi(\omega)$ in the proximity of an EPD and far away from it can be deduced from Eq. (8.33).

1. Proximity to the EPD : The EPD occurs at $\kappa_{\mathrm{EP}}/\mathrm{m} = \Gamma\omega_0 \rightarrow \kappa_{EP} = \frac{A}{2h}E''$ leading to a degenerate resonant frequency $\omega_{\pm}^R = \omega_{\mathrm{EP}} = \omega_0\sqrt{1 + \Gamma/\omega_0}$. Straightforward algebra allows us to rewrite the denominator of Eq. (8.33) in a simpler form, leading to the following expression

for $\xi(\omega)$

$$\xi_{\mathrm{EP}}(\omega)=\frac{1}{\pi}\frac{(\Gamma\omega_0)^3\,\omega}{\left[\left(\omega^2-\omega_{\mathrm{EP}}^2\right)^2+(\Gamma\omega_0)^2\right]^2} \tag{8.34}$$

At the vicinity of $\omega\simeq\omega_{\mathrm{EP}}$, the DoS can be further approximated as

$$\xi_{EP}\left(\omega\approx\omega_{EP}\right)\approx\frac{1}{\pi}\frac{(\Gamma\omega_0)^3\,\omega_{\mathrm{EP}}}{\left[4\omega_{\mathrm{EP}}^2\left(\omega-\omega_{\mathrm{EP}}\right)^2+(\Gamma\omega_0)^2\right]^2}\approx\frac{1}{2\pi}\frac{(\Gamma/2)^3}{\left[\left(\omega-\omega_{\mathrm{EP}}\right)^2+(\Gamma/2)^2\right]^2} \tag{8.35}$$

where in the last step, we have assumed that $\omega_{\mathrm{EP}}=\omega_0\sqrt{1+\Gamma/\omega_0}=\omega_0\left[1+\mathcal{O}\left(\Gamma/\omega_0\right)\right]\approx\omega_0$. The last expression in Eq. (8.35) is equal to the expression of Eq. (8.11).

2. Limit of $(\kappa/\mathrm{m})\gg\Gamma\omega_0$: In this case the resonant frequencies are at positions $\omega_-^R\approx\omega_0$ and $\omega_+^R\approx\sqrt{\omega_0^2+2(\kappa/\mathrm{m})}$ (see discussion above Eq 8.22, 8.23). In the vicinity of $\omega_-=\omega_0$ the denominator of Eq. (8.33) can be further simplified leading to the following expression for the DoS:

$$\xi_\infty\left(\omega\approx\omega_-^R\right)\approx\frac{1}{8\pi}\frac{\Gamma/2}{\left(\omega-\omega_{\frac{R}{2}}\right)^2+(\Gamma/2)^2} \tag{8.36}$$

Similarly in the vicinity of $\omega_+^R=\sqrt{\omega_0^2+2(\kappa/\mathrm{m})}$, the denominator of Eq 8.33 can be further simplified leading to the following expression for the DoS:

$$\xi_\infty\left(\omega\approx\omega_+^R\right)\approx\frac{1}{8\pi}\frac{\Gamma/2}{\left(\omega-\omega_+^R\right)^2+(\Gamma/2)^2} \tag{8.37}$$

which is valid under the constraint that $(\kappa/k_1<<1)$

Combining Eqs. (8.36, 8.37) we can come up with the approximate description Eq 8.33 of the LDoS in all frequency range when $\kappa\gg\kappa_{EP}$. Using the results of Eq 8.35, 8.37 we can evaluate the ratio $\mathcal{P}\left(\omega_e=\omega_{EP}\right)=4$.

A more detailed analysis can reveal small deviations from the four-fold enhancement of $\mathcal{P}\left(\omega_e=\omega_{EP}\right)=\frac{\xi_{EP}(\omega_{EP})}{\xi_\infty\left(\omega_+^R\right)}$. Specifically from Eq 8.34, when it is evaluated at EPD we get

$$\xi_{\mathrm{EP}}\left(\omega_{EP}\right)=\frac{1}{\pi\Gamma}\sqrt{1+\frac{\Gamma}{\omega_0}}\approx\frac{1}{\pi\Gamma}\left(1+\frac{1}{2}\frac{\Gamma}{\omega_0}\right)+\mathcal{O}\left(\left(\frac{\Gamma}{\omega_0}\right)^2\right) \tag{8.38}$$

In a similar manner, we evaluate $\xi_\infty\left(\omega_+^R\right)$ using Eq 8.33. specifically by substituting the value $\omega_+^R = \sqrt{\omega_0^2 + 2(\kappa/\mathrm{m})}$ in this expression, we get

$$\xi_\infty\left(\omega_+^R\right) = \frac{1}{4\pi\Gamma}\sqrt{1+\frac{2\kappa}{k_1}} \approx \frac{1}{4\pi\Gamma}\left(1+\frac{\kappa}{k_1}\right) + \mathcal{O}\left(\left(\frac{\kappa}{k_1}\right)^2\right) \tag{8.39}$$

Taking the ratio between Eq 8.38, 8.39, we finally get

$$\mathcal{P}\left(\omega_e = \omega_{EP}\right) \approx 4\frac{\left(1+\frac{1}{2}\frac{\Gamma}{\omega_0}\right)}{\left(1+\frac{\kappa}{k_1}\right)} \approx 4\left(1-\frac{\kappa}{k_1}+\frac{1}{2}\frac{\Gamma}{\omega_0}\right); \tag{8.40}$$

The validity of the above approximations has been confirmed numerically by comparing the expressions in Eqs. (8.32, 8.33) of the main text with the exact numerical results of $\xi(\omega)$ for our metamaterial. In these simulations, the value of $x_2(\omega)$ from Eq. (8.27), has been evaluated using the dispersion characteristics of the dynamic modulus. The numerical results together with the theory is shown in Figure 8.7.

Acknowledgements

RT and AG acknowledge the financial support from the Solid Mechanics Program of the Army Research Office (ARO) (Award No.: W911NF2010160) and the Dynamics, Control, and System Diagnostics (DCSD) Program of the National Science Foundation (NSF) (Award No.: NSF-CMMI-1925530). TK and AK acknowledge the financial support from the DCSD Program of the NSF (Award No.: NSF-CMMI-1925543) and from the Simons Foundation for Collaboration in MPS grant No 733698. We also acknowledge the assistance of Dr. Jizhe Cai on PDMS sample fabrication

Chapter 9

Conclusion

This chapter provides a summary of the research accomplishments made in this thesis that meet the objectives outlined in the introduction chapter. Additionally, we discuss potential future research directions based on the knowledge gaps we identified in our study.

9.1 Research Accomplishments

9.1.1 Research Thrust I : Investigating the fundamental structure-property-function relationship in hierarchically architected vertically aligned carbon nanotube (VACNT) foams.

The research objectives set for this research thrust and the key findings related to each are summarized below.

1. Investigate the fundamental origin of the preconditioning effect in VACNT foams and similar fibrous materials using synchrotron X-ray scattering and mass attenuation experiments.

    (a) Quasi-static compression of VACNT foams results in a disruption of vertical alignment and a decrease in Herman's orientation factor across all hierarchical levels. Anisotropy in density causes a collective, progressive buckling that initiates in the bottom (less dense) region. This region being undergone larger compression, exhibits plastic deformation and permanent densification upon unloading. High-density samples show greater densification and plastic strain compared to low-density samples.

(b) Repeated quasi-static compression leads to a broadening of the 002 x-ray scattering peak. Our findings, supported by data from transmission electron microscopy, reveal that the peak broadening is due to nanoscale strain induced in the multi-walled structure of CNTs as a result of bulk compression (Figure 9.1(a)). The irreversible nanoscale strain, in addition to mesoscale rearrangement of CNTs and increased tortuosity, gives rise to the preconditioning effect.

2. Investigate the dissipative properties of VACNT foams through stress-relaxation, quasistatic compression, and dynamic mechanical analysis using a custom-built dynamic mechanical analyzer. Develop a constitutive model to accurately capture the observed behavior in these experiments.

   (a) In contrast to findings reported in existing literature on VACNT foams, our research reveals that VACNTs exhibit no stress-relaxation (Figure 9.1(b)), indicating a rate-independent behavior. To verify this, we conducted a comprehensive broadband dynamic mechanical analysis using a meticulously constructed and precisely calibrated experimental setup. Our results demonstrate that the dynamic modulus and loss-factor remain constant across frequencies up to 1200 Hz, suggesting a strain-rate independent behavior.

   (b) In our DMA experiments, we observed an amplitude-dependent softening phenomenon known as the Payne effect, where the dynamic modulus decreases with increasing strain amplitude (Figure 9.1(b)).

   (c) We have developed a unique rate-independent friction damping-based constitutive model for VACNT foams that accurately captures both the strain-rate independent behavior and the Payne effect (Figure 9.1(b)).

   (d) In a multilayered system consisting of vertically aligned carbon nanotubes (VACNTs) with stiff interlayers made of aluminum beads, we observe a phenomenon of wave slow-down, where a high-amplitude impulse travels at a reduced speed. The wave slow-down is attributed to friction damping and Payne effect (Figure 9.1(b)).

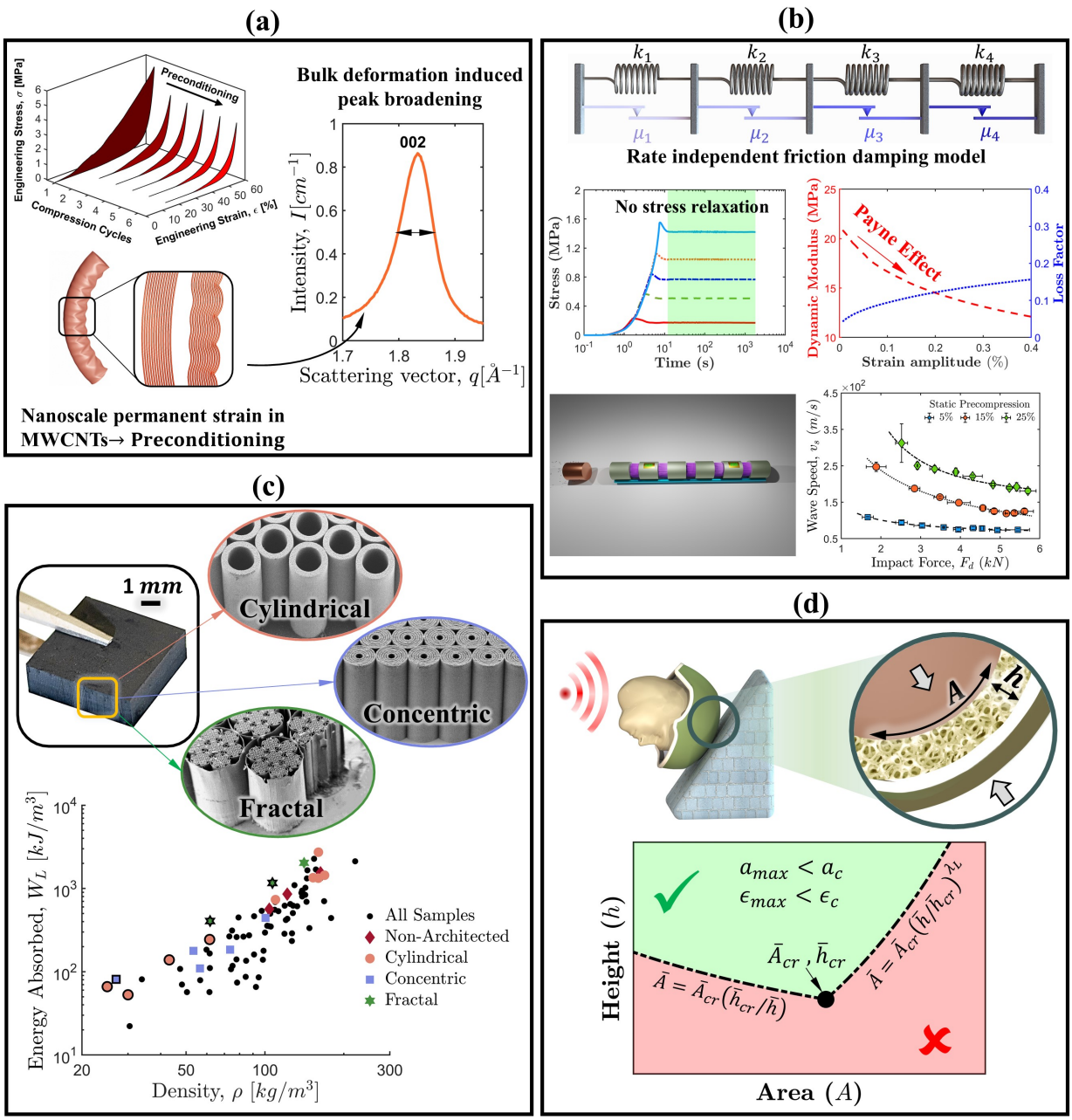

Figure 9.1: Summary of key findings from research thrust-I

3. Improve the specific mechanical properties of VACNT foams by incorporating various mesoscale architectures using photolithography. Study the morphology and mechanical properties of the resultant architected VACNT foams using quasistatic compression, electron microscopy, and phenomenological models.

   (a) We demonstrated a synergistic enhancement in the specific mechanical properties of

VACNT foams with a mesoscale architecture of hexagonally packed cylinders (Figure 9.1(c)). We found that as the cylinders became thinner, there was an improvement in the vertical alignment of CNTs and an increase in the number density of CNTs. This intriguing size effect resulted in high energy absorption at low densities.

(b) We have developed a phenomenological model to illustrate the role of the number density of carbon nanotubes (CNTs) and the curved surface area of cylinders, leveraging lateral interactions between cylinders, which give rise to the size effect.

(c) In addition to the improvement in specific mechanical properties, we observed a more favorable density-dependent scaling of mechanical properties in VACNT foams with a mesoscale architecture of concentric cylinders. Specifically, we noted a shift in density-dependent scaling from an inefficient cubic scaling to a more desirable linear scaling as the internal gap between concentric cylinders is increased. Moreover, as the gap between cylinders increases, we observed a transition in the deformation mode from progressive shell buckling to column buckling, leading to improved scaling and better energy absorption efficiency.

4. To develop a scale-free model for shock absorber design, with focus on investigating the role of sample geometry in energy-absorbing pads and its connection with the mechanical properties of foam. The goal is to minimize the peak acceleration imparted to protective objects.

(a) By employing dimensional analysis and a streamlined kinematic model, we derive conditions on the thickness and cross-sectional area of an energy-absorbing pad to maintain peak acceleration and maximum compression strain in foam within desired limits (Figure 9.1(d)).

(b) We also demonstrate a methodology to achieve the thinnest and most lightweight energy-absorbing pad from foams with a given set of mechanical properties. Contrary to popular belief, we found that foams with a nonlinear stress-strain response can lead to thin and lightweight energy absorbers in various applications.

(c) Implementing our streamlined model and dimensional analysis, we demonstrate optimal performance in architected VACNT foams. We have found that VACNT foams with

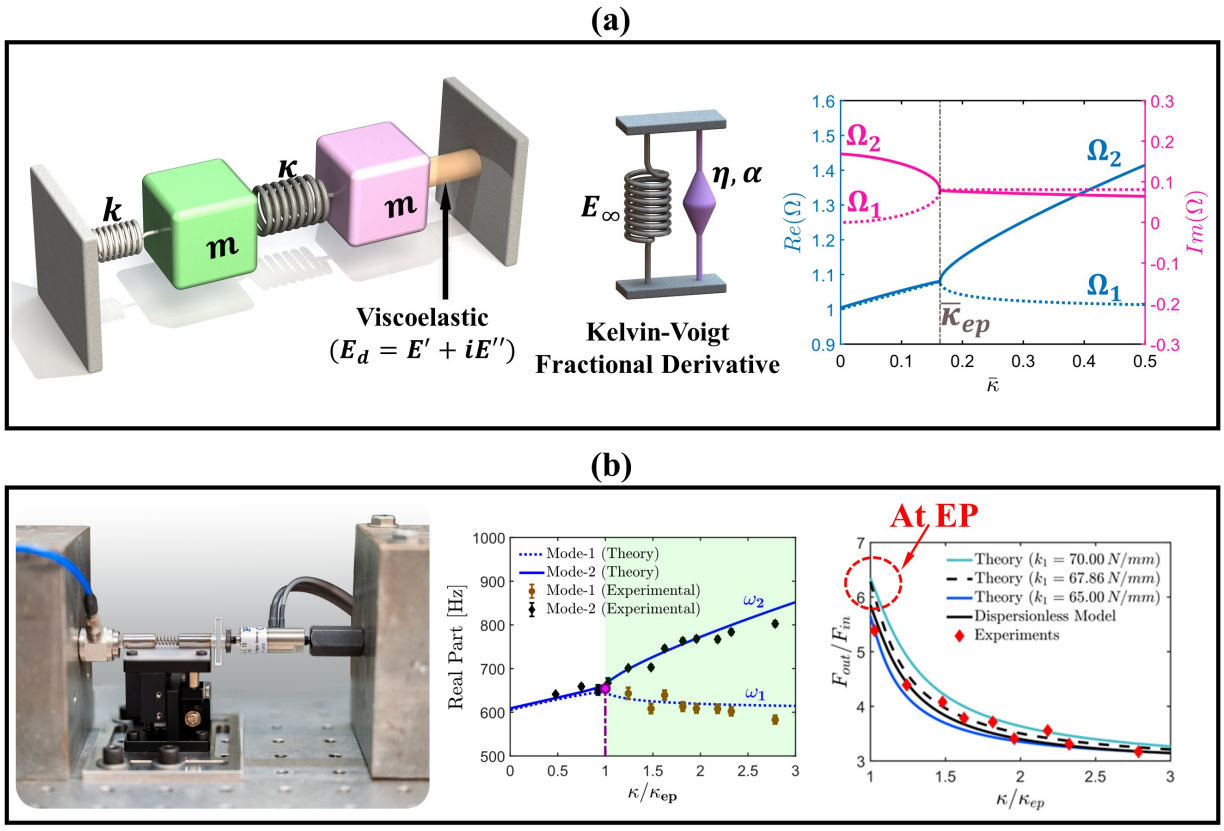

Figure 9.2: Summary of key findings from research thrust-II

higher-order fractal architectures will result in the most lightweight energy absorbers, and VACNT foams with sparsely packed cylinders will result in the thinnest energy absorbers for mass and volume constrained applications, respectively.

9.1.2 Research Thrust II : Studying the formation of exceptional points (EP) in passive non-Hermitian metamaterials with viscoelastic damping.

The research objectives set for this research thrust and the key findings related to each are summarized below.

1. Establish a theoretical framework for using viscoelastic materials as non-Hermitian elements to create exceptional points for highly sensitive sensors and actuators.

   (a) We theoretically demonstrated that among various viscoelastic materials, only those following the Kelvin-Voigt fractional derivative model (Figure 9.2(a)) exhibit a desirable,

nearly frequency-independent loss tangent for the formation of an exceptional point in a passive system. Additionally, we experimentally measured the frequency-dependent loss tangent of various viscoelastic materials. Soft materials like Polydimethylsiloxane (PDMS) follow KVFD model and will result in an exceptional point, whereas natural rubber will not due to a strong dependence of loss-tangent on frequency.

2. Experimentally achieving an exceptional point in a passive elastodynamic metamaterial and demonstrating its ramifications in achieving an enhancement in applied actuation force.

   (a) We experimentally demonstrated an exceptional point in a passive system of coupled mechanical oscillators with non-Hermiticity achieved using viscoelastic PDMS—a KVFD material (Figure 9.2(b)).

   (b) We demonstrated an unusual enhancement of the applied actuation force—a boosting in conventional Purcell enhancement by a factor of 2 when the system operates at the EP compared to when it operated away from EP (Figure 9.2(b)). This is a first-of-its-kind experimental demonstration of emissivity enhancement due to an exceptional point in any physical system.

9.2 Future Research Directions

- **Strain Recovery** : VACNT foams synthesized using various CVD processes display a discrepancy in strain recovery across the literature. To investigate this, we conducted synchrotron X-ray scattering and mass attenuation measurements at Argonne National Laboratory on various samples exhibiting varying degrees of strain recovery. Preliminary analysis suggests that the bulk density and density gradient have an effect on strain recovery. However, further analysis is needed to establish a connection between strain recovery and the deformation-induced changes in hierarchical order.

- **VACNT foam composite** : The bending strength of VACNT foams can be enhanced by infiltrating low-density polymeric foam into the architected VACNT foam structure. To achieve this, VACNT foams can be synthesized with architectures on a much larger length scale ($\sim\ mm$), and the empty spaces can be filled with low-density polymeric foams. While

the VACNTs will improve the stiffness of the composite, the polymeric foam matrix will prevent the CNTs from disintegrating due to repetitive compression and potentially improve strain recovery as well.

- **Enhanced vibration isolation at EP** : Our preliminary analysis indicates that a dynamical system operating near exceptional point degeneracy exhibits improved vibration isolation. In a quarter-car model system, we observed that any impulse resulting from an uneven road settles much faster in the vicinity of exceptional point degeneracy. Further analysis of other systems and experiments are required to corroborate these initial findings.

Appendix A

Synchrotron X-ray scattering

Data correction and reduction

We collected 2D X-ray scattering patterns simultaneously on WAXS, MAXS, and SAXS detectors, while scanning the VACNT sample along its thickness. Before integrating the 2D data to reduce it into 1D intensity profiles, the data was first preprocessed by applying multiple corrections listed in Figure A.1 [254, 255].

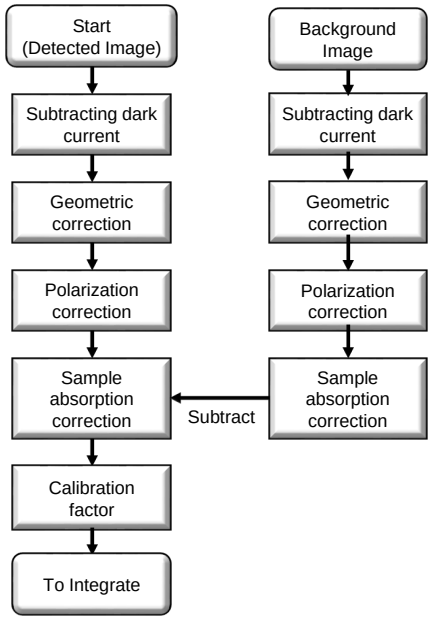

Figure A.1: Sequence of data correction. Detected image is the 2D scattering pattern for X-rays scattered from the VACNT sample, whereas the background image is for scattering without any sample (from ambient air).

The corrected data is then reduced into 1D intensity profiles $I(q)$ and $I(\phi)$ by performing radial and azimuthal integrations, respectively.

$$I(q) = \frac{\int_{\phi-\Delta\phi}^{\phi+\Delta\phi} I(q,\phi)\, d\phi}{\int_{\phi-\Delta\phi}^{\phi+\Delta\phi} d\phi} \qquad I(\phi) = \frac{\int_{q-\Delta q}^{q+\Delta q} I(q,\phi)\, dq}{\int_{q-\Delta q}^{q+\Delta q} dq} \tag{A.1}$$

where I is the intensity recorded at coordinate (q, ϕ) on detector screen, q is the magnitude of scattering vector, and ϕ is the azimuthal angle with the horizontal axis (Figure 3.5). A representative WAXS scattering pattern with integration directions indicated are shown in Figure 3.5. WAXS and MAXS scattering patterns have $\phi_0 = 45°$ azimuthal offset due to the orientation of detectors with respect to scan direction [48].

For radial integration ($I(q)$), the intensities were integrated for a polar 10° thick wedge centered at $\phi = 90°$ ($\phi = 135°$ for WAXS and MAXS due to 45° offset) (Figure 3.10(a)). For azimuthal integration ($I(\phi)$), the intensities were integrated for an arc shaped strip centered at q corresponding to length scale of interest ($2\pi/q$) from $\phi = 0°$ to 90° ($\phi = 45°$ to 135° for WAXS and MAXS) (Figure 3.5)

Using azimuthal intensity profile $I(\phi)$, Herman's orientation factor can be calculated as follows

$$\langle cos^2\phi \rangle = \frac{\int_0^{\frac{\pi}{2}} I(\phi) sin(\phi) cos^2(\phi) d\phi}{\int_0^{\frac{\pi}{2}} I(\phi) sin(\phi) d\phi} \qquad HOF = \frac{1}{2}\left(3\langle cos^2\phi \rangle - 1\right) \tag{A.2}$$

HOF for MAXS and SAXS data are plotted in Figure 3.7. Similar to WAXS data, the orientation decays in the deformed region. An identical trend in orientation factor for all three detectors' data indicates an outright effect of compression on all length scales.

WAXS peak fitting

We used a weighted sum of Gaussian distributions (Gaussian mixture model) to fit the polar 002 peak. An example of peak fitting is shown in Figure A.2. A two-component Gaussian mixture model (GMM) given below yields the best fit for 002 peak.

$$I(q) = \underbrace{a_1 e^{-\frac{(q-\mu_1)^2}{b_1^2}}}_{\text{Minor Peak}} + \underbrace{a_2 e^{-\frac{(q-\mu_2)^2}{b_2^2}}}_{\text{Major Peak}} + \underbrace{c}_{\text{Offset}} \tag{A.3}$$

where c is the offset, μ_1, μ_2 are peak positions, $\frac{b_1}{\sqrt{2}}$, $\frac{b_2}{\sqrt{2}}$ are standard deviations and a_1, a_2 are weightage of minor and major peaks, respectively. FWHM of minor and major peaks can be calculated using following relations

$$FWHM_1 = 2b_1\sqrt{ln(2)} \qquad FWHM_2 = 2b_2\sqrt{ln(2)} \tag{A.4}$$

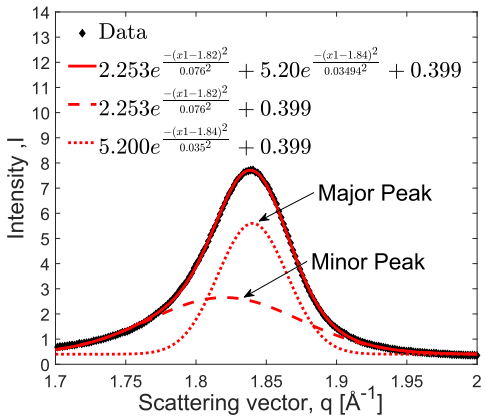

Figure A.2: Peak fitting of 002 peak using GMM

Peak positions and FWHMs of major and minor peaks components for HD and LD sample are plotted in Figure A.3. Peak broadening is observed for both major and minor components in the deformed region which indicates a common source of peak broadening. Both the peaks shifted towards higher q i.e. towards less interwall spacing d [256]. However, the shift is uniform along whole forest which is counterintuitive as compared to other results. Likely, the peak shift is due to an error in measuring sample to detector distance (SDD). We calculated that $\pm 1\,mm$ change in SDD could shift the peak position by 0.44%. The comparative shift of peak position in the bottom region as compared to top region is also not very significant to make any conclusive remarks.

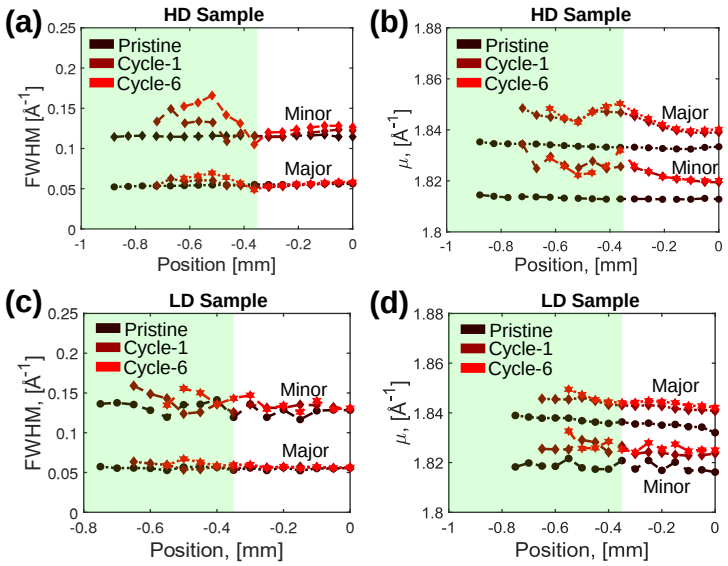

Figure A.3: Polar FWHM of major and minor peaks of (a) HD sample (c) LD sample. Peak position of major and minor peaks (b) HD sample (d) LD sample.

Tortuosity and Polar FWHM

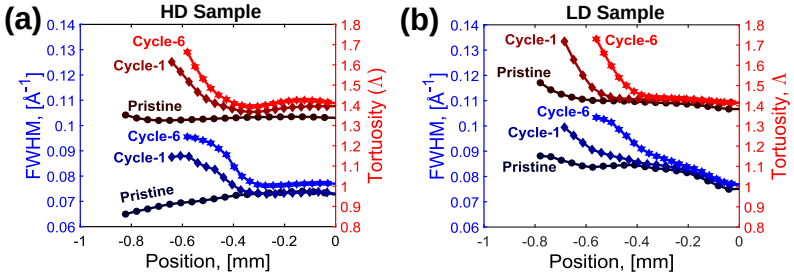

Figure A.4: Polar FWHM of 002 peak and tortuosity for (a) HD samples and (b) LD samples

Appendix B

Architected VACNT foams

Effect of intrinsic density and lateral interactions on SEA

Damping capacity δ is the ratio of energy dissipated W_{dis} (area enclosed within the loading-unloading curve) to the total work done on the material W_L (area under the loading curve)

$$\delta = \frac{W_{\text{dis}}}{W_L} \tag{B.1}$$

We found the damping capacity $\delta \approx 0.83 \pm 0.04$ for all architected VACNT foam samples independent of thickness, gap, and internal-diameter of the mesoscale cylinders. W_{dis} and W_L are in kJ/m^3, whereas δ is a dimensionless quantity. If the bulk density of architected VACNT foam sample is ρ_b, then the specific energy absorption is defined as,

$$SEA = \frac{W_{dis}}{\rho_b} = \delta \frac{W_L}{\rho_b} \tag{B.2}$$

$$SEA = \delta \frac{1}{\rho_b} \int_0^{\epsilon_{\max}} \frac{F_L}{A} d\epsilon \tag{B.3}$$

where, F_L is the force response of architected VACNT foam and A is the total cross-section area (25 mm^2). Assuming F_c is the force response from compression of an isolated cylinder and F_i is the contribution from lateral interactions with neighboring cylinders (due to cylinder's outer surface), then the total force (F_L) is written as

$$F_L = nF_c + nF_i \tag{B.4}$$

where, n is the total number of cylinders in the sample. Substituting this in above equation yields

$$SEA = \delta \frac{1}{\rho_b} \int_0^{\epsilon_{\max}} \frac{nF_c + nF_i}{A} d\epsilon \tag{B.5}$$

$$SEA = \delta \frac{1}{\rho_b} \int_0^{\epsilon_{\max}} \frac{nC_A}{A} \left(\sigma_c + \sigma_i\right) d\epsilon \tag{B.6}$$

where, C_A is the cross-section area of an individual cylinder, σ_c and σ_i are the equivalent stresses for F_c and F_i, respectively, and $nC_A/A = V_f$ is the fill factor. Substituting V_f yields,

$$SEA = \delta \frac{V_f}{\rho_b} \int_0^{\epsilon_{\max}} \left(\sigma_c + \sigma_i\right) d\epsilon \tag{B.7}$$

$$SEA = \delta \frac{1}{\rho_i} \int_0^{\epsilon_{\max}} \left(\sigma_c + \sigma_i\right) d\epsilon \tag{B.8}$$

where, $\rho_i = \rho_b/V_f$ is the intrinsic density of CNT cylinders (i.e., density of VACNT forest within the cylinders' wall region), which we found to be a function of thickness but independent of gap and internal diameter.

$$SEA = \delta \frac{1}{\rho_i} \left[\int_0^{\epsilon_{\max}} \sigma_c d\epsilon\right] + \delta \frac{1}{\rho_i} \left[\int_0^{\epsilon_{\max}} \sigma_i d\epsilon\right] \tag{B.9}$$

Since VACNT foams exhibit a nonlinear stress response in compression, we assume $\sigma_c = f_1(\rho_i) f_2(\epsilon)$. Where $f_1(\rho_i)$ accounts for dependency of elastic modulus on intrinsic density and $f_2(\epsilon)$ accounts for nonlinearity. We hypothesize that the stress (σ_i) due to lateral interactions between outer walls of neighboring cylinders must be a function of normalized outer curved surface area (A_c/A). So, we assume $\sigma_i = g_1\left(\frac{A_c}{A}\right) g_2(\epsilon)$. Where $g_1\left(\frac{A_C}{A}\right)$ accounts for lateral interactions and $g_2(\epsilon)$ accounts for nonlinearities. Substituting these in above equation yields,

$$SEA = \delta f_1\left(\rho_i\right) \frac{1}{\rho_i} \int_0^{\epsilon_{\max}} f_2(\epsilon) d\epsilon + \delta g_1\left(\frac{A_c}{A}\right) \frac{1}{\rho_i} \int_0^{\epsilon_{\max}} g_2(\epsilon) d\epsilon \tag{B.10}$$

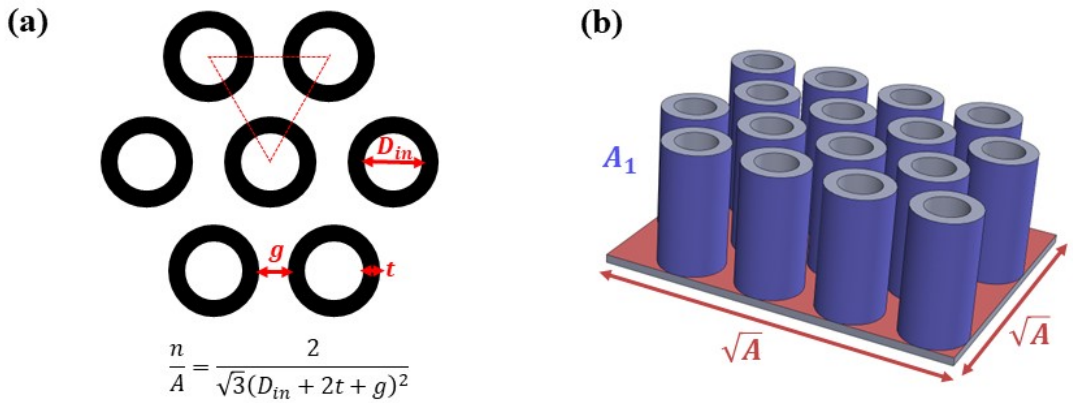

Figure B.1: (a) Calculation of number of cylinders per unit area (b) Total outer curved surface area of cylinders (A_1) and total area of the sample (A).

Integrals $\int_0^{\epsilon_{\max}} f_2(\epsilon)d\epsilon$ and $\int_0^{\epsilon_{\max}} g_2(\epsilon)d\epsilon$ are independent of design variables (t, g, D_{in}), so assuming them to be constants, i.e., $\int_0^{\epsilon_{\max}} f_2(\epsilon)d\epsilon = C_1$ and $\int_0^{\epsilon_{\max}} g_2(\epsilon)d\epsilon = C_2$

$$SEA = \delta f_1(\rho_i)\frac{C_1}{\rho_i} + \delta g_1\left(\frac{A_c}{A}\right)\frac{C_2}{\rho_i} \tag{B.11}$$

$$IEA = \rho_i \times SEA = \delta\left[C_1 f_1(\rho_i) + C_2 g_1\left(\frac{A_c}{A}\right)\right] \tag{B.12}$$

where, IEA is the intrinsic energy absorption. On fitting the experimental data for $D_{in} = 50\mu m$, we found $C_1 \approx 2, C_2 \approx 30.29$, $f_1(\rho_i) = \rho_i$, and $g_2\left(\frac{A_C}{A}\right) = \left(\frac{A_C}{A}\right)^{1.125}$

Normalized curved surface area of cylinders can be calculated as follows

Total number of cylinders in the sample (Figure B.1(a)), $n = \frac{2A}{\sqrt{3}(D_{in}+2t+g)^2}$

Total outer curved surface area (Figure B.1(b)),

$$A_1 = \frac{2A}{\sqrt{3}\left(D_{\text{in}} + 2t + g\right)^2} \times \underbrace{\pi\left(D_{\text{in}} + 2t\right)h}_{\text{Curved Surface Area}} \tag{B.13}$$

Cylinders on the boundaries only touch four other cylinders, so 1/3 of the curved surface area

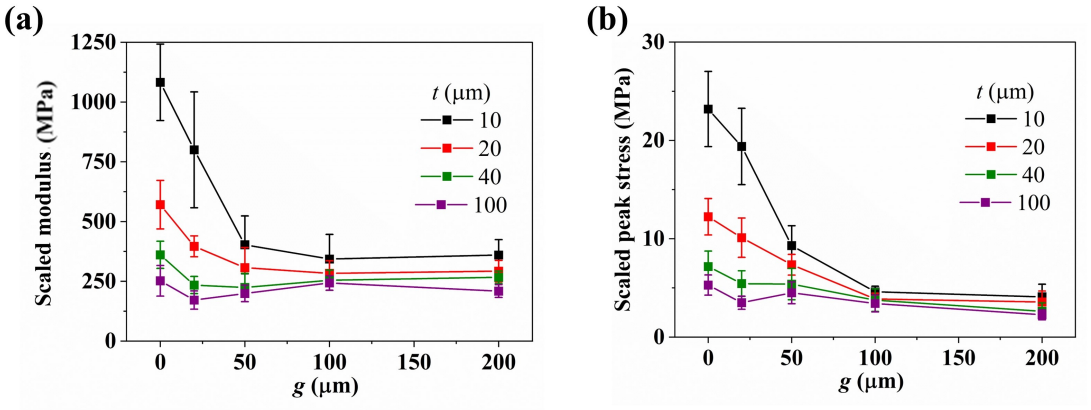

Figure B.2: (a) Scaled modulus and (b) scaled peak stress as functions of t and g

of cylinders on the boundaries must be subtracted. The total area needed to be subtracted is,

$$A_2 = \underbrace{4}_{\text{Total boundaries}} \times \frac{1}{3} \times \frac{\sqrt{A}}{(D_{\text{in}} + 2t + g)} \times \pi \left(D_{\text{in}} + 2t\right) h \times 0.5 \tag{B.14}$$

Where, factor of 0.5 is taken to account if cylinders at the boundary are sliced.

$$\frac{A_1 - A_2}{A} = \pi \left(D_{in} + 2t\right) h \left[\frac{2}{\sqrt{3}\left(D_{in} + 2t + g\right)^2} - \pi \left(D_{in} + 2t\right) h \frac{2}{3\sqrt{A}} \frac{1}{\left(D_{in} + 2t + g\right)}\right] \tag{B.15}$$

Contact curved surface area between cylinders will be half of total area

$$\frac{A_c}{A} = \frac{A_1 - A_2}{2A} = \pi \left(D_{in} + 2t\right) h \left[\frac{1}{\sqrt{3}\left(g + D_{in} + 2t\right)^2} - \frac{1}{3\sqrt{A}} \frac{1}{\left(D_{in} + 2t + g\right)}\right] \tag{B.16}$$

Scaled modulus and scaled peak stress

Similar to SEA, the trend reversal in $t : g$ parameter interaction plots of E^* and σ_p^* disappears after multiplying them by the intrinsic density (ρ_i), underscoring the competing effects between size-effect and the effect of interaction among adjacent cylinders. Scaled modulus $(= E^* \times \rho_i)$ and scaled peak stress $\left(= \sigma_p^* \times \rho_i\right)$ are plotted in the Figure B.2

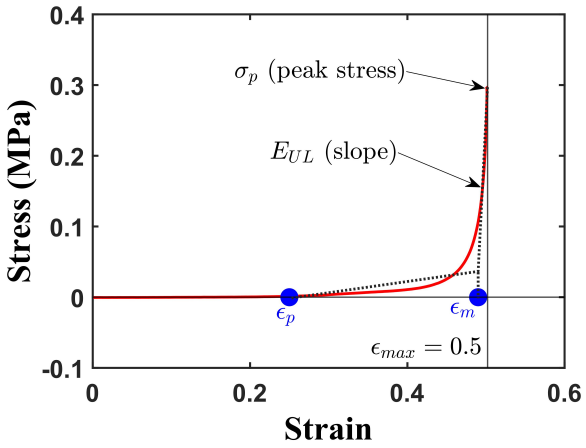

Figure B.3: Typical unloading curve for VACNT foam sample with three different strain regimes indicated (ϵ_{max}) to ϵ_m, ϵ_m to ϵ_p, ϵ_p to 0). Nonlinearity is approximated by dividing the curve into two intersecting linear fits.

Relationship between SEA, σ_p^*, and E^*

Let the area under the unloading curve (work done by the material) be W_{UL}, then

$$W_L = W_{dis} + W_{UL} \tag{B.17}$$

$$\frac{W_L}{W_{dis}} = 1 + \frac{W_{UL}}{W_{dis}} \tag{B.18}$$

$$\frac{1}{\delta} = 1 + \frac{W_{UL}}{W_{dis}} \tag{B.19}$$

$$\frac{SEA \times \rho_b}{W_{UL}} = \frac{\delta}{1-\delta} \quad (W_{\text{dis}} = SEA \times \rho_b) \tag{B.20}$$

W_{UL} can be calculated by adding the area under the unloading curve in three different regimes of strain [58] as shown in Figure B.3

$$W_{UL} = \int_0^{\epsilon_p} 0 \times d\epsilon + \int_{\epsilon_p}^{\epsilon_m} \sigma_1 d\epsilon + \int_{\epsilon_m}^{\epsilon_{\max}} \sigma_2 d\epsilon \tag{B.21}$$

Where ϵ_p is the permanent strain, ϵ_m is the strain at the intersection of two approximated linear regimes ($0.48 < \epsilon_m < 0.49$) shown in Figure B.3, and ϵ_{max} is the maximum compressive

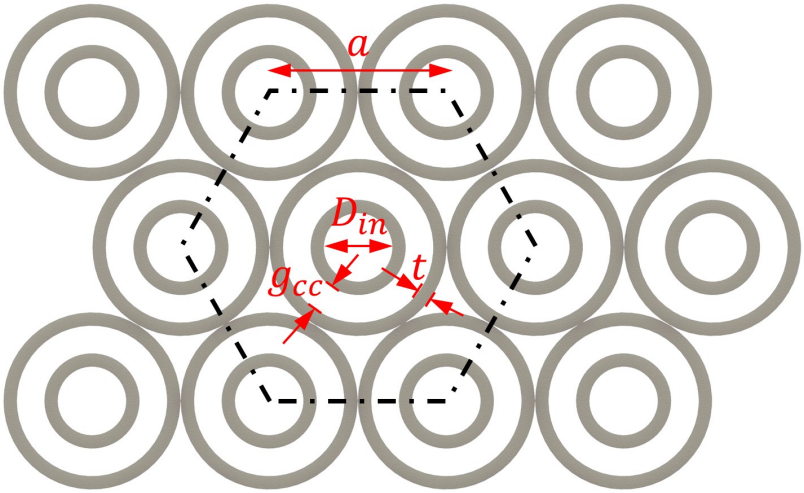

Figure B.4: A schematic of hexagonal closed packed architecture of concentric cylinders (n = 2)

strain ($\epsilon_{max} = 0.5$)

$$\sigma_1 = (\epsilon - \epsilon_p)\frac{(\sigma_p + E_{UL}(\epsilon_m - \epsilon_{\max}))}{(\epsilon_m - \epsilon_p)}, \quad \sigma_2 = \sigma_p + E_{UL}(\epsilon - \epsilon_{\max}) \tag{B.22}$$

where, σ_1 is the linear fit for stress as a function of strain in the first linear regime and σ_2, is the linear fit for stress as a function of strain in the second linear regime (Figure B.3). E_{UL} is the unloading modulus and σ_p is the peak stress.

$$W_{UL} = \sigma_p\left[\frac{2\epsilon_{\max} - \epsilon_m - \epsilon_p}{2}\right] - E_{UL}\left[\frac{(\epsilon_{\max} - \epsilon_m)(\epsilon_{\max} - \epsilon_p)}{2}\right] \tag{B.23}$$

$$SEA = \frac{\delta}{1-\delta} \times \left[\sigma_p^*\left[\frac{2\epsilon_{\max} - \epsilon_m - \epsilon_p}{2}\right] - E^*\left[\frac{(\epsilon_{\max} - \epsilon_m)(\epsilon_{\max} - \epsilon_p)}{2}\right]\right] \tag{B.24}$$

where, $\sigma_p^* = \frac{\sigma_p}{\rho_b}$ is the specific peak stress and $E^* = \frac{E_{UL}}{\rho_b}$ is the specific modulus

Derivation of fill factor

B.0.1 Concentric Cylinders

Cross-section area of m_{th} concentric cylinder

$$A_m = \frac{\pi}{4}\left[(D_{in} + 2tm + 2g_{cc}(m-1))^2 - (D_{in} + 2t(m-1) + 2g_{cc}(m-1))^2\right] \tag{B.25}$$

$$A_m = \pi t \left(D_{in} + 2tm - t + 2g_{cc}(m-1)\right) \tag{B.26}$$

$$\text{Total Area } = \sum_{m=1}^{n} A_m = \pi t \left(nD_{in} + tn(n+1) - nt + 2g_{cc} \left(\frac{n(n+1)}{2} - n \right) \right) \tag{B.27}$$

$$A_T = \pi nt \left(D_{in} + tn + g_{cc}(n-1)\right) \tag{B.28}$$

From Figure B.4

$$a = D_{in} + 2tm + 2g_{cc}(m-1) \tag{B.29}$$

$$\text{Hexagon Area, } \mathrm{A_H} = \frac{3\sqrt{3}}{2} \left(D_{in} + 2tn + 2g_{cc}(n-1)\right)^2 \tag{B.30}$$

$$\text{Fill Factor, } V_f = \frac{3A_T}{A_H} = \frac{2\pi nt \left(D_{in} + tn + g_{cc}(n-1)\right)}{\sqrt{3} \left(D_{in} + 2tn + 2g_{cc}(n-1)\right)^2} \tag{B.31}$$

B.0.2 Fractal architecture

In fractal architecture, for each order, the outer diameter of the outermost cylinder that is arranged in hexagonal pattern can be calculated using the following equation

$$D_k = 3^k D_{in} + \left(3^{k+1} - 1\right) t_w \tag{B.32}$$

Where, D_{in} is the inner diameter and t_w is the wall thickness of the innermost cylinder. Both D_{in} and t_w are constant for all fractal orders (Figure B.5)

We derived the expression for the total area of outermost cylinder after subtracting the area of empty space as follows

$$A_k = \pi t_w \left(\frac{(D_{in} + 3t_w)}{4} \left(7^{k+1} - 3^{k+1}\right) - \frac{t_w}{3} \left(7^{k+1} - 1\right) \right) \tag{B.33}$$

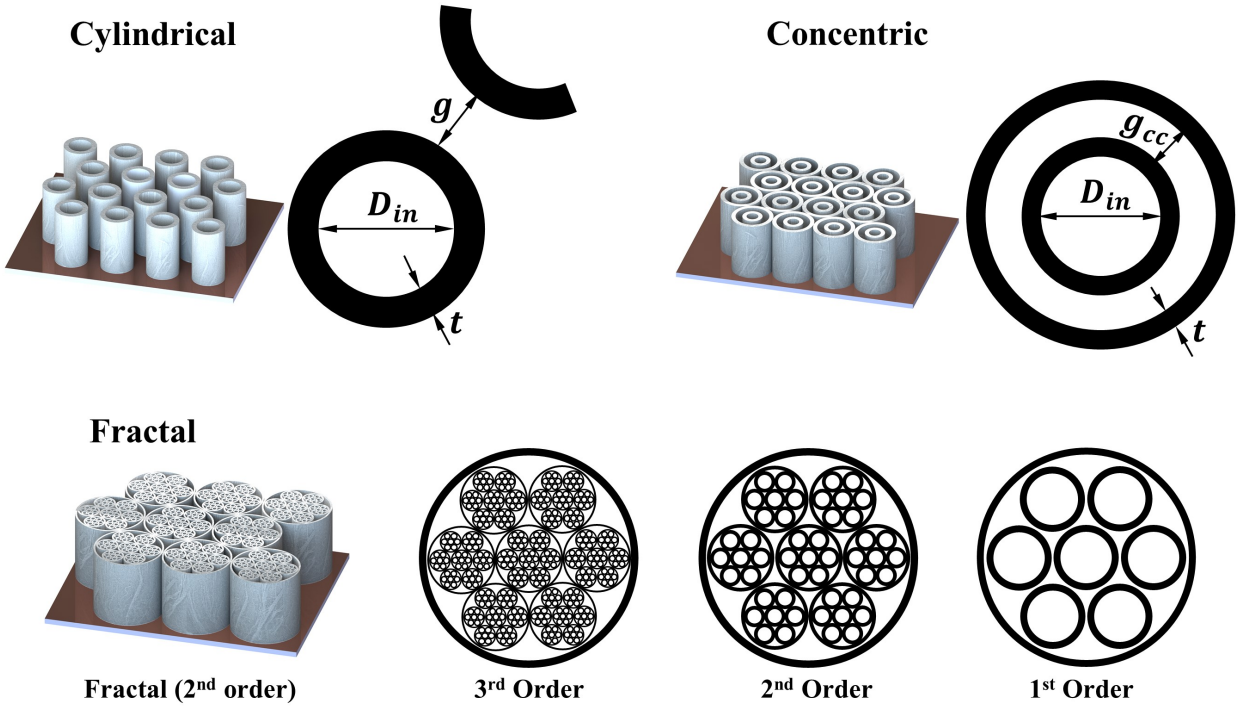

Figure B.5: Illustrations of various architectures

Using the expressions for D_k and A_k we can calculate the volume fraction (V_f) for a fractal architecture of k^{th} order as follows

$$V_f = \frac{A_k}{\frac{\sqrt{3}}{2}\left(D_k\right)^2} \tag{B.34}$$

$$V_f = \frac{2\pi t_w}{\sqrt{3}} \times \frac{1}{\left(3^k D_{in} + \left(3^{k+1}-1\right) t_w\right)^2} \times \left(\frac{\left(D_{in}+3t_w\right)}{4}\left(7^{k+1}-3^{k+1}\right) - \frac{t_w}{3}\left(7^{k+1}-1\right)\right) \tag{B.35}$$

B.0.3 Cylindrical architecture

$$V_f = \frac{2\pi\left(D_{in}+t\right)t}{\sqrt{3}\left(g+D_{in}+2t\right)^2} \tag{B.36}$$

Where D_{in} and t are the inner diameter and wall thickness of cylinders whereas g is the external gap between the cylinders as shown in Figure B.5

Appendix C

Non-Hermitian elastodynamics

Differential Frictional Damping

For coupled oscillators dimer with differential frictional damping, governing equations of motion are as follows

$$m\ddot{x}_1 + k_1 x_1 + (\gamma_1 N_1) \times \operatorname{sgn}(\dot{x}_1) + \kappa (x_1 - x_2) = 0 \tag{C.1}$$

$$m\ddot{x}_2 + k_2 x_2 + (\gamma_2 N_2) \times \operatorname{sgn}(\dot{x}_2) + \kappa (x_2 - x_1) = 0 \tag{C.2}$$

For steady state solution, assuming $x_1 = X_1 e^{i\omega t}, x_2 = X_2 e^{i\omega t}$

$$\operatorname{sgn}(\dot{x}_1) = \frac{\dot{x}_1}{|\dot{x}_1|} = i = \sqrt{-1} \tag{C.3}$$

Substituting $N_1 = k_1 \times x_1$, $N_2 = k_2 \times x_2$ (Structural damping due to spring's material)

$$-\omega^2 m X_1 + k_1 X_1 (1 + i\gamma_1) + \kappa (X_1 - X_2) = 0 \tag{C.4}$$

$$-\omega^2 m X_2 + k_2 X_2 (1 + i\gamma_2) + \kappa (X_2 - X_1) = 0 \tag{C.5}$$

$$\text{Let } k_1 = k_2 = k = \omega_0^2 m, \Omega = \frac{\omega}{\omega_0}, \frac{\kappa}{k} = \bar{\kappa} \tag{C.6}$$

$$\begin{aligned} X_1 \left(-\Omega^2 + 1 + i\gamma_1 + \bar{\kappa}\right) - X_2(\bar{\kappa}) = 0 \\ X_2 \left(-\Omega^2 + 1 + i\gamma_2 + \bar{\kappa}\right) - X_1(\bar{\kappa}) = 0 \end{aligned} \tag{C.7}$$

$$\begin{bmatrix} -\Omega^2+1+i\gamma_1+\bar{\kappa} & -\bar{\kappa} \\ -\bar{\kappa} & -\Omega^2+1+i\gamma_2+\bar{\kappa} \end{bmatrix} \begin{Bmatrix} X_1 \\ X_2 \end{Bmatrix} = 0 \tag{C.8}$$

$$[\mathcal{H}]\{\psi\} = 0 \tag{C.9}$$

$$\Lambda(\Omega) = |\mathcal{H}| = \left(-\Omega^2+1+i\gamma_1+\bar{\kappa}\right)\left(-\Omega^2+1+i\gamma_2+\bar{\kappa}\right) - \bar{\kappa}^2 = 0 \text{ (For non - trivial Solutions)} \tag{C.10}$$

$$\Lambda(\Omega) = |\mathcal{H}| = \Omega^4 - 2\Omega^2 - i\left(\gamma_2+\gamma_1\right)\Omega^2 - 2\bar{\kappa}\Omega^2 + 1 + i\left(\gamma_2+\gamma_1\right) + i\left(\gamma_1+\gamma_2\right)\bar{\kappa} + 2\bar{\kappa} - \gamma_1\gamma_2 = 0 \tag{C.11}$$

PT Symmetric case

$$\gamma_1 = -\gamma(\text{ Gain }), \gamma_2 = +\gamma(\text{ Loss }) \quad (\gamma > 0) \tag{C.12}$$

$$\Lambda(\Omega) = \Omega^4 - 2\Omega^2 - 2\bar{\kappa}\Omega^2 + 1 + 2\bar{\kappa} + \gamma^2 = 0 \tag{C.13}$$

$$\Lambda(\Omega) = \Omega^4 + \Omega^2(-2-2\bar{\kappa}) + 1 + 2\bar{\kappa} + \gamma^2 = 0 \text{ (Biquadratic Equation)} \tag{C.14}$$

$$\Omega^2 = 1 + \bar{\kappa} \pm \sqrt{\bar{\kappa}^2 - \gamma^2} \tag{C.15}$$

For roots to be real and equal at exceptional point, the term inside square-root should be equal to zero

$$\bar{\kappa}^2 - \gamma^2 = 0 \tag{C.16}$$

$$\bar{\kappa}_{ep} = \gamma \tag{C.17}$$

Passive non-Hermitian case (no Loss-Loss)

$$\gamma_1 = 0(\text{ no Loss }), \gamma_2 = \gamma(\text{ Loss }) \tag{C.18}$$

$$\Lambda(\Omega) = |\mathcal{H}| = \Omega^4 - 2\Omega^2 - i(\gamma)\Omega^2 - 2\bar{\kappa}\Omega^2 + 1 + i(\gamma) + i(\gamma)\bar{\kappa} + 2\bar{\kappa} = 0 \text{ (Biquadratic Equation)} \tag{C.19}$$

$$\Omega^2 = \frac{2 + i\gamma + 2\bar{\kappa} \pm \sqrt{4\bar{\kappa}^2 - \gamma^2}}{2} \tag{C.20}$$

For roots to be equal at exceptional point

$$4\bar{\kappa}^2 - \gamma^2 = 0 \tag{C.21}$$

$$\bar{\kappa}_{ep} = \frac{\gamma}{2} \tag{C.22}$$

Kelvin-Voigt Solid

Governing equations of motion for coupled oscillators with a Kelvin-Voigt viscoelastic solid of cross-section area A and length L as the dissipative element. First, we consider the PT symmetric case to derive the location of exceptional point in the parameter space

$$\begin{aligned} -\omega^2 m X_1 + k_1 X_1 + \kappa\left(X_1 - X_2\right) = 0 \\ -\omega^2 m X_2 + k_2 X_2 + \kappa\left(X_2 - X_1\right) = 0 \end{aligned} \tag{C.23}$$

$$\text{where } k_1 = \frac{A}{L}\left(E_\infty + i\omega\eta_1\right), k_2 = \frac{A}{L}\left(E_\infty + i\omega\eta_2\right) \tag{C.24}$$

$$\text{Assuming } k = \frac{E_\infty A}{L} = m\omega_0^2, \Omega = \frac{\omega}{\omega_0}, \bar{\kappa} = \frac{\kappa}{k} \tag{C.25}$$

$$\begin{aligned} -\Omega^2 X_1 + X_1 + i\Omega\gamma_1 X_1 + \bar{\kappa}\left(X_1 - X_2\right) = 0 \\ -\Omega^2 X_2 + X_2 + i\Omega\gamma_2 X_2 + \bar{\kappa}\left(X_2 - X_1\right) = 0 \end{aligned} \tag{C.26}$$

$$\text{where } \gamma_1 = \frac{\eta_1}{m\omega_0}\frac{A}{L}, \quad \gamma_2 = \frac{\eta_2}{m\omega_0}\frac{A}{L} \tag{C.27}$$

$$\begin{bmatrix} -\Omega^2 + 1 + i\Omega\gamma_1 + \bar{\kappa} & -\bar{\kappa} \\ -\bar{\kappa} & -\Omega^2 + 1 + i\Omega\gamma_2 + \bar{\kappa} \end{bmatrix} \begin{Bmatrix} X_1 \\ X_2 \end{Bmatrix} = 0 \tag{C.28}$$

$$\Lambda(\Omega) = \Omega^4 - i\left(\gamma_1 + \gamma_2\right)\Omega^3 + \left(-2\bar{\kappa} - 2 - \gamma_1\gamma_2\right)\Omega^2 + i\Omega\left(\gamma_1 + \gamma_2\right)\left(1 + \bar{\kappa}\right) + 2\bar{\kappa} + 1 = 0 \tag{C.29}$$

PT Symmetric case

$$\gamma_1 = -\gamma(\text{ Gain }), \quad \gamma_2 = \gamma(\text{ Loss }) \tag{C.30}$$

$$\Lambda(\Omega) = \Omega^4 + \left(-2\bar{\kappa} - 2 + \gamma^2\right)\Omega^2 + 2\bar{\kappa} + 1 = 0 \text{ (Biquadratic Equation)} \tag{C.31}$$

$$\left(-2\bar{\kappa}-2+\gamma^2\right)^2-4(2\bar{\kappa}+1)=0 \quad \text{(For real and equal roots)} \tag{C.32}$$

$$\bar{\kappa}=\frac{1}{2}\left(\gamma^2-2\gamma\right),\bar{\kappa}=\frac{1}{2}\left(\gamma^2+2\gamma\right) \tag{C.33}$$

But $\bar{\kappa}>0\ \forall\ \gamma\in\mathcal{R}$

$$\bar{\kappa}_{ep}=\frac{1}{2}\left(\gamma^2+2\gamma\right) \tag{C.34}$$

Passive non-Hermitian case (no Loss-Loss)

$$\gamma_1=0(\text{ no Loss }),\gamma_2=\gamma(\text{ Loss }) \tag{C.35}$$

$$\Lambda(\Omega)=\Omega^4-i(\gamma)\Omega^3-2(\bar{\kappa}+1)\Omega^2+i\Omega(\gamma)(1+\bar{\kappa})+2\bar{\kappa}+1=0 \text{ (Quartic Polynomial)} \tag{C.36}$$

Above equation cannot be solved analytically; however, from numerical solutions, we observed

$$\bar{\kappa}_{ep}\approx\frac{1}{4}\left(\frac{2}{5}\gamma^2+2\gamma\right) \tag{C.37}$$

Standard Linear Solid

Governing equations for coupled oscillators with SLS material of cross-sectional area A and length L as the dissipative element

$$m\ddot{x_1}+k_1x_1+\kappa\left(x_1-x_2\right)=0 \tag{C.38}$$

$$m\ddot{x_2}+k_2x_2+\kappa\left(x_2-x_1\right)=0 \tag{C.39}$$

$$k_2=k_d=\frac{A}{L}E_d=\frac{A}{L}\left(E_\infty+E_t\frac{\omega^2\tau^2}{1+\omega^2\tau^2}+iE_t\frac{\omega\tau}{1+\omega^2\tau^2}\right) \tag{C.40}$$

$$k_d=k_\infty+k_t\frac{\omega^2\tau^2}{1+\omega^2\tau^2}+ik_t\frac{\omega\tau}{1+\omega^2\tau^2} \tag{C.41}$$

$$-\omega^2mX_1+k_1X_1+\kappa\left(X_1-X_2\right)=0 \tag{C.42}$$

$$-\omega^2mX_2+\left(k_\infty+k_t\frac{\omega^2\tau^2}{1+\omega^2\tau^2}+ik_t\frac{\omega\tau}{1+\omega^2\tau^2}\right)X_2+\kappa\left(X_2-X_1\right)=0 \tag{C.43}$$

$$k_1=k,k_\infty=\frac{E_\infty A}{h},k_t=\frac{E_tA}{h},\bar{\kappa}=\frac{\kappa}{k},\Omega=\frac{\omega}{\omega_0},\omega_0=\sqrt{\frac{k}{m}},T=\omega_0\tau_1 \tag{C.44}$$

$$\begin{bmatrix} -\Omega^2+1+\bar{\kappa} & -\bar{\kappa} \\ -\bar{\kappa} & -\Omega^2+\frac{1}{k}\left(k_\infty+\frac{k_t(\Omega^2T^2)}{(1+\Omega^2T^2)}+\frac{ik_t(\Omega T)}{(1+\Omega^2T^2)}\right)+\bar{\kappa} \end{bmatrix} \begin{Bmatrix} X_1 \\ X_2 \end{Bmatrix} = 0 \tag{C.45}$$

Determinant of above matrix gives a sixth order polynomial of *Omega* as follows

$$\Omega^6T_1^2+\Omega^4\left(1-\frac{k_\infty}{k_1}T_1^2-\frac{k_{t,1}}{k_1}T_1^2-\bar{\kappa}T_1^2\right)-\Omega^3\left(i\frac{k_{t,1}}{k_1}T_1\right)-\Omega^2\left(\bar{\kappa}+\frac{k_\infty}{k_1}\right) \tag{C.46}$$

$$-\Omega^2(1+\bar{\kappa})\left(1-\frac{k_\infty}{k_1}T_1^2-\frac{k_{t,1}}{k_1}T_1^2-\bar{\kappa}T_1^2\right)-\Omega^4(1+\bar{\kappa})T_1^2 \tag{C.47}$$

$$+\Omega(1+\bar{\kappa})\left(i\frac{k_{t,1}}{k_1}T_1\right)+(1+\bar{\kappa})\left(\bar{\kappa}+\frac{k_\infty}{k_1}\right)-\bar{\kappa}^2\left(1+\Omega^2T_1^2\right)=0 \tag{C.48}$$

Solving the above equation gives six roots, among which only two roots represent the two modes of the system

Kelvin-Voigt Fractional Derivative (KVFD) Solid

Governing equations for coupled oscillators with KVFD material of cross-sectional area A and length L as the dissipative element

$$m\ddot{x}_1+k_1x_1+\kappa\left(x_1-x_2\right)=0 \tag{C.49}$$

$$m\ddot{x}_2+k_2x_2+\kappa\left(x_2-x_1\right)=0 \tag{C.50}$$

Derivation of relaxation modulus

Assuming the modulus of spring is E_∞, damping coefficient and exponent for springpot are η and α respectively. Total stress response of KVFD solid for an applied strain $\epsilon(t)$

$$\sigma(t)=E_\infty\epsilon(t)+\eta\frac{d^\alpha\epsilon(t)}{dt^\alpha}\quad(0<\alpha<1) \tag{C.51}$$

$\epsilon(t)=\epsilon_0H(t)$ (Applying step strain to calculate the stress relaxation modulus)

$$\frac{d^\alpha\epsilon_0H(t)}{dt^\alpha}=\frac{d^{[\alpha]+1}}{dt^{[\alpha]+1}}\left(\frac{d^{\alpha-[\alpha]-1}\epsilon_0H(t)}{dt^{\alpha-[\alpha]-1}}\right) \tag{C.52}$$

where, $[\alpha]$ is the greatest integer function. Since $0 < \alpha < 1$, $[\alpha]$=0

Applying Riemann–Liouville fractional integral method

$$\epsilon_0 \frac{d}{dt}\left(\frac{d^{\alpha-1}H(t)}{dt^{\alpha-1}}\right) = \epsilon_0 \frac{d}{dt}\left(\frac{1}{\Gamma(1-\alpha)}\int_{-\infty}^{t}\frac{H(t')}{(t-t')^{\alpha}}dt'\right) \tag{C.53}$$

$$\epsilon_0 \frac{d}{dt}\left(\frac{1}{\Gamma(1-\alpha)}\int_{0}^{\infty}\frac{H(t-p)}{(p)^{\alpha}}dp\right)\left(t-t' \to p\right) \tag{C.54}$$

$$\epsilon_0 \frac{d}{dt}\left(\frac{1}{\Gamma(1-\alpha)}\left(\int_{0}^{t}\frac{H(t-p)}{(p)^{\alpha}}dp + \int_{t}^{\infty}\frac{H(t-p)}{(p)^{\alpha}}dp\right)\right) \tag{C.55}$$

$$\epsilon_0 \frac{d}{dt}\left(\frac{1}{\Gamma(1-\alpha)}\left(\int_{0}^{t}p^{-\alpha}dp\right) + 0\right) \tag{C.56}$$

$$\frac{\epsilon_0}{\Gamma(1-\alpha)}\frac{d}{dt}\left(\frac{t^{1-\alpha}}{1-\alpha}\right) = \frac{\epsilon_0}{\Gamma(1-\alpha)}t^{-\alpha} \tag{C.57}$$

$$\sigma(t) = E_{\infty}\epsilon_0 + \eta\frac{\epsilon_0}{\Gamma(1-\alpha)}t^{-\alpha} \tag{C.58}$$

$$E(t) = \frac{\sigma(t)}{\epsilon_0} = E_{\infty} + \eta\frac{1}{\Gamma(1-\alpha)}t^{-\alpha} \quad \text{(Relaxation Modulus)} \tag{C.59}$$

Derivation of dynamic modulus

$$\epsilon(t) = \epsilon_0 + \epsilon_d e^{i\omega t} \tag{C.60}$$

$$\sigma(t) = \sigma_{\infty} + \sigma_d e^{i\omega t} = E_{\infty}\epsilon_0 + E_{\infty}\epsilon_d e^{i\omega t} + \epsilon_d\eta\frac{d^{\alpha}e^{i\omega t}}{dt^{\alpha}} \tag{C.61}$$

$$\frac{d^{\alpha}e^{i\omega t}}{dt^{\alpha}} = \frac{d}{dt}\left(\frac{d^{\alpha-1}e^{i\omega t}}{dt^{\alpha-1}}\right) = \frac{d}{dt}\left(\frac{1}{\Gamma(1-\alpha)}\int_{-\infty}^{t}\frac{e^{i\omega t'}}{(t-t')^{\alpha}}dt'\right) \quad (\alpha - 1 < 0) \tag{C.62}$$

$$\frac{d^{\alpha}e^{i\omega t}}{dt^{\alpha}} = \frac{d}{dt}\left(\frac{1}{\Gamma(1-\alpha)}\int_{0}^{\infty}\frac{e^{i\omega t}e^{-i\omega p}}{(p)^{\alpha}}dp\right) \quad \left(t-t' = p\right) \tag{C.63}$$

$$\frac{d^{\alpha}e^{i\omega t}}{dt^{\alpha}} = \frac{d}{dt}\left(e^{i\omega t}\frac{1}{\Gamma(1-\alpha)}\frac{1}{i\omega}(i\omega)^{\alpha}\int_{0}^{\infty}e^{-x}x^{1-\alpha-1}dx\right) \quad (i\omega p = x) \tag{C.64}$$

$$\frac{d^{\alpha}e^{i\omega t}}{dt^{\alpha}} = \frac{1}{\Gamma(1-\alpha)}(i\omega)^{\alpha}\frac{d}{dt}\left(e^{i\omega t}\frac{1}{i\omega}\right)\int_{0}^{\infty}e^{-x}x^{1-\alpha-1}dx \tag{C.65}$$

$$\frac{d^{\alpha}e^{i\omega t}}{dt^{\alpha}} = \frac{1}{\Gamma(1-\alpha)}(i\omega)^{\alpha}e^{i\omega t}\Gamma(1-\alpha) \tag{C.66}$$

$$\sigma_d e^{i\omega t} = \left(E_{\infty} + \eta(i\omega)^{\alpha}\right)\epsilon_d e^{i\omega t} \tag{C.67}$$

$$E_d = E_\infty + \eta(i\omega)^\alpha = E_\infty + \eta\omega^\alpha\left(\cos\left(\frac{\pi}{2}\alpha\right) + i\sin\left(\frac{\pi}{2}\alpha\right)\right) \quad \text{(Dynamic Modulus)} \tag{C.68}$$

Substituting the expression of dynamic modulus in governing equations

$$k_2 = k_d = \frac{A}{L}E_d = \frac{A}{L}\left(E_\infty + \eta\cos\left(\frac{\pi}{2}\alpha\right)\omega^\alpha + i\eta\sin\left(\frac{\pi}{2}\alpha\right)\omega^\alpha\right) \tag{C.69}$$

$$k_1 = k, k_\infty = \frac{E_\infty A}{L}, \gamma = \frac{\eta\omega_0^\alpha A}{L}, \Omega = \frac{\omega}{\omega_0}, \omega_0 = \sqrt{\frac{k}{m}} \tag{C.70}$$

$$\frac{k_d}{k} = \frac{1}{k}\left(k_\infty + \gamma\cos\left(\frac{\pi}{2}\alpha\right)\Omega^\alpha + i\gamma\sin\left(\frac{\pi}{2}\alpha\right)\Omega^\alpha\right) \tag{C.71}$$

$$\begin{bmatrix} -\Omega^2 + 1 + \bar{\kappa} & -\bar{\kappa} \\ -\bar{\kappa} & -\Omega^2 + \frac{1}{k}\left(k_\infty + \gamma\cos\left(\frac{\pi}{2}\alpha\right)\Omega^\alpha + i\gamma\sin\left(\frac{\pi}{2}\alpha\right)\Omega^\alpha\right) + \bar{\kappa} \end{bmatrix} \begin{Bmatrix} X_1 \\ X_2 \end{Bmatrix} = 0 \tag{C.72}$$

Bibliography

[1] Lorna J Gibson. "Cellular solids". In: *Mrs Bulletin* 28.4 (2003), pp. 270–274.

[2] Michael F Ashby. "The properties of foams and lattices". In: *Philosophical Transactions of the Royal Society A: Mathematical, Physical and Engineering Sciences* 364.1838 (2006), pp. 15–30.

[3] Julia R Greer and Vikram S Deshpande. "Three-dimensional architected materials and structures: Design, fabrication, and mechanical behavior". In: *MRS Bulletin* 44.10 (2019), pp. 750–757.

[4] Sha Yin et al. "Light but tough bio-inherited materials: Luffa sponge based nickel-plated composites". In: *Journal of the mechanical behavior of biomedical materials* 94 (2019), pp. 10–18.

[5] Madeleine Grossman et al. "Hierarchical toughening of nacre-like composites". In: *Advanced Functional Materials* 29.9 (2019), p. 1806800.

[6] S Koumlis and L Lamberson. "Strain rate dependent compressive response of open cell polyurethane foam". In: *Experimental Mechanics* 59.7 (2019), pp. 1087–1103.

[7] Mohammad Reza Shariatmadari, Russell English, and Glynn Rothwell. "Effects of temperature on the material characteristics of midsole and insole footwear foams subject to quasi-static compressive and shear force loading". In: *Materials & Design* 37 (2012), pp. 543–559.

[8] J Baumeister, J Banhart, and M1 Weber. "Aluminium foams for transport industry". In: *Materials & design* 18.4-6 (1997), pp. 217–220.

[9] Robert O Ritchie. "The conflicts between strength and toughness". In: *Nature materials* 10.11 (2011), pp. 817–822.

[10] Roderic Lakes. "Materials with structural hierarchy". In: *Nature* 361.6412 (1993), pp. 511–515.

[11] Komal Chawla et al. "Superior mechanical properties by exploiting size-effects and multiscale interactions in hierarchically architected foams". In: *Extreme Mechanics Letters* 57 (2022), p. 101899.

[12] Nayeon Lee et al. "Hierarchical multiscale structure–property relationships of the red-bellied woodpecker (Melanerpes carolinus) beak". In: *Journal of The Royal Society Interface* 11.96 (2014), p. 20140274.

[13] Anyuan Cao et al. "Super-compressible foamlike carbon nanotube films". In: *Science* 310.5752 (2005), pp. 1307–1310.

[14] Ramathasan Thevamaran, Eric R Meshot, and Chiara Daraio. "Shock formation and rate effects in impacted carbon nanotube foams". In: *Carbon* 84 (2015), pp. 390–398.

[15] Abhishek Gupta et al. "Origins of mechanical preconditioning in hierarchical nanofibrous materials". In: *Extreme Mechanics Letters* 50 (2022), p. 101576.

[16] Ming Xu et al. "Carbon nanotubes with temperature-invariant viscoelasticity from–196 to 1000 C". In: *Science* 330.6009 (2010), pp. 1364–1368.

[17] Jordan R Raney, Abha Misra, and Chiara Daraio. "Tailoring the microstructure and mechanical properties of arrays of aligned multiwall carbon nanotubes by utilizing different hydrogen concentrations during synthesis". In: *Carbon* 49.11 (2011), pp. 3631–3638.

[18] Komal Chawla, Abhishek Gupta, and Ramathasan Thevamaran. "Disrupting Density-Dependent Property Scaling in Hierarchically Architected Foams". In: *ACS nano* 17.11 (2023), pp. 10452–10461.

[19] Tobias A Schaedler et al. "Ultralight metallic microlattices". In: *Science* 334.6058 (2011), pp. 962–965.

[20] Fang Qian et al. "Ultralight conductive silver nanowire aerogels". In: *Nano letters* 17.12 (2017), pp. 7171–7176.

[21] VS Deshpande and NA Fleck. "High strain rate compressive behaviour of aluminium alloy foams". In: *International Journal of Impact Engineering* 24.3 (2000), pp. 277–298.

[22] Brooks H Smith et al. "Characterization of steel foams for structural components". In: *Metals* 2.4 (2012), pp. 399–410.

[23] Lucas R Meza, Satyajit Das, and Julia R Greer. "Strong, lightweight, and recoverable three-dimensional ceramic nanolattices". In: *Science* 345.6202 (2014), pp. 1322–1326.

[24] Xiaoyu Zheng et al. "Ultralight, ultrastiff mechanical metamaterials". In: *Science* 344.6190 (2014), pp. 1373–1377.

[25] Rodion Kononchuk et al. "Exceptional-point-based accelerometers with enhanced signal-to-noise ratio". In: *Nature* 607.7920 (2022), pp. 697–702.

[26] Mohammad-Ali Miri and Andrea Alu. "Exceptional points in optics and photonics". In: *Science* 363.6422 (2019), eaar7709.

[27] Hossein Hodaei et al. "Enhanced sensitivity at higher-order exceptional points". In: *Nature* 548.7666 (2017), pp. 187–191.

[28] Şahin Kaya Özdemir et al. "Parity–time symmetry and exceptional points in photonics". In: *Nature materials* 18.8 (2019), pp. 783–798.

[29] Yanghao Fang, Tsampikos Kottos, and Ramathasan Thevamaran. "Universal route for the emergence of exceptional points in PT-symmetric metamaterials with unfolding spectral symmetries". In: *New Journal of Physics* 23.6 (2021), p. 063079.

[30] Arunn Suntharalingam et al. "Noise resilient exceptional-point voltmeters enabled by oscillation quenching phenomena". In: *Nature Communications* 14.1 (2023), p. 5515.

[31] Yabin Jin et al. "Exceptional points for crack detection in non-Hermitian beams". In: *Journal of Sound and Vibration* 572 (2024), p. 118162.

[32] Danilo Braghini et al. "Non-Hermitian elastic waveguides with piezoelectric feedback actuation: non-reciprocal bands and skin modes". In: *Journal of Physics D: Applied Physics* 54.28 (2021), p. 285302.

[33] Qian Wu, Yangyang Chen, and Guoliang Huang. "Asymmetric scattering of flexural waves in a parity-time symmetric metamaterial beam". In: *The Journal of the Acoustical Society of America* 146.1 (2019), pp. 850–862.

[34] Romain Fleury, Dimitrios Sounas, and Andrea Alu. "An invisible acoustic sensor based on parity-time symmetry". In: *Nature communications* 6.1 (2015), pp. 1–7.

[35] Chengzhi Shi et al. "Accessing the exceptional points of parity-time symmetric acoustics". In: *Nature communications* 7.1 (2016), pp. 1–5.

[36] AR Hutson, JH McFee, and DL White. "Ultrasonic amplification in CdS". In: *Physical Review Letters* 7.6 (1961), p. 237.

[37] Vikrant J Gokhale and Mina Rais-Zadeh. "Phonon-electron interactions in piezoelectric semiconductor bulk acoustic wave resonators". In: *Scientific reports* 4.1 (2014), pp. 1–10.

[38] Joseph Schindler et al. "PT-symmetric electronics". In: *Journal of Physics A: Mathematical and Theoretical* 45.44 (2012), p. 444029.

[39] Carl M Bender et al. "Observation of PT phase transition in a simple mechanical system". In: *American Journal of Physics* 81.3 (2013), pp. 173–179.

[40] Abhishek Gupta et al. "Reconfigurable enhancement of actuation forces by engineered losses in non-Hermitian metamaterials". In: *Extreme Mechanics Letters* 59 (2023), p. 101979.

[41] Abhishek Gupta and Ramathasan Thevamaran. "Requisites on material viscoelasticity for exceptional points in passive dynamical systems". In: *Journal of Physics: Materials* 6.3 (2023), p. 035011.

[42] Yue-Ying Fan et al. "Single-and multi-wall carbon nanotubes produced using the floating catalyst method: Synthesis, purification and hydrogen up-take". In: *Carbon* 44.11 (2006), pp. 2160–2170.

[43] Kenji Hata et al. "Water-assisted highly efficient synthesis of impurity-free single-walled carbon nanotubes". In: *Science* 306.5700 (2004), pp. 1362–1364.

[44] David Murgado and Ramathasan Thevamaran. "Independent control of dynamic material properties by exploiting structural hierarchy and intrinsic structural gradients". In: *Materials Today Communications* 23 (2020), p. 100865.

[45] Mostafa Bedewy et al. "Collective mechanism for the evolution and self-termination of vertically aligned carbon nanotube growth". In: *The Journal of Physical Chemistry C* 113.48 (2009), pp. 20576–20582.

[46] Ramathasan Thevamaran, Jordan R Raney, and Chiara Daraio. "Rate-sensitive strain localization and impact response of carbon nanotube foams with microscale heterogeneous bands". In: *Carbon* 101 (2016), pp. 184–190.

[47] Roderic S Lakes. *Viscoelastic solids*. CRC press, 2017.

[48] Steven J Weigand and Denis T Keane. "DND-CAT's new triple area detector system for simultaneous data collection at multiple length scales". In: *Nuclear Instruments and Methods in Physics Research Section A: Accelerators, Spectrometers, Detectors and Associated Equipment* 649.1 (2011), pp. 61–63.

[49] L Schatzmann, P Brunner, and HU Stäubli. "Effect of cyclic preconditioning on the tensile properties of human quadriceps tendons and patellar ligaments". In: *Knee Surgery, Sports Traumatology, Arthroscopy* 6.1 (1998), S56–S61.

[50] J. L. Emery, J. H. Omens, and A. D. McCulloch. "Strain Softening in Rat Left Ventricular Myocardium". In: *Journal of Biomechanical Engineering* 119.1 (Feb. 1997), pp. 6–12. ISSN: 0148-0731.

[51] Alessandro Nava et al. “Experimental observation and modelling of preconditioning in soft biological tissues”. In: *International Symposium on Medical Simulation*. Springer. 2004, pp. 1–8.

[52] MJ Munoz et al. “An experimental study of the mouse skin behaviour: damage and inelastic aspects”. In: *Journal of biomechanics* 41.1 (2008), pp. 93–99.

[53] Alexander Lion. “A constitutive model for carbon black filled rubber: experimental investigations and mathematical representation”. In: *Continuum Mechanics and Thermodynamics* 8.3 (1996), pp. 153–169.

[54] Leonard Mullins. “Softening of rubber by deformation”. In: *Rubber chemistry and technology* 42.1 (1969), pp. 339–362.

[55] Julie Diani, Bruno Fayolle, and Pierre Gilormini. “A review on the Mullins effect”. In: *European Polymer Journal* 45.3 (2009), pp. 601–612.

[56] Kristin S. Miller et al. “Effect of Preconditioning and Stress Relaxation on Local Collagen Fiber Re-Alignment: Inhomogeneous Properties of Rat Supraspinatus Tendon”. In: *Journal of Biomechanical Engineering* 134.3 (Mar. 2012). 031007. ISSN: 0148-0731.

[57] Xiaojun Liang et al. “Phase transitions during compression and decompression of clots from platelet-poor plasma, platelet-rich plasma and whole blood”. In: *Acta biomaterialia* 60 (2017), pp. 275–290.

[58] Jonghwan Suhr et al. “Fatigue resistance of aligned carbon nanotube arrays under cyclic compression”. In: *Nature nanotechnology* 2.7 (2007), pp. 417–421.

[59] Ramathasan Thevamaran et al. “Anomalous impact and strain responses in helical carbon nanotube foams”. In: *RSC Advances* 5.37 (2015), pp. 29306–29311.

[60] JR Raney, F Fraternali, and C Daraio. “Rate-independent dissipation and loading direction effects in compressed carbon nanotube arrays”. In: *Nanotechnology* 24.25 (2013), p. 255707.

[61] Onnik Yaglioglu et al. “Wide range control of microstructure and mechanical properties of carbon nanotube forests: a comparison between fixed and floating catalyst CVD techniques”. In: *Advanced Functional Materials* 22.23 (2012), pp. 5028–5037.

[62] Shelby B Hutchens, Lee J Hall, and Julia R Greer. “In situ mechanical testing reveals periodic buckle nucleation and propagation in carbon nanotube bundles”. In: *Advanced Functional Materials* 20.14 (2010), pp. 2338–2346.

[63] Min-Feng Yu et al. “Strength and breaking mechanism of multiwalled carbon nanotubes under tensile load”. In: *Science* 287.5453 (2000), pp. 637–640.

[64] Brian G Demczyk et al. “Direct mechanical measurement of the tensile strength and elastic modulus of multiwalled carbon nanotubes”. In: *Materials Science and Engineering: A* 334.1-2 (2002), pp. 173–178.

[65] Michael FL De Volder et al. “Carbon nanotubes: present and future commercial applications”. In: *science* 339.6119 (2013), pp. 535–539.

[66] Abha Misra et al. “Synthesis and characterization of carbon nanotube–polymer multilayer structures”. In: *ACS nano* 5.10 (2011), pp. 7713–7721.

[67] Xiaodong Yang, Pengfei He, and Huajian Gao. “Modeling frequency-and temperature-invariant dissipative behaviors of randomly entangled carbon nanotube networks under cyclic loading”. In: *Nano Research* 4.12 (2011), pp. 1191–1198.

[68] R Barretta et al. “Nonlocal inflected nano-beams: A stress-driven approach of bi-Helmholtz type”. In: *Composite Structures* 200 (2018), pp. 239–245.

[69] JM Kinaret, T Nord, and S Viefers. “A carbon-nanotube-based nanorelay”. In: *Applied Physics Letters* 82.8 (2003), pp. 1287–1289.

[70] Marc Dequesnes, SV Rotkin, and NR Aluru. “Calculation of pull-in voltages for carbon-nanotube-based nanoelectromechanical switches”. In: *Nanotechnology* 13.1 (2002), p. 120.

[71] T Blesgen et al. “Multiscale mass-spring models of carbon nanotube arrays accounting for mullins-like behavior and permanent deformation”. In: *Multiscale Modeling & Simulation* 11.2 (2013), pp. 545–565.

[72] AA Zbib et al. “The coordinated buckling of carbon nanotube turfs under uniform compression”. In: *Nanotechnology* 19.17 (2008), p. 175704.

[73] Ramathasan Thevamaran, Fernando Fraternali, and Chiara Daraio. “Multiscale mass-spring model for high-rate compression of vertically aligned carbon nanotube foams”. In: *Journal of Applied Mechanics* 81.12 (2014), p. 121006.

[74] A Needleman et al. “Deformation of plastically compressible hardening-softening-hardening solids”. In: *Acta Mechanica Sinica* 28.4 (2012), pp. 1115–1124.

[75] Shelby B Hutchens, Alan Needleman, and Julia R Greer. “Analysis of uniaxial compression of vertically aligned carbon nanotubes”. In: *Journal of the Mechanics and Physics of Solids* 59.10 (2011), pp. 2227–2237.

[76] Prashant K Purohit. “Compression of Fiber Networks Modeled as a Phase Transition”. In: *Mechanics and Physics of Solids at Micro-and Nano-Scales* (2019), pp. 131–155.

[77] Xiaojun Liang et al. “Compression and recovery of carbon nanotube forests described as a phase transition”. In: *International Journal of Solids and Structures* 122 (2017), pp. 196–209.

[78] Heimo Schnablegger and Yashveer Singh. “The SAXS guide: getting acquainted with the principles”. In: *Austria: Anton Paar GmbH* (2011), pp. 1–124.

[79] John H Hubbell. “Tables of x-ray mass attenuation coefficients and mass energy-absorption coefficients”. In: *http://physics. nist. gov/PhysRefData/XrayMassCoef/* (1996).

[80] Ming Xu et al. “Alignment control of carbon nanotube forest from random to nearly perfectly aligned by utilizing the crowding effect”. In: *Acs Nano* 6.7 (2012), pp. 5837–5844.

[81] Eric R Meshot et al. “Quantifying the hierarchical order in self-aligned carbon nanotubes from atomic to micrometer scale”. In: *ACS nano* 11.6 (2017), pp. 5405–5416.

[82] D Reznik et al. “X-ray powder diffraction from carbon nanotubes and nanoparticles”. In: *Physical review B* 52.1 (1995), p. 116.

[83] Dilip K Singh, PK Iyer, and PK Giri. “Diameter dependence of interwall separation and strain in multiwalled carbon nanotubes probed by X-ray diffraction and Raman scattering studies”. In: *Diamond and Related Materials* 19.10 (2010), pp. 1281–1288.

[84] C-H Kiang et al. “Size effects in carbon nanotubes”. In: *Physical Review Letters* 81.9 (1998), p. 1869.

[85] Jiong Zhao et al. “TEM observations of buckling and fracture modes for compressed thick multiwall carbon nanotubes”. In: *Carbon* 49.1 (2011), pp. 206–213.

[86] Marino Arroyo and Ted Belytschko. “Nonlinear mechanical response and rippling of thick multiwalled carbon nanotubes”. In: *Physical Review Letters* 91.21 (2003), p. 215505.

[87] Mostafa Bedewy et al. “Population growth dynamics of carbon nanotubes”. In: *ACS nano* 5.11 (2011), pp. 8974–8989.

[88] Hiroshi Furuta et al. “Crystal structure analysis of multiwalled carbon nanotube forests by newly developed cross-sectional X-ray diffraction measurement”. In: *Applied physics express* 3.10 (2010), p. 105101.

[89] Ludovica Lattanzi et al. “Nonlinear viscoelasticity of freestanding and polymer-anchored vertically aligned carbon nanotube foams”. In: *Journal of Applied Physics* 111.7 (2012), p. 074314.

[90] F Fraternali et al. “Multiscale mass-spring models of carbon nanotube foams”. In: *Journal of the Mechanics and Physics of Solids* 59.1 (2011), pp. 89–102.

[91] Ulrike GK Wegst et al. “Bioinspired structural materials”. In: *Nature materials* 14.1 (2015), pp. 23–36.

[92] Roderic Lakes and Roderic S Lakes. *Viscoelastic materials*. Cambridge university press, 2009.

[93] TH Fang et al. “Revealing extraordinary intrinsic tensile plasticity in gradient nano-grained copper”. In: *Science* 331.6024 (2011), pp. 1587–1590.

[94] Ramathasan Thevamaran et al. “Dynamic creation and evolution of gradient nanostructure in single-crystal metallic microcubes”. In: *Science* 354.6310 (2016), pp. 312–316.

[95] Christine Ortiz and Mary C Boyce. “Bioinspired structural materials”. In: *Science* 319.5866 (2008), pp. 1053–1054.

[96] Xiaoyu Zheng et al. “Multiscale metallic metamaterials”. In: *Nature materials* 15.10 (2016), pp. 1100–1106.

[97] Ali Miserez et al. “The transition from stiff to compliant materials in squid beaks”. In: *Science* 319.5871 (2008), pp. 1816–1819.

[98] Zhen Yin, Florent Hannard, and Francois Barthelat. “Impact-resistant nacre-like transparent materials”. In: *Science* 364.6447 (2019), pp. 1260–1263.

[99] Etienne Munch et al. “Tough, bio-inspired hybrid materials”. In: *Science* 322.5907 (2008), pp. 1516–1520.

[100] James Utama Surjadi et al. “Mechanical metamaterials and their engineering applications”. In: *Advanced Engineering Materials* 21.3 (2019), p. 1800864.

[101] Sicong Shan et al. “Multistable architected materials for trapping elastic strain energy”. In: *Advanced Materials* 27.29 (2015), pp. 4296–4301.

[102] Babak Haghpanah et al. “Elastic architected materials with extreme damping capacity”. In: *Extreme Mechanics Letters* 17 (2017), pp. 56–61.

[103] Zhiyong Tang et al. “Nanostructured artificial nacre”. In: *Nature materials* 2.6 (2003), pp. 413–418.

[104] Lucas R Meza et al. “Reexamining the mechanical property space of three-dimensional lattice architectures”. In: *Acta Materialia* 140 (2017), pp. 424–432.

[105] Lucas R Meza et al. “Resilient 3D hierarchical architected metamaterials”. In: *Proceedings of the National Academy of Sciences* 112.37 (2015), pp. 11502–11507.

[106] Roderic Lakes. “Cellular solid structures with unbounded thermal expansion”. In: *Journal of materials science letters* 15.6 (1996), pp. 475–477.

[107] Namiko Yamamoto et al. “Thin Films with Ultra-low Thermal Expansion”. In: *Advanced Materials* 26.19 (2014), pp. 3076–3080.

[108] Michael De Volder et al. “Diverse 3D microarchitectures made by capillary forming of carbon nanotubes”. In: *Advanced materials* 22.39 (2010), pp. 4384–4389.

[109] Davor Copic et al. “Fabrication of high-aspect-ratio polymer microstructures and hierarchical textures using carbon nanotube composite master molds”. In: *Lab on a Chip* 11.10 (2011), pp. 1831–1837.

[110] Ludovica Lattanzi et al. “Geometry-Induced Mechanical Properties of Carbon Nanotube Foams”. In: *Advanced Engineering Materials* 16.8 (2014), pp. 1026–1031.

[111] Ludovica Lattanzi et al. “Dynamic behavior of vertically aligned carbon nanotube foams with patterned microstructure”. In: *Advanced Engineering Materials* 17.10 (2015), pp. 1470–1479.

[112] Goo-Hwan Jeong et al. “Effect of catalyst pattern geometry on the growth of vertically aligned carbon nanotube arrays”. In: *Carbon* 47.3 (2009), pp. 696–704.

[113] Gary L Farley. “Effect of specimen geometry on the energy absorption capability of composite materials”. In: *Journal of Composite Materials* 20.4 (1986), pp. 390–400.

[114] RA Alia et al. “The energy-absorption characteristics of metal tube-reinforced polymer foams”. In: *Journal of Sandwich Structures & Materials* 17.1 (2015), pp. 74–94.

[115] Bing Cao et al. “How to optimize materials and devices via design of experiments and machine learning: Demonstration using organic photovoltaics”. In: *ACS nano* 12.8 (2018), pp. 7434–7444.

[116] Zhiqiang Lin et al. “Biomimetic carbon nanotube films with gradient structure and locally tunable mechanical property”. In: *Advanced Functional Materials* 25.46 (2015), pp. 7173–7179.

[117] Ying Li and Martin Kröger. “Viscoelasticity of carbon nanotube buckypaper: zipping–unzipping mechanism and entanglement effects”. In: *Soft Matter* 8.30 (2012), pp. 7822–7830.

[118] Thomas Feser et al. “Effects of transient dynamic loading on the energy absorption capability of composite bolted joints undergoing extended bearing failure”. In: *Composite Structures* 247 (2020), p. 112476.

[119] J Patrick Royston. “An extension of Shapiro and Wilk’s W test for normality to large samples”. In: *Journal of the Royal Statistical Society: Series C (Applied Statistics)* 31.2 (1982), pp. 115–124.

[120] Trevor S Breusch and Adrian R Pagan. “A simple test for heteroscedasticity and random coefficient variation”. In: *Econometrica: Journal of the econometric society* (1979), pp. 1287–1294.

[121] James Durbin and Geoffrey S Watson. “Testing for serial correlation in least squares regression. III”. In: *Biometrika* 58.1 (1971), pp. 1–19.

[122] George EP Box and David R Cox. “An analysis of transformations”. In: *Journal of the Royal Statistical Society: Series B (Methodological)* 26.2 (1964), pp. 211–243.

[123] MC Saha et al. “Effect of density, microstructure, and strain rate on compression behavior of polymeric foams”. In: *Materials Science and Engineering: A* 406.1-2 (2005), pp. 328–336.

[124] Umud Esat Ozturk and Gunay Anlas. "Energy absorption calculations in multiple compressive loading of polymeric foams". In: *Materials & Design* 30.1 (2009), pp. 15–22.

[125] Bin Jiang et al. "Ultralight metal foams". In: *Scientific reports* 5.1 (2015), pp. 1–8.

[126] Ali Can Kaya et al. "Strain hardening reduces energy absorption efficiency of austenitic stainless steel foams while porosity does not". In: *Materials & Design* 143 (2018), pp. 297–308.

[127] G Castro and SR Nutt. "Synthesis of syntactic steel foam using gravity-fed infiltration". In: *Materials Science and Engineering: A* 553 (2012), pp. 89–95.

[128] D Ruan et al. "Compressive behaviour of aluminium foams at low and medium strain rates". In: *Composite structures* 57.1-4 (2002), pp. 331–336.

[129] Linquan Ping et al. "Vertically aligned carbon nanotube arrays as a thermal interface material". In: *APL Materials* 7.2 (2019), p. 020902.

[130] Tobias A Schaedler and William B Carter. "Architected cellular materials". In: *Annual Review of Materials Research* 46 (2016), pp. 187–210.

[131] Jens Bauer et al. "Approaching theoretical strength in glassy carbon nanolattices". In: *Nature materials* 15.4 (2016), pp. 438–443.

[132] JB Berger, HNG Wadley, and RM McMeeking. "Mechanical metamaterials at the theoretical limit of isotropic elastic stiffness". In: *Nature* 543.7646 (2017), pp. 533–537.

[133] Carlos M Portela et al. "Supersonic impact resilience of nanoarchitected carbon". In: *Nature Materials* 20.11 (2021), pp. 1491–1497.

[134] Ke Liu, Rachel Sun, and Chiara Daraio. "Growth rules for irregular architected materials with programmable properties". In: *Science* 377.6609 (2022), pp. 975–981.

[135] Lorna J. Gibson and Michael F. Ashby. *Cellular Solids: Structure and Properties*. Cambridge university press, 1997.

[136] RW Pekala, CT Alviso, and JD LeMay. "Organic aerogels: microstructural dependence of mechanical properties in compression". In: *Journal of non-crystalline solids* 125.1-2 (1990), pp. 67–75.

[137] Ling Qiu et al. "Biomimetic superelastic graphene-based cellular monoliths". In: *Nature communications* 3.1 (2012), p. 1241.

[138] Hongyou Fan et al. "Modulus–density scaling behaviour and framework architecture of nanoporous self-assembled silicas". In: *Nature materials* 6.6 (2007), pp. 418–423.

[139] Po-Yu Chen, Joanna McKittrick, and Marc André Meyers. "Biological materials: functional adaptations and bioinspired designs". In: *Progress in Materials Science* 57.8 (2012), pp. 1492–1704.

[140] Marcus A Worsley et al. "Mechanically robust and electrically conductive carbon nanotube foams". In: *Applied Physics Letters* 94.7 (2009), p. 073115.

[141] RA Alia et al. "The energy-absorbing characteristics of composite tube-reinforced foam structures". In: *Composites Part B: Engineering* 61 (2014), pp. 127–135.

[142] GB Muravskii. "On frequency independent damping". In: *Journal of Sound and Vibration* 274.3-5 (2004), pp. 653–668.

[143] Xuchun Gui et al. "Carbon nanotube sponges". In: *Advanced materials* 22.5 (2010), pp. 617–621.

[144] Haolun Wang et al. “Ultralight, scalable, and high-temperature–resilient ceramic nanofiber sponges”. In: *Science Advances* 3.6 (2017), e1603170.

[145] BJ Ramirez and V Gupta. “Evaluation of novel temperature-stable viscoelastic polyurea foams as helmet liner materials”. In: *Materials & Design* 137 (2018), pp. 298–304.

[146] FM Shuaeib et al. “A new motorcycle helmet liner material: The finite element simulation and design of experiment optimization”. In: *Materials & design* 28.1 (2007), pp. 182–195.

[147] J Zhang and MF Ashby. “Mechanical selection of foams and honeycombs used for packaging and energy absorption”. In: *Journal of Materials Science* 29 (1994), pp. 157–163.

[148] Ke Li, X-L Gao, and Jun Wang. “Dynamic crushing behavior of honeycomb structures with irregular cell shapes and non-uniform cell wall thickness”. In: *International Journal of Solids and Structures* 44.14-15 (2007), pp. 5003–5026.

[149] AT Barnes et al. “Dynamic crushing of aluminum foams: Part I–Experiments”. In: *International Journal of Solids and Structures* 51.9 (2014), pp. 1631–1645.

[150] Meng Li et al. “Crashworthiness design optimisation of metal honeycomb energy absorber used in lunar lander”. In: *International Journal of crashworthiness* 16.4 (2011), pp. 411–419.

[151] Wen Chen et al. “Stiff isotropic lattices beyond the Maxwell criterion”. In: *Science advances* 5.9 (2019), eaaw1937.

[152] Cameron Crook et al. “Plate-nanolattices at the theoretical limit of stiffness and strength”. In: *Nature communications* 11.1 (2020), p. 1579.

[153] Li Zheng et al. “Unifying the design space and optimizing linear and nonlinear truss metamaterials by generative modeling”. In: *Nature Communications* 14.1 (2023), p. 7563.

[154] Yujia Wang et al. “Achieving the theoretical limit of strength in shell-based carbon nanolattices”. In: *Proceedings of the National Academy of Sciences* 119.34 (2022), e2119536119.

[155] Widianto P Moestopo et al. “Knots are not for naught: Design, properties, and topology of hierarchical intertwined microarchitected materials”. In: *Science Advances* 9.10 (2023), eade6725.

[156] Fady F Abayazid and Mazdak Ghajari. “Viscoelastic circular cell honeycomb helmet liners for reducing head rotation and brain strain in oblique impacts”. In: *Materials & Design* (2024), p. 112748.

[157] Chan Soo Ha et al. “Rapid inverse design of metamaterials based on prescribed mechanical behavior through machine learning”. In: *Nature Communications* 14.1 (2023), p. 5765.

[158] KC Rusch. “Load-compression behavior of brittle foams”. In: *Journal of Applied Polymer Science* 14.5 (1970), pp. 1263–1276.

[159] Amir Hassani, Ali Habibolahzadeh, and Hassan Bafti. “Production of graded aluminum foams via powder space holder technique”. In: *Materials & Design* 40 (2012), pp. 510–515.

[160] QM Li, I Magkiriadis, and John J Harrigan. “Compressive strain at the onset of densification of cellular solids”. In: *Journal of cellular plastics* 42.5 (2006), pp. 371–392.

[161] RR Cousins. “A theory for the impact behavior of rate-dependent padding materials”. In: *Journal of applied polymer science* 20.10 (1976), pp. 2893–2903.

[162] Kapil Bharadwaj Bhagavathula et al. “Density, microstructure, and strain-rate effects on the compressive response of polyurethane foams”. In: *Experimental Mechanics* (2022), pp. 1–15.

[163] Rika Wright Carlsen et al. "A quantitative relationship between rotational head kinematics and brain tissue strain from a 2-D parametric finite element analysis". In: *Brain Multiphysics* 2 (2021), p. 100024.

[164] Gordon S Mustin. *Theory and practice of cushion design*. Shock and Vibration Information Center, US Department of Defense, 1968.

[165] Joachim Gross et al. "Elastic properties of crosslinked resorcinol-formaldehyde gels and aerogels". In: *Journal of non-crystalline solids* 211.1-2 (1997), pp. 132–142.

[166] B Maheswaran, K Chawla, and R Thevamaran. "Mitigating Oblique Impacts by Unraveling of Buckled Carbon Nanotubes in Helmet Liners". In: *Experimental Mechanics* 64.2 (2024), pp. 197–209.

[167] Yeonsu Jung et al. "How can we make carbon nanotube yarn stronger?" In: *Composites Science and Technology* 166 (2018), pp. 95–108.

[168] Siddhartha Pathak et al. "Viscoelasticity and high buckling stress of dense carbon nanotube brushes". In: *Carbon* 47.8 (2009), pp. 1969–1976.

[169] V Domínguez-Rocha et al. "Environmentally induced exceptional points in elastodynamics". In: *Physical Review Applied* 13.1 (2020), p. 014060.

[170] Ben Lustig et al. "Anomalous energy transport in laminates with exceptional points". In: *Journal of the Mechanics and Physics of Solids* 133 (2019), p. 103719.

[171] Matheus IN Rosa, Matteo Mazzotti, and Massimo Ruzzene. "Exceptional points and enhanced sensitivity in PT-symmetric continuous elastic media". In: *Journal of the Mechanics and Physics of Solids* 149 (2021), p. 104325.

[172] Xiaopeng Li et al. "Experimental demonstration of extremely asymmetric flexural wave absorption at the exceptional point". In: *Extreme Mechanics Letters* 52 (2022), p. 101649.

[173] Yanghao Fang, Tsampikos Kottos, and Ramathasan Thevamaran. "Emergence of Exceptional Points in Periodic Metastructures With Hidden Parity-Time Symmetric Defects". In: *Journal of Applied Mechanics* 89.12 (2022), p. 121003.

[174] Ramathasan Thevamaran et al. "Asymmetric acoustic energy transport in non-Hermitian metamaterials". In: *The Journal of the Acoustical Society of America* 146.1 (2019), pp. 863–872.

[175] Kun Ding et al. "Experimental demonstration of an anisotropic exceptional point". In: *Physical review letters* 121.8 (2018), p. 085702.

[176] Xuefeng Zhu et al. "P t-symmetric acoustics". In: *Physical Review X* 4.3 (2014), p. 031042.

[177] Jörg Doppler et al. "Dynamically encircling an exceptional point for asymmetric mode switching". In: *Nature* 537.7618 (2016), pp. 76–79.

[178] Guy Elbaz et al. "Encircling exceptional points of Bloch waves: mode conversion and anomalous scattering". In: *Journal of Physics D: Applied Physics* 55.23 (2022), p. 235301.

[179] Zhengyou Liu et al. "Locally resonant sonic materials". In: *science* 289.5485 (2000), pp. 1734–1736.

[180] Neil Boechler, Georgios Theocharis, and C Daraio. "Bifurcation-based acoustic switching and rectification". In: *Nature materials* 10.9 (2011), pp. 665–668.

[181] Mahmoud I Hussein, Michael J Leamy, and Massimo Ruzzene. "Dynamics of phononic materials and structures: Historical origins, recent progress, and future outlook". In: *Applied Mechanics Reviews* 66.4 (2014).

[182] Nicholas Fang et al. "Ultrasonic metamaterials with negative modulus". In: *Nature materials* 5.6 (2006), pp. 452–456.

[183] Kathryn H Matlack et al. "Composite 3D-printed metastructures for low-frequency and broadband vibration absorption". In: *Proceedings of the National Academy of Sciences* 113.30 (2016), pp. 8386–8390.

[184] Carl M Bender and Stefan Boettcher. "Real spectra in non-Hermitian Hamiltonians having P T symmetry". In: *Physical review letters* 80.24 (1998), p. 5243.

[185] Chen Shen et al. "Synthetic exceptional points and unidirectional zero reflection in non-Hermitian acoustic systems". In: *Physical Review Materials* 2.12 (2018), p. 125203.

[186] Lydie Ferrier et al. "Unveiling the Enhancement of Spontaneous Emission at Exceptional Points". In: *arXiv preprint arXiv:2203.02245* (2022).

[187] Eduard N Tsoy. "Coupled oscillators with parity-time symmetry". In: *Physics Letters A* 381.5 (2017), pp. 462–466.

[188] Ramy El-Ganainy et al. "Non-Hermitian physics and PT symmetry". In: *Nature Physics* 14.1 (2018), pp. 11–19.

[189] Carl M Bender. *PT symmetry: In quantum and classical physics*. World Scientific, 2019.

[190] Weijian Chen et al. "Exceptional points enhance sensing in an optical microcavity". In: *Nature* 548.7666 (2017), pp. 192–196.

[191] Jinhan Ren et al. "Ultrasensitive micro-scale parity-time-symmetric ring laser gyroscope". In: *Optics letters* 42.8 (2017), pp. 1556–1559.

[192] Martino De Carlo et al. "High-sensitivity real-splitting anti-PT-symmetric microscale optical gyroscope". In: *Optics letters* 44.16 (2019), pp. 3956–3959.

[193] Jan Wiersig. "Enhancing the sensitivity of frequency and energy splitting detection by using exceptional points: application to microcavity sensors for single-particle detection". In: *Physical review letters* 112.20 (2014), p. 203901.

[194] Rodion Kononchuk and Tsampikos Kottos. "Orientation-sensed optomechanical accelerometers based on exceptional points". In: *Physical Review Research* 2.2 (2020), p. 023252.

[195] Carl M Bender et al. "Twofold transition in PT-symmetric coupled oscillators". In: *Physical Review A* 88.6 (2013), p. 062111.

[196] Zhongming Gu et al. "Controlling sound in non-hermitian acoustic systems". In: *Physical Review Applied* 16.5 (2021), p. 057001.

[197] A Srikantha Phani. "Dissipation driven degeneracies". In: *Applied Physics Letters* 121.23 (2022), p. 231701.

[198] Linlin Geng et al. "Topological mode switching in modulated structures with dynamic encircling of an exceptional point". In: *Proceedings of the Royal Society A* 477.2245 (2021), p. 20200766.

[199] William N Findley and Francis A Davis. *Creep and relaxation of nonlinear viscoelastic materials*. Courier corporation, 2013.

[200] Ali Mostafazadeh. "Pseudo-Hermiticity versus PT symmetry: the necessary condition for the reality of the spectrum of a non-Hermitian Hamiltonian". In: *Journal of Mathematical Physics* 43.1 (2002), pp. 205–214.

[201] Christian E Rüter et al. “Observation of parity–time symmetry in optics”. In: *Nature physics* 6.3 (2010), pp. 192–195.

[202] Joseph Schindler et al. “Experimental study of active LRC circuits with PT symmetries”. In: *Physical Review A* 84.4 (2011), p. 040101.

[203] Kun Ding et al. “Emergence, coalescence, and topological properties of multiple exceptional points and their experimental realization”. In: *Physical Review X* 6.2 (2016), p. 021007.

[204] Bo Peng et al. “Parity–time-symmetric whispering-gallery microcavities”. In: *Nature Physics* 10.5 (2014), pp. 394–398.

[205] Carl M Bender, Dorje C Brody, and Hugh F Jones. “Complex extension of quantum mechanics”. In: *Physical Review Letters* 89.27 (2002), p. 270401.

[206] Singiresu S Rao and Fook Fah Yap. *Mechanical vibrations*. Vol. 4. Addison-wesley New York, 1995.

[207] Behzad Babaei et al. “Efficient and optimized identification of generalized Maxwell viscoelastic relaxation spectra”. In: *Journal of the mechanical behavior of biomedical materials* 55 (2016), pp. 32–41.

[208] D Jalocha, A Constantinescu, and R Neviere. “Revisiting the identification of generalized Maxwell models from experimental results”. In: *International Journal of Solids and Structures* 67 (2015), pp. 169–181.

[209] Julie Diani et al. “Predicting thermal shape memory of crosslinked polymer networks from linear viscoelasticity”. In: *International Journal of Solids and Structures* 49.5 (2012), pp. 793–799.

[210] H Schiessel and A Blumen. “Hierarchical analogues to fractional relaxation equations”. In: *Journal of Physics A: Mathematical and General* 26.19 (1993), p. 5057.

[211] James F Kelly and Robert J McGough. “Fractal ladder models and power law wave equations”. In: *The Journal of the Acoustical Society of America* 126.4 (2009), pp. 2072–2081.

[212] Francesco Mainardi. *Fractional calculus and waves in linear viscoelasticity: an introduction to mathematical models*. World Scientific, 2010.

[213] Rui Xiao, Hongguang Sun, and Wen Chen. “An equivalence between generalized Maxwell model and fractional Zener model”. In: *Mechanics of Materials* 100 (2016), pp. 148–153.

[214] Damian Craiem and Ricardo L Armentano. “A fractional derivative model to describe arterial viscoelasticity”. In: *Biorheology* 44.4 (2007), pp. 251–263.

[215] Antonio Gomez et al. “Experimental evidence of shear waves in fractional viscoelastic rheological models”. In: *Scientific Reports* 12.1 (2022), pp. 1–15.

[216] Ronald L Bagley and PJ Torvik. “A theoretical basis for the application of fractional calculus to viscoelasticity”. In: *Journal of Rheology* 27.3 (1983), pp. 201–210.

[217] Shu Zhang, Chunguang Xia, and Nicholas Fang. “Broadband acoustic cloak for ultrasound waves”. In: *Physical review letters* 106.2 (2011), p. 024301.

[218] Jinwoong Cha, Kun Woo Kim, and Chiara Daraio. “Experimental realization of on-chip topological nanoelectromechanical metamaterials”. In: *Nature* 564.7735 (2018), pp. 229–233.

[219] H Nassar et al. “Non-reciprocal wave propagation in modulated elastic metamaterials”. In: *Proceedings of the Royal Society A: Mathematical, Physical and Engineering Sciences* 473.2202 (2017), p. 20170188.

[220] Carl M Bender. "Making sense of non-Hermitian Hamiltonians". In: *Reports on Progress in Physics* 70.6 (2007), p. 947.

[221] Tosio Kato. *Perturbation theory for linear operators*. Vol. 132. Springer Science & Business Media, 2013.

[222] Roney Thomas et al. "Giant nonreciprocity near exceptional-point degeneracies". In: *Physical Review A* 94.4 (2016), p. 043829.

[223] Sid Assawaworrarit, Xiaofang Yu, and Shanhui Fan. "Robust wireless power transfer using a nonlinear parity–time-symmetric circuit". In: *Nature* 546.7658 (2017), pp. 387–390.

[224] Haitan Xu et al. "Topological energy transfer in an optomechanical system with exceptional points". In: *Nature* 537.7618 (2016), pp. 80–83.

[225] Peng Peng et al. "Anti-parity–time symmetry with flying atoms". In: *Nature Physics* 12.12 (2016), pp. 1139–1145.

[226] JM Lee, Tsampikos Kottos, and B Shapiro. "Macroscopic magnetic structures with balanced gain and loss". In: *Physical Review B* 91.9 (2015), p. 094416.

[227] Dengke Zhang et al. "Observation of the exceptional point in cavity magnon-polaritons". In: *Nature communications* 8.1 (2017), pp. 1–6.

[228] A Guo et al. "Observation of P T-symmetry breaking in complex optical potentials". In: *Physical review letters* 103.9 (2009), p. 093902.

[229] Zin Lin et al. "Unidirectional invisibility induced by P T-symmetric periodic structures". In: *Physical Review Letters* 106.21 (2011), p. 213901.

[230] Hossein Hodaei et al. "Parity-time–symmetric microring lasers". In: *Science* 346.6212 (2014), pp. 975–978.

[231] Liang Feng et al. "Single-mode laser by parity-time symmetry breaking". In: *Science* 346.6212 (2014), pp. 972–975.

[232] Yu-Hung Lai et al. "Observation of the exceptional-point-enhanced Sagnac effect". In: *Nature* 576.7785 (2019), pp. 65–69.

[233] Mohammad P Hokmabadi et al. "Non-Hermitian ring laser gyroscopes with enhanced Sagnac sensitivity". In: *Nature* 576.7785 (2019), pp. 70–74.

[234] Rodion Kononchuk et al. "Enhanced Signal-to-Noise Performance of EP-based Electromechanical Accelerometers". In: *arXiv preprint arXiv:2201.13328* (2022).

[235] Zin Lin et al. "Enhanced spontaneous emission at third-order Dirac exceptional points in inverse-designed photonic crystals". In: *Physical review letters* 117.10 (2016), p. 107402.

[236] Adi Pick et al. "General theory of spontaneous emission near exceptional points". In: *Optics express* 25.11 (2017), pp. 12325–12348.

[237] Adi Pick et al. "Enhanced nonlinear frequency conversion and Purcell enhancement at exceptional points". In: *Physical Review B* 96.22 (2017), p. 224303.

[238] Juanjuan Ren, Sebastian Franke, and Stephen Hughes. "Quasinormal modes, local density of states, and classical Purcell Factors for coupled loss-gain resonators". In: *Physical Review X* 11.4 (2021), p. 041020.

[239] Sebastian Franke et al. "Fermi's golden rule for spontaneous emission in absorptive and amplifying media". In: *Physical Review Letters* 127.1 (2021), p. 013602.

[240] Q Zhong et al. "Control of spontaneous emission dynamics in microcavities with chiral exceptional surfaces". In: *Physical Review Research* 3.1 (2021), p. 013220.

[241] M Khanbekyan and J Wiersig. "Decay suppression of spontaneous emission of a single emitter in a high-Q cavity at exceptional points". In: *Physical Review Research* 2.2 (2020), p. 023375.

[242] A Hashemi et al. "Linear response theory of open systems with exceptional points". In: *Nature Communications* 13.1 (2022), pp. 1–12.

[243] Edward M Purcell, Henry Cutler Torrey, and Robert V Pound. "Resonance absorption by nuclear magnetic moments in a solid". In: *Physical review* 69.1-2 (1946), p. 37.

[244] Paul Adrien Maurice Dirac. "The quantum theory of the emission and absorption of radiation". In: *Proceedings of the Royal Society of London. Series A, Containing Papers of a Mathematical and Physical Character* 114.767 (1927), pp. 243–265.

[245] Eric Betzig and Robert J Chichester. "Single molecules observed by near-field scanning optical microscopy". In: *Science* 262.5138 (1993), pp. 1422–1425.

[246] Peter Muhlschlegel et al. "Resonant optical antennas". In: *science* 308.5728 (2005), pp. 1607–1609.

[247] M Khajavikhan et al. "Thresholdless nanoscale coaxial lasers". In: *Nature* 482.7384 (2012), pp. 204–207.

[248] Jennifer T Choy et al. "Enhanced single-photon emission from a diamond–silver aperture". In: *Nature Photonics* 5.12 (2011), pp. 738–743.

[249] Mikołaj K Schmidt et al. "Elastic Purcell Effect". In: *Physical Review Letters* 121.6 (2018), p. 064301.

[250] Mathias Fink et al. "Subwavelength focussing in metamaterials using far field time reversal". In: *Acoustic Metamaterials*. Springer, 2013, pp. 141–168.

[251] Esteban Broitman. "Indentation hardness measurements at macro-, micro-, and nanoscale: a critical overview". In: *Tribology Letters* 65.1 (2017), pp. 1–18.

[252] Abhishek Gupta and Ramathasan Thevamaran. "Requisites on viscoelasticity for exceptional points in passive elastodynamic metamaterials". In: *arXiv preprint arXiv:2209.04960* (2022).

[253] A Srikantha Phani. "On the necessary and sufficient conditions for the existence of classical normal modes in damped linear dynamic systems". In: *Journal of Sound and Vibration* 264.3 (2003), pp. 741–745.

[254] Brian Richard Pauw. "Everything SAXS: small-angle scattering pattern collection and correction". In: *Journal of Physics: Condensed Matter* 25.38 (2013), p. 383201.

[255] Brian Richard Pauw et al. "The modular small-angle X-ray scattering data correction sequence". In: *Journal of applied crystallography* 50.6 (2017), pp. 1800–1811.

[256] Yuejian Wang et al. "Crystal structure of graphite under room-temperature compression and decompression". In: *Scientific reports* 2.1 (2012), pp. 1–7.